Structural and Chemical Characterization of Multi-cation Mixed-halide Perovskite

Huyen T. Pham

November 2021

Australian National University

A thesis submitted for the degree of Doctor of Philosophy

of The Australian National University

Department of Electronic Materials Engineering

Research School of Physics

College of Sciences

Declaration

I certify that this thesis does not incorporate, without acknowledgement any material previously submitted for a degree or diploma in any university, and that, to the best of my knowledge, it does not contain any material previously published or written by another person except where due reference is made in the text. The work in this thesis is my own, except for the contributions made by others as described in the Acknowledgements.

Huyen Pham

October 2021

Acknowledgements

The completion of this thesis would not have been possible without the unconditional support and generous help from my supervisors, colleagues, family, and friends.

First and foremost, I am extremely thankful to my primary supervisor, A/Prof. Jennifer Wong-Leung. It was a big honour and luck to become one of Jenny's students on the research journey at ANU. During my PhD, Jenny has provided countless insights and her great personal qualities have made my experience as a student a very happy one. I am deeply grateful for her valuable advice, inspiration, and encouragement for research, dedicated and meticulous feedback for the experimental work and writing. I would not have the knowledge and achievements as today without her guidance.

I would like to thank Prof. Klaus Weber and Dr. The Duong for being part of my supervisor panel, for providing insightful comments and helpful advice. Dr. The Duong deserves very special thanks. He has helped greatly with my experiments, particularly with TEM sample preparation, device fabrication and characterisation. It was a great pleasure working with Dr. The.

This thesis could not have been done without the experimental equipment and technical support. I also extend my thanks to the Australian National Fabrication Facility staff (Dr. Mark Lockrey, Dr. Olivier Lee Cheong Lem, Dr. Li Li, Dr. Kaushal Vora, Dr. Fouad Karouta, and Mrs. Sue Berkeley) and the Centre for Advanced Microscopy staff (Dr. Felipe Kremer and Dr. Frank Brink, Mrs. Josie Smith) for their excellent support and companionship.

I wish to thank our collaborators at the University of Oxford: Prof. Michael Johnston and Dr. Jay Patel for preparing the TEM sample by thermal evaporation method and for useful discussions and generous help.

I am also very grateful to our collaborators, Dr. William Rickard at Curtin University for his help on Focus Ion Beam-Time of Flight-Secondary Ion Mass Spectrometry (FIB-ToF-SIMS) measurement and for many fruitful discussions. Dr. Yanting Yin and Prof. Gunther Andersson at Flinders University for obtaining the X-Ray Photoelectron Spectroscopy (XPS) measurement.

I would like to extend my gratitude to our collaborators at Solar lab, Research School of Engineering, ANU: Dr. Yiliang, Dr. Arafat, Dr. Nandi, Grace, and Naeimeh for preparing the TEM samples and sharing their knowledge with me.

I am also deeply grateful to my group leader, Distinguished Prof. Chennupati Jagadish for his encouragement, and comments on my research. Additionally, I also want to thank Prof. Hoe Tan for helpful comments on my research during the group meeting.

My heartfelt thanks to my friends and co-workers in our group, Zahra, Nikita, Anha, Aswani, Shiyu, Gayatri, Fanlu, Sonachand, Ahmed, Huma, Wei, Mohammed, Dr. Julie, Dr. Dipankar, Dr. Zhicheng, Dr. Naiyin, and Dr. Vidur. I would like to express my sincere thanks to all of them for their great assistance, kindness, and friendship. I also appreciate my friends at Graduate House including Titus, Lin, and Yishuan Tsai for having dinner together and sharing PhD life in Canberra. Thank you all for making my PhD life such a wonderful experience.

Studying and living far away from home are always challenges. I am glad to have found some of my best friends in Canberra. I would like to thank my Vietnamese friends for their precious friendship, unwavering support, and tolerance for my unmeant caprice.

Finally, I would like to take this opportunity to say a big thank you to my dear partner Tam, who has encouraged me to pursue the PhD program here at ANU. My parents, younger brother, and grandparents deserve special thanks for their continuous support, encouragement, and unconditional love which help me to overcome all the challenges during my PhD journey.

Abstract

Perovskite solar cells (PSCs) have demonstrated a breakthrough in power conversion efficiency (PCE), making them the fastest developing solar cell technology in history. The highest efficiency of PSCs up to 25.5% reported in 2021 is already rivalling the best of Si solar cells.[1] However, the commercialization of PSCs faces two major challenges: the instability of the perovskite layer and the toxicity of lead. Furthermore, the exact mechanism behind their tremendous increase in efficiency and outstanding optical properties remains unclear. Especially, the atomic structure and microstructure of hybrid metal halide perovskite layers are also not well understood yet.

Recently, several inorganic cations (Rb, Cs) have been incorporated into the mixed-halide perovskite materials to improve the stability of PSCs. Nonetheless, the underlying mechanism of how those cations affect the microstructure and stability of perovskite materials is still unclear. In this study, we use low-dose electron microscopy and atomic structure simulations to identify the microstructure, crystal structure and defects of the multi-cation mixed-halide perovskite. We demonstrate that Cs^+ cation is uniformly incorporated throughout the perovskite layer, while Rb^+ cation is segregated as a discrete Rb-rich phase at the grain boundary. Our electron diffraction studies show the coexistence of cubic and tetragonal structures in the perovskite film at room temperature.

We use a combination of low-dose electron microscopy studies and atomic structure simulations to identify a common twinning structure in both cubic and tetragonal phases of the multi-cation mixed-halide perovskite. We also present clear evidence of $\{111\}$ twins in the cubic (c) structure which are equivalent to $\{011\}$ twins in the tetragonal (t) structure. Then, a unique way for differentiating between the tetragonal and cubic forms of these twins is developed. Our systematic electron diffraction analyses and simulations demonstrate unequivocally that the same twinning structure is present in both phases, notably with a perfectly coherent $\{111\}_c$ twin boundary and a semi-coherent $\{011\}_t$ twin boundary. The atomic configuration of the twin boundary is discussed with possibilities of being AX_3 centred (with A=Cs, FA, MA and X=I, Br) or B-site centred (Pb) for both crystal structures. We propose that the twin boundary is a key nucleation region for phase segregation which acts as a potential well or barrier to electrons and holes depending on its composition and hence bandgap.

Moreover, we systematically investigate the impact of MACl and CsCl additives upon the morphology, grain size, crystal structure, defects, optical properties, and PV performance of FA-based PSCs. We demonstrate that the MACl and CsCl additions have a great potential to stabilize the cubic $FAPbI_3$ with a $2 \times 2 \times 2$ supercell expansion and the $Im\bar{3}$ space group. The morphology and crystal structure of the nanotwins (NTs) and stacking faults (SFs) of the perovskite films are studied. A detailed analysis employing electron diffraction patterns shows that both the NTs and SFs are on the $\{111\}_c$ planes. In addition, the optimized PSCs with 10 mol% CsCl exhibit the best device performance with a PCE of 21.98%. These results prove that the incorporation of CsCl into the perovskite precursor mixture is an extremely effective method to obtain high-quality film formation, resulting in a highly efficient and stable PSC device.

Finally, we investigate the key role of halide anions in additives using CsX (X = I, Br, and Cl) on the microstructure, crystal structure, structural defects, optoelectronic properties and photovoltaic parameters of $FAPbI_3$ PSCs. Among the additives tested, $FAPbI_3$ perovskite film with CsCl showed the highest photoluminescence (PL) intensity, longest PL lifetime and highest PCE compared to these films with I and Br anions. The morphology and crystallography of $\{111\}_c$ NTs and SFs are studied using transmission electron microscopy (TEM) and selected area electron diffraction pattern (SAED). The microstructure, crystallography and atomic structure model of two twin boundaries intersecting with an angle of around 70.5° are presented. Furthermore, the relation between the structure of twins and the hexagonal phase is discussed. We also systematically investigate the degradation pathways and their underlying mechanism for CsX-$FAPbI_3$ perovskite compositions under ambient conditions.

This study provides a thorough understanding of the crystallography and defects in multi-cation mixed-halide perovskite. Furthermore, the influence of defects on optical properties and device performance is investigated. All the contents presented in this thesis are expected to boost the progress towards improving the efficiency and stability of the PSCs, paving the way for practical applications of this technology in the near future.

Publications

Journal papers

1. H. T. Pham, T. Duong, W. D. A. Rickard, F. Kremer, K. J. Weber, J. Wong-Leung. "Understanding the Chemical and Structural Properties of Multiple-Cation Mixed Halide Perovskite". *J. Phys. Chem. C*, 123, 43, **2019**, 26718-26726.
2. M. A. Mahmud, T. Duong, Y. Yin, H. T. Pham, D. Walter, J. Peng, Y. Wu, L. Li, H. Shen, N. Wu, *et al*. "Double-Sided Surface Passivation of 3D Perovskite Film for High-Efficiency Mixed-Dimensional Perovskite Solar Cells". *Adv. Funct. Mater*. **2019**, 1907962.
3. T. Duong, H. T. Pham, T. C. Kho, P. Phang, K. C. Fong, D. Yan, Y. Yin, J. Peng, M. A. Mahmud, S. Gharibzadeh, *et al.* "High Efficiency Perovskite-Silicon Tandem: The Effect of Surface Passivation Versus Bulk Incorporation of 2D Perovskite". *Adv. Energy Mater*. **2020**, 1903553.
4. H. T. Pham, T. Duong, K. J. Weber, J. Wong-Leung. "Insights into Twinning Formation in Cubic and Tetragonal Multi-Cation Mixed-Halide Perovskite". *ACS Materials Lett*. 2, 4, **2020**, 415–424.
5. S. Moghadamzadeh, S. Gharibzadeh, T. Duong, I. M. Hossain, T. Abzieher, H. T. Pham, H. Hu, U. Lemmer, B. A. Nejand, U. W. Paetzold. "Triple-cation Low-bandgap Thin-films for High-Efficiency 4-Terminal All-Perovskite Tandem Solar Cells". *J. Mater. Chem. A.* **2020**, 8, 24608.
6. Md. A. Mahmud, T. Duong, Y. Yin, J. Peng, Y. Wu, T. Lu, H. T. Pham, H. Shen, D. Walter, H. T. Nguyen, *et al.* "In-situ Formation of Mixed-dimensional Surface Passivation Layers in Perovskite Solar Cells with Dual-isomer Alkylammonium Cations". *Small*. **2020,** 2005022, 1-10.
7. T. Duong, H. T. Pham, Y. Yin, J. Peng, M. A. Mahmud, Y. Wu, H. Shen, J. Zheng, T. P. Tran, T. Lu, *et al.* **"**High Efficiency Perovskite-Silicon Tandem Solar Cells through Surface Passivation with Long Alkyl Chain Length Organic Cations"**.** *J. Mater. Chem. A.* **2021,** 9, 18454-18465.
8. H. T. Pham, Y. Yin, G. Andersson, K. J. Weber, T. Duong, and J. Wong-Leung. "Unravelling the Influence of Additive on the Formation of Nanotwins, Stacking Faults

and Cubic Supercell Structure in FA-based Perovskite Solar Cells". *Nano Energy*. **2021.** 366, 106226.

9. Md. A. Mahmud, H. T. Pham, T. Duong, Y. Yin, J. Peng, Y. Wu, W. Liang, L. Li, A. Kumar, H. Shen *et al.* "Combined Bulk and Surface Passivation in Dimensionally Engineered 2D-3D Perovskite Films via Chlorine Diffusion". *Adv. Funct. Mater*. **2021,** 2104251, 1-11.
10. T. Duong, A. John, H. Chen, H. T. Pham, K. Murugappan, T. P. Tran, and A. Tricoli, and K. Catchpole. Mixed-dimensional Organic-inorganic Metal Halide Perovskites (OIMHP) for High Performance and Stable NO_2 Gas Sensors. *Mater. Adv.* **2022**, 3, 1263-1271.
11. N. Mozaffari, T. Duong, M. M. Shehata, A. D. Bui, H. T. Pham, Y. Yin, A. O. Mayon, J. Zheng, Md. A. Mahmud, G. D. Tabi, *et al*. Effective Surface Passivation of Perovskite Solar Cells with Mixed Guanidinium and Octylammonium Cations. *Solar RRL*. **2022**, 2200355.
12. H. T. Pham, K. J. Weber, T. Duong, and J. Wong-Leung. Impact of Halide Anion in CsX (X = I, Br, Cl) on the Microstructure and Photovoltaic Performance of $FAPbI_3$ Perovskite Solar Cells. *Solar RRL*. **2022**, 2200345, 1-11.
13. G. D. Tabi, H. T. Pham, H. Zhan, D. Walter, A. O. Mayon, J. Peng, T. Duong, M. Ismael, H. Shen, L. Duan et al. LiI doping of mixed-cation mixed-halide perovskite solar cells: defect passivation, controlled crystallization and transient ionic response. *J. Mater. Chem. A*. **2022**.
14. Y. Wu, N. Wu, H. Nguyen, H. T. Pham, C. Zhu, W. Liang, L. C. Lem, W. D. A. Rickard, Y. Han, J. Peng. *et al*. The Role of the $MA_2Pb_3I_8(DMSO)_2$ Intermediate Phase on the Passivation of Grain Boundaries in Halide Perovskites. **2022** (submitted).
15. H. T. Pham, B. D. Anh, K. J. Weber, J. Wong-Leung, and T. Duong. Microstructure and Crystal Structure of Surface Passivation Layer in 2D-3D Perovskite Solar Cells. **2022** (in preparation).

Conference presentations

1. H. T. Pham, T. Duong, W. D. A. Rickard, K. J. Weber, and J. Wong-Leung. “Insights into The Microstructure and Elemental Composition of Multi-cations Mixed-halides Perovskite”. ACMM26 2020, Canberra, Australia.
2. H. T. Pham, T. Duong, W. D. A. Rickard, K. J. Weber, and J. Wong-Leung. “Unravelling the Microstructure of Perovskite”. ICONN 2020, Brisbane, Australia.
3. H. T. Pham, T. Duong, W. D. A. Rickard, F. Kremer, K. J. Weber, and J. Wong-Leung. “The Influence of Inorganic Cations in the Elemental Composition, Morphological and Structural Properties of Organometal Halide Perovskites”. ICMAT 2019, Marina Bay Sands, Singapore.

Table of Contents

List of Figures

List of Tables

List of abbreviations

AFM	Atomic Force Microscopy
BF	Bright Field
BFP	Back Focal Plane
c	Cubic
CDF	Centred Dark Field
CSL	Coincident Site Lattice
DP	Diffraction Pattern
DF	Dark Field
DMF	Dimethylformamide
DMSO	Dimethyl sulfoxide
EDS(X)	Energy Dispersive X-ray Spectroscopy
EELS	Electron Energy Loss Spectroscopy
EM	Electron Microscopy
ETL	Electron Transport Layer
FA	Formamidinium
$FAPbI_3$	$CH(NH_2)_2PbI_3$
fcc	Face-centred Cubic
FTO	Fluorine-doped Tin Oxide
FF	Fill Factor
FIB	Focused Ion Beam
FWHM	Full-With at Half Maximum
ITO	Indium-doped Tin Oxide
HAADF	High-angle Annular Dark Field
hcp	Hexagonal Close-packed
HTL	Hole Transport Layer
HRTEM	High-resolution Transmission Electron Microscopy
MA	Methylammonium
$MAPbI_3$	$CH_3NH_3PbI_3$
NT	Nanotwin
OIMHP	Organic-inorganic Metal Halide Perovskite

PCE	Power Conversion Efficiency
PFM	Piezoresponse Force Microscopy
PL	Photoluminescence
PSCs	Perovskite Solar Cells
PV	Photovoltaic
PTAA	poly [bis(4-phenyl) (2, 4, 6-trimethylphenyl) amine]
SAED	Selected Area Electron Diffraction
SEM	Scanning Electron Microscopy
SF	Stacking Fault
STEM	Scanning Transmission Electron Microscopy
t	Tetragonal
TB	Twin Boundary
TEM	Transmission Electron Microscopy
ToF-SIMS	Time of Flight Secondary Ion Mass Spectroscopy
TRPL	Time-resolved Photoluminescence
XRD	X-ray Diffraction
XPS	X-ray Photoemission Spectroscopy

Chapter 1. Introduction

This chapter gives an overview of renewable energy and the motivation for this research. The aims of the project are also presented in this chapter, which are desired essential for understanding the microstructure, crystal structure, and defects of various perovskite compositions. Furthermore, the main outcomes and the outline of the project will also be discussed.

1.1 Thesis motivation

Global energy consumption is predicted to significantly increase in the next decades due to the rising energy demand for industrial and economic development. The environmental impact and depletion of fossil fuel resources have placed a higher demand on sustainable and renewable energy sources. Recently, research and development into promising new materials and technologies for renewable energy sources have been under the spotlight in both academia and industry. Renewable energy sources, including wind, solar, tidal, waves, biomass, geothermal, etc., will be a saviour in the energy crisis. Among those, solar energy is one of the most successful candidates in the international effort to reduce our dependence on fossil fuels. It can be converted into electricity directly via a photovoltaic (PV) effect in an optoelectronic device called “solar cell”. Solar cell technology is capable of providing an eco-friendly and cost-effective PV energy generation for sustainably powering economic growth.

Among various technologies investigated, a new arrival in the solar cell technologies family is the organic-inorganic metal halide perovskite (OIMHP). Perovskite solar cells (PSCs) have received enormous interest due to their remarkable performance achieved in optoelectronic and PV devices. There are more than 20000 publications since 2009 on PSCs with a record of 25.5% efficiency in 2021.[1] This value is already rivalling the best crystalline Si solar cells (27.6% efficiency) and the best thin-film solar cell technologies (23.4% efficiency).[1] PSCs have demonstrated a breakthrough in power conversion efficiency (PCE), making them the fastest developing solar cell technology in history. With many advantages over conventional crystalline Si solar cells such as rapid development, flexible substrates, low-

temperature processing, and low-cost fabrication, PSCs are set to be a game-changer in the next-generation PV industry in the foreseeable future.

OIMHP materials have attracted extensive attention due to its excellent properties such as long diffusion lengths, fast charge separation, high charge-carrier mobilities, lightweight and semi-transparency, etc., that make them ideal materials for solar cell applications.[2-4] Interestingly, the bandgap of OIMHP materials is tuneable over a wide range through the variation of its composition, which opens up another promising application for PSCs in high-performance perovskite/Si tandem device architectures with potential PCEs over 30%.[5, 6] Hence, PSCs have now become the lab champions for "third-generation" photovoltaics.[7]

However, despite impressive laboratory progress in this area, the commercialization of PSCs faces several challenges. The first issue is the instability of the perovskite layer under the influence of light, moisture, and heat. Secondly, most of reported high efficiencies for PSCs were obtained on a very small device with a typical area of ~0.1 cm^2 in the lab conditions,[8] while the high performance of large perovskite solar panels has not been demonstrated yet.[9, 10] Generally, the possibility to grow and deposit high-quality perovskite films over large areas is the key factor to achieve the excellent performance of large-scale PSCs. The lifetime of such large-area PSCs is another issue that needs to be figured out. The last challenge is relevant to the possible environmental pollution and human health effect, as PSCs possess toxic and harmful lead component.

In addition, the exact mechanism behind their tremendous increase in efficiency and outstanding optical properties (such as long charge carrier lifetime and strong absorption) remains unclear. Especially, the atomic structure and microstructure of OIMHP layers are also not well understood yet. In many cases, fundamental knowledge about the actual phase, crystal structure and space group of perovskite layers have not been rigorously investigated. OIMHP materials undergo complicated phase transitions as a function of the temperature.[11] Therefore, our limited understanding of these phase stabilities results in problems regarding electronic structure, band structure, optical properties and device efficiency that cannot be understood.

1.2 Thesis objectives and scope

As discussed above, the limitation in understanding the microstructure and crystal structure of perovskite materials results in a lack of knowledge about the intrinsic mechanism behind the impressive device performance. Therefore, the main objective of this PhD project is to contribute to knowledge about the microstructure, crystal structure, elemental composition, and defects in OIMHP materials. Moreover, the impact of the microstructure on the optical properties and device performance will also be studied.

To achieve this, the OIMHP materials and solar cell devices were characterised by electron microscopy techniques. However, the as-fabricated perovskite film is susceptible to electron beam damage. A long electron beam exposure may result in the disappearance of diffraction spots and defect's morphology.[12, 13] In order to minimise the damage of OIMHP materials under electron beam, we develop the low-dose technique and a rapid acquisition condition. Furthermore, to avoid damaging sample preparation steps, different perovskite compositions are deposited directly on ITO/glass substrates and TEM Cu or Au grids for electron microscopy analysis. This PhD thesis has been conducted with the aims to:

- Characterise the microstructure, crystal structure, and elemental composition of various photoactive OIMHP materials using low-dose electron microscopy and simulation software (CrystalMaker, SingleCrystal, CrystalDiffract).

- Demonstrate the influence of Rb^+ and Cs^+ cations on the morphology, crystallographic structure, phase transition, defects, and chemical composition of multi-cation mixed-halide perovskites.

- Characterise the morphology and crystallography of twin defects in multi-cation mixed-halide perovskite film using electron microscopy techniques, CrystalMaker and SingleCrystal software.

- Investigate the impact of additives upon the morphology, grain size, crystal structure, defects, optical properties, and PV performance of FA-based PSCs.

- Study the influence of additives on the formation of nanotwin (NT) and stacking fault (SF) defects in FA-based PSCs.

- Finally, demonstrate the impact of halide anions in CsX (X = I, Br, Cl) on the microstructure, optical properties, and device performance of $FAPbI_3$ PSCs.

1.3 Thesis outline

This PhD thesis addresses the progress and achievement in the microstructural characterisation and the development of novel PV materials for solar cells. It provides a thorough understanding and highlights new approaches to clarify the impressive efficiency of PSCs. The thesis includes 8 chapters:

Chapter 1 presents a motivation for the research, and outlines the thesis objective, scope, and challenge.

Chapter 2 reviews the literature on the current development of various solar cells technology, the progress on PSCs, and fundamental knowledge about structural and material properties of perovskites. In detail, the crystal structures, and actual phases of OIMHP materials at different temperatures will be provided. The review also focuses on the structure of the PSC devices, hysteresis behaviour, and different fabrication methods of the perovskite layer. The final section in this chapter discusses the crystallography of twins and their impact on various properties of different materials.

Chapter 3 provides details on the experimental method to prepare various perovskite compositions, the device fabrication process and the basic principles of different characterisation techniques used in this thesis. Various kinds of electron beam damage and challenges in handling the OIMHP materials under electron beam will also be provided.

Chapter 4 studies the chemical and structural properties of $Rb_{0.03}Cs_{0.07}FA_{0.765}MA_{0.135}PbI_{2.55}Br_{0.45}$ perovskite composition. The simulation and experimental results clarify further the fundamental understanding of the morphology, microstructure, crystal structure, phase segregation, and elemental composition of multi-cation mixed-halide perovskites. The Rb^+ and Cs^+ cations were typically segregated at the grain boundary of the perovskite film as a discrete Rb- and Cs-rich phase. However, the Cs^+ cation was also found to be incorporated into the perovskite structure. Furthermore, we show the evidence for the coexistence of cubic and tetragonal phases in the diffraction patterns at room

temperature. The results presented in this chapter offer additional insights into the cation incorporation in mixed-halide perovskite materials.

Chapter 5 explores the twinning formation in cubic and tetragonal multi-cation mixed-halide perovskite. We develop a combination of low-dose electron microscopy studies, atomic structure model, and electron diffraction pattern simulations to identify a common twinning structure in both the cubic and tetragonal phases of the $Rb_{0.05}Cs_{0.095}MA_{0.1425}FA_{0.7125}PbI_2Br$ hybrid perovskite. A unique way of differentiating between the tetragonal (t) and cubic (c) forms of these twins was developed. This provides new insights into the microstructure and defects in multi-cation mixed-halide perovskite materials.

Chapter 6 investigates the influence of MACl and CsCl additives on the formation of cubic supercell structure, nanotwins (NTs) and stacking faults (SF) in FA-based PSCs. In addition, the microstructure and crystal structure of NT and SF defects were investigated using electron microscopy techniques. The NT and SF densities can be changed by varying the concentration of the additive in the perovskite precursor mixture, which have an impact on the optical properties and hence the PV performance of PSCs. These results prove that the incorporation of CsCl in the perovskite precursor mixture is an extremely effective method to obtain high-quality film formation, resulting in a highly efficient and stable PSC device.

Chapter 7 investigates the key role of halide anions on the microstructure, crystal structure, structural defects, optoelectronic properties and PV parameters of $FAPbI_3$ PSCs with the use of CsX additives (X = I, Br, and Cl). By introducing CsCl into $FAPbI_3$, the perovskite film showed the highest PL intensity, longest PL lifetime and highest PCE compared to the films with CsI and CsBr additions. The morphology and crystallography of $\{111\}_c$ NTs and SFs are studied using transmission electron microscopy (TEM) and selected area electron diffraction (SAED). The $\{111\}_c$ TBs intersect at 70.5º as commonly observed in perovskite materials.[14-16] The microstructure, crystallography and atomic structure model of two twin boundaries (TBs) intersecting at an angle of around 70.5° are presented. Finally, we systematically investigate the degradation pathways and their underlying mechanism for CsX-$FAPbI_3$ perovskite under ambient conditions.

Chapter 8 presents our conclusions and summarizes the main contribution of this thesis. The opportunities and strategies for the future direction are also highlighted in order to further

enhance the fundamental knowledge about microstructure and clarify the mechanism behind the impressive performance of PSCs.

Chapter 2. Literature review

This chapter discusses the history and current development of various solar cell technologies and the progress of PSCs. The fundamental knowledge about crystallography of the OIMHP materials commonly used in PVs will be presented. And most importantly, the actual phases of perovskite materials at different temperatures will also be reviewed. The content presented here will allow a better understanding of crystallography and the influence of twins on various properties of different materials. Furthermore, up-to-date research progress on the microstructure and defects of PSCs is summarized.

2.1 History of solar cells

In 1839, for the first time, Edmond Becquerel discovered the photovoltaic effect that was used to explain how to convert the energy from the sun into electricity. Soon after, the photoconductivity of selenium (Se) was discovered by an English electrical engineer, Willoughby Smith, in 1873. He found that the electrical resistance of Se changed significantly with the amount of light falling on it. In 1883, the first design of Se solar cells was proposed by an American inventor named Charles Fritts. Albert Einstein was awarded the Nobel Prize in 1921 for his theories on the photoelectric effect, which is the process by which the electron is emitted from the metal surface by light.[17]

Semiconductor materials are considered as one of the key components in designing the PV devices. They are commonly used as the absorber layer of solar cell devices and governed essentially by the value of their bandgap.[18] When sunlight shines on the solar cell devices, electrons absorb the energy of photon and move from the valence band into the conduction band of a semiconductor material. Only the photons with energy higher than the bandgap of a semiconductor can be absorbed. This causes the dissipation of excess energy from those photons via a process called thermalization, in which the excited electrons relax to the edge of conduction band. This is the fundamental origin of the solar cell efficiency limitation, as we must choose between minimizing the thermalization loss and/or having a low bandgap absorber layer to extend the absorbable photon range. In general, an ideal solar cell device has a direct

bandgap between 1.1 and 1.4 eV to absorb the maximum number of photons from the sun's radiation and achieve the highest solar energy conversion efficiency (~34%).[19]

2.1.1 Silicon photovoltaics

In 1918, Jan Czochralski developed a technique to grow single-crystal Si ingots opening up opportunities for mass fabrication of devices. In 1954, three scientists in Bell Labs (USA) (Daryl Chapin, Calvin Fuller, and Gerald Pearson) introduced the first crystalline Si-based solar cell which had a PCE of 4.5%.[20] The technological progress and PCE of Si solar cells continued to improve at breakneck speed. In 1985, the researchers at the University of New South Wales achieved a record over 20% efficiency for Si solar cells under 1-sun conditions. Since then, the record efficiency of Si solar cells has increased to 25.6% in 2014 and to 26.7% in 2017.[21, 22] Currently, the entire photovoltaic (PV) market is predominantly occupied by the so-called first-generation solar cell technology which comprises chiefly single crystalline silicon cells due to their high efficiency and long lifetime (~30 years). However, the efficiency of single-junction Si solar cells has almost reached the theoretical Shockley-Queisser limit of 30% for single-junction devices.[23, 24] Therefore, researchers are now looking for alternative technologies to achieve highly efficient and long-term stability devices, which also provides diversity to the PV market.[25]

2.1.2 Thin-film photovoltaics

Thin-film technologies are considered as the second-generation of PV solar cells and include materials such as copper indium gallium selenide (CIGS), cadmium telluride (CdTe), and hydrogenated amorphous silicon (α-Si:H).[26]

CIGS based solar cell technology is one of the most prospective thin-film technologies due to the ease of large-scale manufacturing. In 1976, the first thin film CIGS solar cell was reported by Kazmerski *et al*. with a PCE of 4.5%.[27] In 2019, the lab record efficiency of CIGS was 23.35% which is comparable to commercial crystalline Si but less expensive and easy to fabricate.[28] However, the efficiency of commercial CIGS modules still lags significantly behind that of Si-based modules. CIGS is a narrow direct bandgap semiconductor. In addition, the bandgap of CIGS material can be adjusted from 1.04 to 1.68 eV by varying the Ga/In ratio. The CIGS layers with 1 μm thick (100 times thinner than a crystalline silicon solar

cell) have efficient sunlight absorption. The typical structure of CIGS solar cell device is composed of substrate/Mo/CIGS/CdS/SnO:Al/metal grid.[29]

CdTe is a II-VI compound semiconductor and possesses an ideal band gap of approximately 1.43 eV with good absorption and low energy losses. In 1972, the first laboratory CdTe was introduced by Bonnet and Rabnehorst with a PCE of 6%.[30] Solar cells based on this compound were commercially developed and have up to 22.1% efficiency.[1] CdTe solar cells can be fabricated through low-temperature processes, allowing flexible and affordable production, thus making them the most commercially successful thin-film PV technology.

With a direct bandgap, α-Si:H film in a few microns thickness can absorb a large fraction of solar radiation, starting from 1.7 eV and reaching the highest absorption capability from 2 eV.[31] The highest PCE for single-junction planar thin-film α-Si:H solar cell is 14%.[1] α-Si:H material is widely employed in various thin-film solar cell technologies as photoactive and doped layers. However, the thinner absorbing layer and light degradation problem cause the limitation in device efficiency using this material.

In summary, thin-film technologies have a significantly lower cost compared to conventional Si technology, but the rarity of materials, toxicity, and environmental issues have restricted the commercialization of the second-generation solar cell. Furthermore, the reliability of thin-film technologies is also questionable.[29]

2.1.3 Emerging photovoltaics

In the field of PVs, emerging technologies based on dye-sensitized solar cells (DSSCs), copper zinc tin sulfide (CZTS), organic photovoltaics (OPVs), quantum dot solar cells (QDSCs), PSCs, and perovskite/Si tandem cells have shown tremendous potential to surpass the current PCE of single-junction solar cell based on Si.[32] These are novel technologies which are promising but not commercially developed yet.

DSSCs have gained widespread attention due to their good PV performance, particularly under low-light intensity and their low-cost fabrication.[33] The basic principle of DSSC is based on a photo-electrochemical cell. Figure 2.1a shows a typical DSSC device, which is composed of three main components including a photoanode, a counter electrode, and a liquid electrolyte.[34] The photoanode is commonly made from a mesoporous metal oxide layer (such as TiO_2, ZnO, SnO_2) deposited on a transparent conductive oxide (TCO) (such as

indium doped tin oxide (ITO), fluorine-doped tin oxide (FTO)). Iodide-triiodide (I^-/I_3^-) solution is the most common electrolyte, while platinum (Pt) coated conductive glass substrate is usually used as the counter electrode. The liquid electrolyte has been replaced in recent DSSCs to achieve a solid-state device, but the rest of the components remain the same. This includes a hole transport layer (HTL), an absorber layer, an electron transport layer (ETL) and a TCO layer (see Figure 2.1b). The role of the HTL is to collect holes from the absorber layer, transport them towards the cathode and block electrons. The ETL has the same function but transport electrons instead of holes. Recently, the DSSC devices have achieved record efficiencies exceeding 13% under full sun illumination.[35] However, DSSCs can also encounter the instability problems, mainly temperature instability and solvent permeation of the liquid electrolyte.

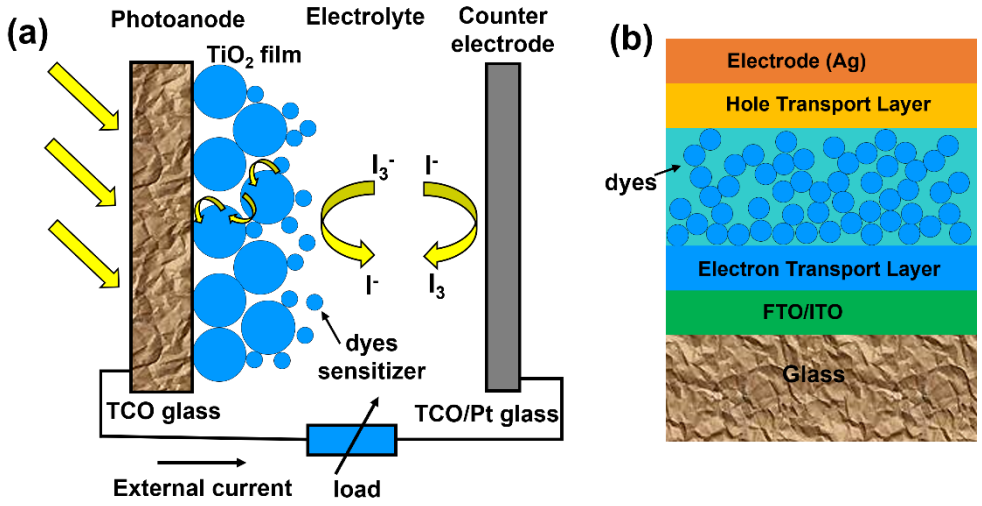

Figure 2.1. Schematic diagram of the (a) DSSC device and (b) solid-state DSSC device. Adapted from [36].

CZTS solar cells use an active layer of Cu_2ZnSnS_4 with the kesterite crystal structure. Although CZTS cells have many similar properties to second-generation CIGS cells, they do not use toxic compounds such as cadmium or rare indium but use abundant and non-toxic materials. The bandgap of CZTS is tuneable in a wide range of energies (from 1.5 to 2.1 eV) by alloying with other elements such as Ge or Mg, thus making it ideal for the topmost cells in Si-based tandem cell stacks.[37] The record efficiency for a pure CZTS cell is 12.6%.[38-41] The disadvantages of CZTS include the material complexity and quality.[42]

OPV is also another promising solar cell technology with fast-growing PCE. The most attractive advantage of OPV cells is solution processability, enabling the low-cost large-area production via scalable printing technologies.[43] However, currently small area spin-coating is the main fabrication method of OPV. Although the PCEs of single-junction OPV cells have surpassed 17%,[44] the large amount of waste from its solution fabrication makes it unsuitable for large-scale production. Therefore, fabrication scalability is an important factor that must be taken into account when designing highly efficient OPV materials.

QDSCs use solution processed semiconductor nanocrystals as a light absorber.[45] PbS or PbSe quantum dot (QD) based solar cells are currently recognized as the best candidates in the QDSCs.[46] Similar to OPVs, the advantages of QD solar cells include the flexible bandgap tuning of the active layer by changing the dot size, the low-temperature and solution-based fabrication process. However, the use of toxic or rare materials, such as Se, is also a disadvantage for QD solar cells. Since the first publication, the efficiency of QD solar cells has increased dramatically and now exceeds the value of 18.1%.[1] If the current obstacles, including the distribution and stability of QDs, the ease of fabrication, and the improvement of mid-gap states/inherent disorder in QD films, can be resolved, solar cells based on QDs will be highly promising for commercialization.[47, 48] Figure 2.2 shows the solar cell efficiency over time for a variety of different PV technologies.

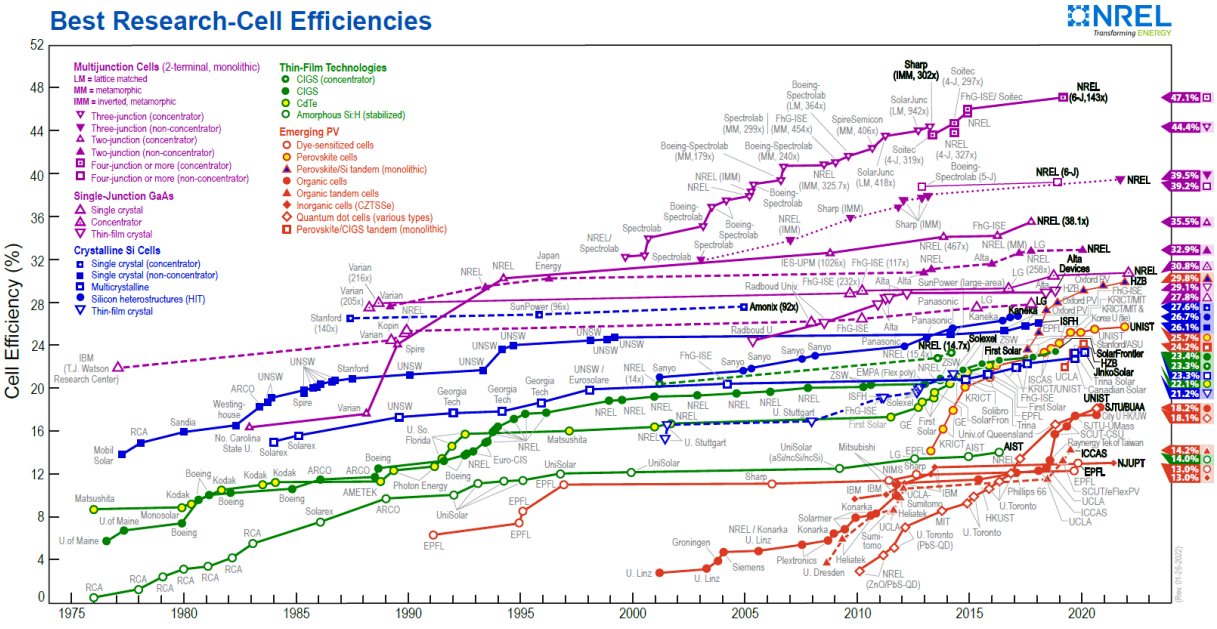

Figure 2.2. Best cell efficiencies chart of photovoltaic technologies by research published by National Renewable Energy Laboratory (NREL). Adapted from [1]

2.2 Perovskite solar cells

2.2.1 Overview of perovskite solar cells

In 1990, Mitzi *et al*. demonstrated that the OIMHP have great optoelectronic properties for applications in the field of LEDs, photodetectors, transistors and solar cells.[49] The first PSCs were reported by Miyasaka *et al.* in 2009. In addition, the OIMHP was utilized as a light-absorbing layer in DSSCs, with an initial PCE of 3.8%.[50] However, not much attention was paid to these devices due to the poor stability of perovskites in the liquid electrolyte which lasted only for a few seconds. In 2012, Park *et al.* fabricated the first solid-state PSC that can overcome this problem. Spiro-MeOTAD (2,2′,7,7′-tetrakis (N,N-di-p-methoxyphenylamine)-9,9′-spirobifluorene) was employed as the HTL and the device reached a value of 9.7% efficiency.[51] This modification not only improved the efficiency but also significantly enhanced the long-term stability of solid-state PSC. Since then, the number of publications on PSCs has been dramatically increasing, with more than 3000 publications in 2017 alone.[52]

The operation of PSCs is basically similar to that of most other solar cells based on inorganic materials like silicon or CIGS. After being absorbed in the photoactive layer of PSCs, the light energy usually generates either free charge carriers (electrons and holes) or excitons (electron-hole pairs). Electron and hole transport layers (ETL and HTL) with different work functions are placed on the opposite faces of the perovskite layer, producing an electric field that motivates the flow of photocurrent.

Snaith *et al*. fabricated the PSC by introducing mesoporous Al_2O_3 (ms-Al_2O_3) between compact TiO_2 (cp-TiO_2) and the perovskite layer, and achieved a PCE of 10.9%.[23] In 2013, Burschka *et al.* obtained a PCE of 15% for a perovskite-sensitized solar cell by introducing a two-step solution process.[53] At the same time, Snaith *et al*. fabricated a vapour-deposited organometal trihalide PSC based on a planar heterojunction thin-film structure that had a PCE of over 15% with a V_{OC} of 1.07 V.[54] In 2015, Yang *et al.* reported a device efficiency of 20.2% by improving the quality of the $FAPbI_3$ film.[55] In 2017, they further investigated the incorporation of iodide ions into the perovskite precursor solution to reduce the concentration of defect states, and reported a certified PCE of 22.1% under 1 sun illumination.[56] Recently, researchers at Ulsan National Institute of Science and Technology (UNIST) and the Swiss Federal Institute of Technology Lausanne (EPFL) have reached a new record certified PCE of 25.2% in a single-junction PSC with long-term operational stability (450 hours).[57] Such

remarkable development in the efficiency of PSC over the past ten years is unprecedented by any other PV material, which makes them a promising next-generation PV technology.

The perovskite/Si tandem solar cells are expected to overcome the efficiency limit of single-junction devices and shorten the route to commercialisation of PSCs.[58] In 2014, Loper *et al*. reported the PCE of 13.4% using perovskite/Si four-terminal tandem solar cell. This value can be remarkably improved up to 31.6% PCE with the optimization of both optical and electrical properties.[59] In the next year, Mailoa *et al*. demonstrated the first perovskite/Si two-terminal tandem solar cell achieved a PCE of 14.3%; and according to the simulation works on the optimization of cell structure, they can push this value up to 32% PCE.[60] Recently, Oxford PV has reported perovskite/silicon tandem solar cells that achieve lab certified PCE up to 29.8%,[1] outperforming both perovskite and silicon single-junction devices.

2.2.2 Perovskite solar cell device structure

Device architecture is one of the significant contributors to the performance of PSCs. Figure 2.3 illustrates the PSC device configurations that can be classified into the conventional n-i-p and inverted p-i-n devices. The typical PSC device includes a glass substrate, a transparent conducting oxide layer, an electron transport layer (ETL), an active perovskite absorber layer, and a hole transport layer (HTL), and an electrode. In the n-i-p structure, the light is absorbed in the solar cell device from the ETL side while the device is illuminated through the HTL side in the p-i-n structure.

Figure 2.3a shows the most common conventional n-i-p PSC architecture including the mesoporous and planar heterojunction devices. In the mesoporous device architecture, several metal oxides (TiO_2, ZnO_2, Al_2O_3, and ZrO_2) have been used as the isolator to prevent the undesirable migration of holes to the electron-transport side or served as the scaffold to support the perovskite. The typical mesoporous device has the following structure: an ETL of compact TiO_2 (cp-TiO_2) and mesoporous TiO_2 (ms-TiO_2) on an FTO or ITO coated glass substrate, an OIMHP absorber layer, spiro-MeOTAD served as HTL, and the Au electrode. The planar PSC device structure is an evolution of the mesoscopic architecture, where the mesoporous layer is removed, and the OIMHP layer is sandwiched between the planar HTL and planar ETL. SnO_2 is also a common ETL alternative for these planar n-i-p PSCs.

Figure 2.3b illustrates the typical architecture of an inverted p-i-n device, which has a reverse sequence of ETL and HTL compared to the conventional structure. To adapt the fabrication conditions, poly(3,4-ethylenedioxythiophene)-poly(styrenesulfonate) (PEDOT:PSS), poly[bis(4-phenyl)(2,4,6-trimethylphenyl)amine] (PTTA), and NiO_x are often used as HTL and deposited on the surface of an ITO/glass substrate. The most common choices for the ETLs used in the inverted p-i-n structure are phenyl-C61-butyric acid methyl ester (PCBM) or C_{60}. Finally, Al or Ag contacts are thermally evaporated on the top of ETL.

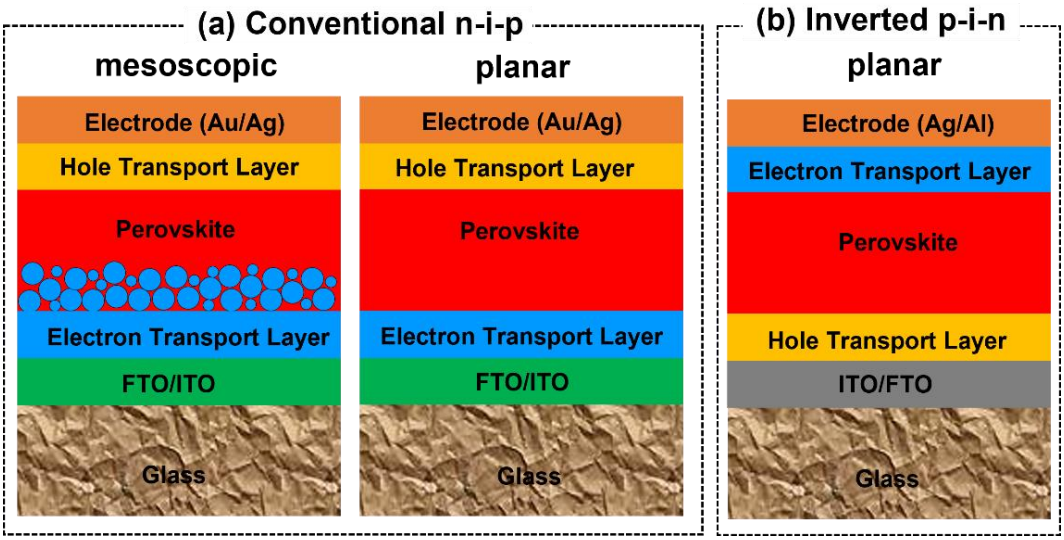

Figure 2.3. Schematic of typical PSC device architectures (a) conventional n-i-p and (b) inverted p-i-n structures.

2.2.3 Current-voltage (J-V) hysteresis

The current-voltage (J-V*)* characterisation under standard illumination conditions can be used to evaluate the device performance of a PSC. There are four important parameters extracted from this curve including the open-circuit voltage (V_{OC}) (*x*-intercept), the short-circuit current (J_{SC}) (*y*-intercept), the fill factor (FF) (area under the curve), and the PCE (see Figure 2.4).

The J_{SC} is the current passing through a solar cell device when the applied voltage is zero. It is a measure of the number of charge carriers produced and eventually collected at the electrodes under short-circuit conditions.

The V_{OC} is defined as the maximum value of voltage at zero current density of the solar cell. The V_{OC} corresponds to the amount of forward bias on the solar cell due to the bias of the junction with the light-generated current.

The FF quantifies the shape of the J-V curve as presented in the following equation:

$$FF = \frac{J_{mpp}V_{mpp}}{J_{SC}V_{oc}}$$

where V_{mpp} and J_{mpp} are the voltage and current density at the point of maximum output power, respectively.

Finally, the PCE can be determined as follows:

$$PCE = \frac{V_{oc}J_{sc}FF}{P_{in}}$$

where P_{in} is the input power density.

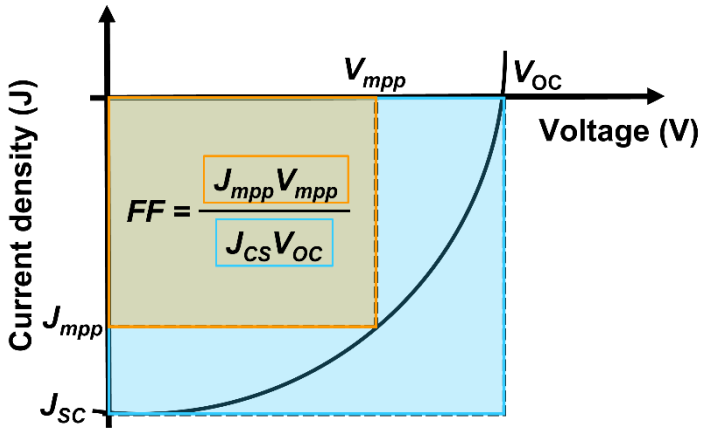

Figure 2.4. J-V characteristic of a photovoltaic device.

In organic-inorganic metal halide PSCs, hysteresis is commonly observed between the forward and reverse scans of J-V curve (see Figure 2.5).[61-63] Hysteresis makes the determination of the device efficiency more difficult.[61, 64] The severity of the hysteresis can be defined by the H-index (hysteresis index), which can be calculated as follows:

$$\text{H-index} = \frac{PCE_{reverse} - PCE_{forward}}{PCE_{reverse}}$$

where $PCE_{reverse}$ and $PCE_{forward}$ are the power conversion efficiencies for the reverse scan with biased voltage from V_{OC} to 0 V, and forward scan with biased voltage from 0 V to V_{OC}, respectively.

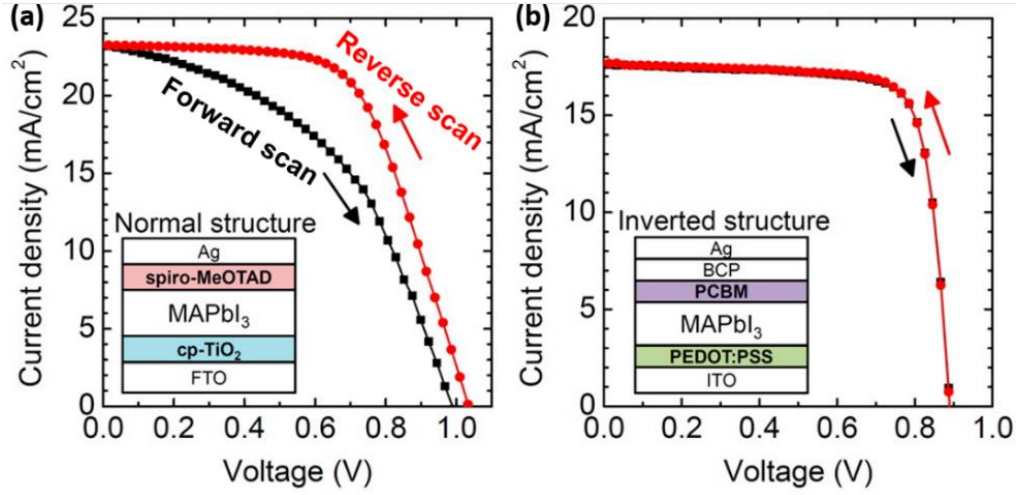

Figure 2.5. J-V curves for photovoltaic device at different scan directions (black colour forward scan and red colour reverse scan) for (a) conventional structure with spiro-MeOTAD as an HTL and TiO_2 as an ETL, (b) inverted structure with PCBM as an ETL and PEDOT:PSS as an HTL. The black curve versus the red curve shows the hysteresis within the device depending on the direction of the voltage scan. Adapted with permission from [65].

In early 2014, Snaith *et al.* reported the hysteresis in three types of PSC architectures including conventional planar heterojunction, conventional mesoscopic cells with ms-TiO_2 and mesoscopic superstructure with ms-Al_2O_3.[63] This hysteresis strongly depends on cell architecture, the pre-conditioning of device (illumination history and applied voltage), the contact materials, as well as the quality of perovskite layer. OIMHP materials are in essence dual ionic-electronic conductors, where halide ions in particular shield electric fields in the perovskite and respond slowly to changes in voltage. This is supported by first principles studies estimating the activation energy of ionic species in perovskite.[66]

Kang and Park have proposed three factors that possibly caused the hysteresis including (a) the ferroelectric property of perovskite layer associated with slow polarization, (b) the surface or bulk defects of perovskite layer behaving as traps for charges, and (c) excess ions owing to interstitial defects (iodide or organic cation) being able to migrate.[62] Recent studies have also indicated that varying materials used as the ETL, HTL and passivation layers has a

marked effect on hysteresis.[67] The interfaces between the perovskite and the ETL/HTL are the site of surface defects, which are reduced through surface passivation. Reenen *et al.* used a numerical drift-diffusion model to prove that both ion transport and trap-mediated interface recombination can give rise to experimental J-V hysteresis.[68] On the other hand, Calado *et al.* used optoelectronic photocurrent transient measurements to demonstrate that interface engineering can eliminate or at least reduce J-V hysteresis caused by ion migration in PSCs.[69] The hysteretic behaviour of PSCs, as reported by Walter *et al.*, is governed by the interplay between ion migration and trap-mediated recombination throughout the perovskite absorber layer.[70] Furthermore, experimental factors including scan rate and direction, pre-scan conditions and external electric field were found to influence hysteresis.[71]

2.2.4 Fabrication of the perovskite materials

Since 2009, enormous international research efforts have concentrated on enhancing the quality of the perovskite layer, which is a critical factor determining the PSC device performance. The microstructure properties of the perovskite film such as morphology, crystallinity, defects, and phase purity are determined by fabrication approaches, which then directly impact the device efficiency. Different fabrication methods of perovskite films have been developed, including approaches based on solution processing and thermal evaporation.

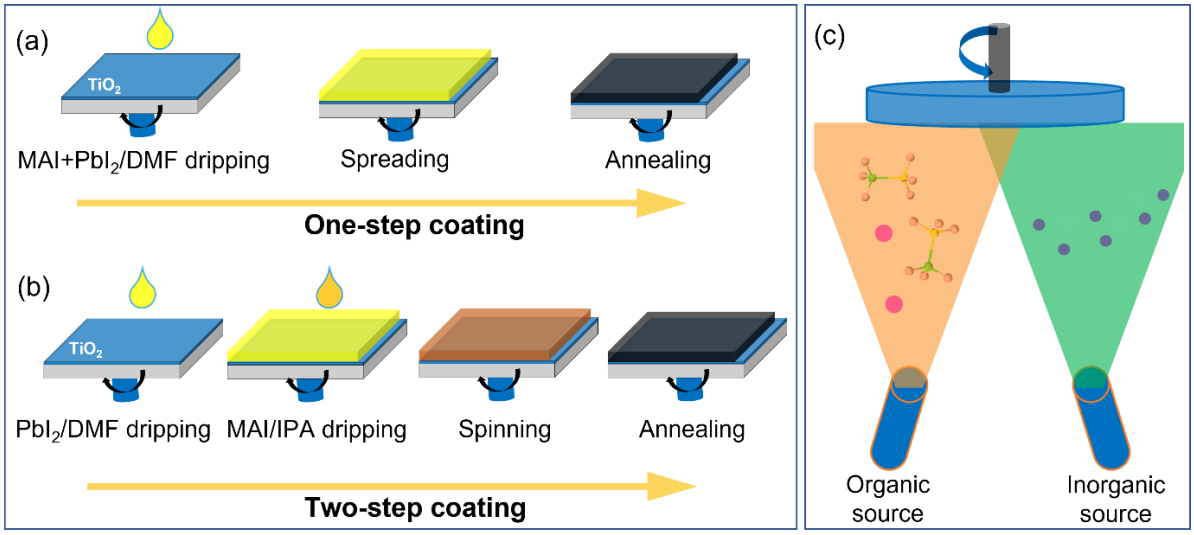

Figure 2.6. Schematic of perovskite fabrication by solution processing method: (a) one-step and (b) two-step solution process. (c) Schematic of perovskite fabrication by thermal evaporation method. Adapted from [72]

Solution processing

Currently, solution processing is one of the most popular techniques being used worldwide for perovskite fabrication. This method can effectively produce a smooth perovskite thin film along with well-defined elemental composition and thickness. The simplicity, without the necessity to have complex and expensive vacuum systems, is one of the main advantages of solution processing. Furthermore, it also allows compositional variation with the use of additives into the precursor solution that can vary the optical properties and device performance.[73] There are two main solution processing techniques, namely single-step and two-step spin coating.

Single-step solution processing is the most widely used technique from the early stages of perovskite research till now due to the low-cost requirement, high speed, and simplicity. In this technique, the perovskite precursor is generally prepared by dissolving perovskite precursors in solvents such as N-methyl-2-pyrrolidone (NMP), γ-butyrolactone (GBL), N,N′-dimethylformamide (DMF), and dimethyl sulfoxide (DMSO).[74, 75] For instance, $MAPbI_3$ precursor is prepared by mixing 1M methyl ammonium iodide (MAI) and 1M lead iodide (PbI_2) in the DMF or DMF/DMSO solvent. Then, the perovskite precursor solution is spin-coated over the pre-cleaned substrate. Immediately after spin-coating, the substrates are annealed on a hotplate at a temperature of 80 to 150 °C as shown in Figure 2.6a. However, one-step precursor solution usually results in non-uniform perovskite film with high surface roughness, high density of defects and pinholes.[76] To improve the quality the perovskite prepared by single-step solution process, Xiao *et al.* introduced an anti-solvent treatment (chlorobenzene or toluene) during spin-coating.[77] The presence of anti-solvent supports the nucleation initiation and speeds up the crystallization rate, creating a compact, highly uniform, and pinhole-free perovskite film. Until now, the best cell efficiencies are usually achieved with single-step coating method.[78]

Two-step spin coating was introduced by Burschka *et al.* in 2013, where a PbI_2 layer was first deposited onto the ms-TiO_2 film by spin coating a PbI_2 solution in DMF at 70 ºC.[53] Subsequently, the dried PbI_2 film was dipped in MAI solution for 20 s or spin-coated with the MAI solution on the PbI_2 layer (Figure 2.6b). Finally, the sample was annealed on a hotplate to form the perovskite structure. In the spin-coating method, the spinning time and speed of MAI solution on the PbI_2 film are important factors governing the quality of the perovskite layer.[79] In contrast, for dip-coating approach, the dipping time and concentration play a major role. The main advantages of two-step technique in perovskite film fabrication are better control of

morphology and crystallization. This technique has attracted huge attention after its first introduction.[53, 80, 81] However, the main challenges of this technique include the incomplete conversion of PbI_2 and uncontrolled surface roughness. These can be solved by incorporating additives into the perovskite precursor solution and using precursor solvent engineering.[82]

Thermal evaporation

Compared with the solution method, thermal evaporation allows the fabrication of good quality crystallites, uniform, and pinhole free perovskite films. Thermal evaporation is a common technique for thin-film deposition. The organic and inorganic source powders are heated in different boats and evaporated in a high vacuum chamber (Figure 2.6c). The molar ratio is managed by evaporation rate and process temperature. The thickness of the perovskite film can be accurately controlled by monitoring the deposition rate of each precursor. This synthetic method also allows the formation of the perovskite films without high temperature annealing and is therefore ideal for applications in flexible optoelectronics devices.[83] This process avoids the use of toxic solvents and can produce the perovskite films without any detriment to the underlying layers of tandem cells. Last but not least, evaporation is a conventional semiconductor fabrication method and can be easily scaled for commercial fabrication of solar cells. In 2013, Snaith *et al.* fabricated the $CH_3NH_3PbI_{3-x}Cl_x$ perovskite using dual-source vapour deposition at 10^{-5} bar, with MAI and PbI_2 ratio of 4:1.[54] The disadvantage of this method is the need for high vacuum conditions, which may increase the production cost.

2.3 Perovskite materials

2.3.1 Overview of OIMHP materials

The term “perovskite” (namely after the Russian mineralogist, *Lev Perovski*) was used to name the $CaTiO_3$ mineral, which was first discovered in 1939 by a German scientist, Gustav Rose in the Ural Mountains of Russia.[84] Later on, any material that has the same crystal structure as $CaTiO_3$ is commonly described as “perovskite”. Perovskites are a family of crystalline materials with chemical formula ABX_3, where the A-site represents a cation such as (e.g., Ca^{2+}, Ba^{2+}, Sr^{2+}, and La^{3+}); the B-site represents a metal cation (e.g., Ti^{4+}, Mg^{2+}, Al^{3+}, and Ta^{5+}); and a halide anion is located at the X-site (typically O^{2-}).

For OIMHP materials, the A-site can be occupied by the monovalent organic cations $CH_3NH_3^+$ (methylammonium, MA) and $NH_2CH{=}NH_2^+$ (formamidinium, FA) or inorganic cations (Rb^+ and Cs^+) whereas the B-site is typically occupied by a Pb^+, Ge or Sn^+ cations and halide anions (typically I^-, Br^-, Cl^-) are on the X-site. The A-site cation may be doped with other inorganic metal cations (such as Rb^+, Cs^+) for the purposes of increasing device performance and long-term stability, reducing bulk defects and ion migration.[85, 86] Figure 2.7 indicates the ideal perovskite structure, which is characterised by a cubic framework of corner-sharing $[BX_6]^{4-}$ octahedra (space group $Pm\bar{3}m$) where the B cation is located at the center of the unit cell, with the A cations at the corners and the X anions at the center of the faces. The atomic displacements from these ideal cubic positions can cause various structural phase transitions, and hence change the material properties. For instance, changing the chemical compositions of A, B and X can change the band gap of OIMHP materials. Filip *et al.* demonstrated that the tunability of the optical band gap originates from the changes in the density of states resulting from the effects of the inclusion of various cations and anions on the X–Pb–X bond angle and length.[87]

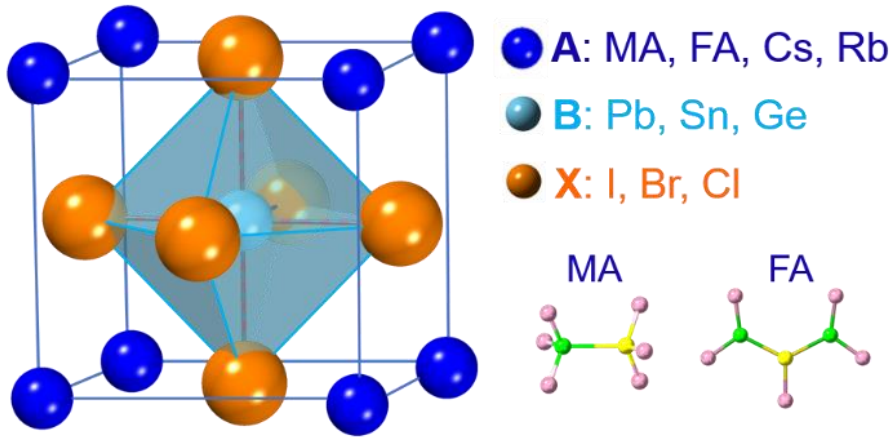

Figure 2.7. General structure of cubic perovskite material.

There are two main factors used to predict the stability of perovskite materials based on the chemical formula. The first one is the Goldschmidt tolerance factor (*t*)[88] obtained from the ionic radii as presented in the following equation:

$$t = \frac{r_A + r_X}{\sqrt{2}(r_B + r_X)}$$

where r_A represents the ionic radius of the A-site cation (r_{Rb} = 152 pm, r_{Cs} = 167 pm, r_{MA} = 217 pm, r_{FA} = 253 pm); r_B indicates the ionic radius of B-site cation (r_{Pb} = 119 pm, r_{Ge} = 211 pm, r_{Sn} = 225 pm); and r_X is the ionic radius of the X-site anion (r_I = 198 pm, r_{Br} = 185 pm, r_{Cl} = 175 pm).

The second one is the octahedral factor (μ)[89] which is the ratio between the ionic radii of the B cation and the X anion, as given below:

$$\mu = \frac{r_B}{r_X}$$

In general, materials tend to form the perovskite phase if the tolerance factor (t) is close to 1. Reaney *et al.* demonstrated that oxide perovskites with $0.9 < t < 1$ are predicted to form an ideal cubic structure with corner-sharing and untilted octahedra at room temperature.[90] A tolerance factor of $0.71 < t < 0.9$ gives rise to a distorted perovskite structure with tilted octahedra. When the tolerance factor is outside of these two ranges, non-perovskite hexagonal structures with face-sharing octahedra are formed instead. This principle was originally proposed for oxide perovskite,[91] but it can be applicable for OIMHPs. The OIMHP materials are expected to form a cubic phase for a tolerance factor t close to 1, a tetragonal phase for $0.8 < t < 0.9$, an orthorhombic phase for $t < 0.8$, and a non-perovskite hexagonal phase for $t > 1$.[91] Commonly, a hybrid perovskite material with the same chemical formulation can have more than one phase, depending on the fabrication methods and annealing temperature.[91]

2.3.2 Octahedral tilting in OIMHP materials

Octahedral tilting in perovskite materials is described by the Glazer notation,[92, 93] in which all tilt systems are characterized by a combination of different parameters. The letters *a*, *b*, and *c* are employed to illustrate the three tilt axes including [100], [010] and [001], respectively. Three superscripts "+, −, 0" represent the relative tilt direction between adjacent octahedral layers. In detail, in-phase and out-of-phase octahedral tilting are denoted with superscripts "+" and "–" after the appropriate letter representing tilt axis, meaning that the octahedral tilt in the same or opposite direction, respectively (see Figure 2.8). A "0" superscript is used when no tilts occur around an axis. For instance, the tilt system $a^0b^+b^-$ has no tilting around [100] axis, the in-phase tilting around [010] axis, and the out-of-phase tilting around [001] axis. Figure 2.8 illustrates two common kinds of octahedral tilts including in-phase and out-of-phase tilt modes. In-phase octahedral rotations around a common axis are defined when every octahedron rotates

by the same magnitude in the same direction along the axis, resulting in an unchanged unit cell parameter along this axis. When the sign of rotation varies for every octahedron along the rotating axis, we have out-of-phase rotations around the common axis and the unit cell parameter doubles.

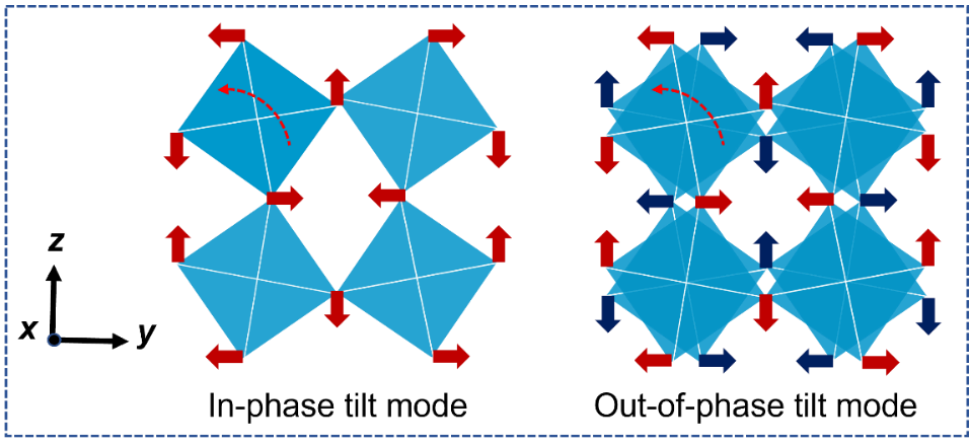

Figure 2.8. A schematic of octahedral tilts such as in-phase tilt octahedral tilting along *x* axis and out-of-phase octahedral tilting along *y* and *z* directions in perovskite structure.

Glazer reported 23 possible simple tilt systems in 1975,[92, 93] however only 15 different space groups were actually recognised in crystal systems and several of these tilt systems have the same space group. Howard & Stokes demonstrated the various potential tilt systems for perovskites using a group theoretical analysis.[94] Figure 2.9 shows the diagram of 15 different space groups illustrating the relationship of the group and subgroup between tilt systems of perovskite materials.

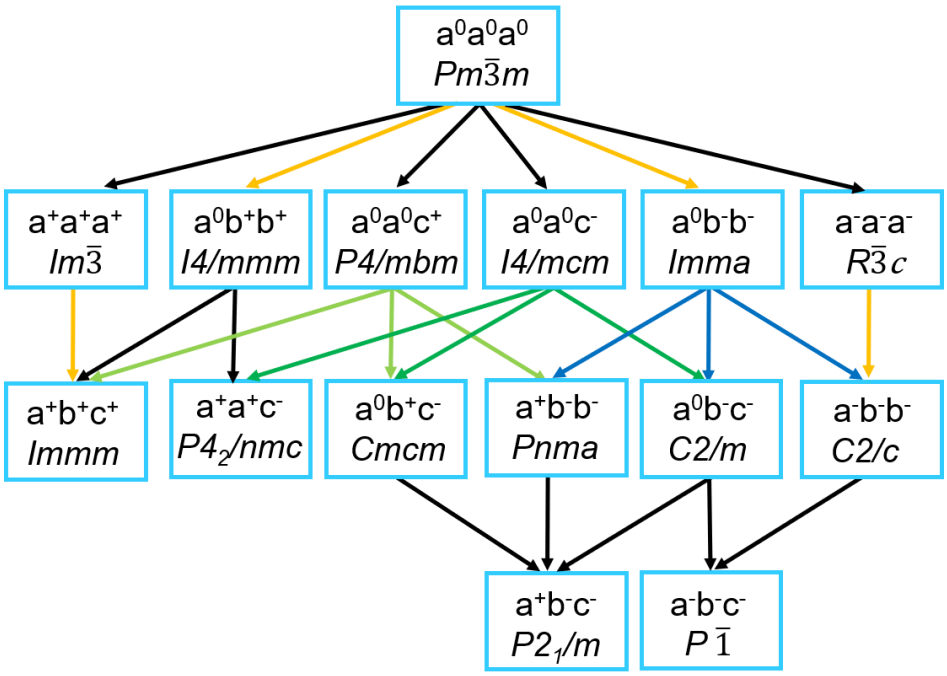

Figure 2.9. The relationship of group and subgroup between tilt systems of perovskite materials by Howard and Stokes. Adapted with permission from [94].

The perovskite materials have various structural phases at different temperatures owing to the undersized A cation causing an instability in the octahedral tilt which can be explained geometrically by the Goldschmidt tolerance factor. Figure 2.10 shows three phases observed in metal halide perovskite materials including α-phase (cubic), β-phase (tetragonal), and γ-phase (orthorhombic).[95] The cubic phase with space group *Pm*$\bar{3}$*m* has no tilt ($a^0a^0a^0$) in Glazer notation. The tetragonal phase has either a space group *P4/mbm* with in-phase tilt ($a^0a^0c^+$) or space group *I4/mcm* with out-of-phase tilt ($a^0a^0c^-$). For instance, the $MAPbI_3$ perovskite has the *I4/mcm* phase at intermediate temperature while the *P4/mbm* phase was observed in inorganic perovskites. Finally, the orthorhombic phase with space group *Pnma* has $a^-a^-b^+$ tilts including one in-phase tilt and two out-of-phase tilts.

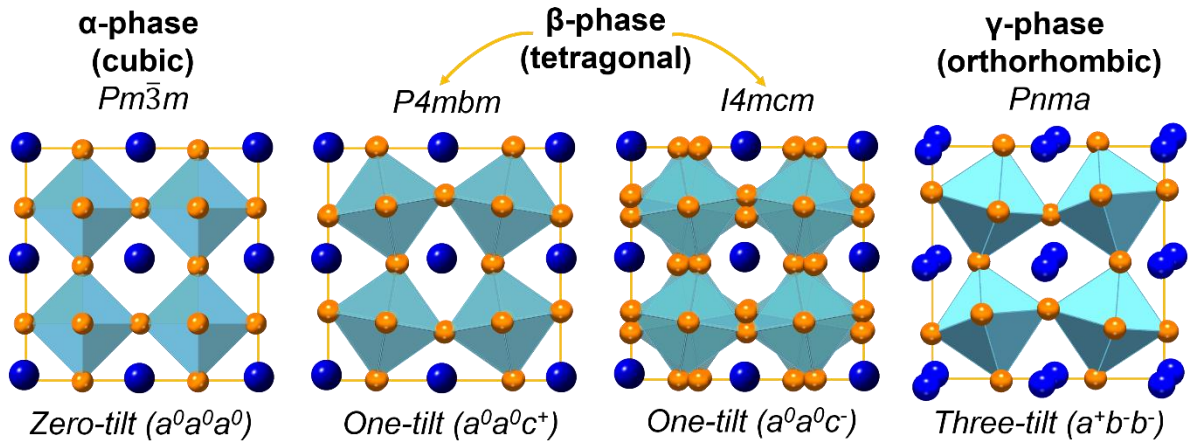

Figure 2.10. Three phases commonly observed in perovskite materials. Cubic α-phase ($Pm\bar{3}m$) has no activated tilted mode. Tetragonal β-phase (*P4/mbm, I4/mcm*) contains an in-phase tilt or out-of-phase tilt along one axis. Orthorhombic γ-phase (*Pnma*) has one in-phase tilt and two equal out-of-phase tilt modes.

Since the lattice structure of corner-sharing octahedra is flexible, ionic perovskite is prone to go through the deformity related to the octahedral tilting and the off-centering of the A- and B-site cations. Together with the change in lattice parameter, each phase is defined by the existence of octahedral tilting. When the octahedron in the perovskite structure is tilted in some particular way, it leads to the tilting of neighbouring octahedra. The octahedra tilting can result in the most crucial outcome: doubling the periodic unit cell axes and structure this is often associated with cation ordering. In detail, the tilting can make the cation-anion (B-X) bond in one octahedron rotated in an opposite direction to that in an adjacent octahedron, leading to a doubling of the periodic distances perpendicular to the tilt axis. Simultaneously, if the cation-anion (B-X) bond distance is kept unchanged, then the distance between two B cations must be smaller and therefore the lattice constant along the tilt axis is reduced. Because the unit cell axes can be doubled by octahedra tilting, additional reflections are formed which lie on half-integral reciprocal-lattice planes. These extra reflections in the electron diffraction patterns now can be indexed with some indices odd, while the ordinary reflections (the main reflections) have all *hkl* even.[93]

2.3.3 Tetragonal and cubic perovskite structures

The difference between atomic structure of cubic and tetragonal perovskite is shown in Figure 2.11. There are no critical differences between the two structures, except a small rotation of

PbI_6 octahedra along the *c*-axis. The tetragonal phase can be considered as a pseudocubic phase with lattice parameter $a_t = a_c \times \sqrt{2}$, $c_t = c_c \times 2$. In the cubic structure, the *a* and *b* are 45° rotated axes of the tetragonal unit cell (see Figures 2.11c-d). Table 2.1 shows the crystal parameters of tetragonal and cubic structures in $MAPbI_3$ and $FAPbI_3$ perovskites.

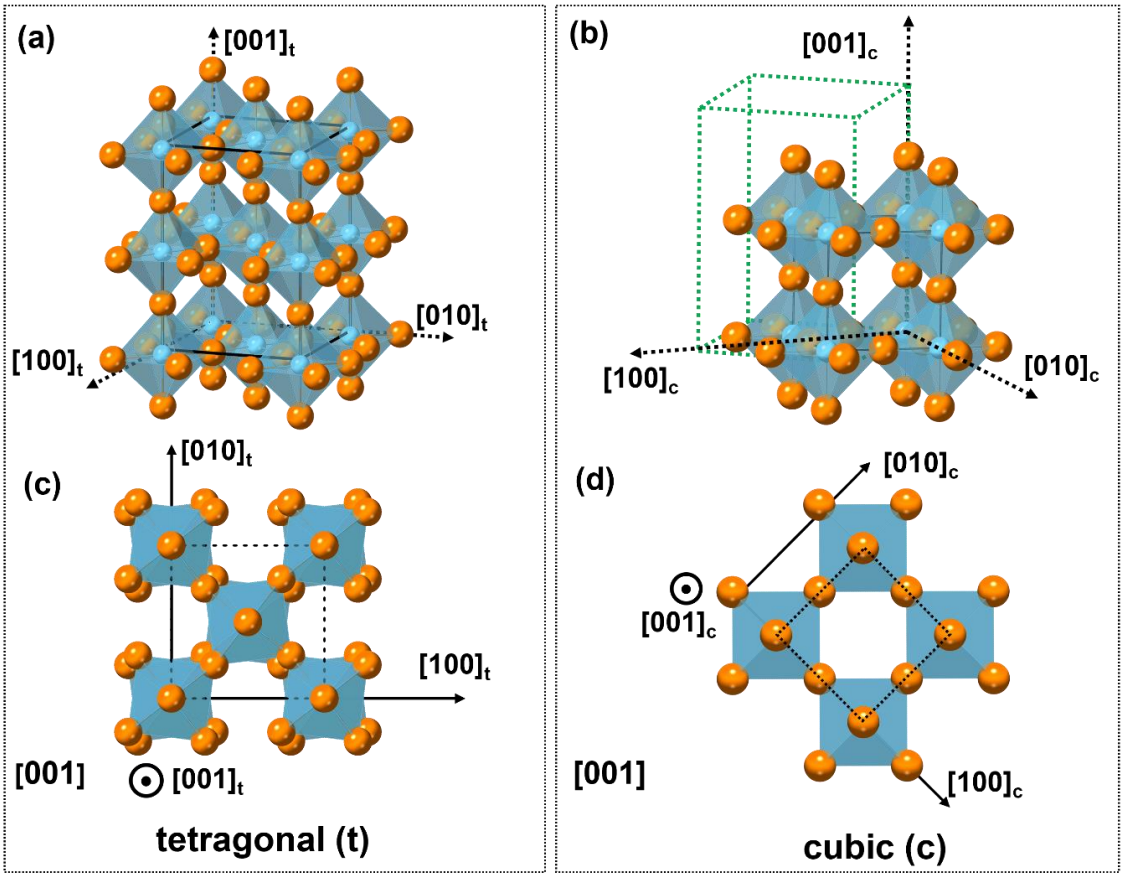

Figure 2.11. Atomic structure models of $MAPbI_3$ perovskites with (a) tetragonal and (b) cubic structure. Atomic structure of (c) tetragonal and (d) cubic structure along [001] zone axis. The subscripts "t"' and "c" represent the index in the tetragonal and cubic structure, respectively.

Table 2.1. Crystal parameters of tetragonal structure ($MAPbI_3$) and cubic structure ($MAPbI_3$ and $FAPbI_3$).

Tetragonal structure			**Cubic structure**					
$MAPbI_3$			**$MAPbI_3$**			**$FAPbI_3$**		
Plane	d (Å)	2θ	Plane	d (Å)	2θ	Plane	d (Å)	2θ
(002)	6.321000	13.99928	(100)	6.31728	14.0076	(100)	6.3620	13.9086
(002)	6.321000	14.03335	(100)	6.31728	14.0417	(100)	6.3620	13.9425
(110)	6.257188	14.14277	(001)	6.31728	14.0417	(001)	6.3620	13.9425
(112)	4.446889	19.95034	(110)	4.4669	19.8597	(110)	4.49861	19.7187
(112)	4.446889	19.99916	(110)	4.4669	19.9082	(110)	4.49861	19.7669
(211)	3.774262	23.55269						
(211)	3.774262	23.61056						
(202)	3.624746	24.53903	(111)	3.64728	24.3851	(111)	3.6731	24.211
(202)	3.624746	24.59939	(111)	3.64728	24.445	(111)	3.6731	24.2706
(004)	3.160500	28.21313	(200)	3.15864	28.2301	(200)	3.18100	28.0276
(004)	3.160500	28.28288	(200)	3.15864	28.2999	(200)	3.18100	28.0969
(220)	3.128594	28.50691						
(220)	3.128594	28.57741						
(213)	2.884753	30.97444						
(213)	2.884753	31.05134						
(114)	2.821060	31.69194	(210)	2.82517	31.6446	(210)	2.84517	31.4164
(114)	2.821060	31.77072	(210)	2.82517	31.7232	(210)	2.84517	31.4944
(310)	2.798299	31.95657						
(310)	2.798299	32.03605						
(312)	2.558773	35.04031	(211)	2.57902	34.7565	(211)	2.59728	34.5044
(312)	2.558773	35.12793	(211)	2.57902	34.8433	(211)	2.59728	34.5044
(224)	2.223445	40.53979	(220)	2.23350	40.3494	(220)	2.24931	40.0536
(224)	2.223445	40.64230	(220)	2.23350	40.4514	(220)	2.24931	40.1548
(400)	2.212250	10.75402						
(400)	2.212250	40.85712						
(006)	2.10617	42.9055	(221)	2.10576	43.0233	(221)	2.12067	42.5978
(006)	2.10617	43.0146	(300)	2.10576	43.0233	(300)	2.12067	42.706

2.3.4 Crystal structure of OIMHP materials

a. $MAPbI_3$ perovskite material

Methylammonium lead iodide ($MAPbI_3$) is amongst the most common OIMHP materials for PV applications, achieving about 21% PCE.[96] A challenging issue for $MAPbI_3$ PSCs is the stability of various crystal structures at different temperatures. Figure 2.12 shows three main phases observed in $MAPbI_3$ material as a function of temperature. From the experimental results, $MAPbI_3$ has an orthorhombic phase with the *Pnma* space group at temperature below 165 K (-108ºC) using synchrotron X-ray powder diffraction and time-of-flight neutron diffraction.[97] The orthorhombic phase has in-phase (+) rotations along the [010] axis and out-of-phase (–) octahedral tilts along the [100] and [001] axes, which can be interpreted by an $a^-b^+a^-$ tilt pattern in Glazer notation. When the temperature increases above 162K (-111 ºC), $MAPbI_3$ adopts a tetragonal structure with *I4/mcm or I4cm* space group ($a = b = 8.859$ Å, $c = 12.649$ Å) and an $a^0a^0c^+$ or $a^0a^0c^-$ tilt pattern. The lattice parameters of the tetragonal structure become more isotropic with $c/2a$ moving closer to 1. Also, the molecular disorder rises to the point where the transition to a cubic phase happens at about 327 K (54 ºC). This transition can be observed clearly from the temperature dependent neutron diffraction and changes in the heat capacity.[98] The cubic phase has space group $Pm\bar{3}m$ with a lattice parameter $a = 6.304$ Å and the associated octahedral tilting pattern is $a^0a^0a^0$ in the Glazer notation.

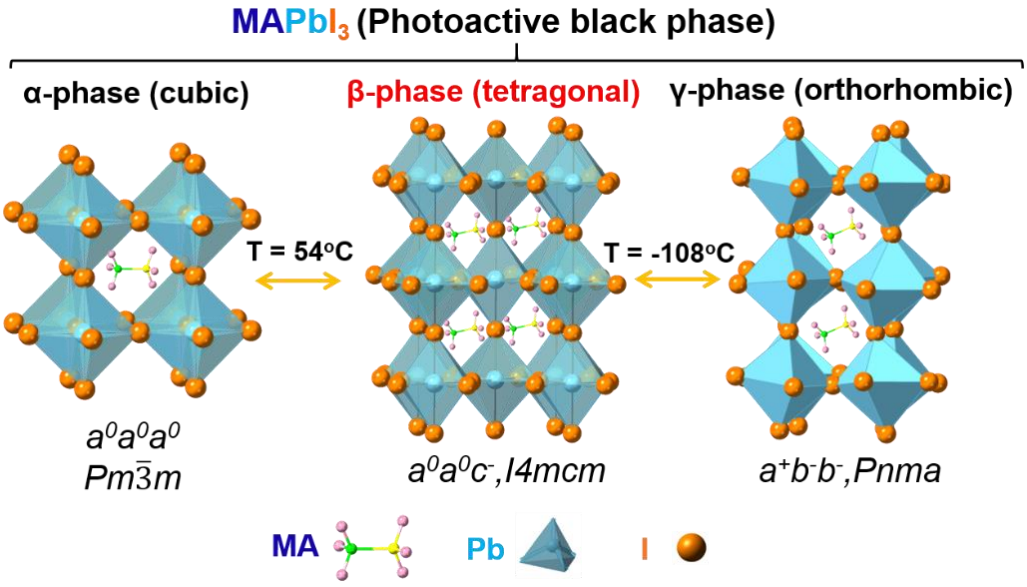

Figure 2.12. Crystal structure and phase transitions of $MAPbI_3$ perovskites at different temperatures.

b. $FAPbI_3$ perovskite material

Since 2013, highly efficient PSCs are predominantly fabricated with FA-based perovskites because of their superior thermal and moisture stability compared to MA.[99, 100] Formamidinium lead triiodide ($CH(NH_2)_2PbI_3$, $FAPbI_3$) has the narrowest optical bandgap (1.45 eV) in comparison with $MAPbI_3$ (1.57 eV) and $CsPbI_3$ (1.73 eV), and this value is close to the ideal bandgap for creating high-efficiency PSCs.[6] The FA cation has a larger effective radius (2.53Å) compared to the MA cation (2.17Å). As mentioned earlier, the cation radius changes the Goldschmid tolerance factor (an indication of the stability of the perovskite structure for a certain component combination). $FAPbI_3$ has the structure tolerance factor of 1.036 which is close to the ideal value of 1.

Figure 2.13 illustrates the crystal structure of $FAPbI_3$ perovskite undergoing complicated phase transition as a function of temperature. There are two main phases commonly observed in $FAPbI_3$, the yellow hexagonal non-perovskite phase (δ-$FAPbI_3$, $P6_3/mmc$, a = 8.6667 Å, c = 7.9077 Å) and the black cubic perovskite phase (α-$FAPbI_3$, $Pm\bar{3}m$, a = 6.3506 Å).[101] As shown in section 2.4.3, the δ-$FAPbI_3$ phase is also best described as a 2H structure with the octahedral layers twinned every alternate layer (creating a periodic SF sequence) compared to the cubic α-$FAPbI_3$ structure. Only the black cubic $FAPbI_3$ phase is a useful photoactive perovskite phase.[102] Zhu *et al.* demonstrated that the $FAPbI_3$ nanocrystals undergo a phase transition from a perfect cubic lattice with space group $Pm\bar{3}m$ to a cubic supercell with space group $Im\bar{3}$ in the pressure range of 0−3 GPa.[103] The cubic $FAPbI_3$ phase can be obtained at higher temperatures either by crystallization from solution at high temperatures or thermal annealing of the δ-$FAPbI_3$ hexagonal form (e.g. 150 to 180°C). However, the photoactive cubic $FAPbI_3$ can easily be transformed into the undesired photoinactive hexagonal $FAPbI_3$ under ambient conditions at room temperature because of the large size of the FA^+ cation. A distinction of $FAPbI_3$ is that face-sharing octahedra δ-phase (yellow colour) is in competition with the corner-sharing octahedra perovskite phase (black colour); this is also the case for $CsSnI_3$. Consequently, obtaining a stable and highly crystalline black cubic $FAPbI_3$ perovskite phase at room temperature is a challenge in the field of PSCs.

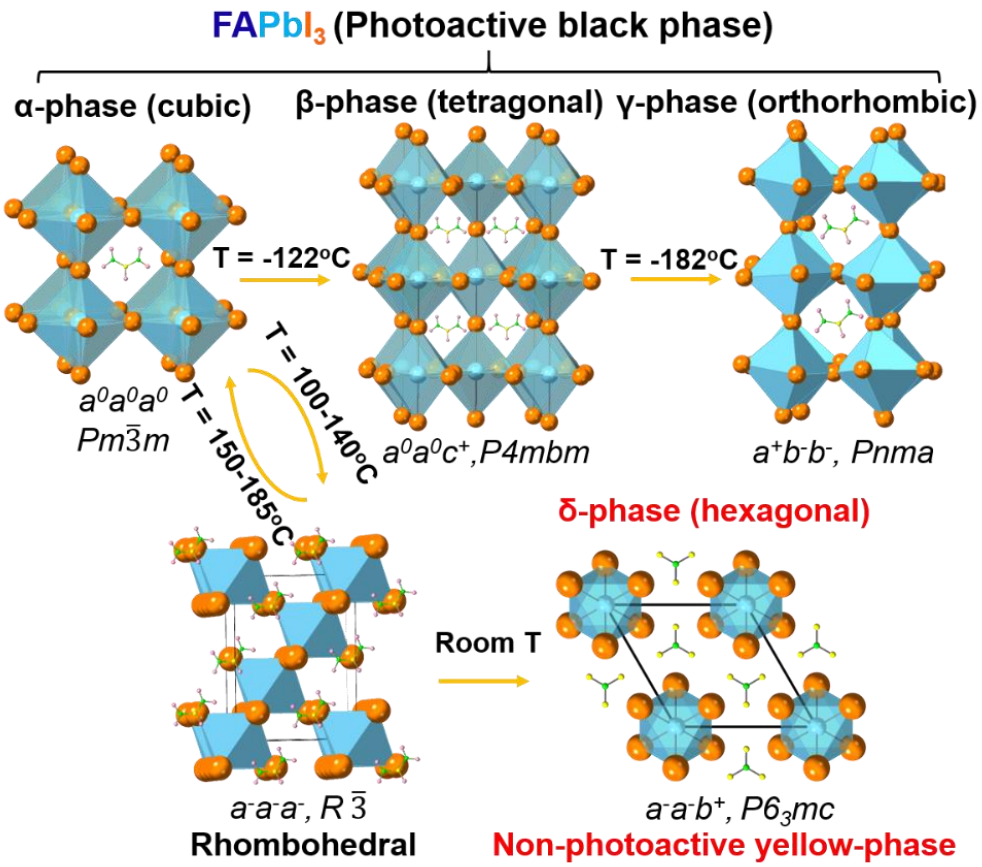

Figure 2.13. Crystal structure and phase transitions of $FAPbI_3$ perovskites at different temperatures.

2.4 Defects of perovskite materials

2.4.1 Crystallographic theory of twins

Twins are one of the most widespread types of defects in many crystalline materials including semiconductors (such as GaAs, AlGaAs, InP), metals (such as Pt, Au, Ag, Cu) and ceramics ($BaTiO_3$).[104-108] Twins appear when two crystals in materials sharing the same crystal lattice plane obey a certain symmetry rule. Amongst several symmetry rules, the most common one defines the twin as the mirror image of the matrix crystal structure across a common plane named the twin plane. The lattice compositions of the twin and matrix lamellae are to preserve symmetry with respect to the twin boundary (TB). Figure 2.14b shows the morphology and structure of TB splitting up the internal grain into two separate structures: matrix and twin. TBs are precisely constructed following the ordered arrangement of twin lamellae within the grains which then strongly affect the mechanical, electronic, optical and magnetic properties of

materials.[104] The twin defects in a structure can have either a positive or negative impact on various properties of the materials. The difference between TB and high-angle grain boundary is shown in Figure 2.14. Compared with traditional high-angle grain boundaries, TBs usually exhibit much higher mechanical and thermal stability.[109]

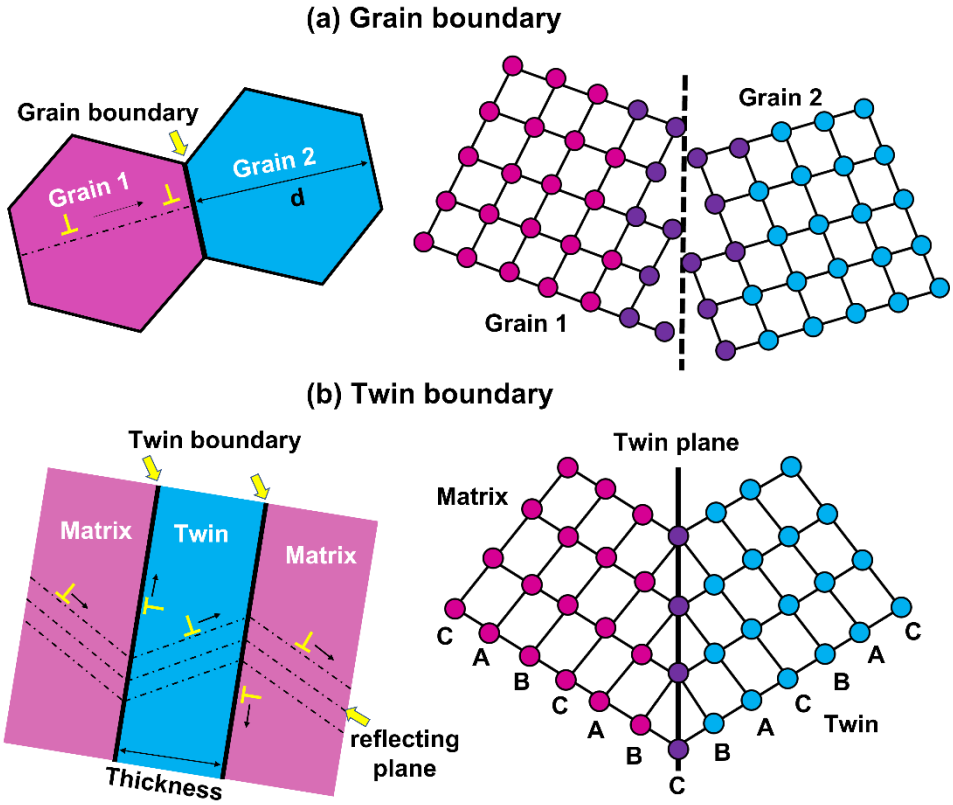

Figure 2.14. Schematic diagram of (a) the grain boundary and (b) TB. The yellow symbol (⊥) indicates the dislocation motion, which is blocked by grain boundary. Adapted from [104, 109].

There are three types of interfaces which can be classified depending on the degree of atomic matching namely coherent, partly coherent, and incoherent interfaces (Figure 2.15). The coherent interface has a perfect match between the two adjacent crystals along the interface, which means that there is no lattice mismatch. This coherent interface can be seen between two phases with similar atom size, lattice parameter, or chemical composition. This is different in the case of semi-coherent interfaces, in which the periodic misfit dislocations accommodate the disregistry between the two crystal structures in the interface. When the atomic configuration of the interface plane shows a big difference between the two adjacent crystals, e.g. poor lattice match across the interface, we have an incoherent interface. The incoherent interface usually

occur if there are significant differences in the atomic bonding and/or the lattice parameters in crystals.

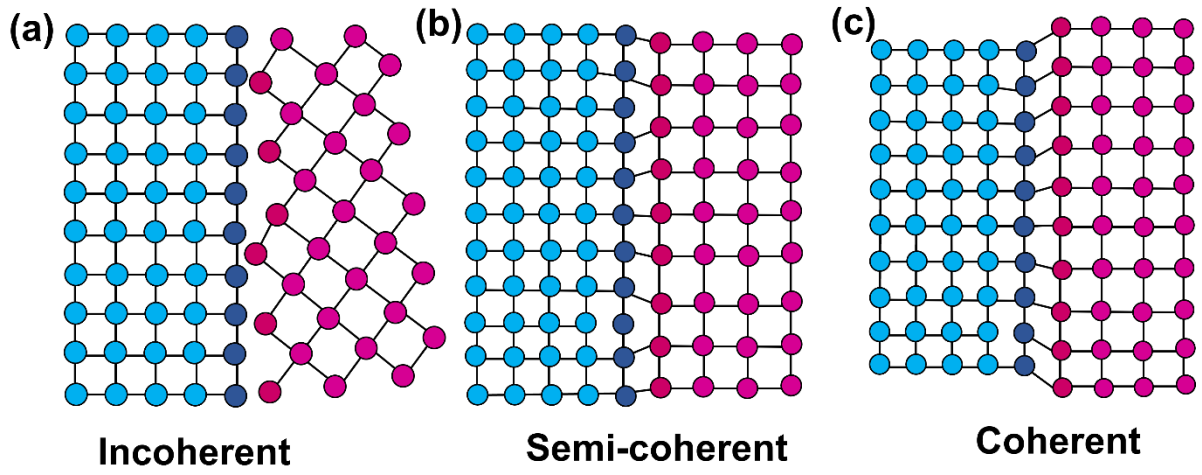

Figure 2.15. Schematic diagram of (a) incoherent, (b) semi-coherent, and (d) coherent interface boundaries. Adapted from [110].

Figure 2.16 shows two main types of interfaces between twin and matrix including coherent and semi-coherent. The coherent twin plane has atoms aligned along a twin plane (coherent boundary) with mirror symmetry. Figure 2.16a illustrates the atomic structure of twin plane belonging to both crystals without any lattice mismatch. A coherent TB is commonly observed in face-centred cubic (fcc) metals or cubic inorganic perovskite materials with low interfacial energy.[108] For the semi-coherent TB, the interactions show no different behaviour in comparison with the grain boundary (Figure 2.16b).

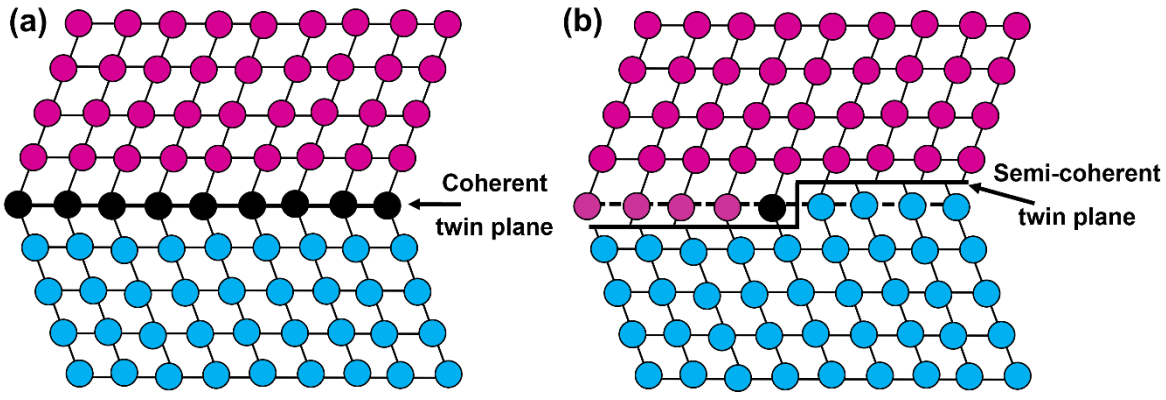

Figure 2.16. Schematic diagram of (a) coherent TB, (b) semi-coherent TB.

There are four parameters including K_1, K_2, η_1, η_2 used to describe the matrix-twin crystallographic relationship as shown in Figure 2.17a.[111] K_1 represents the twin plane and η_1 is the shear factor where the twinned materials above the twin plane have been distorted with respect to the matrix below. The twin plane K_2 containing the direction η_2 is sheared through the angle ϕ by the twinning process but is not distorted, that is $\eta_2 = \eta_2'$. The K_2 plane is referred to as the second undistorted plane.

If the orientation relationship between twin and matrix is defined by a simple reflection across K_1 then the reciprocal lattice will have the same relationship. Figure 2.17b shows the atomic positions of annealing twins that occur in fcc metals. The stacking sequence across the twin plane is also a mirror image ABCAB|C|BACBA. In this case η_1 is perpendicular to $[1\bar{1}0]$, K_1 (111), η_1 $[11\bar{2}]$ and electron diffraction patterns of the twin and matrix are mirror reflections across the (111) plane (180° rotation around [111]).

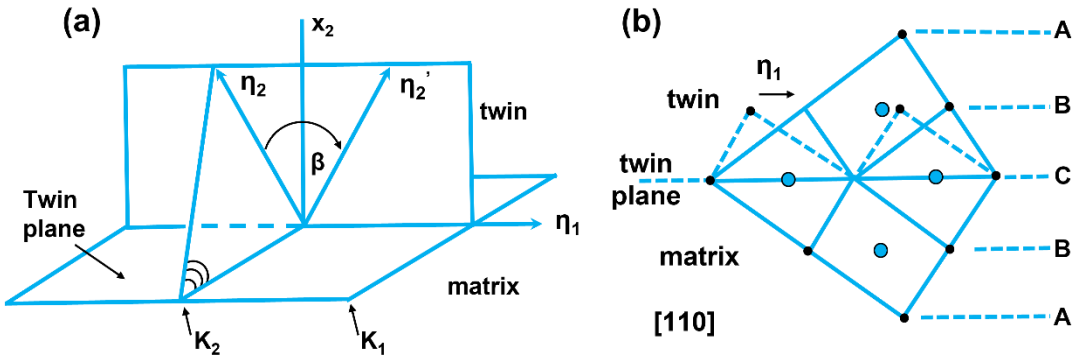

Figure 2.17. (a) The geometry of the twin parameters. (b) Atomic positions of {111} twin in fcc structure with ABC stacking is reversed inside the twin.

Figure 2.18 illustrates an example of the morphology and crystallography of {111} cubic twin in $BaTiO_3$ material.[108] The morphology of twin is highlighted in the bright-field TEM (BF-TEM) image with a red dashed line defining the {111} TB. The SAED pattern illustrates the superimposed reflections of both twin and matrix with the beam direction parallel to a $[1\bar{1}0]$ zone axis. The {111} reflections are perpendicular to the $\{11\bar{2}\}$ reflections of matrix and twin plane. The {111} twin plane gives rise to coincident {111} reflections parallel to the twin axis. The cubic twin formation can be explained as a shear operation of (111) planes with $\pm\frac{1}{3}[11\bar{2}]$ shear vectors. The coherent TB is confirmed by HR-TEM image in Figure 2.18b.

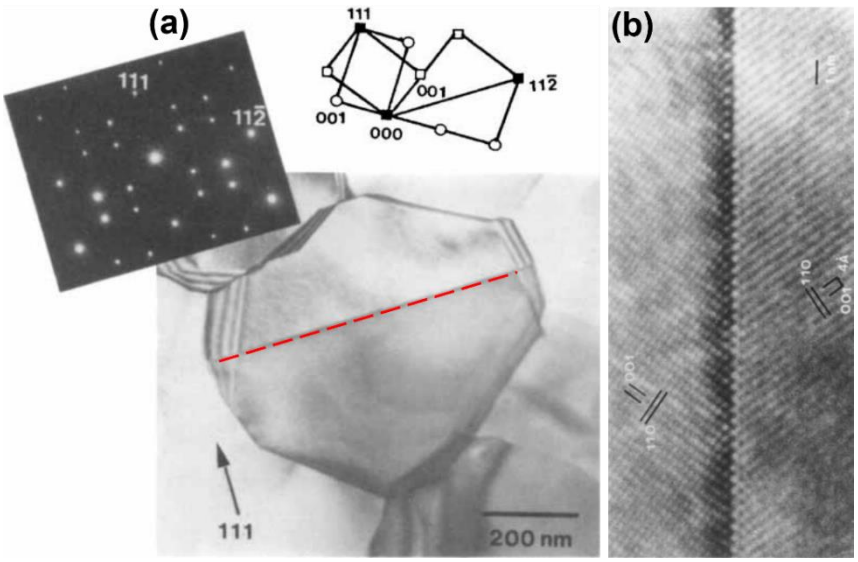

Figure 2.18. (a) A BF-TEM image and the SAED pattern in [110] zone axis of {111} TB in $BaTiO_3$ material. (b) HR-TEM image of {111} TB in $BaTiO_3$ material. Adapted with permission from [49].

2.4.2 The impact of twins on the properties of materials

Twins have attracted substantial attention for applications in crystal growth, mechanical engineering, biomedical diagnosis, optics, and catalysis.[112] The formation of twins can modify the structure and morphologies of the materials.[113] Therefore, it has a wide range of effects on numerous properties of the specimens, including mechanical properties, [105, 114, 115], optical and electrical properties,[116, 117] ferromagnetic and ferroelectric properties,[118, 119] and superconductivity.[120]

Many research groups have confirmed that twins have various impacts on the optical properties of materials. [121] For instance, the optical absorption and defect states are enhanced by TBs in crystalline semiconductors.[122, 123] Ikonic *et al*. have demonstrated that TB can create shallow states near the valence band and conduction band boundaries. The TB is capable of enhancing the optical absorption and possibly without reducing the PV performance, since the carrier recombination is not effective at shallow energy levels.[122, 124] The strong impact of twins on the optical properties has been reported using the first-principle calculations.[122, 123] Wang *et al*. observed the twin configurations in most Si nanocrystals with diameters larger than 6 nm using HR-TEM. They demonstrated that the microstructural defects have a significant influence on the optical properties as these are possible reasons for the

photoluminescence (PL) peak intensity reduction.[125] Twinning or polytypic superlattices modify the optical properties and electronic structure of the material with inter-band and intra-band optical transitions. [126, 127] Woo *et al*. used the TEM and PL to demonstrate that twins behave as carrier recombination centers, and significantly affect the optical properties of the InP nanowires.[128]

Twins also have different impacts on the electronic properties of materials. Ikonic *et al*. reported the theoretical studies of electronic structure of TBs and twinning superlattice in the bulk PbS materials. They demonstrated that twinning with anionic or cationic interface possess much narrower or wider band gaps than that of bulk material, indicating that these structures may display interesting electronic properties.[124] Kim *et al*. used first principles calculations to demonstrate the modification of the interatomic distance at a 60º TB to supply structural misfits can modify the electronic structure of Bi_2Te_3. The electronic structure modification creates occupied states within the original bandgap in a favourable condition to produce carriers and increases the density of states near the conduction band minimum. The incoherent TB and different twinning structures in Cu are also reported to affect the flow of electric current under mechanical stress.[129]

Twins play a critical role to manage the ferroelastic, ferroelectric, and ferromagnetic properties of materials. The absence of cubic symmetry at the TBs in Pt nanoparticles was found to give rise to permanent magnetic moments.[130] Furthermore, Pb nanoparticles exhibit permanent magnetic moments and ferromagnetic behaviour (coercivity and hysteresis) in a wide range of temperatures from 0 to 300K. Another study reported how the movement of TB modifies the magnetic domain structure by mechanical stress in single crystal $Ni_{50.0}Mn_{28.5}Ga_{21.5}$. After the formation of TB, the structure of magnetic domains split into individual ones and can be restored under the application of a weak magnetic field.[131]

2.4.3 Stacking fault defects

Stacking faults (SFs) are two-dimensional (2D) planar defects that can be observed in semiconductor materials (such as Si, Ge, GaAs, InP) and various metals (such as Au, Ag, Cu) with fcc structure. The formation of SFs in the fcc structure result of changes in the atomic plane stacking sequence in the ⟨111⟩ directions. SFs typically have very low formation energies.[124] Figure 2.19 illustrates the difference between a perfect crystal and a crystal disrupted by a SF. The stacking sequence ABCABCA produces a cubic structure and

ABABABA produces a hexagonal structure. The bonding arrangement is different at the interface compared to a perfect crystal and changes the electronic wave functions, and hence the local band structure around the SF. The most common example of SFs can be found in close-packed crystal structures.

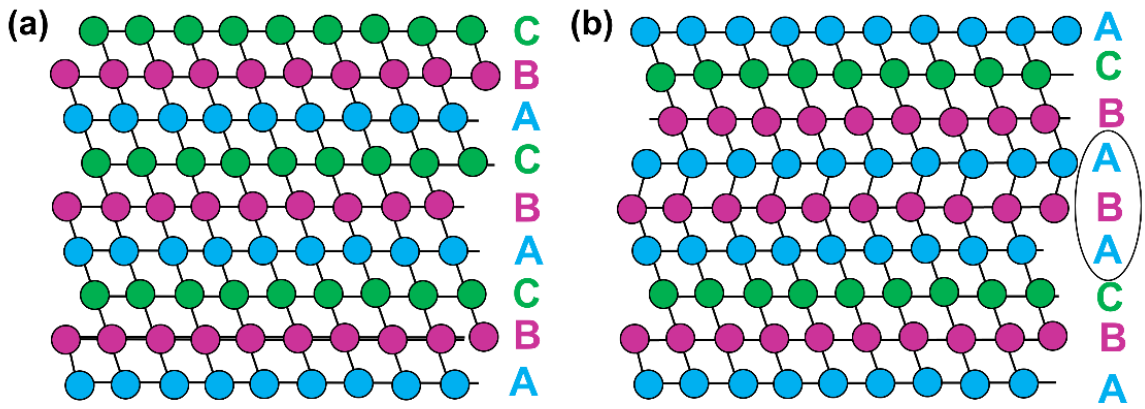

Figure 2.19. Schematic diagram of (a) perfect crystal, (b) stacking fault sequences.

In semiconductor materials, SF defects are generated unintentionally from mechanical deformation or during nanowire growth.[126, 127] SFs act as recombination sites in dislocation-free silicon, and edge dislocations reduce the PL intensity in multi-crystalline silicon.[126, 127] However, SFs may also be produced intentionally. Yoo *et al*. used a combination of theoretical and experimental measurements to study the impact of SFs on the device performance of the CdTe solar cells. SFs are detrimental to device performance because of increased carrier recombination.[132]

2.4.4 Nanotwins (NTs)

The nanotwin (NT) structures are comprised of a high density of twins where the thickness of individual twin is in the nanometre scale. They have coherent boundaries to enhance the physical and mechanical properties of metals.[133] NTs are also commonly observed in perovskite materials.[15, 134-136] The dislocation-TBs interactions are the origin of the unique mechanical properties of NT materials, which are different from dislocation-GBs and dislocation-dislocation interactions.[133] In contrast to the twin-free nanocrystal, the dislocation propagation inside the grains can be efficiently barred by TBs.[137] Therefore, the perfection of TBs is highly important for the strengthening effect of NT materials.

NTs have received a great deal of attention in metals (such as Pt, Au, Cu, Ni) and semiconductors (such as GaAs, InP, Si, Ge) thanks to their interesting electrical and mechanical properties.[104-106, 138-140] Many research groups have reported the unique properties of NTs using TEM and HR-TEM techniques. Luo *et al.* reported that the formation of NTs in Au films may lead to the gradual transformation of local grain boundaries from high-angle to low-angle misorientations.[139] The existence of NTs can impact the physical properties of materials.[140] For metals, TBs are normally detrimental to the electrical properties of materials because the conducting electrons can be strongly scattered at NTs (as planar defects).[104] For semiconductors, Kim *et al*. have proven that varying the interatomic range at the 60° twin boundary (TB) of NTs can modify the electronic structure of Bi_2Te_3.[141] However, the morphology and crystallography of NTs in OIMHP materials have not been investigated since these materials are susceptible to electron beam damage. Notably, a long electron beam exposure may result in the disappearance of twin domains and their associated diffraction spots.[12]

2.4.5 Stacking sequences in OIMHP materials

Symmetry is used to study crystals, identify repeating parts of molecules in crystallography. In relation to perovskites, Helen Megaw discovered a high-symmetry structure type that can be viewed as an idealized version of a lower-symmetry structure, which is known as aristo-type.[142] In OIMHP materials, the polytypes determine the ratio between black cubic and yellow hexagonal phases for different compositions.[143] The structure of perovskite materials can be expressed as close-packed AX_3 layers with the octahedral interstitials occupied by B-site cations. The cubic perovskite structure ($Pm\bar{3}m$) is an aristo-type with a cubic close-packed (c) stacking, where the AX_3 layers has an *ABCABC* stacking sequence with corner-sharing BX_6 octahedra (Figure 2.20). On the other hand, when at least the AX_3 layers are partly packed in an *AB'AB'AB'* sequence (*B'* is a twin reflection of *B*), a hexagonal close-packed (*h*) structure is formed as shown in Figure 2.20c, leading to a 2H structure which is also known as the δ-phase. In this case, the octahedra have a face-sharing (B_2X_9) arrangement, which means few X anions are needed to form a 3D network. The hexagonal (4H and 6H) polytypes are usually comprised of a combination of both *h* and *c* stacking sequences, giving rise to both face-sharing and corner-sharing octahedra (Figures 2.20d-e).

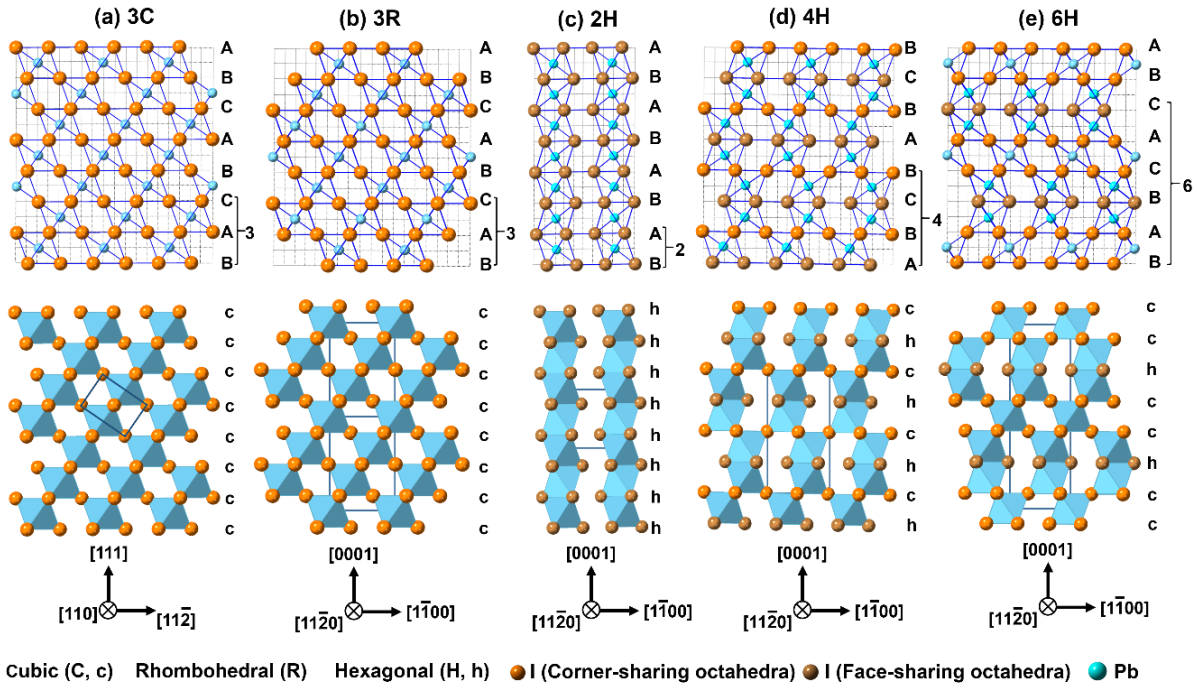

Figure 2.20. Comparison of relevant structures considered in this study, their space group, lattice constant and stacking sequences. Adapted from [144].

The different stacking possibilities can create the formation of various promising polytypes with different properties related to the octahedral connectivity, for example, different band structures.[144] In addition, the band-gap is defined by the number of iodide anions shared between two neighboring Pb ions and is enlarged by higher connectivity. Kamminga *et al.* employed density functional theory to calculate the electronic structure of $(C_6H_5CH_2NH_3)_2PbI_4$ perovskite and indicated that increasing the connectivity of PbI_6 octahedra from corner-sharing, via edge-sharing, to face-sharing results in a remarkable enhancement in the band gap.[143, 145] Moreover, it has been reported that the nanostructure of halide perovskites is defined by various factors, such as octahedra connectivity, local symmetry breaking, TBs, strain gradients, and phase coexistence.

Table 2.2. Comparison of relevant structures considered in this study, their space group, lattice constant and stacking sequences. Adapted from [144].

Crystal system	Space group	a [Å]	b [Å]	c [Å]	Ramsdell notation	ABC	h-c notation	Tilt system
Cubic	$Pm\bar{3}m$	6.35	6.35	6.35	3C	ABC	c	$a^0a^0a^0$
Cubic	$Im\bar{3}$	12.55	12.55	12.55	3C	ABC	c	$a^+a^+a^+$
Tetragonal	*I4mcm*	6.35	12.55	12.55		ABC	c	$a^0a^0c^-$
Orthorhombic	*Pnma*	8.34	12.63	9.04		ABC	c	$a^+b^-b^-$
Rhombohedral	*R3c*	8.9	8.9	10.89	3R	ABC	c	$a^-a^-a^-$
Rhombohedral	$R\bar{3}$	17.74	17.74	10.87	3R	ABC	c	$a^-a^-a^-$
Hexagonal	$P6_3/mmc$	8.67	8.67	7.91	2H	AB	h	$a^-a^-b^+$
Hexagonal	$P6_3/mmc$	8.81	8.81	15.21	4H	ABCB	hc	$a^-a^-b^+$
Hexagonal	$P6_3/mmc$	8.84	8.84	22.45	6H	ABCACB	hcc	$a^-a^-b^+$

2.4.6 Twinning in OIMHP materials

Twins are important defects governing material and device properties, and they are commonly observed in perovskite materials. Twin formation can occur during the crystallization of materials from the vapour, liquid or solid precursors.[146, 147] A phase transformation can also create twinned crystals, for example when the crystal structure transforms from tetragonal (*I4cm*) to cubic ($Pm\bar{3}m$) in perovskite materials. Generally, the twins are defects and can be characterised by an operation as belonging to the reflection, rotation, and centrosymmetry type. Twins typically have a twinning plane whereby the crystal structure of the twin is essentially the mirror image of the crystal structure of the matrix.[147] The crystallographic relation between the twinned sections is defined by three possible transformation parameters: a mirror plane in reflection twins, a rotation axis in rotation twins, and an inversion centre in centrosymmetry twins.

Recently, several research groups have focused on observing and understanding the influence of twin domain structure on the optical properties and device performance in metal halide perovskite.[148-150] To date, there are very few studies on defect properties in OIMHP

materials, and so far their main focus has been on twins, grain boundaries and associated intrinsic defects in $MAPbI_3$.[16, 149-155] For instance, Liu *et al.*, explored the correlation between the chemical modification and ferroelastic twin domains in $MAPbI_3$ thin films using multimodal imaging techniques.[150] Hermes *et al*. was the first group to use piezo-response force microscopy (PFM) to observe the twin domain in $MAPbI_3$.[153] They have suggested that the domain-like structures consist of ferroelastic twin domains formed in $MAPbI_3$ during the transition from the cubic to tetragonal phase as a result of strain.[153] These striped domains have a thickness from 100 to 300 nm in one grain but vary between different grains. Another group employed a combination of various techniques including PFM, polarized light optical microscopy, and photothermal induced resonance to provide solid evidence for the ferroelastic behaviour of polycrystalline $MAPbI_3$.[16] It was proven that the nanoscale ferroelastic domain is altered with applied stress, and they proposed strain engineering as a new parameter to control the optoelectronic properties of $MAPbI_3$ perovskite. Another interesting study shows that the TBs in single crystal $MAPbI_3$ do not affect the carrier transport across them or act as non-radiative recombination centers. The mild electronic nature of the TBs is likely to be related to their unique defect structure.[156]

Understanding the morphology and crystallography of the twin domain is essential to clarify how it affects the optical properties and device performance of PSCs. Rothmann *et al*. have reported clear evidence of twin domains in tetragonal $MAPbI_3$ by employing low-dose TEM and diffraction patterns.[149] In their work, they propose that the TB is parallel to the $\{112\}$ plane and the twin's formation is governed by a small difference in the lattice spacing of the (002) and (110) planes. Another work by Liu *et al*. investigated the crystallographic orientation and piezoelectric properties of twin domain in $MAPbI_3$ perovskite using advanced PFM and electron backscatter diffraction. They reported that the orientation relationship across the twin walls in $MAPbI_3$ is a 90º rotation around $\langle\overline{1}1\overline{1}\rangle$. They observed evidence of non-ferroelectric contributions to the PFM responses of this $MAPbI_3$ sample.[157] The clarification of whether the twin domain affects the ferroelectric properties of $MAPbI_3$ perovskite is still debatable. Furthermore, until now most of studies on twin domains only focused on the $MAPbI_3$ and MA-based perovskite materials.

For FA-based perovskites, the influence of TBs on electron-hole transport, recombination and charge separation has also been demonstrated in various theoretical studies.[148, 158] McKenna used density functional theory to predict the structure and

electronic properties of twin defects in $FAPbI_3$ materials.[148] The {111} TB in cubic $FAPbI_3$ is predicted to be highly stable with a very low formation energy and minimal impact on carrier transport. In multi-cation mixed-halide perovskite materials, the formation of an I-rich phase at the TB can be promoted even at low temperature due to the presence of mobile halide ion vacancies. Such an I-rich phase can facilitate electron-hole recombination and reduce the open-circuit voltage of the device.[148, 159, 160] Recently, Kim *et al*. have attributed the contrast observed by Kelvin probe force microscopy (KPFM) measurements on $(FAPbI_3)_{0.85}(MAPbBr_3)_{0.15}$ perovskite to periodic twin domains.[161] However, experimental reports on the morphology and crystallography of twins and grain boundaries in FA-based and multi-cation mixed-halide perovskites are not widely elaborated despite the fact that these groups of materials are more promising for solar cell applications.

Chapter 3. Experimental methodology and electron microscopy

This chapter describes various experimental and characterisation methods that have been conducted to find out the morphology, elemental composition, crystal structure, defects, optical properties of OIMHP materials and their effect on the performance of PSC devices. First of all, the synthetic procedure of perovskite solution and the fabrication of the devices are described. Next, some essential information on the operation and purpose of using the material characterisation techniques such as X-ray diffraction will be clarified. Then, the basic principle of optical characterisation and surface chemistry techniques are shown in this chapter. Finally, the basic principle of several electron microscopy techniques used to investigate the microstructure in different perovskite materials is discussed.

3.1 Perovskite precursor solution

3.1.1 Materials

The list of materials and suppliers for perovskite precursor solution and device fabrication are showed in Table 3.1:

Table 3.1. List of materials and the suppliers.

Type	Materials	Supplier
Inorganic salt	Rubidium iodide (RbI)	Sigma-Aldrich, 99.9%
	Rubidium bromine (RbBr)	Sigma-Aldrich, 99.6%
	Caesium iodide (CsI)	Sigma-Aldrich, 99.999%
	Caesium chlorine (CsCl)	Sigma-Aldrich, 99.9%
	Caesium bromine (CsBr)	Sigma-Aldrich, 99.999%
	Lead iodide (PbI_2)	Sigma-Aldrich, 99%
	Lead bromide ($PbBr_2$)	Sigma-Aldrich, 99.999%
	Lead chlorine ($PbCl_2$)	Sigma-Aldrich, 99.999%
Organic salt	Formamidinium iodide (FAI)	GreatCell Solar, 99%
	Formamidinium bromide (FABr)	GreatCell Solar, 99.99%
	Methylammonium iodide (MAI)	Sigma-Aldrich
	Methylammonium bromide (MABr)	GreatCell Solar
	Methylammonium chloride (MACl)	GreatCell Solar, >99%
Electron transport layer	Spiro-MeOTAD	Lum-Tech
	Poly[bis(4-phenyl)(2,5,6-trimentlyphenyl)amine (PTAA)	Lum-Tech
	N,N-dimethylformamide (DMF)	Sigma-Aldrich, Anhydrous 99.8%
	N,N-dimethylformamide (DMSO)	Sigma-Aldrich, Anhydrous 99.9%
	Chlorobenzene	Sigma-Aldrich, 99.8%
	Lithium bis(trifluoromethanesulfonyl)imide (LiTFSI)	Sigma-Aldrich, 99.95% trace metal basis
	4-tert-butylpyridine (4-tBP)	Sigma-Aldrich, 99.95%

3.1.2 Perovskite solution preparation

a. $Rb_{0.03}Cs_{0.07}FA_{0.765}MA_{0.135}PbI_{2.55}Br_{0.45}$ perovskite

The multi-cation mixed-halide perovskite precursor solution was prepared by mixing 1.1 M FAI, 0.2 M MABr, 0.2 M $PbBr_2$, and 1.2 M PbI_2 in the 1ml mixed solvent DMF/DMSO with a volume ratio 4:1. The volumes of 30 µL RbI and 70 µL CsI in 1.3 M DMSO solutions were added to 1 mL of perovskite stock solution. Then, 144 µL of DMF and 36 µl of DMSO were added to the mixed solution and diluted to a final concentration of 1 M.

b. $Rb_{0.05}Cs_{0.095}MA_{0.1425}FA_{0.7125}PbI_2Br$ perovskite

To prepare the perovskite stock solution, 1.1 M FAI, 1.2 M PbI_2, 0.2 M MABr and 0.2 M $PbBr_2$ were dissolved in 1 ml solvent of DMF/DMSO (4:1 vol/vol) mixture. Then, 30 µL RbI and 70 µL CsI in 1.3 M DMSO solutions were added to 1 mL of perovskite stock solution. Finally, 144 µL of DMF and 36 µl of DMSO were added to the mixed solution and diluted to a final concentration of 1 M.

c. $FAPbI_3$ perovskite with CsCl and MACl additions

Pure $FAPbI_3$ perovskite precursor solution (1 ml) was obtained by mixing 1.3 M FAI and 1.3 M PbI_2 in the DMF/DMSO (4/1 vol/vol). For CsCl incorporated perovskites, different amounts of CsCl powder were added to the $FAPbI_3$ precursor solution to achieve different molar percentages of 5, 10 and 15%. For MACl incorporated perovskites, different amounts of MACl powder were added into the $FAPbI_3$ precursor to achieve various molar percentages of 10, 20, 30 and 40%.

d. Cs-doped $FAPbI_3$ perovskite

To prepare the pure $FAPbI_3$ precursor solution (1 ml), 1.3 M FAI and 1.3 M PbI_2 were mixed in the DMF/DMSO (4/1 vol/vol). For different Caesium halides, CsX (X = I, Br) incorporated perovskites, 10 mol% of CsX + 10 mol% PbX_2 powder were added to the $FAPbI_3$ precursor solution. For CsCl, 10 mol% of CsCl was added into the $FAPbI_3$ precursor. All the perovskite precursors were mixed well before use.

3.1.3 Transmission electron microscopy specimen preparation

The OIMHP film was spin-coated onto the C film side (instead of Cu or Au side) of a Cu or Au TEM grid to obtain homogenous and uniform sample film as shown in Figure 3.1. The spin-coating was conducted with a 2-step procedure consisting of 4000 rpm for 10 s (with 1000 rpm/s acceleration rate) and 6000 rpm for 25 s (with 6000 rpm/s acceleration rate), respectively. To speed up the crystallization rate, 150 µl of chlorobenzene is quickly dropped in the middle of the sample at 10 s before the program ends. Finally, the sample was annealed by a hotplate at 100 °C for 30 min. The whole process was done inside a glove box with constant N_2 flow.

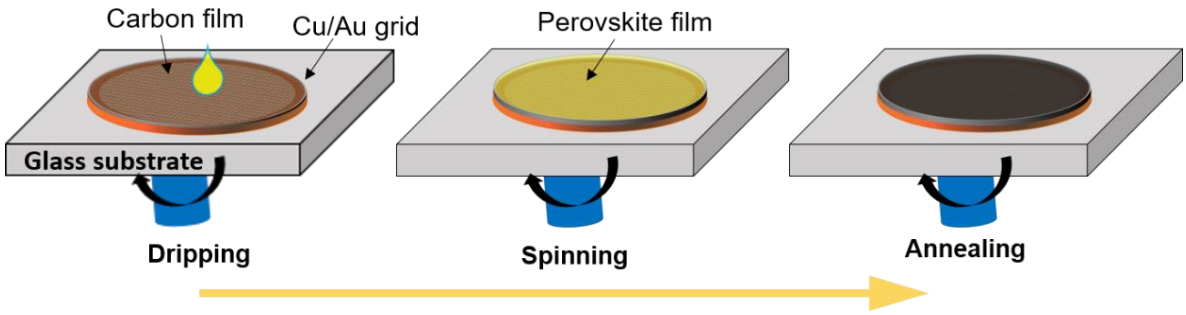

Figure 3.1. Schematic of perovskite thin film deposition on TEM Cu or Au grids using the solution method.

3.2 Device fabrication and characterisation

3.2.1 Device fabrication

a. Substrate cleaning

The substrates (ITO or FTO/glass) were cut into pieces with dimensions 1.45 × 1.25 cm and cleaned with detergent for 90 minutes, then ultrasonically cleaned with acetone, isopropanol, and ethanol for 15 minutes in each solvent sequentially. They were then UV Ozone treated for 30 minutes before transferring to a N_2 purging glove box immediately.

b. Electron transport layer (ETL)

The deposition of 70 nm cp-TiO_2 layer on the pre-cleaned ITO/glass substrates was conducted by spin coating method using the titanium tetra-isopropoxide (TTIP) in isopropyl alcohol solution, with the spinning speed of 5000 rpm for 15 s, followed by annealing in air at 500 °C

for 30 minutes. Next, the substrate is coated with 100 nm of ms-TiO_2 layer via spin-coating method using the solution of 30 NR-D TiO_2 paste in ethanol (1:12 weight ratio) with the spinning speed of 5000 rpm. The samples are again calcinated in the air at 500^oC for 30 minutes and then transferred to a N_2-filled glove box.

c. Perovskite thin film.

The perovskite thin film was deposited on TiO_2 layer coating on ITO/glass the substrates using two-step spin coating procedure. This technique can produce the perovskite films with better control of morphology and crystallization. After covering the substrate with perovskite precursor solution, the substrate was first rotated at a spin rate of 2000 rpm for 10 s (with the ramp rate of 1000 rpm/s) and then at a spin rate of 4000 rpm for 25 s (with a ramp rate of 1000 rpm/s). During the second step, 150 µl of chlorobenzene is quickly dropped in the middle of sample 10 s prior to the end of the spinning program. Immediately after spin-coating, the substrates were placed on a hotplate and annealed at 100 ^0C for 30 minutes.

d. Hole transport layer (HTL)

The Spiro-OMeTAD solution was obtained by dissolving 72 mg Spiro-OMeTAD in 1 ml chlorobenzene. To enhance the p-type conductivity, 17.5 µL of Li-TFSI in 520 mg/mL acetonitrile and 28.5 µL of 4-tBp were added into the solution. Then, the Spiro-OMeTAD layer was deposited on the perovskite film by spin-coating at 4000 rpm for 30 s. After that, the coated substrates were dried overnight in a humidity-controlled box to ensure sufficient oxidation of the Spiro-OMeTAD film.

To obtain the 1 ml PTAA solution, the powder was mixed in 10 mg/ml toluene with an additive of 7.5 µl Li-TFSI in 170 mg/ml acetonitrile and 4 µl 4-tBP. Again, the PTAA layer was spin-coated on the perovskite film at 3000 rpm for 30 s with an acceleration rate of 3000 rpm/s.

e. Electrode

An Au contact with 100 nm thickness was evaporated on the surface of HTL by thermal evaporation via a shadow mask for a cell active area of 0.16 cm^2.

3.2.2 Device characterisation

a. J-V *measurement*

All the J-V measurements of PSC devices were obtained from a solar simulator system one Sun condition (100 mW/cm^2, AM 1.5G, 25 ^{o}C). A certified FraunhoferCalLab reference cell was employed to calibrate the light intensity prior to the measurements. For the reverse and forward scans, the voltage range was maintained at 1.25 V→−0.1 V and −0.1 V→1.25 V, respectively. Unless otherwise stated, all the measurements were done at a dwell time of 200 ms and a scan of 50 mV/s with a voltage step of 10 mV.

3.3 Materials characterisation

3.3.1 X-ray diffraction

X-ray diffraction (XRD) is an effective instrument to characterize the chemical composition, crystalline structure, lattice parameters, strain, and physical properties of materials and thin films by studying the scattered intensity of an X-ray beam interacting with a specimen as a function of incident and scattered angle, polarization, and wavelength or energy. When an X-ray beam is incident on a crystal, the beam can be scattered and diffracted by the electron clouds surrounding the atoms in the crystal as shown in Figure 3.2. Assuming d is the interplanar spacing of the crystal, diffracted beams from successive planes travel an extra length of $2dsin\,\theta$, where θ is the angle between the incident beam and diffracting plane. When this length is equal to an integer multiple of the wavelength of the X-ray ($n\lambda$), the constructive interference occurs and θ is known as the Bragg angle. Depending on the number of consecutive atomic planes in the crystal lattice (known as *(h,k,l)* in Miller notation), the effect of reflection will be cumulative and thus intensifies the constructive interference. In summary, the condition for constructive interference is satisfied by Bragg's law as follows:[162]

$$2d_{hkl}sin\theta = n\lambda$$

where d_{hkl} is the interplanar spacing of the crystal, θ is the angle of incidence of the two parallel rays, n is a positive integer, and λ is the beam wavelength. After recording and analysing diffracted beams by a detector, typical diffraction peaks are observed in the XRD pattern for different angles 2θ with the peak intensity corresponding to particular crystal planes.

In this work, the crystal structure of as-fabricated perovskite films was analysed using a PANalytical X'pert Pro X-ray equipped with a Cu $K\alpha_1$ source (λ = 1.5406 Å) and operated at 45 kV and 40 mA at Research School of Physics – ANU. The divergence slit is 1/32°. We obtained the XRD patterns by scanning 2θ angles with step size 0.01° and an integration time of 0.5 s per step at room temperature.

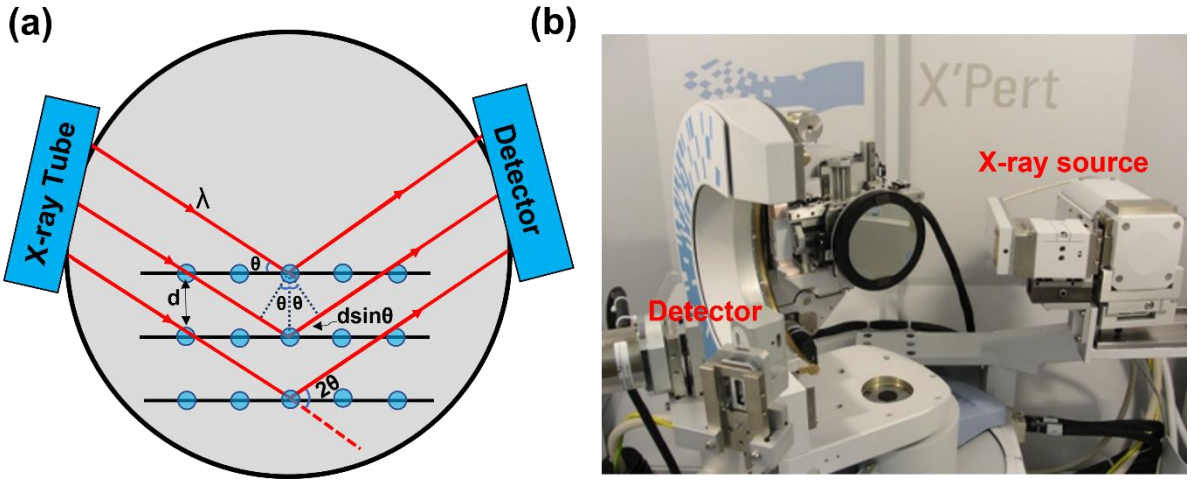

Figure 3.2. (a) The working principle of powder X-ray diffraction and (b) photograph of the PANalytical X'pert Pro X-ray diffractometer.

The CrystalDiffract software was used to calculate powder X-ray diffraction patterns for different perovskite compositions ($MAPbI_3$, $FAPbI_3$, PbI_2) in cubic, tetragonal, and hexagonal phases. The simulation is obtained using a monochromatic radiation type with a Cu $K\alpha_1$ source (λ = 1.5406 Å), a Gaussian peak function, and an instrument peak broadening of 0.1°.

3.3.2 Absorbance Characterization

Absorbance and transmission measurements of various perovskite compositions were obtained with an Ultraviolet-Visible-Near-Infrared (UV-vis-NIR) Spectroscopy (Perkin Elmer Lambda 1050 spectrophotometer) in integrating sphere mode at School of Engineering – ANU.

3.3.3 Photoluminescence Spectroscopy

Photoluminescence (PL) spectroscopy is an optical characterisation method for semiconductors. By exposing a light source such as a laser onto the semiconductor, the incident

photons can transfer their energy to excite electrons to the conduction band, creating holes in the valence band. The non-radiative recombination by emitting phonons or transferring energy to other particles, or radiative recombination of the excited electrons in the conduction band and holes in the valence band to generate photons can result in the emission of photons. In PL spectroscopy, the emitted photons are observed, from which information about the electron energy levels and carrier lifetime can be extracted.

In this thesis, a custom built steady-state PL system with a PIMAX512 CCD camera and an ACTON spectrometer was used to analyse the PL spectra of perovskite films. The samples are excited by a 355 nm pulsed laser with a fluence of ~1 $\mu J/cm^2$ and a repetition rate of 1 kHz. A Horiba LabRAM HR Evolution system equipped with a time-correlated single-photon counting (TCSPC) made by DeltaPro-DD at School of Engineering (ANU) was employed to measure the time-resolved photoluminescence (TRPL) decay. The samples are excited by a 508 nm diode laser (DD-510L, Horiba) with a pulse duration of 110 ps, fluence of ~10 $\mu J/cm^2$/pulse, and a repetition rate of 312.5 kHz. All PL and TRPL measurements of OIMHP films on glass substrate were collected at room temperature and in air.

3.3.4 X-ray Photoelectron Spectroscopy

X-ray photoelectron spectroscopy (XPS) is an extremely powerful tool for studying the surface chemistry of solid materials, which has a basic principle based on the photoelectric effect as shown in Figure 3.3.[163, 164] XPS is a quantitative analysis technique, providing various information such as surface elemental composition, oxidation and chemical state of elements, or empirical formula of a compound. The average depth of XPS analysis is about 10 nm. XPS analysis is based on the interaction of a high energy X-ray beam with the sample surface. During XPS analysis, the core electron of an atom absorbs completely the energy of the X-ray photon, so the electronic structure of the material can be studied. When the energy of photon is large enough, it can knock the core electron of an atom out of the sample surface, so-called a photoelectron. The ionisation energy of a core electron is a measure of its binding energy to the atom at the surface.

Additionally, the surrounding environment of an element is also strongly related to the binding energy of core electron. As one atom can be bonded to various chemical species, the binding energy of its electron depends on the bonding arrangement. In XPS analysis, this variation in binding energy can be detected with the corresponding XPS peak shift, or known

as “chemical shift”, which can be employed to determine the chemical state of the element at the surface. This chemical shift is normally between 0.1 and 10 eV. Particularly, because the number of photoelectrons from an element is proportional to the atomic concentration of that element in the sample, XPS measurement can also be used to determine the elemental composition of a compound.

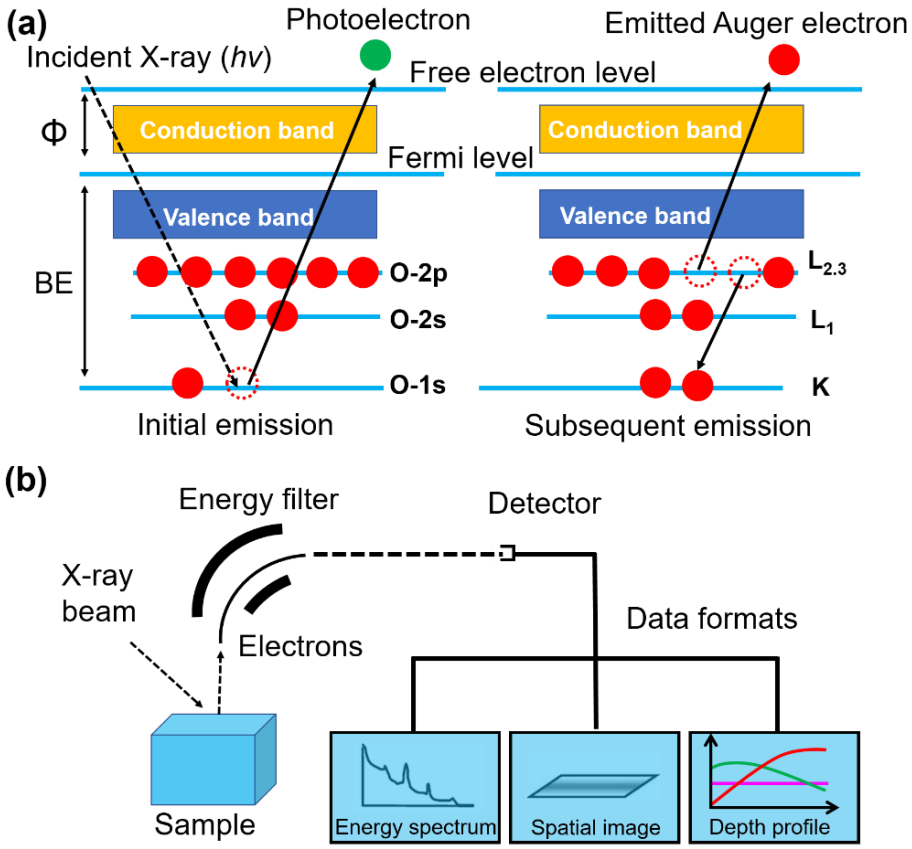

Figure 3.3. Schematic figures showing the working principle of XPS measurement. (a) The photoelectron emission and a subsequent Auger de-excitation process with the different electronic energy levels. (b) The basic components of an XPS instrument.

In this work, XPS has been used to study the surface chemistry of $FAPbI_3$ perovskite with and without CsCl/MACl addition. XPS measurement was conducted with a SPECS (Berlin) machine at Flinders University in an ultra-high vacuum apparatus with base pressure of a few 10^{-10} mbar. Electrons from sample surface were excited with the Mg Kα line (12 kV, 200 W) from a UHV non-monochromatic X-ray source and recorded by an electrostatic energy analyser.[165, 166] Survey scan and high-resolution scan were conducted at a pass energy of 40 and 10 eV, respectively. The XPS peak intensity of various elements is normalized with the

atomic sensitive factor (ASF) before relative concentration is calculated.[167] The spectra were not calibrated as no sample charging was observed. The C-C/CH_3 species was identified at about 284.8 ± 0.2 eV while C-N was fitted at 286.0 ± 0.2 eV. The sample temperature was maintained below 32 ^{o}C using cooling fans.

3.4 Electron Microscopy

3.4.1 Overview of Electron Microscopy

Electron microscopy (EM) techniques, including SEM, TEM, STEM, CL, and EDS are powerful characterisation tools to analyse the morphology, crystal structure and microstructure of materials at the nano and atomic scale. The working principle of these techniques relies on the interaction of an electron beam with the specimen under test, which can produce a wide variety of signals as illustrated in Figure 3.4.

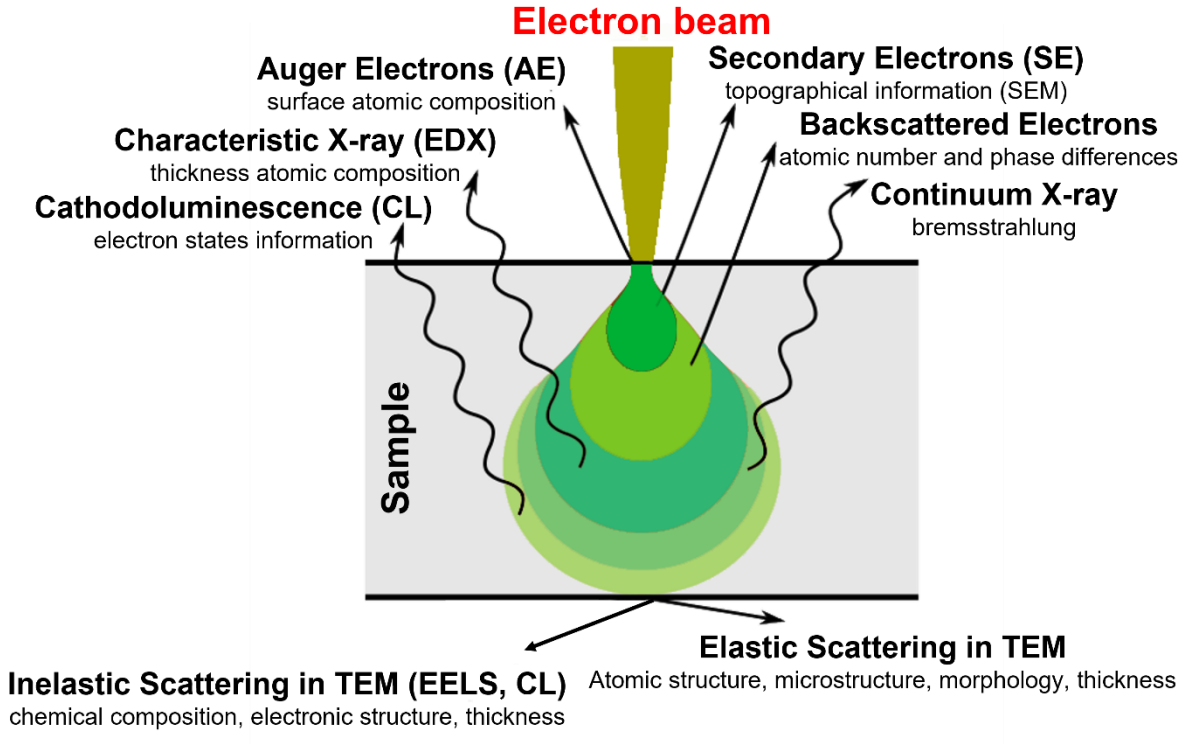

Figure 3.4. The phenomena resulting from the interaction of the electron beam with the specimen. Adapted from [168].

3.4.2 Scanning Electron Microscopy

Scanning electron microscopy (SEM) is a powerful and widely used instrument for investigating the surface morphology, microstructure, crystallography, elemental composition, other chemical and physical properties of material.[169] The resolution of a SEM depends on the instrument ranging from 500 nm to 1 nm. All SEM equipment consists of common components including an electron source/emitter/gun (thermionic, Schottky or field-emission); magnetic lenses used to condense and focus electron beam from the gun; electromagnetic coils to scan the electron beam across the specimen; a circular aperture to form a circular electron probe; a goniometer stage to allow sample to be moved; detectors to collect scattered electrons; electronic/computer system to display/record images and a vacuum system.

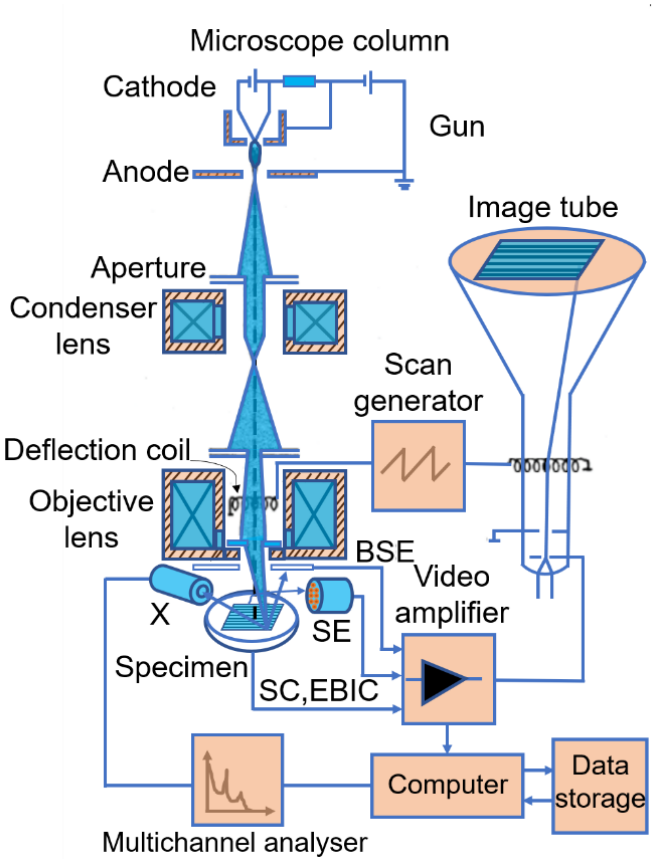

Figure 3.5. A schematic diagram of working principle of SEM. Adapted from [170].

Figure 3.5 indicates the diagram of basic operation principle in SEM, which can be represented as a microscope column. In this column, at the top, an energetic electron beam is produced and accelerated by an electron gun composed of a cathode and an anode. Commonly, the SEM instrument operates at a high electron energy ranging from 0.1 to 30 keV. This electron

beam, after alignment as mentioned by apertures, electrostatic and/or magnetic lenses, and electromagnetic coils, will form a narrow and focused beam to scan on the surface of specimen in a raster (*x-y*) pattern. Finally, the finely modified beam will be focused on a series of closely spaced but discrete locations on the specimen for imaging (Figure 3.5).

The secondary electrons (SEs) and back-scattered electrons (BSEs) are the most common signals used for imaging in SEM. All SEM images presented in this thesis were obtained using SE mode.

a. Secondary electrons

SEs are produced after being ejected from the specimen surface by incident electrons via an inelastic scattering mechanism. In the case of a metal, this inelastic scattering forces out weakly bound conduction band electrons. For the materials with ionic or covalent bonds, the beam of electrons ejects weakly bound valence electrons from surface atoms. The binding energy of SEs is ranging from 1-15 eV with respect to the original atoms. Typically, the electron beam has high energies from 0.1 to 30 eV. However, due to its low kinetic energy transfer, SEs are normally ejected from the sample surface with kinetic energies below 5eV. Therefore, SE signals can only characterize a few nanometres below the sample surface, and it provides details of the specimen surface topography. The surface tilt can significantly enhance the SEs emission and topographic contrast. The quantification of the SEs yield is calculated using the following equation:

$$\delta = N_{SE}/N_B,$$

where N_{SE} is the number of secondary electrons emitted from the specimen and N_B is the number of incident beam (primary) electrons.

b. Backscattered electrons

BSEs are produced when the electron beam interacts with the specimen and are backscattered within the specimen. The initial beam will lose a portion of its initial energy (E_0) depending on the path length within the sample. Before escaping from the specimen surface, BSEs are scattered and deflected by the electric fields of the atoms in the specimen, but they still carry a large fraction of their incident energy intact. The BSEs coefficient (η) is quantified by the ratio of the number of backscattered electrons (N_{BSE}) to the number of electrons that enter the

specimen (N_B). The BSEs coefficient increases the topographic contrast (increasing tilt of surface) and composition contrast (increasing atomic number of target). In SEM characterization, BSEs can provide information about the chemical composition, crystallography, topography and atomic mass of the specimen. BSE images are sensitive to the atomic number of elements within the specimen.

For PSCs, SEM has been widely employed to study the surface morphology of perovskite film as well as the cross-sectional view of the PSC device, in order to optimize the fabrication process.[171] In this study, the morphology and thickness of perovskite films were observed by the FEI Verios SEM instrument at Australian National Fabrication Facility (ANFF - ANU). In order to minimise the damage of OIMHP material under electron beam, we obtained the SEM images at low energy with 2 kV acceleration voltage and 25 pA probe current.

3.4.3 Focused Ion Beam Time of Flight Secondary Ion Mass Spectrometry

Time of flight secondary ion mass spectrometry (ToF-SIMS) is an effective analytical method, which enables the molecular and chemical composition analysis of material surfaces by identifying the secondary ions sputtered from the specimen with their time-of-flight. ToF-SIMS is widely employed to study various materials including semiconductors, metals, ceramics, polymers, inorganic materials, glass, and biomaterials.

The operation principle of SIMS relies on the bombardment of high energy ions (1-25 keV) onto the sample surface and then measuring the mass of ejected secondary ions. The transfer of energy from the primary ions to the surface atoms produces a collision cascade via the atomic collision mechanism. This amount of energy allows the surface atoms and molecular components to exceed the surface binding energy. Since the ejected particles, either neutral or charged, come from the top one or two atomic layers, SIMS is known to be very surface sensitive (Figure 3.6a).

In some cases, some ions have the same energy but travel with different velocities because of the differences in mass. To analyse these, ToF mass spectroscopy is conducted by accelerating the generated ions and then measuring the flight time of each ion. In ToF-SIMS analysis, the secondary ions are extracted and collected to produce the mass spectra and map. The integrated peak intensity of any element, compound or isotope in their mass/charge spectra can be shown as an intensity map over the region of interest. Mass spectra, depth profiles (ion

intensity versus depth measurements) and ion (elemental or molecular) imaging are all outputs from a typical analysis. Here, the ToF-SIMS measurement is integrated into a focused ion-beam scanning electron microscope (FIB-SEM) system and referred to as FIB-ToF-SIMS.

Unlike other elemental characterization techniques such as EDS, FIB-ToF-SIMS is capable of light element detection[172] and trace element mapping.[173] The finely focused ion beam of a FIB-SEM and the small information volume of SIMS analysis enables high spatial and depth resolution elemental maps (lateral resolution < 50 nm, depth resolution < 20 nm) thus making this technique suitable for the analysis of PSCs. In order to minimize the sample damage when using FIB-ToF-SIMS analysis, the primary ions with lower energy (e.g. 10 - 20 kV) should be employed. It should be noted that the low beam currents can only sputter a few hundreds of angstroms of materials from the specimen surface, therefore the mapped region was used for site-specific sample.

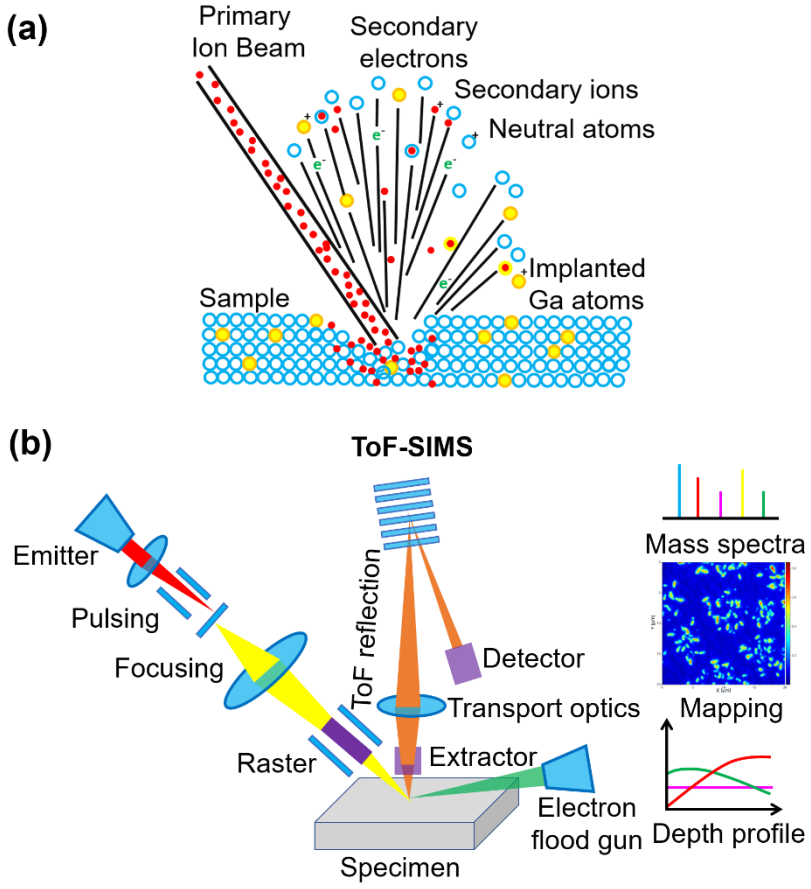

Figure 3.6. A schematic diagram of the working principle of ToF-SIMS. Adapted from [174].

In this work, elemental maps and depth profiles of multi-cation mixed-halide perovskite samples were examined by a Tescan Lyra3 FIB-SEM based ToF-SIMS (referred to as FIB-ToF-SIMS) with a monoisotopic ^{69}Ga ion source and fitted with a Tofwerks C-TOF detector at the John de Laeter Centre, Curtin University. Positive and negative ions were collected in separate analyses over 20 × 20 μm^2 areas with the typical analysis depth being 600 nm (measured by SEM imaging of the edge of the analysis pit). To minimise layer mixing and elemental migration due to ion beam heating, the analysis was performed with a 20 kV ion beam energy and a 50 pA current. These conditions were the lowest energy and current possible whilst still achieving sufficient signal for analysis.

3.4.4 Transmission Electron Microscopy

TEM is one of the most effective instruments for the investigation and analysis of material microstructure. The TEM can be used to characterize the structural and chemical composition of specimens up to and including atomic resolution. In the TEM technique, a high energy electron beam is transmitted through a very thin specimen which is usually 0.05 – 0.4 μm thick. The interactions between the electrons and crystal reveal features regarding the morphology, composition, atomic contrast, crystal structure, grain boundaries and defects of the sample. The basic operation principle of TEM is shown in Figure 3.7. A TEM system includes an electron gun, condenser lens (at least two), condenser aperture, sample holder, objective lens, objective aperture, selected area electron diffraction (SAED) aperture, intermediate lens, projector lens (at least two) and an imaging system. The accelerating electrons from the electron gun first pass through the condenser lens with apertures which adjust the intensity and convergence angle of the electron beam.

Figures 3.7a and b show the two common modes of TEM operation - imaging and diffraction, respectively.[175] The objective lens is one of the most essential lenses as it determines the quality of a TEM characterisation and sample information. Generally, the electron beam after passing through the objective lens will produce a diffraction pattern (DP) in the back focal plane (BFP) and an image in the image plane. By adjusting the strength of the current in the intermediate and projector lenses, either the diffraction pattern (BFP) or image (image plane) is projected on the screen. The objective aperture should be inserted during the alignment to enhance the image contrast. The sample region for diffraction analysis can be chosen using the SAED aperture. The intermediate and/or diffraction lens is used to control the magnification and camera length.

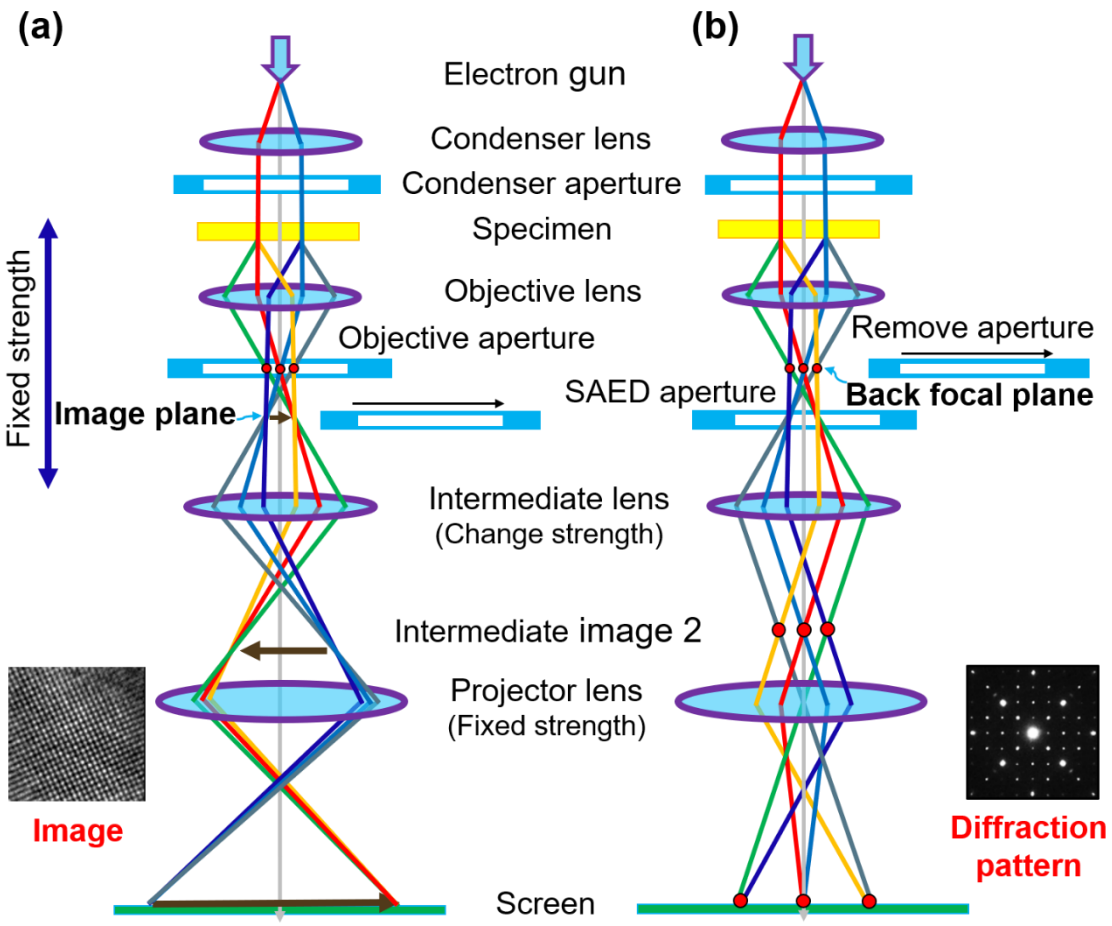

Figure 3.7. Schematic of lens setup for the TEM in (a) imaging and (b) diffraction mode. Adapted from [175].

a. Bright-field and dark-field imaging

TEM imaging mode is conducted with an objective aperture, one of the most important apertures in TEM instrument. Several imaging modes are possible such as bright-field (BF), dark-field (DF) and centred dark field (CDF). BF images are most commonly used for crystalline materials. A BF image can be taken by inserting an objective aperture in the BFP of the objective lens to select the transmitted (direct) beam and remove the contributions of all diffracted beams to the image formation (Figure 3.8a). When we shift the aperture to collect the diffracted beam, a DF image is formed (Figure 3.8b). However, the quality of DF image is usually poor due to the aberration and astigmatism of the diffracted electron beam, which is far from the optic axis.[175] An improved technique is to tilt the incident illumination on the specimen so that the diffracted beam is along the optic axis and hence does not suffer from

spherical aberration. The dark field TEM pattern image formed in this way, is thus called a CDF image (Figure 3.8c).

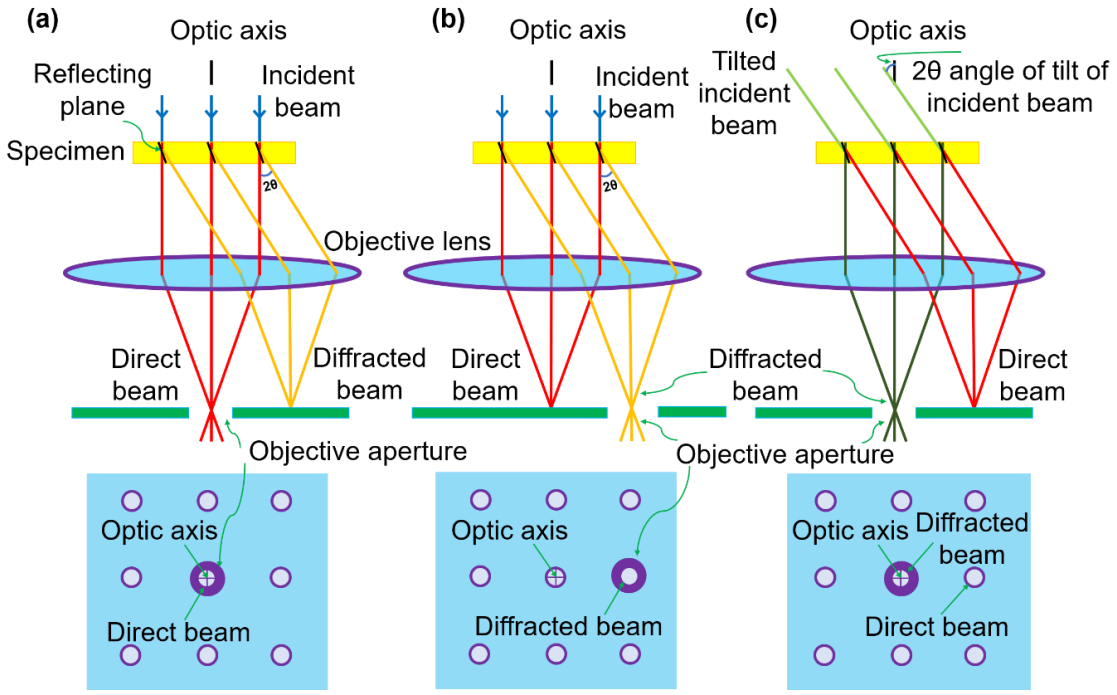

Figure 3.8. Schematic of the objective lens and objective aperture setup to produce (a) BF, (b) DF and (c) CDF image. Adapted from [175].

b. Selected Area Electron Diffraction Patterns

For diffraction mode, a SAED aperture is inserted in the image plane of the objective lens and a virtual aperture is created in the plane of the specimen as shown in Figure 3.9. Basically, when the electron beam coming to the specimen surface, this virtual aperture only allows the electrons falling inside its selected dimensions to go through into the imaging system and contribute to the SAED pattern. In crystalline specimens, the wave nature of the electron beam, and the regular spaced atomic planes of crystal lead to diffraction. Diffraction will dominate scattering and nearly all scattered electron intensity will occur at discrete angles and from a diffraction pattern in the BFP. This occurs because scattering in an ordered array of atoms (crystal) results in constructive and destructive interference peaked at a precise angle, the spot in a diffraction pattern.

SAED is an important tool in TEM, which is strongly useful to study the crystal structure of selected regions. For PSCs, the diffraction patterns of individual grains have been employed

to identify various crystal structures of perovskite materials, such as cubic, tetragonal, hexagonal and orthorhombic phases. In addition, SAED patterns can be used to calculate the interplanar distance by measuring the distance between relevant diffraction spots and taking the reciprocal of that distance. The crystal defects, for instance, twins, SFs, and grain boundaries, are also visible in the SAED patterns.

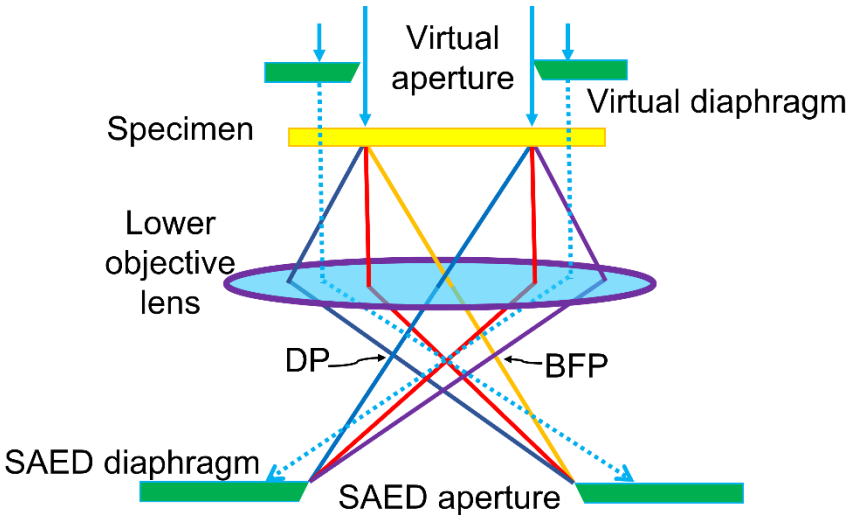

Figure 3.9. Ray diagram showing SAED pattern formation. Adapted from [175].

In this study, a JEOL 2100F FEGTEM instrument (located at the Centre for Advanced Microscopy, ANU) was operated at 200 keV to study morphology, crystal structure, microstructure and elemental composition of the perovskite film. In order to minimise the damage of OIMHP materials under electron beam, we employ the low-dose TEM technique with a dose rate of about 2 e $Å^{-2}$ s^{-1} and rapid acquisition condition. The condenser aperture size is 40 μm, an exposure time is 0.5 seconds, a spot size of 3 to 5 was used (depending on the thickness of the specimen) and the beam was spread to reduce the dose rate. To enhance the contrast of BF-TEM images, the 20 μm objective aperture was used. The Gatan Orius SC200D (2k × 2k) diffraction camera was used to collect the SAED patterns and BF-TEM images. All TEM images and SAED patterns were recorded from the non-exposed regions of the sample. When collecting the SAED pattern, we used selected area aperture to select the region of interest. The yellow circle in BF-TEM images in Chapters 4, 5, 6, 7 indicates the area selected to collect the diffraction pattern.

The SingleCrystal software was used to calculate diffraction patterns for different perovskite compositions ($MAPbI_3$, $FAPbI_3$, PbI_2) in cubic, tetragonal, rhombohedral, and

hexagonal phases. The simulation is obtained using a beam voltage of 200 keV, a camera length of 1000 mm, a spot size of 0.02 1/Å and a crystal thickness of 100 nm.

3.4.5 Scanning Transmission Electron Microscopy

In scanning transmission electron microscopy (STEM), the electron is focused to an extremely small probe (within nanometer- and angström-size) and is scanned over the specimen by deflection coils. Two types of STEM images can be collected corresponding to the transmitted electrons that are used to create the image, including BF and DF images. STEM mainly use an annular detector to produce annular dark-field (ADF) images. The angular range of electrons falling onto this detector can be adjusted by changing camera length with the intermediate lenses in STEM mode. Another typical image can be obtained by STEM is high-angle ADF (HAADF) image, in which the annular detector only collects the Rutherford-like scattering electrons, i.e. the electrons are scattered under large angles by the specimen. Since the intensity of HAADF image is approximately proportional to the square of the atomic number (Z^2) and to the thickness of the specimen, this type of STEM technique is also known as Z-contrast imaging, which is sensitive to both sample's chemical composition and thickness.

In this thesis, a JEOL 2100F FEGTEM system (located at the Centre for Advanced Microscopy, ANU) was used to obtain the HAADF-STEM image of the multi-cation mixed-halide perovskite film in Chapter 4.

3.4.6 Energy-dispersive X-ray Spectroscopy

Energy-dispersive X-ray Spectroscopy (EDS) is a technique suitable for quantitatively analysing the chemical composition of target materials using X-ray signals emitted from the materials. EDS is a technique normally coupled with electron microscopes such as SEM or TEM which are equipped with an EDS spectrometer system. Basically, when the electron beam from an SEM or TEM system interacts with the solid material, X-rays are generated and emitted from the surface of the material, which can be detected by the EDS detector. These X-ray signals are transformed to voltage pulses by the detector, and then electronically translated into a signal in a specific channel in a computer-controlled storage system. The intensity of the EDS signal is displayed as a function of X-ray energies and EDS peaks intrinsic to the elements are used to determine the chemical composition of the material.

In this thesis, a JEOL 2100F FEGTEM system equipped with a JEOL solid-state detector (SSD) EDS system (located at the Centre for Advanced Microscopy, ANU) was used to obtain the element mapping of multi-cation mixed-halide perovskite films. The microscope is also capable of STEM imaging in DF and HAADF modes.

3.5 Electron beam damage

EM is one of the most powerful techniques for the investigation and analysis of the material microstructure. However, the specimens, especially beam sensitive materials including polymers, inorganic materials, and biological samples, may be damaged by the interaction with electrons, e.g. radiolysis, atomic displacement, knock-on damage or sputtering, and heating. The energy of the incident beam governs the damage level on the structure and/or the chemistry of the specimen. For instance, the radiation damage of organic and biological samples is mostly due to ionization (in which the samples absorb the amount of energy from 10 to 1000 eV per event) and plasmon excitations, which are mainly responsible for the sample heating.

Furthermore, at different length scales, the damage mechanisms proceed differently: the distortion of crystal lattices due to the atomic displacement and knock-on damage can be observed at a resolution of less than a nanometer; while the changes in morphology because of surface heating, sputtering, and electrostatic charging are observed in the nanometer and micrometer scales. Therefore, electron beam damage is known as a physical limit and is the factor determining the achievable artefact free resolution in the characterization of beam sensitive materials by EM. The analysis and understanding of beam damage are important to facilitate the investigation of these beam sensitive materials with the minimum amount of damage. Figure 3.10 shows one of the electron beam damage classifications according to the elastic and inelastic scattering.

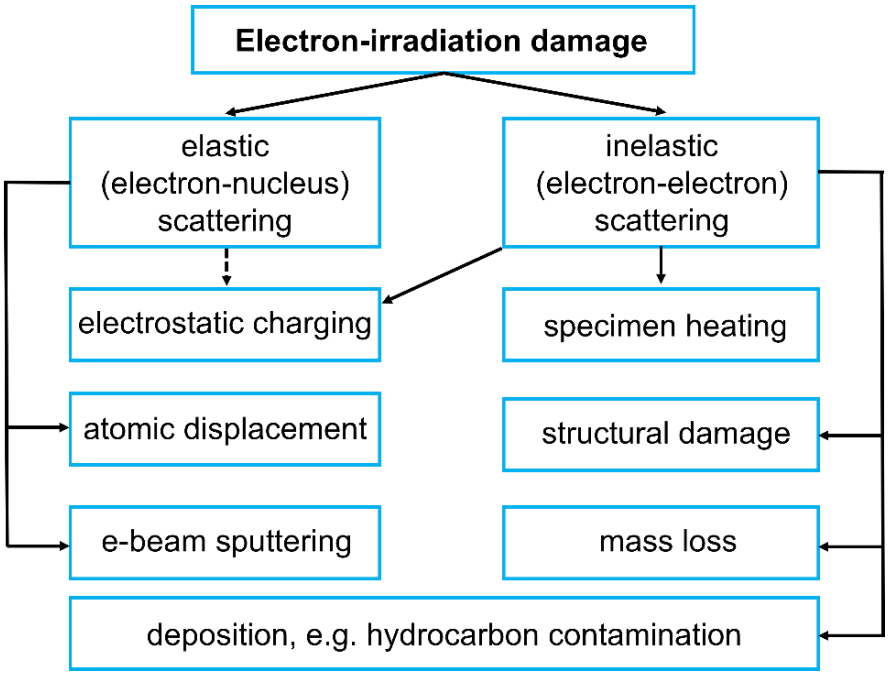

Figure 3.10. Classification of electron beam damage corresponding to the type of electron scattering and the effects produced in the sample. Adapted from [176].

3.5.1 Radiolysis

Radiolysis originates from the electronic excitation and ionization of the sample in electron-electron interactions in inelastic scattering process. This damage can lead to the breaking of chemical bonds within certain materials and atomic displacements. Organic and polymer samples have high sensitivity to the electron-electron interaction because the chemical bonds in these materials can be easily broken, resulting in a new structure. The basic structure of polymer materials can be modified when the electrons destroy the polymer chain. The side groups of such polymer also can be broken off under the effect of electrons, forming reactive free radicals which can crosslink with each other to create a new structure. If the polymer samples have crystalline structure, the radiation damage can destroy its crystalline structure, and this can be quantified by measuring the loss of diffraction contrast during imaging or the loss of sharp peak in the diffraction pattern.[175]

There are various methods can be used to minimize beam damage in organic and polymer samples:[175]

- Use of low-dose image techniques. Electron dose in TEM is defined as the charge density (C/m^2), which can be converted to the number of electrons/unit area (usually e/nm^2) with $e = 1.6 \times 10^{-19}$ C.

- Sample coating with metallic film.

- Sample cooling to or below liquid N_2 temperatures if possible.

- Employing low-dose STEM imaging with highly sensitive electron detectors.

3.5.3 Electron beam heating

When the electron beam with high energy bombards a specimen, the temperature of the specimen can increase due to inelastic scattering between the incoming electron and particles. Photons can also heat the sample, and this is the main damage mechanism for polymers and biological tissue. In practice, it is difficult to quantify the sample heating since the result can be varied and affected by many factors, such as the sample's thermal conductivity, thickness, and surface condition, or the size, energy and current of electron beam. For a sample with very high thermal conductivity, heating can be ignored. However, for the low thermal conductive sample, heating can be quite remarkable. For instance, beam heating for metallic sample is normally very tiny but extremely high for small ceramic particles, may be up to temperatures of ~1700 ^oC.

Beam heating is one of the issues in the TEM at high incident currents. The level of heating depends on the condenser-lens aperture and the diameter of electron probe. With the same incident beam current, the temperature increase involved in STEM imaging technique should be lower compared to that in TEM imaging.[176] SEM imaging normally uses a bulk sample so the heat flow is dispersed in three dimensions and the temperature increment is quite small. However, if an organic thin film on a TEM Cu grid is loaded for SEM imaging with an incident energy ranging from 500 eV to 2 keV, the local temperature can rise up to few hundred degrees for a stationary probe.[177] Beam damage and heat are the main consequences of inelastic scattering process and can be disastrous for all kinds of TEM specimens under certain conditions. To reduce the heat transfer effect, we can cool down the sample, use lower voltages and thinner specimens.[175]

3.5.4 Knock-on damage and sputtering

In high-voltage TEM, the damage in inorganic crystal samples can be classified into two basic forms: knock-on atomic displacement or ionization. The “knock-on damage” happens via electron-nucleus scattering for crystalline solid samples. This kind of damage causes the displacement of atoms and leaves point defects in the crystal lattice. The “knock-on damage” is called “sputtering” if atoms are ejected from the sample surface. When the incident electron energy is higher than the displacement energy of elements within the characterized material, we normally can observe the atomic displacement.[178] The knock-on and sputtering damages may appear in all materials if the accelerating voltage is high enough, which can change the surface chemistry or produce non-characteristic crystal defects in the sample.

For metallic samples, knock-on atomic displacement is the primary damage.[175] Because of the momentum conservation, only a small amount of incident electron beam energy is absorbed by a nucleus. With that, even the binding energy of lattice atoms is quite small (~5–60 eV), and a high electron beam energy is required to remove an atom from its original position in the lattice. Therefore, knock-on atomic displacement can be avoided by using an incident electron beam energy lower than the incident-energy threshold of the characterized material.

3.6 Electron beam damage in OIMHP materials

OIMHP materials are known to be unstable under a wide range of conditions, such as exposure to air, moisture, heat, UV, and electron beams.[179, 180] The morphological, structural, chemical, and optical properties of metal halide perovskites can be dramatically changed under a high-energy electron beam exposure via three main mechanisms of phase transformation, defect formation, and/or material decomposition.[180] The structure of perovskite materials undergoes complicated phase transformation under the exposure of electron beam. Chen *et al.* investigated the structural instability of the $MAPbI_3$ single crystals by TEM and observed that $MAPbI_3$ is extremely sensitive to the exposure of electron beam and quickly decomposes into the PbI_2 phase.[13] $MAPbI_3$ perovskite starts to decompose into hexagonal PbI_2 structure under total electron irradiation dose of 150 $eÅ^{-2}$.[13, 181] Another study demonstrated that the structure and composition of $MAPbI_3$ perovskite change with increasing electron dose.[12] Manekkathodi *et al.* used in-situ TEM to observe the structural phase transition and the formation of hexagonal PbI_2 phase during degradation of $Cs_{0.05}MA_{0.10}FA_{0.85}Pb(I_{0.85}Br_{0.15})_3$

perovskite under electron beam exposure.[182] The mechanisms of electron beam damage in perovskite materials vary with the material composition.

A long electron beam exposure may result in the disappearance of diffraction spots, striped twin domains, and SFs. Figure 3.11 shows BF-TEM images of Cs doped perovskite film under a weak beam expose. The contrast of some grains slightly changed under a weak beam exposure. The twin domain started to damage after 2 mins of exposure and disappear after 3 mins of weak electron beam exposure. Moreover, Figure 3.11d illustrates the appearance of the cracks at grain boundaries of perovskite films and the uniform darker contrast.

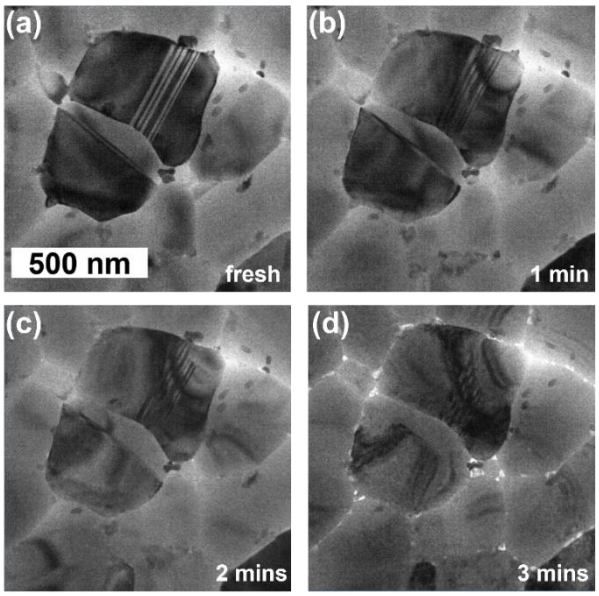

Figure 3.11. BF-TEM images of the same region of $FAPbI_3$ perovskite films with CsX additions after low dose electron beam exposure with a dose rate of about 2 e $Å^{-2}$ s^{-1} for (a) brief, (b) 1 min, (c) 2 mins and (d) 3 mins.

There are several ways to reduce the damage of metal halide perovskite under electron beam. One is to set low accelerating voltages and have a low-energy electron beam during measurements. However, the spatial resolution when using these parameters is certainly low. The second method is to employ a low-dose electron beam technique. Reducing electron dose would of course decrease the amount of electron signal but this method is very useful to minimize all three types of beam damage. Recently, the development in aberration-corrected STEM and relevant in-situ electron spectroscopy methods, together with the developments of different low-dose techniques, have facilitated the fundamental investigation of the microstructure, atomic structure and functionality information of metal halide perovskites and

associated optoelectronic devices. In this thesis, to minimise the damage of halide inorganic-organic perovskite material under electron beam, a low-dose TEM technique with a dose rate of about 2 e $Å^{-2}$ s^{-1} and a rapid acquisition condition was employed. All TEM images and SAED patterns were recorded from the non-exposed regions of the sample.

Chapter 4. Chemical and Structural Properties of Multi-cation Mixed-halide Perovskite

This chapter aims to describe the impact of Rb^+, Cs^+ cations on the microstructure, crystal structure, and elemental composition of multi-cation mixed-halide perovskite. Our time-of-flight secondary ion mass spectrometry results reveal that Rb^+ and Cs^+ cations were typically segregated at the grain boundary of perovskite film as a discrete Rb, Cs-rich phase. However, Cs^+ cation was also found to be incorporated into the perovskite structure. Our electron diffraction studies show the visibility of forbidden reflections in the electron diffraction patterns. We propose that these forbidden reflections are a direct result of the perovskite structure and attribute them to superlattice reflections. Furthermore, we show evidence for the coexistence of cubic and tetragonal phases in the diffraction patterns at room temperature. The results presented in this research offer additional insight into the cation incorporation in mixed halide perovskite materials.

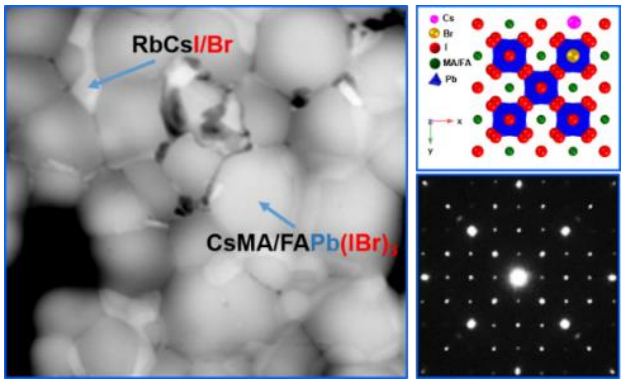

4.1 Introduction

PSCs have demonstrated a breakthrough in PCE, making them the fastest developing solar cell technology in history. However, a common problem is the stability of PSCs under the influence of light, moisture, and heat, which is a primary obstacle to its potential for commercialization. It has been reported recently that the introduction of inorganic cations, e.g. rubidium (Rb) and caesium (Cs), can remarkably enhance the device stability and PCE of PSCs.[85, 86, 91, 183-192] With the insertion of Rb- and Cs-atoms in the OIMHP, a different perovskite structure may be obtained because of the smaller atomic radius of Rb^+ (152 pm) and Cs^+ (167 pm) cations in comparison with MA^+ (217 pm) and FA^+ (253 pm) molecular cations. Moreover, a small amount of Rb^+ and Cs^+ cations mixed with MA^+ or FA^+ cations can change the tolerance factor,

resulting in a stability improvement of the photoactive perovskite phase over an extended temperature range.[91, 193] For example, Turren-Cruz *et al.* reported a device based on the $Rb_xCs_yFA_{(1-x-y)}PbI_3$ structure with a polymer-modified layer, which demonstrated excellent stability for up to 1000 hours in a nitrogen atmosphere at room temperature.[190]

However, the interaction between various cations and halides becomes more complicated with every additional component to the perovskite formation. Hu *et al*. employed EDS and in situ XRD to demonstrate that the incorporation of Cs^+ cation into the multi-cation mixed-halide perovskite structure causes a lattice contraction and stabilization of the photoactive perovskite phase.[193] Moreover, the formation of non-perovskite phases is induced by the addition of Rb^+ ions.[85] However, EDS analysis is generally not able to differentiate between Cs and I characteristic X-ray peaks as they overlap with each other and is limited by the energy resolution of the EDS detector. Yadav *et al*., using impedance spectroscopy and analysis of dark J-V characteristics, found that the incorporation of Rb^+ in the perovskite films can reduce trap-assisted recombination and thus increase their conductivity.[194] Until now, the influence of Cs^+ and Rb^+ cations on the crystal structure of perovskite materials and their optoelectronic properties and stability have not been elucidated yet.

Another key issue is that the investigation on morphology, microstructure, elemental composition, and electronic structure of PSC materials has not been completely and systematically reported. This is partly due in some cases to the sensitivity of OIMHP materials, in particular $MAPbI_3$, to electron beam damage during TEM studies.[12, 149, 154, 195-197] Within the literature, there are several inconsistencies between the experimental diffraction data and the visibilities of allowed reflections expected from their respective space groups. Kim *et al*. observed the coexistence of cubic and tetragonal phases in a $MAPbI_3$ film at room temperature, but very few SAED patterns published previously for these perovskite compounds are consistent with the simulation results on both tetragonal and cubic phases.[95, 154] For instance, the reflections of (110) and (020) planes in tetragonal structure are typically visible in XRD measurements. Yet, these diffraction spots along the [001] zone axis are clearly absent in the electron diffraction patterns, and this anomaly was ascribed to the low electron diffraction intensity of organic-inorganic halide components.[198-200] It has been reported that some of the issues encountered with pure $MAPbI_3$ and $FAPbI_3$ perovskites can be resolved by mixing them within the same perovskite structure.[194, 201-204] In general, the microstructure and

atomic structure studies on $MAPbI_3$, $FAPbI_3$ and mixed perovskites still lack adequate and systematic information to clarify the origin of their high performance and poor stability.

In this chapter, we explore the impact of inorganic cations such as Rb^+ and Cs^+ on the morphology, crystal structure and chemical composition of perovskite materials. We performed an extensive study on the $Rb_{0.03}Cs_{0.07}FA_{0.765}MA_{0.135}PbI_{2.55}Br_{0.45}$ hybrid perovskite compound which has shown significantly enhanced efficiency and stability.[205] In order to understand the origin of the high performance PSCs fabricated from this perovskite layer, we deposited simultaneously the perovskite film on substrates (for solar cell application) and TEM grids for parallel microstructural analysis of this layer. Though the crystal structure of that perovskite compound was previously unknown, we use a combination of XRD, TEM and electron diffraction simulation to determine its crystal structure. Moreover, we determine the chemical composition of this perovskite materials using EDS mapping in STEM mode and FIB-ToF-SIMS.[206] The latter involves multi-modal correlative microscopy combining FIB, SEM and SIMS. Our results establish the coexistence of both cubic and tetragonal crystal structures within the mixed perovskite structure as well as the 3D chemical composition of this multi-cation mixed-halide perovskite material, showing Rb^+ segregation within the perovskite layer.

4.2 X-ray diffraction pattern of multi-cation mixed-halide perovskite

To illustrate the subtle difference between the cubic and tetragonal structures, we refer to the simulation XRD pattern of $MAPbI_3$ for cubic and tetragonal structures. We use the subscripts "t" and "c" to represent the index in the tetragonal and cubic structure, respectively. In the XRD simulation of tetragonal $MAPbI_3$, the following diffraction peak positions are very close to each other namely, $(002)_t/(110)_t$, $(112)_t/(020)_t$, $(004)_t/(220)_t$, $(114)_t/(130)_t$ (Figure 4.1a). While this can be separated in the simulation, it is hard to distinguish these in the experimental data as shown in Figure 4.1b because the experimental Bragg peak is wider than the ideal simulation peak. This depends on the optics of the XRD system used for the analysis. In addition, the following diffraction peaks are coincident in the simulated patterns namely $(002)_t/(001)_c$, $(112)_t/(011)_c$, $(004)_t/(002)_c$ or $(114)_t/(012)_c$. It is impossible to separate these reflections in the experimental XRD pattern. To distinguish between the cubic and tetragonal phases, we look at the ratio of the peaks at 13.9º and 19.8º which can be assigned $(002)_t/(001)_c$ and $(112)_t/(011)_c$ respectively. For a cubic phase, the 19.8º peak is more prominent while for the tetragonal phase, the 13.9º peak is the dominant peak. The experimental XRD for $MAPbI_3$ clearly shows a

dominant peak at 14º, consistent with the tetragonal phase. Furthermore, the peaks at 30.5 and 37.5º cannot be indexed to cubic phase and can only be attributed to the (123) and (213) planes of the tetragonal structure, respectively.

The experimental XRD pattern of the multi-cation mixed-halide perovskite films is shown in Figure 4.1b. All the diffraction peaks mostly belong to the perovskite tetragonal phase. The strongest peak at 14.1º corresponds to the (110)/(002) orientations of the black perovskite phase. Moreover, the typical diffraction peaks of perovskite film at the 2θ values of 20, 24.5, 28.5, 30.5, 32, 35 and 40.5º can be clearly observed, corresponding to (112)/(200), (202), (220)/(004), (213), (310), (312) and (224)/(400) planes, respectively. The small peaks at 10.3 and 27.1º are likely related to a Rb-rich phase. This is consistent with XRD patterns for the $RbPbI_3$ phase with (110), (002) and (221) peaks at 10.03, 10.20 and 27.1º, respectively.[207, 208] With the addition of MA and FA, the peaks at 12.6 and 11.6º corresponding to PbI_2 and the non-perovskite δ-$FAPbI_3$ are not observed in this study. Therefore, our results suggest that a small amount of Rb^+ and Cs^+ cations mixed with halide lead perovskite can control the amount of excess PbI_2 and make the black perovskite phase stable at room temperature.

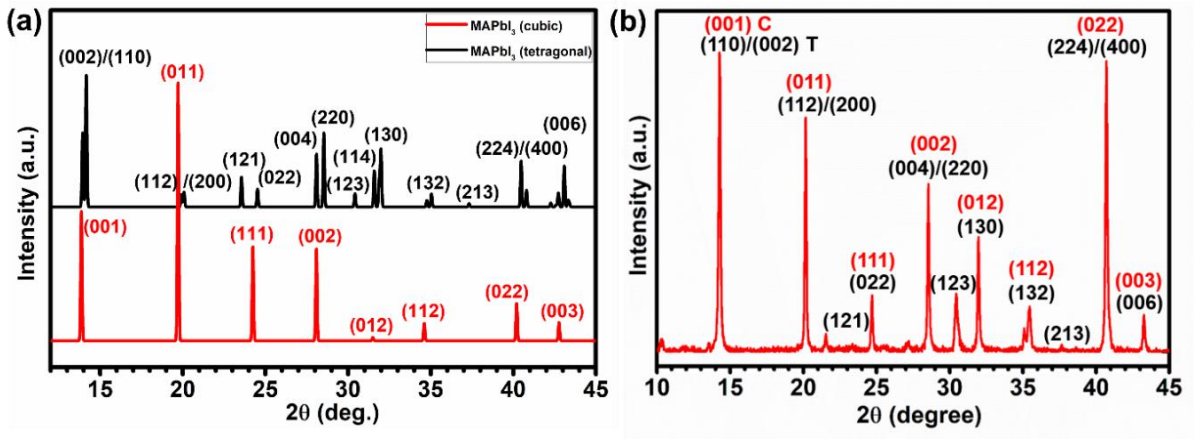

Figure 4.1. (a) Simulation XRD patterns of $MAPbI_3$ for cubic and tetragonal structures. (b) Experimental XRD pattern of the multi-cation mixed-halide perovskite film at room temperature.

However, in XRD analysis of $MAPbI_3$ materials, some diffraction peaks cannot be separated, for example, $(110)_t/(002)_t$ or $(112)_t/(200)_t$ (Figure 4.1b). This can be separated in the simulation result (see Figure 4.1a) but is hard to distinguish them in an experimental observation. Furthermore, for the diffraction peaks that already overlap each other in the

simulated patterns, such as $(110)_t/(100)_c$, $(112)_t/(110)_c$ or $(202)_t/(111)_c$, it is easy to predict that those reflections cannot be separated in the experimental XRD measurement.[209] Thus, it is a challenge to distinguish between the cubic and tetragonal phases using XRD measurement at room temperature.

4.3 Morphology of multi-cation mixed-halide perovskite

Figures 4.2a-b illustrate the top-view SEM images of a perovskite film which is spin-coated on a carbon-coated copper TEM grid, respectively. In Figure 4.2b, it can be observed that the as-fabricated perovskite film exhibits a finely structured surface with many grains in different shapes and sizes, varying in the range of 100-500 nm. The bright particles in both top-view and cross-sectional SEM images can be attributed to the presence of the Rb, Cs-rich phase because of their high atomic number. The thickness of the multi-cation mixed-halide perovskite film on the TEM copper grid was measured to be 100 to 300 nm from the cross-sectional SEM images (Figure 4.2c).

Figure 4.2d shows the low magnification BF-TEM image of multi-cation mixed-halide perovskite film at room temperature. Relatively large perovskite grains with uniform contrast are observed in the capping layer. High angle annular dark-field (HAADF) STEM imaging is sensitive to Z-contrast.[175] The HAADF-STEM of the perovskite film in Figure 4.2e shows some bright particles (due to a high atomic number) mostly distributed at grain boundaries (Figure 4.2e). Thus, Rb may form the particles near the grain boundaries, which appear bright under the SEM and dark-field STEM image.

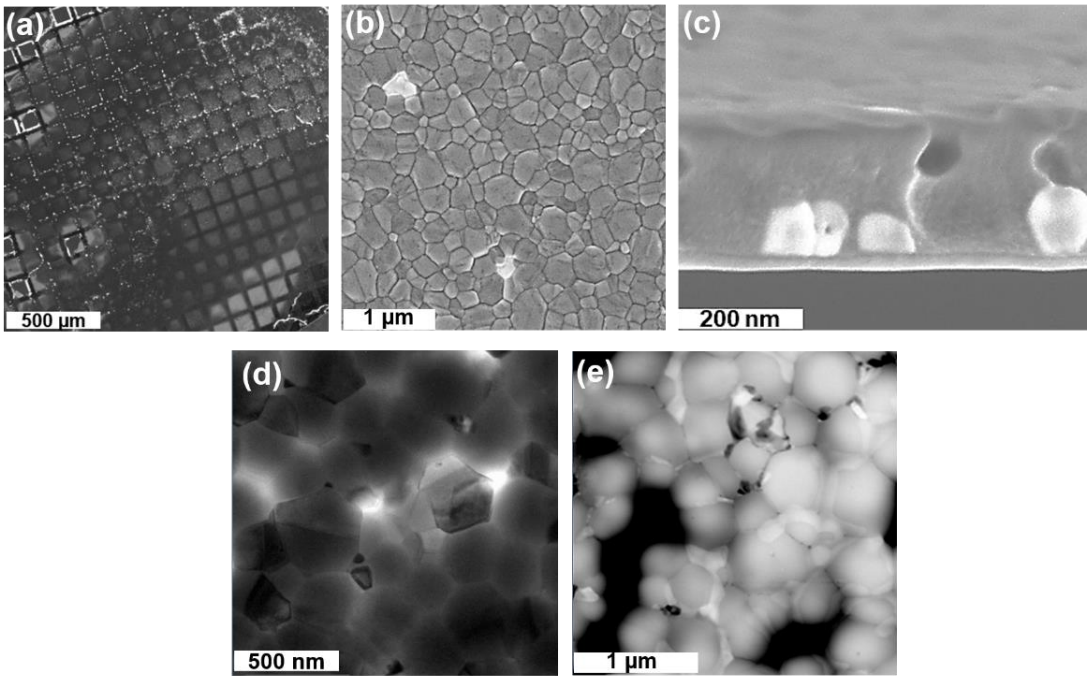

Figure 4.2. (a) Low magnification SEM image and (b) SEM image of the surface morphology of the multi-cation mixed-halide perovskite film on a carbon-coated Cu/Au TEM grids. (c) Cross-sectional SEM image of multi-cation mixed-halide perovskite film on TEM Cu/Au grid. (d) BF-TEM image and (e) HAADF-STEM image of the multi-cation mixed-halide perovskite film.

4.4 Elemental composition of multi-cation mixed-halide perovskite

To determine further the influence of Cs^+ and Rb^+ cations on the multi-cation mixed-halide perovskite structures, HAADF imaging in STEM mode, EDS spectrum and mapping were conducted and shown in Figure 4.3. The STEM-EDS mapping of Rb, Cs, C, N, Pb, I, and Br indicates a similar distribution as compared to the HAADF-STEM image, which implies the homogeneous distribution of those elements (except for Rb and Br) in the perovskite crystals and the uniform incorporation of Cs into the multi-cation mixed-halide perovskite grains. The bright particles in the HAADF-STEM image (Figure 4.3a) and corresponding increase in Rb content in the EDS maps reveal the formation of segregated Rb-rich domains. An increase in Br content is also detected within the bright particles, Rb-rich domains. However, it is difficult to separate the Cs and I energy peaks as they overlap with each other in EDS analysis. For instance, the LI, Ln, $L\alpha^1$ peaks of Cs are overlapped with the Ln, $L\alpha^1$, $L\beta^1$ peaks of I. The corresponding energies are 3.793, 4.141, 4.285 and 3.779, 3.936, 4.219 keV. Therefore,

alternative analysis was required to determine the nature of Rb^+ and Cs^+ cations incorporation within the OIMHP structure.

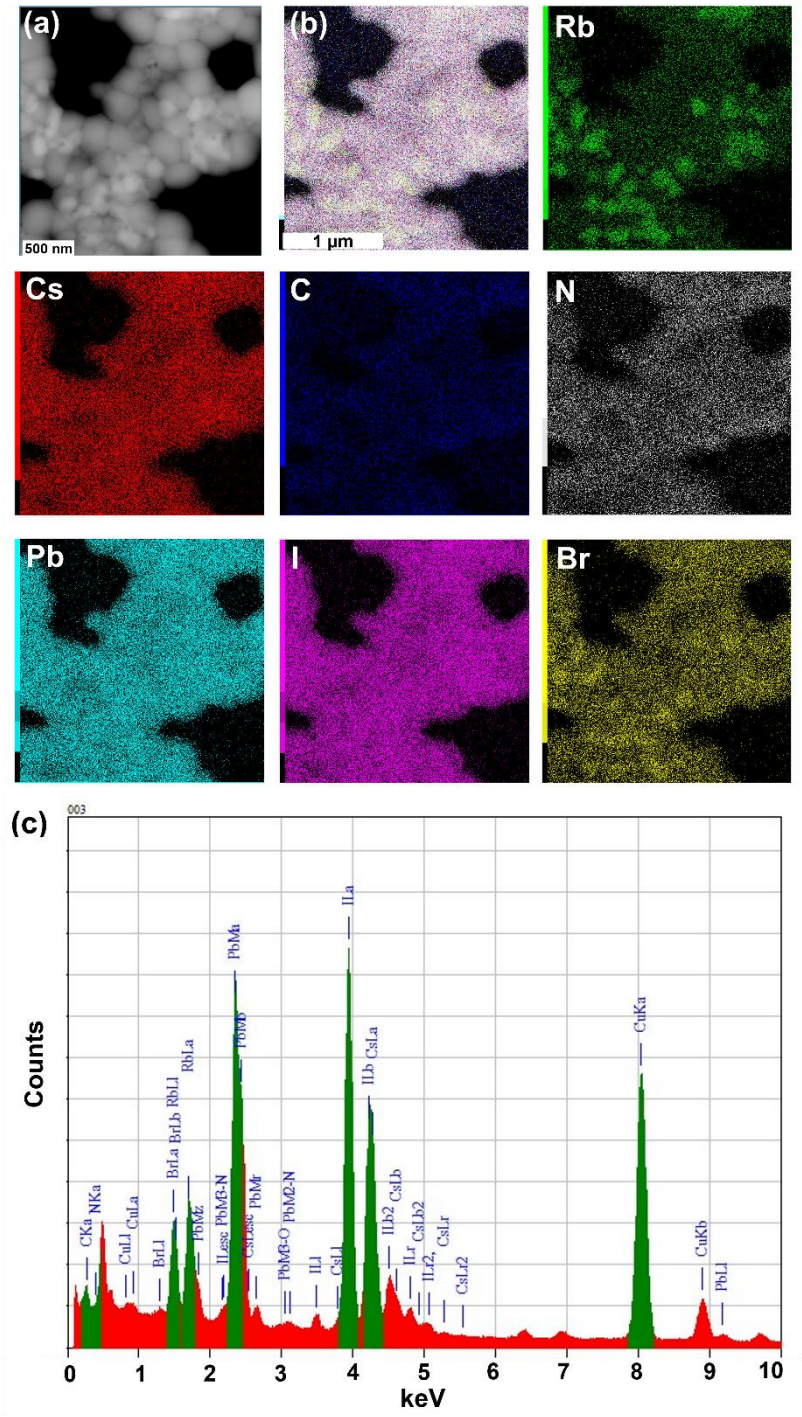

Figure 4.3. (a) HAADF-STEM image with (b) overlay of EDS maps of the multi-cation mixed-halide perovskite film and as labelled EDS maps of the same region shown for Rb (green), Cs (red), C (blue), N (grey), Pb (cyan), I (magenta), Br (yellow) at room temperature. (c) EDX spectrum of the multi-cation mixed-halide perovskite film.

In this case, using FIB-ToF-SIMS analysis can overcome the limitation of EDS. The significant advantage of FIB-ToF-SIMS is that the interaction volume of the secondary ions is smaller than the interaction volume of X-rays generated by electron beam. Therefore, this method provides various advantages over more traditional microanalytical techniques such as EDS including higher sensitivity and better resolution as well as the ability to detect light elements which is not possible using X-ray based methods. Mass spectra, depth profiles (ion intensity versus depth measurements) and ion (elemental or molecular) imaging are all outputs from a FIB-ToF-SIMS analysis. In principle, the number of ions of each species is reflected by the integrated intensity of the peaks corresponding to that element. Figure 4.4a and b show the typical mass spectra of multi-cation mixed-halide perovskite for positive and negative ions, respectively. A strong Rb, Cs, Pb peaks and the presence of MA, FA are observed, as well as Si, gallium isotopes from the substrate and primary ion source (Figure 4.4a). A strong I and Br peaks are observed in Figure 4.4b.

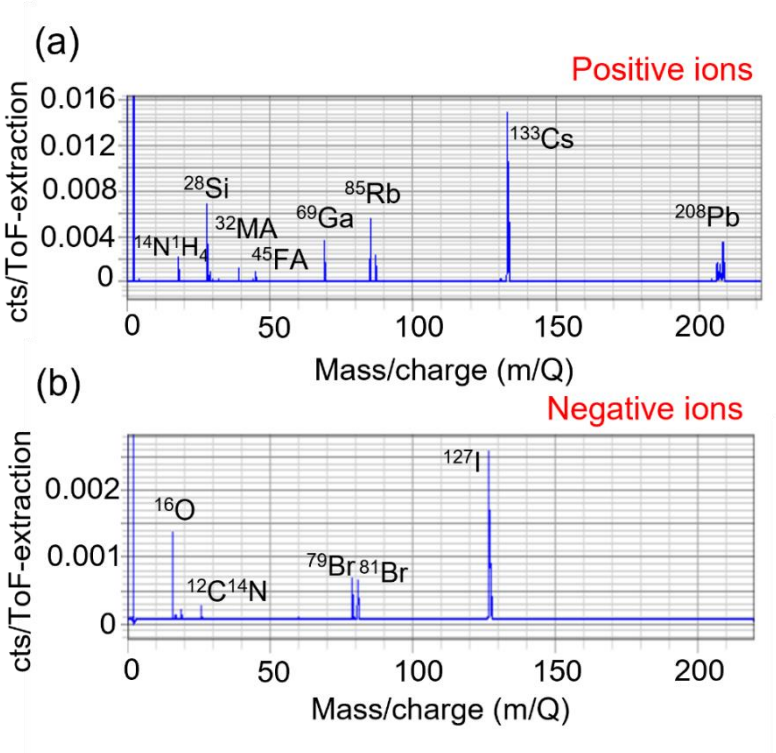

Figure 4.4. Mass spectra of the multi-cation mixed-halide perovskite film with (a) positive ions and (b) negative ions. The primary ion source is monoisotopic ^{69}Ga.

The Rb, Cs, Pb, MA and FA maps were collected as positive ions. The Br and I maps were collected as negative ions. SEM imaging was conducted using secondary electron detector before and after analysis to correlate the surface textures with the SIMS maps. Figures 4.5a, b

show the SEM images of the areas analysed for positive ions and negative ions respectively before analysis. The maps corresponding to the same regions have consequently been labelled a_1-a_5 for the region shown in Figures 4.5a and b_1, b_2 for the region shown in Figure 4.5b. The following ions were identified in the mass spectra and used for the SIMS maps: Rb (85 u (unified atomic mass unit)), Cs (133 u), Pb (208 u), MA (32 u), FA (45 u), I (127 u) and Br (79 u).

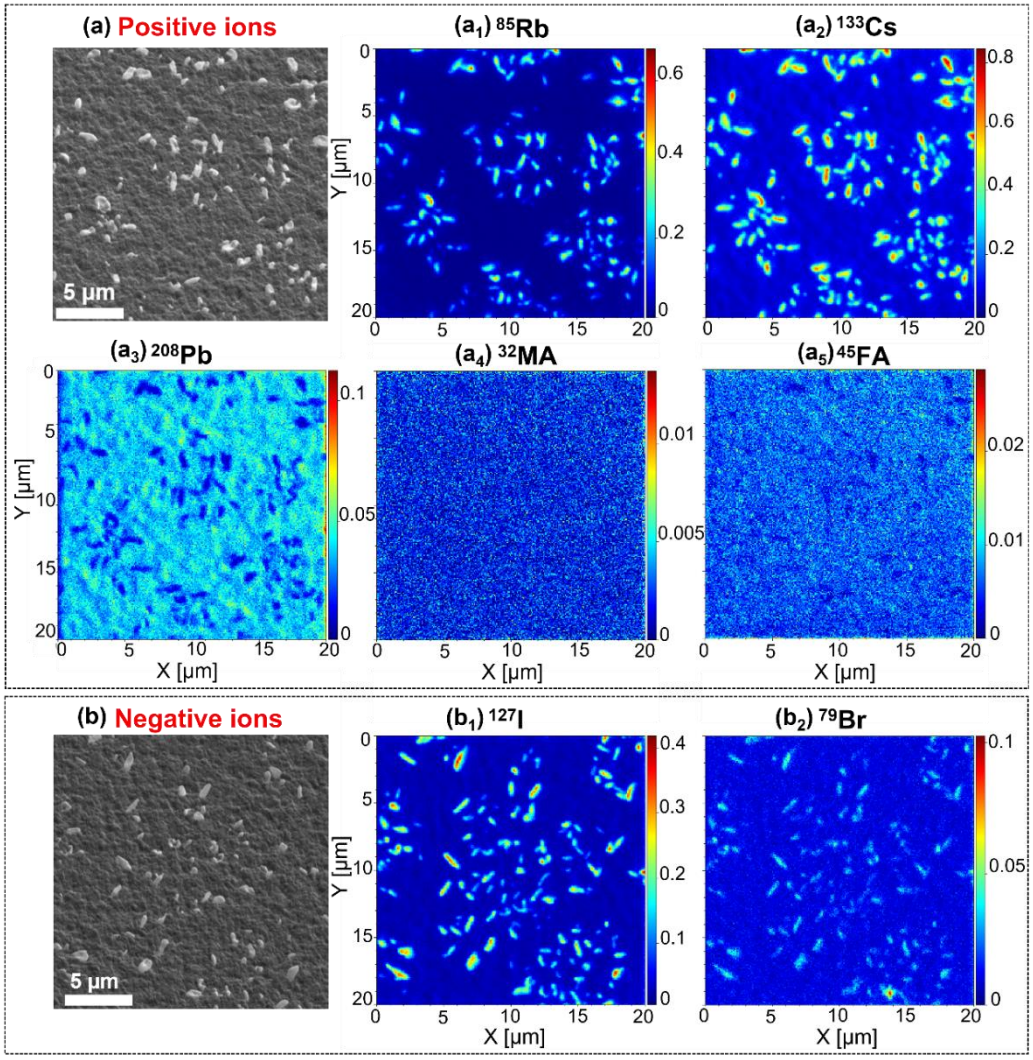

Figure 4.5. (a) Top-view FIB-SEM image for the positive ion beam maps with corresponding top-view FIB-ToF-SIMS ion maps of (a_1) Rb (85 u), (a_2) Cs (133 u), (a_3) Pb (208 u), (a_4) MA (32 u), (a_5) FA (45 u). (b) Top-view FIB-SEM image for negative ion maps with corresponding FIB-ToF-SIMS ion maps of (b_1) I (127 u), and (b_2) Br (79 u). The colour scale denotes the signal intensity for the particular ion for each map.

The FIB-ToF-SIMS results were consistent with the TEM-EDS data described earlier and gave additional insights into the composition of the bright particles in the HAADF-STEM and SEM images. The primary distribution in the perovskite film is composed of MA, FA, Pb, I and Br. The secondary phase, identified in the SEM images as bright particles (Figure 4.2b), is rich in Rb, Cs, I and Br. Thus, the secondary phase is depleted in organics and Pb compared to the primary phase and SEM imaging indicated that it has higher than average atomic number (hence brighter in SEM imaging). And most importantly, the FIB-ToF-SIMS analysis indicates that Rb^+ cation was obviously not incorporated into the perovskite crystal structure whereas Cs^+ cation was incorporated into the perovskite structure. In detail, using an analysis region of bright particles with positive ion beam shown in Figure 4.6a, it can be observed the remarkable peak intensity of Rb, Cs in both mass and depth profile spectra, while the Pb signal is negligible. When analysing out of that bright particle region, only the signals of Cs, Pb can be detected, but not for Rb (Figure 4.6b). For negative ion map in Figure 4.7, the signals of I and Br can be observed on the entire film but are much stronger in the region of bright particles. These results clearly demonstrate the segregation of Rb, Cs with the formation of a Rb and Cs-rich phase in the perovskite film. A lower peak intensity of Cs was also observed on the outside of the bright particle, implying the incorporation of Cs cation into the perovskite structure (Figures 4.6 d-f).

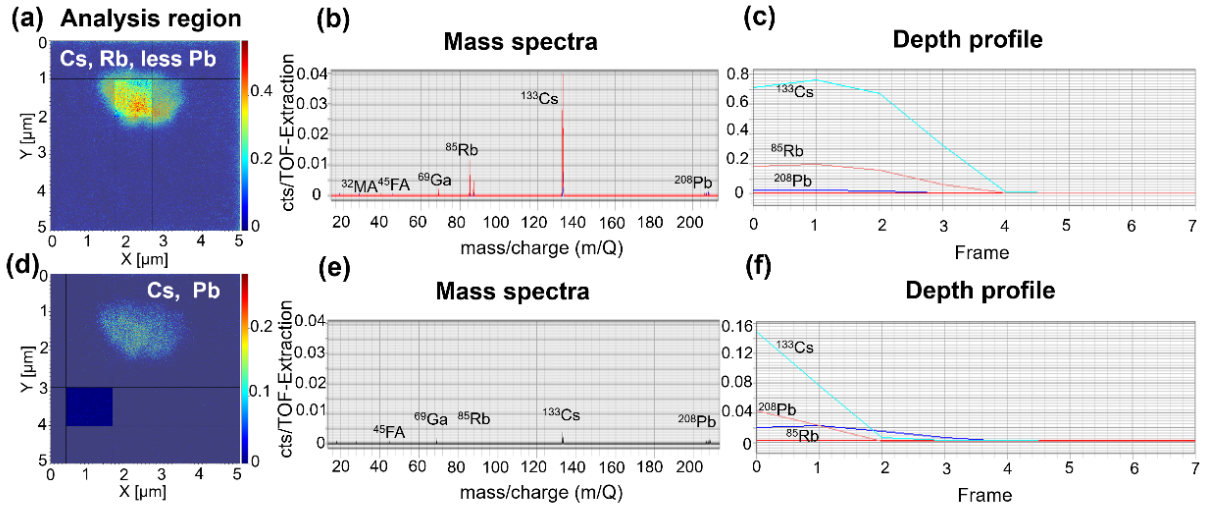

Figure 4.6. Site specific mass spectra and depth profiles extracted from the matrix and inclusions with positive ion beam. (a) Site specific FIB-ToF-SIMS ion map of bright particles. (b) Site specific mass spectra extracted from the matrix (bright particle): the Rb and Cs peaks show very high intensity, demonstrating the Rb and Cs-rich phase. (c) Site specific depth profile extracted from the matrix. (d) Site specific FIB-ToF-SIMS ion map of perovskite film (outside

bright particle). (e) Site specific mass spectra extracted from the matrix: the I and Br peaks show lower intensity. (f) Site specific depth profile extracted from the matrix of perovskite film.

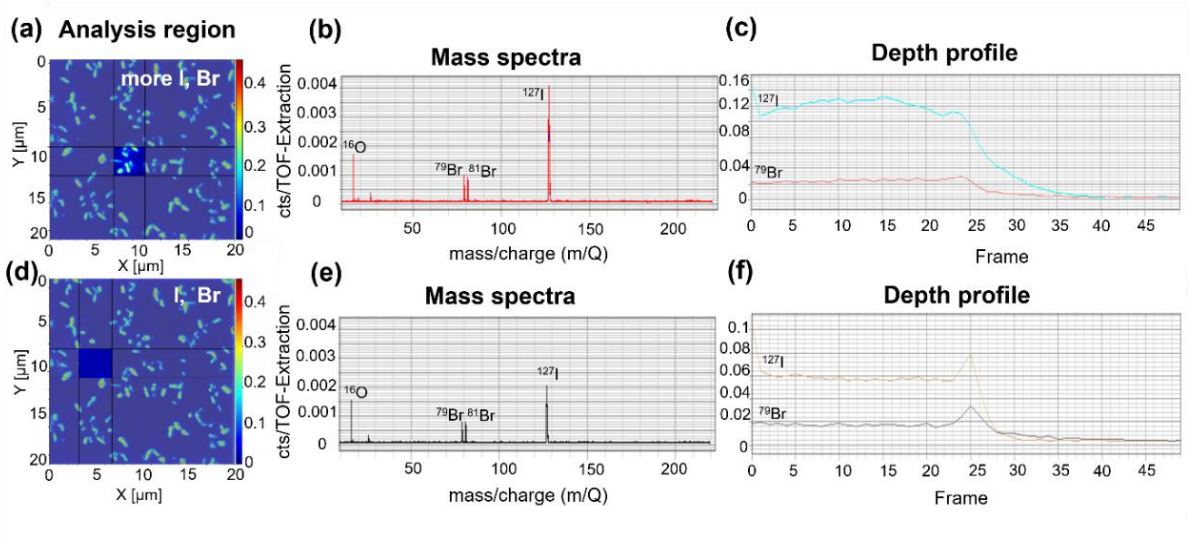

Figure 4.7. Site specific mass spectra and depth profiles extracted from the matrix and inclusion with negative ion beam. (a) Site specific FIB-ToF-SIMS ion map of bright particle. (b) Site specific mass spectra extracted from the matrix (bright particle): the I and Br peaks show very high intensity, demonstrating the I and Br-rich phase. (c) Site specific depth profile extracted from the matrix. (d) Site specific FIB-ToF-SIMS ion map of perovskite film (outside bright particle). (e) Site specific mass spectra extracted from the matrix: the I and Br peaks show lower intensity. (f) Site specific depth profile extracted from the matrix of perovskite film.

Figures 4.8a, b show the cross-sectional FIB-SEM images of the areas analysed for positive ions and negative ions, respectively. The cross-sectional FIB-ToF-SIMS maps corresponding to the same regions have consequently been labelled a_1-a_5 for the region shown in Figures 4.8a and b_1, b_2 for the region shown in Figure 4.8b. In contrast to top-view FIB-ToF-SIMS maps showed above, these maps provide important information on how all elements distribute on the entire bulk structure of perovskite film. It can be confirmed the homogeneous distribution of most elements in the cross-sectional view (except for Rb) and the uniform incorporation of Cs and Br into the multi-cation mixed-halide perovskite film. In agreement with the top-view observation, Rb^+ cation was obviously not incorporated into the perovskite crystal structure. The segregation of Rb, Cs with the formation of a Rb and Cs-rich phase in the perovskite film was also observed.

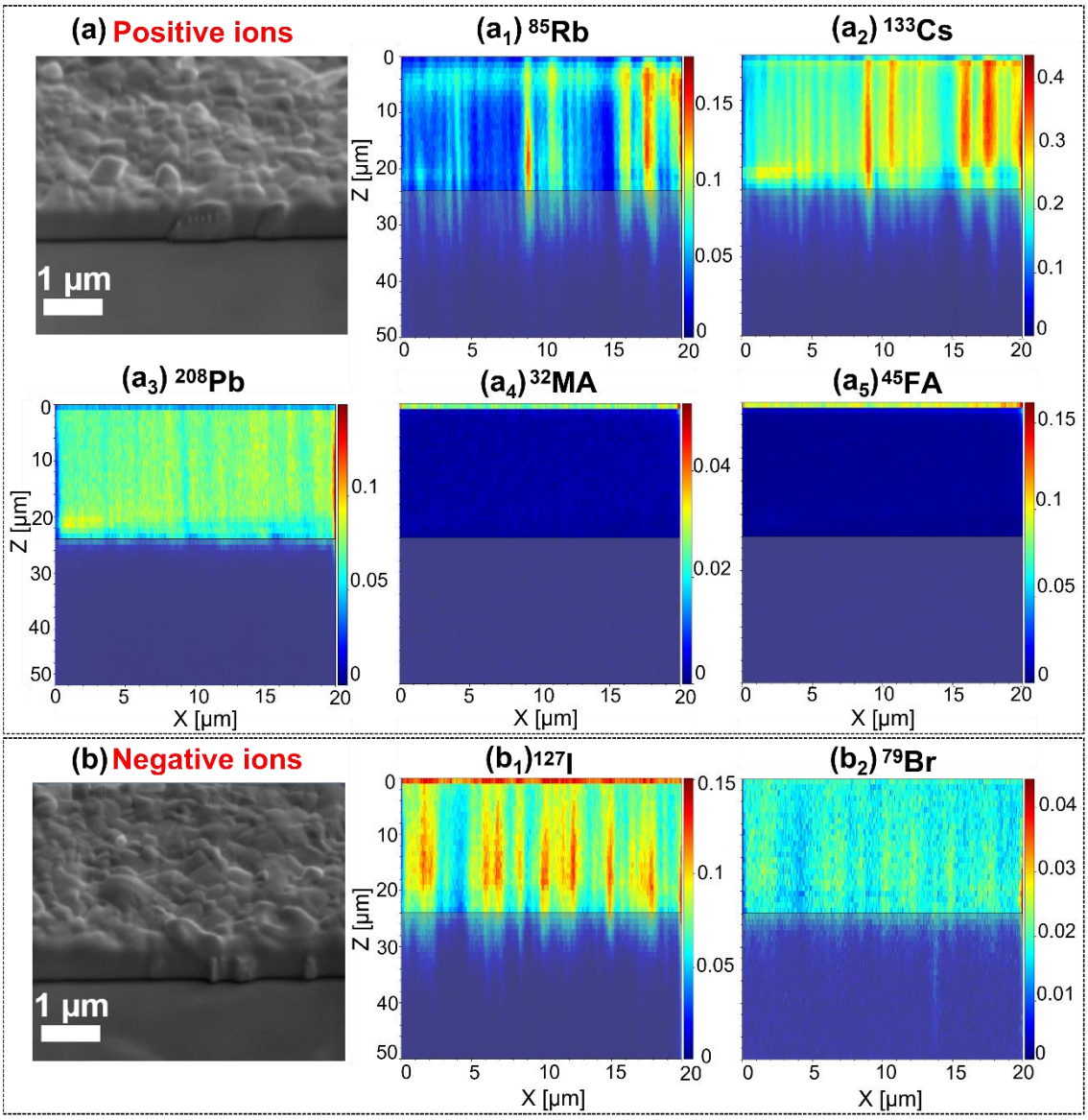

Figure 4.8. (a) Cross-sectional FIB-SEM image for the positive ion beam maps with corresponding cross-sectional FIB-ToF-SIMS maps of (a_1) Rb (85 u), (a_2) Cs (133 u), (a_3) Pb (208 u), (a_4) MA (32 u), (a_5) FA (45 u). (b) Cross-sectional FIB-SEM image for negative ion maps with corresponding cross-sectional FIB-ToF-SIMS maps of (b_1) I (127 u), and (b_2) Br (79 u). The colour scale denotes the signal intensity for the particular ion for each map.

There are some reports in the literature with the distribution of Rb cation in the perovskite films. Our results are consistent with the evidence from XRD measurements for a Rb-rich phase.[193] Kubicki *et al.* proposed that Rb can separate into $RbPbI_3$, $RbCsPbI_3$, or a mixture of Rb halides, mixed Rb-Cs lead iodide, and various rubidium lead bromides (in Rb/Cs/MA/FA systems with Br and I).[210] In our study, since the perovskite film contains Br and I-rich phases, the Rb and Cs-rich phase can be proposed to be a mixed-halide structure

(RbCsI/Br) at the grain boundaries of the perovskite film. We suggest that the Rb, Cs-rich phase acts as a passivation layer, leading to the improved stability and performance of multi-cation mixed-halide perovskite.[210]

4.5 Microstructure and crystal structure of multi-cation mixed-halide perovskite

Figures 4.9a-c present low magnification BF-TEM images of the polycrystalline multi-cation mixed-halide perovskite film spin-coated on the carbon film side of TEM Cu/Au grids. Their corresponding SAED patterns obtained from a single grain highlighted with the yellow circles in Figures 4.9a-c are shown in Figures 4.9d-f. The first-order, second-order, and third-order diffraction spots can be clearly distinguished, demonstrating the excellent crystalline quality of the multi-cation mixed-halide perovskite film. In addition, Cs and Br are incorporated in the perovskite structure in a way that makes the diffraction spots more obvious. The three SAED patterns shown in Figures 4.9d, e, f correspond to the zone axes of $[100]_t$, $[010]_t$ and $[110]_t$, respectively. They are consistent with the calculated electron diffraction patterns of the tetragonal crystal structure using SingleCrystal software from CrystalMaker (Figures 4.10a-c). However, the SAED patterns are equally consistent with the calculated electron diffraction patterns for a cubic crystal system with $Pm\bar{3}m$ space group along the [110], [101] and [010] zone axes (Figures 4.10g-i). Likewise, in Figures 4.9d-e, the observed (004), (040), ($0\bar{4}\bar{4}$), ($\bar{4}00$), and (206) reflections assigned to the tetragonal phase can be indexed to (002), ($\bar{2}20$), ($2\bar{2}\bar{2}$), ($\bar{2}02$), and ($1\bar{3}\bar{1}$) reflections for the cubic phase (Figures 4.9g, h), respectively. The ($2\bar{2}0$), ($\bar{2}24$) planes in the tetragonal phase are also equivalent to (200), ($\bar{2}02$) in the cubic phase as shown in Figures 4.9f, i. Based on these results, it is difficult to distinguish between the cubic and tetragonal phases from the diffraction patterns along these orientations.

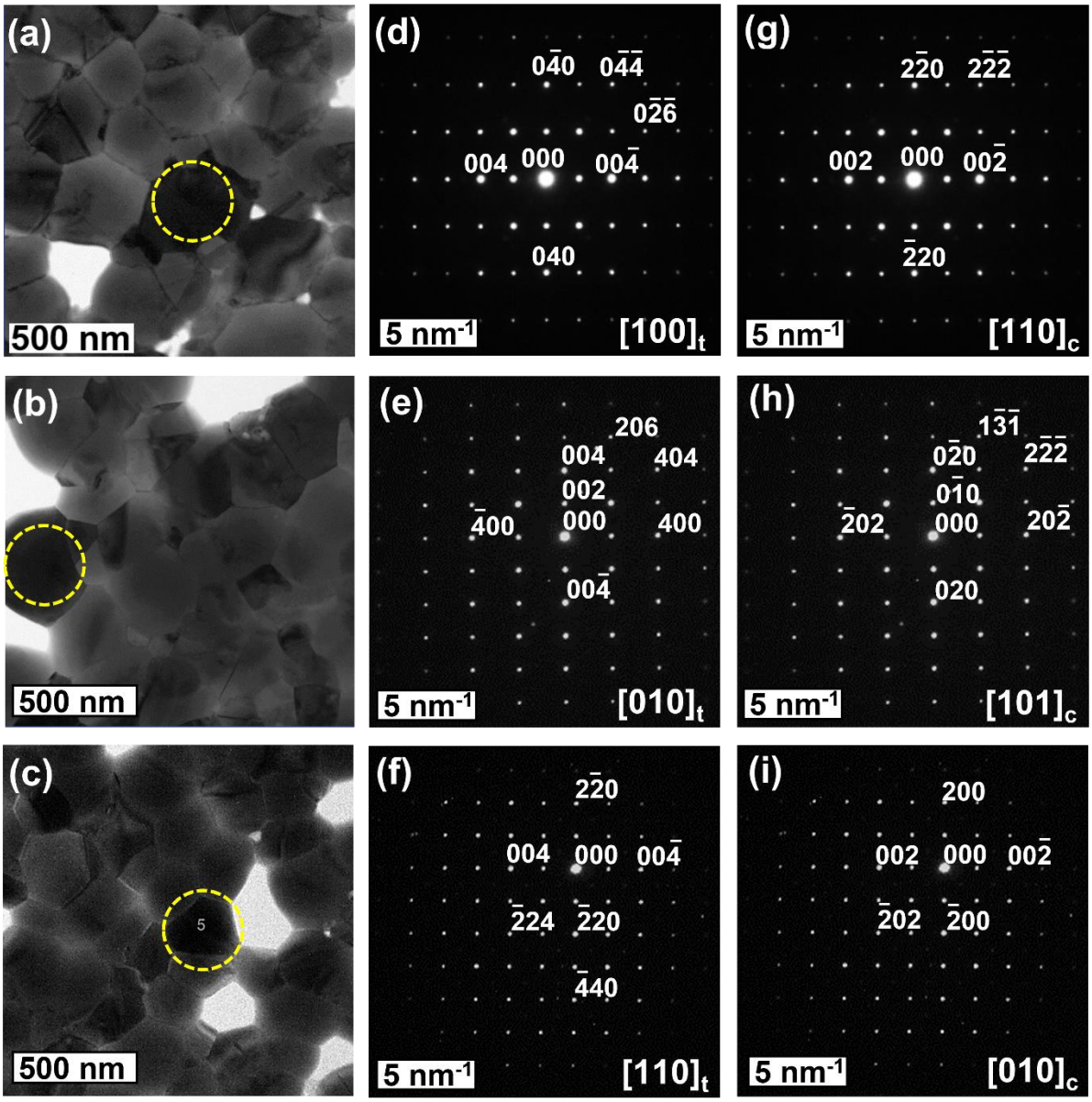

Figure 4.9. (a-c) BF-TEM images of multi-cation mixed-halide perovskite. Experimental SAED patterns of multi-cation mixed-halide perovskite material at room temperature for three different zone axes indexed with equivalent tetragonal (t) and cubic (c) indices namely (d) $[100]_t$ and (g) $[110]_c$, (e) $[010]_t$ and (h) $[101]_c$, (f) $[110]_t$ and (i) $[010]_c$.

In order to distinguish between the cubic and tetragonal phases, the atomic models for both structures were defined in the CrystalMaker software using identical PbI_6 octahedra. The A cations are located in the cage made by four neighbouring PbI_6 octahedra and the main difference between the two crystal structures is the arrangement of MA/FA or other A cations within the cage. Figures 4.10d-f illustrate the atomic arrangements along different zone axes [100], [010] and [110] of tetragonal phase whereas Figures 4.10j-l show the atomic structure of

the cubic phase along the equivalent zone axes [110], [101], and [010] for comparison. As described earlier, in the tetragonal phase, the PbI_6 octahedra are tilted about the *c*-axis compared to the cubic phase. However, the octahedral tilt is not visible along these two sets of orientations. This demonstrates that these orientations are not suitable for differentiating between these two crystal structures in agreement with the experimental results described above.

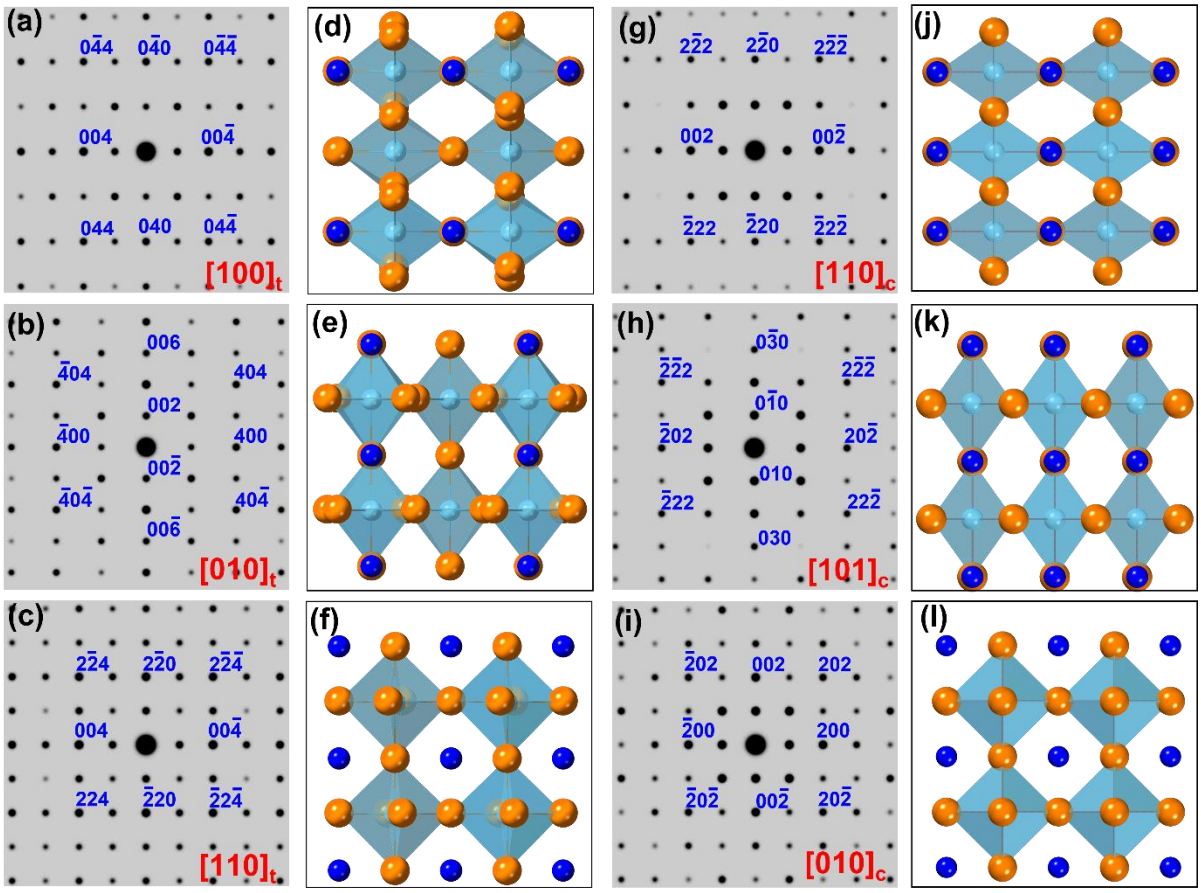

Figure 4.10. Simulated electron diffraction patterns of tetragonal structure for different zone axes (a) $[100]_t$, (b) $[010]_t$, and (c) $[110]_t$ compared to equivalent zone axes in cubic phase (g) $[110]_c$, (h) $[101]_c$ and (i) $[010]_c$, respectively. Atomic structure models of tetragonal phase for three different zone axes (d) $[100]_t$, (e) $[010]_t$ and (f) $[110]_t$ compared to equivalent zone axes in cubic phase (j) $[110]_c$, (k) $[101]_c$ and (l) $[010]_c$, respectively.

To understand and design precisely the property-controlled perovskite materials, it is essential to identify the change in atomic locations that occurs during phase transitions. The tetragonal to cubic phase transition can be clearly illustrated by SAED analyses. The cubic phase has entirely non-tilted PbI_6 octahedra and according to the Glazer notation, the unit cell

can be simply ascribed to a cube enclosing one octahedron. However, the tetragonal phase has an $a^0a^0c^-$ configuration with tilted octahedra about the *c* axis such that adjacent layers in the *c* direction are out-of-phase. This doubles the unit cell in the *c*-direction. Thus, with a phase transition from cubic to tetragonal, this doubling of the unit cell dimensions will result in a half periodicity in the reciprocal space along the *c*-direction.

However, if both tetragonal and cubic phases are present, the diffraction spots arising from both phases would be visible. Figures 4.11a-c show the BF-TEM image of multi-cation mixed-halide perovskite film at room temperature. Their corresponding SAED patterns obtained from a grain highlighted with the yellow circles in Figures 4.11a-c are shown in Figures 4.11d-f. These SAED patterns exhibit a single set of symmetric diffraction spots that can be indexed to the tetragonal crystal structure of the perovskite along the [001], [021] and [201] zone axis, respectively. The additional diffraction spots, such as (100), (010) along to [001] zone axis, are forbidden for the tetragonal structure and yet visible in the SAED patterns (Figure 4.11d). These diffraction spots are known as a "superlattice diffraction" in the tetragonal phase and cannot be indexed with the cubic $Pm\bar{3}m$ phase. Similarly, some weak (100), (010), ½(112), and ½(312) superlattice diffractions are also visible along the $[021]_t$ and $[201]_t$ zone axes in Figures 4.11e and f. Figures 4.11g-i indicate the atomic arrangements along different zone axes [001], [021] and [201] of tetragonal perovskite phase, correspondingly. The SAED patterns in Figures 4.11d-f also can be indexed to the cubic supercell structure with space group $Im\bar{3}$ and the lattice parameter 2*a* (where *a* is the lattice constant of $Pm\bar{3}m$ cubic perovskite) along the [001], $[\bar{1}1\bar{1}]$, and [111]. This will be discussed in more detail in Chapter 6.

There are three possible explanations for the visibility of these forbidden reflections. As mentioned earlier, the tetragonal unit cell has a lattice constant *c* doubled with respect to the cubic unit cell. In the perovskite system, this commonly emerges from the octahedral tilts or rotations. Because the tilting of octahedra in perovskite structure leads to double unit-cell axes, extra reflections can be created which lie on half-integral reciprocal-lattice planes. The existence of these forbidden reflections can be explained by a doubling of the periodic structure in the *a* and *b* directions with a superlattice structure involving a unit cell of 8 octahedra. Specifically, the weak (100), (010), ½(112), and ½(312) superlattice diffractions can be ascribed to a (200), (020), (112) and (312) in this pseudo-cubic unit cell. With respect to the

pseudo-cubic unit cell, the forbidden reflections are indexed with some odd indices. In contrast, the ordinary reflections (the main reflections) have all even indices.[93]

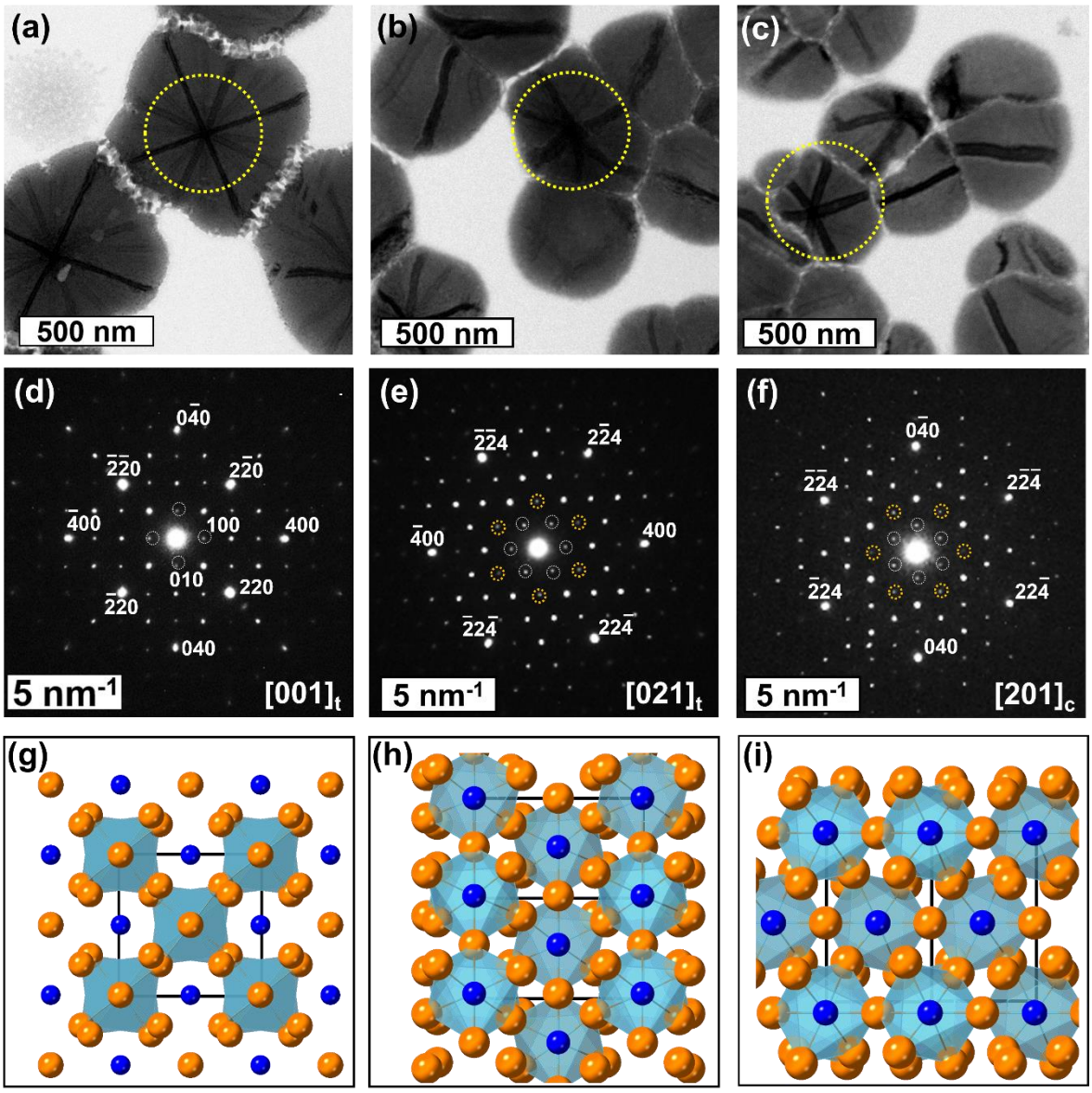

Figure 4.11. (a-c) BF-TEM images of multi-cation mixed-halide perovskite at room temperature. The experimental SAED patterns taken from a yellow circled grains of bright-field TEM images along (d) $[001]_t$, (e) $[021]_t$ and (f) $[201]_t$ zone axes and their corresponding atomic structures assuming a tetragonal structure along these three zone axes in (g), (h) and (i) respectively. The white and yellow circles in the SAED pattern correspond to the superlattice reflections.

While the octahedral tilting can explain a "doubling" of the unit cell and hence the visibility of forbidden reflections, another possible explanation is chemical ordering. In

particular, the A-sites can be occupied by different cations namely MA, FA, or Cs whereas the X-sites can be occupied by I or Br. The optimised multi-cation mixed halide perovskite film has an atomic ratio for I and Br of about 5:1 and a similar cation ratio for FA and MA. These different chemical components can result in different chemical ordering aside of structure symmetries. Chemical ordering will change the relative intensities of the diffracted spots which is determined by the structure factor and sensitive to the ordering of different cations and anions. The superlattice reflections appear because in the perovskite structure, the scattering strength of the A-site atoms differs from that of the B- and X-site atoms.[211] The third possible explanation for the visibility of forbidden reflections in the diffraction patterns is twin formation which has been shown in inorganic perovskite structures.[107, 212-214] Twin formation was reported by Rothmann *et al.* in $MAPbI_3$ with a (112) twin plane.[149] In inorganic perovskites, twinning has been shown to result in superlattice reflections and can explain fractional indices of 1/2 and 1/3. However, the beam sensitivity of our sample limits detailed tilting studies on the same crystal to identify the nature of these forbidden reflections for this study.

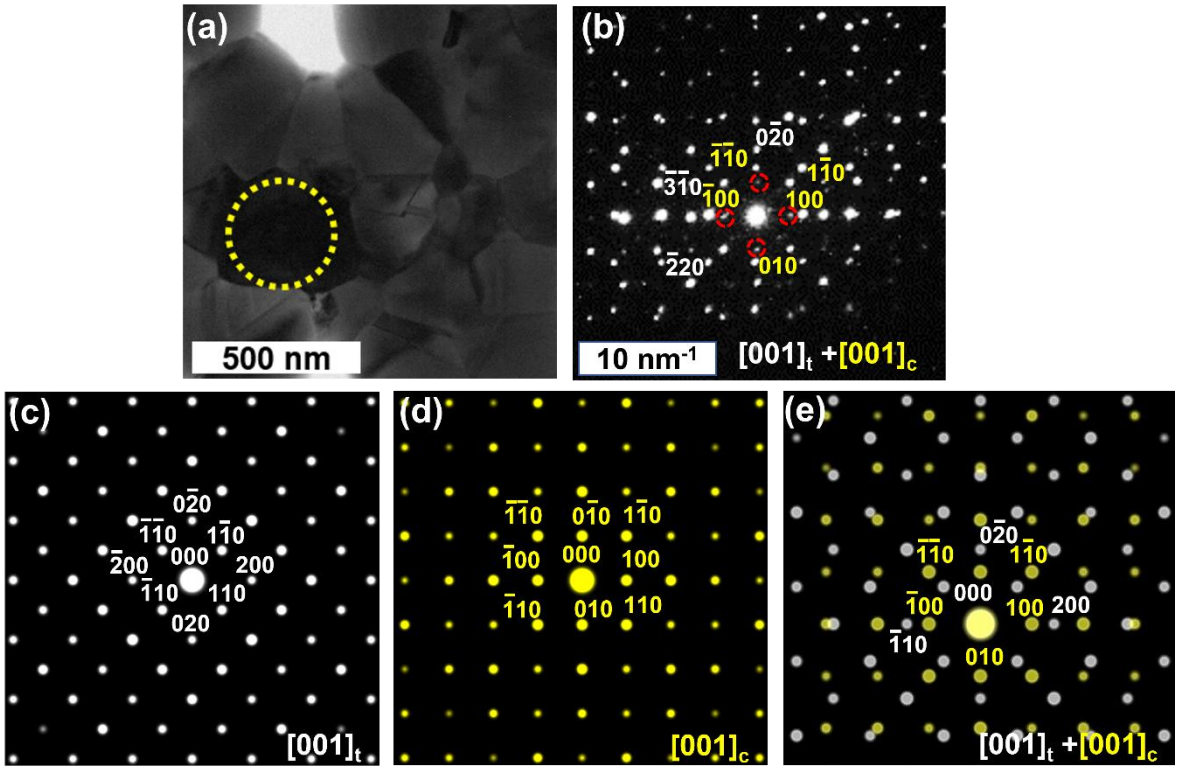

Figure 4.12. (a) BF-TEM image of the multi-cation mixed-halide perovskite film at room temperature. (b) Experimental SAED diffraction pattern taken from grain highlighted in yellow circle in Figure (a). Simulation electron diffraction pattern along the [001] zone axes for (c) tetragonal (white) and (d) cubic (yellow) phase. (e) Simulation of the overlapping SAED of

tetragonal (white) and cubic (yellow) along to [001] zone axes. The red circles in the SAED pattern correspond to the superlattice reflections.

Figure 4.12b shows the diffraction pattern of the perovskite taken from a grain highlighted in yellow circle shown in Figure 4.12a. This diffraction pattern can be indexed as an overlay of two diffraction patterns from the tetragonal phase (see white colour in Figure 4.12c) and the cubic phase (see yellow colour in Figure 4.12d). Both patterns were indexed to be oriented along the [001] zone axes with the $(010)_t||(010)_c$ and $(100)_t||(100)_c$. As discussed earlier, the *a* and *b* axes of the tetragonal unit cell have a 45° rotation with respect to the *a* and *b* axis of the cubic unit cell when aligned to the PbI_6 octahedra. The 45° rotation can be seen when comparing the white circles in Figure 4.12c to the yellow circles in Figure 4.12d. The distinction between the tetragonal and cubic phases was only made with the visibility of the superlattice diffraction spots from tetragonal phase (see red circles shown in Figure 4.12b) which are consistent with the as-mentioned results in previous section. The diffraction pattern is consistent with the simulation results (Figure 4.12d) overlaying the tetragonal phase and the cubic phase with a 45° rotation of the octahedral units between the two (atomic structure models are shown in Figure 2.11, Chapter 2). These results demonstrate the coexistence of the cubic and tetragonal phases in the multi-cation mixed-halide perovskite film at room temperature.

4.6 Device performance

Figure 4.13 presents the J-V curves of a cell with a $Rb_{0.03}Cs_{0.07}FA_{0.765}MA_{0.135}PbI_{2.55}Br_{0.45}$ perovskite film together with a clearly labelled SEM image of the cross-section of the cell. The structure of as-fabricated PSCs device is composed of an ETL of cp-TiO_2 and ms-TiO_2 on an ITO/glass substrate, the multi-cation mixed-halide perovskite absorber layer, PTAA as the HTL and Au layer as the back contact. For the forward scan shown in red colour, the V_{OC}, J_{SC}, FF and PCE of the cell are measured to be about 1.173 V, 22.49 mA/cm^2, 0.748 and 19.7%, respectively. For the reverse scan shown in blue colour, correspondingly, those parameters are recorded to be approximately 1.173 V, 22.57 mA/cm^2, 0.747 and 19.77%. These J-V curves reveal that there is little hysteresis in the cell, and a steady PCE of close to 20% can be extracted. In PSCs, significant hysteresis implies poor efficiency and is caused by various factors, for example, defects in the perovskite layer, accumulated charges (including mobile ions) at interfaces or the difference between the electron- and hole-transport rates.[215, 216] The result is consistent with microstructure results as the perovskite layer has excellent crystallinity.

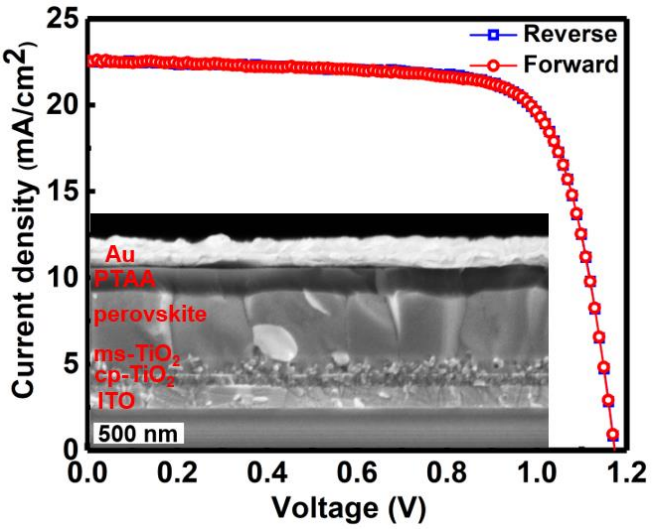

Figure 4.13. J–V curves for the cell using multi-cation mixed-halide perovskite (in reverse (blue) and forward (red) scans) with a scan rate of 50 mV/s.

4.7 Summary

In conclusion, through a systematic characterization strategy, we have successfully demonstrated the influence of inorganic cations such as Rb^+ and Cs^+ on the structural, morphological and elemental composition properties of multi-cation mixed-halide perovskite. In general, it is found that Rb^+ cation was not incorporated into the perovskite crystal structure and only exist separately in the perovskite film as a segregated phase. In contrast, Cs^+ cation was found to be incorporated into the perovskite structure and segregated within a Rb and Cs-rich phase. The Rb and Cs rich phase tends to form at the grain boundaries of the perovskite film thus improving the perovskite film stability. The structure of multi-cation mixed-halide perovskite is also shown to be a mixture of MA and FA phases. The visibility of some forbidden reflections was attributed to three possible explanations, namely (a) superlattice reflections explained by a doubling of the unit cells along the *a* and *b* axes, (b) chemical ordering within the A-site cations and/or the halide site anions and (c) twin formation. Moreover, the coexistence of tetragonal and cubic phases at room temperature was also observed in the diffraction patterns. This study provides a thorough understanding, highlighting new approaches to clarify the high efficiency of multi-cation PSCs.

Chapter 5. Twinning formation in multi-cation mixed-halide perovskite

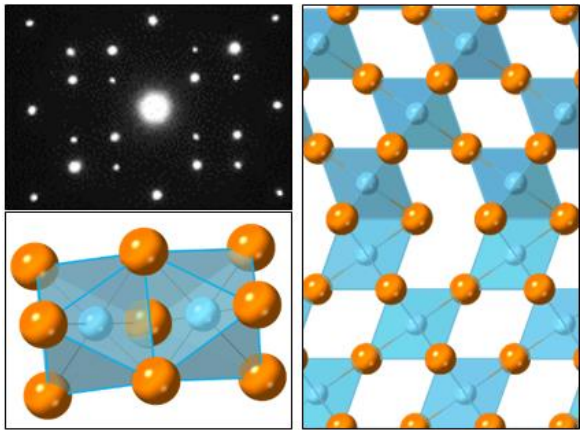

This chapter identifies a common twinning structure in both cubic and tetragonal phases of the multi-cation mixed-halide perovskite using a combination of low-dose electron microscopy studies and atomic structure simulations. For the first time, we present clear evidence of {111} *twins in the cubic phase and the equivalent* {011} *twins in the tetragonal phase using SAED patterns. We develop a unique way of differentiating between the tetragonal and cubic forms of these twins. Our systematic electron diffraction analyses and simulations demonstrate unequivocally that the same twinning structure is present in both phases, notably with a perfectly coherent* $\{111\}_c$ *TB in the cubic phase and a semi-coherent* $\{011\}_t$ *TB in the tetragonal phase. The atomic configuration of the TB is discussed with possibilities of being* AX_3 *centred (with A=Cs, FA, MA and X=I, Br) or B-site centred (Pb) for both crystal structures. We propose that the TB is a key nucleation region for phase segregation which acts as a potential well or barrier to electrons and holes depending on its composition and hence its bandgap.*

5.1 Introduction

The efficiency of solar cells based on OIMHP materials is increasing dramatically with the best efficiency now already rivalling that of the best Si cell efficiency.[1] Many studies on solar cell materials have demonstrated improved performance with the incorporation of different A-site cations (e.g. Rb/Cs/MA or FA) and halide anions (I/ Br or Cl) into the perovskite structure, such as notably excellent optoelectronic properties, high efficiencies as well as enhanced long-term stability.[85, 86, 185, 186, 217-219] These have been reported in both tandem and single-junction solar cells. Thus, multi-cation mixed-halide perovskites with suitable compositions

generally exhibit improved efficiency and stability.[85, 220] As a result, PSCs based on such compositions are attracting considerable attention as the next generation of PV devices with the potential to drive down the cost of PVs further. In order to realise the potential of perovskite solar cells not just on small laboratory-scale devices but in commercial application, a deeper understanding of the material properties, including the structure and activity of defects within the material, is necessary.

It is known that structural defects play an important role in the performance of PSCs. Recently, there have been several reports proposing that phase segregation in multi-cation mixed-halide perovskites poses a critical limitation to the performance of solar cells based on these materials.[168, 221-224] The formation of secondary phases can alter the chemical composition and hence the local band structure at the grain boundaries compared to the bulk grains. It is a key factor in determining the carrier recombination and potential transport of ionic and molecular species within the material.[225-227] However, to date, neither the origins of the power conversion efficiency improvement, nor the physical mechanisms responsible for phase segregation in mixed-halide perovskites have been studied in detail, hampering the progress in material and device development.

In this chapter, we characterise the morphology and crystallography of twins in $Rb_{0.05}Cs_{0.095}MA_{0.1425}FA_{0.7125}PbI_2Br$ films using SEM, TEM, CrystalMaker and SingleCrystal software. For the first time, we present clear evidence of {111} twins in the cubic phase (denoted as $\{111\}_c$) and the equivalent {011} twins in the tetragonal phase (denoted as $\{011\}_t$) using SAED patterns. We develop a unique way of differentiating between the tetragonal and cubic forms of these twins. The relationship between the two twinned sub-crystals is discussed using an atomic model with the concept of coincident site lattice (CSL) for both tetragonal and cubic structures. We establish from the diffraction patterns that the cubic phase has a coherent TB. We propose that the cubic twin interface is AX_3 plane centred with a face-sharing $Pb_2(I/Br)_9$ octahedral structure where the Pb-I octahedral bonding present in the perovskite crystal structure is preserved. This has a significant impact on the segregation of A cations and X anions within the TB especially relevant for mixed cations perovskites. Theoretical studies have predicted that the $\{111\}_c$ TBs in $FAPbI_3$ have very low formation energy and have minimum impact on carrier transport.[148] However, for mixed cations materials, the segregation of Cs and I/Br is highly favourable at the TB, leading to the formation of traps that enhance recombination.[148]

In contrast, the diffraction patterns from the tetragonal twins are consistent with a complex semi-coherent $\{011\}_t$ twin interface. We propose that the tetragonal twin interface is Pb centred to minimise distortion to the Pb-I/Br octahedral bonding in the vicinity of the TB. However, because of the mixed halide composition, the Pb centred twin interface may be a preferred site for the segregation of I anions compared to Br anions. We propose that the $\{111\}_c/\{011\}_t$ TB is a key nucleation region for phase segregation which acts as a potential well or barrier to electrons and holes depending on its composition and hence bandgap. This phase segregation influences both carrier transport and device characteristics such as the open-circuit voltage. In addition, iodine enrichment at grain or TBs may reduce the band gap and hence induces faster electron-hole recombination.[148] This provides new insights into the microstructure of multi-cation mixed-halide perovskite materials.

5.2 Crystal structure of multi-cation mixed-halide perovskite film

The XRD pattern shown in Figure 5.1 reveals a predominantly cubic crystal structure for the film on the ITO/glass substrate, with a dominant peak located at 2θ = 20.5º corresponding to the (011) plane. The other diffraction peaks are also consistent with the typical cubic perovskite structure, appearing at 2θ = 14.4, 25, 29, 32.5 and 35.5º which correspond to the (001), (111), (002), (012), and (112) planes of the cubic phase, respectively. The peaks at 30.5 and 37.5º can be attributed to the (123) and (213) planes of the tetragonal structure, respectively. Multi-cation mixed-halide perovskite has a predominantly cubic structure with a small proportion of tetragonal inclusions.

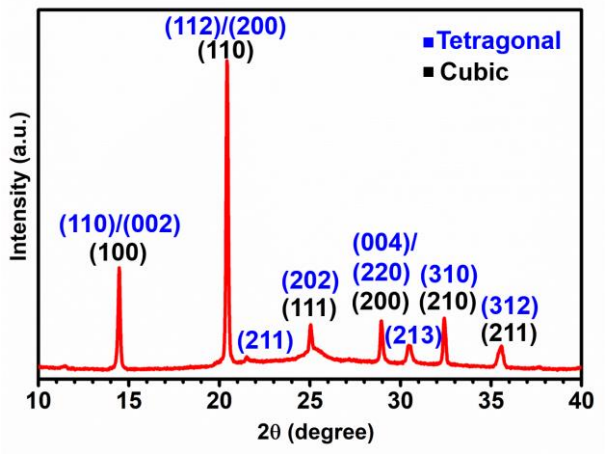

Figure 5.1. Experimental XRD pattern of the multi-cation mixed-halide perovskite film at room temperature.

5.3 Microstructure of the $\{111\}_c$ twins in multi-cation mixed-halide perovskite

5.3.1 Morphology and crystallography of $\{111\}_c$ twins

Figures 5.2a-c are SEM images representing the microstructures of an as-synthesized perovskite film on ITO/glass substrate. The formation of twins is highlighted in these three SEM images with a red dashed line defining the TBs. Twinning can be recognized in SEM because the twin sub-crystals exhibit a different contrast across the TB. The difference in crystal orientation between the twin domains often leads to differences in contrast in the low-voltage SEM images. The presence of single TB, double TBs, and two TBs intersecting at an angle of around 70.5° is highlighted in Figures 5.2a, b and c respectively. The crystallography of the TBs forming an angle of around 70.5° will be discussed in more detail in Chapter 7. There is a lower density of twins in the multi-cation mixed-halide perovskite compared to the twins reported in $MAPbI_3$ previously.[149]

To further confirm these twins in the multi-cation mixed-halide perovskite, we use a low-dose TEM technique[12] with a dose rate of about 2 e $Å^{-2}$ s^{-1} and a rapid acquisition condition to acquire our images and electron diffraction patterns. Figures 5.2d-f show low magnification BF-TEM images of the perovskite film spin-coated on the carbon film side of the TEM Cu/Au grids. These TEM images show single TB, double TBs, and two TBs intersecting at an angle of around 70.5° with a similar morphology and microstructure to the grains shown in the SEM images. Their corresponding SAED patterns taken from grains highlighted with the yellow circles in Figures 5.2e-f are shown in Figures 5.2g-i. The zone axis for these images and SAED was indexed as $[110]_c$ within the cubic framework. Each of these patterns can be indexed as the overlapping diffraction patterns of two different twin crystals A and B. The diffraction spots of individual twins are differentiated in the SAED with the white and yellow rectangles (broken lines). The diffraction spots from the matrix are mirrored with respect to the twin through the twin axis. As expected, the $\{111\}_c$ twin plane gives rise to coincident {111} reflections parallel to the twin axis. The red dashed lines indicate that the twin axis is perpendicular to the {111} plane as shown in Figures 5.2g-i. In addition, the row of reflections perpendicular to the twin axis, namely the {112} reflections, are also coincident and shared both by the matrix and twin. Hence, the {112} reflections are termed as the unsplit row (USR). The diffraction patterns are consistent with a coherent twin interface for $\{111\}_c$ twins.

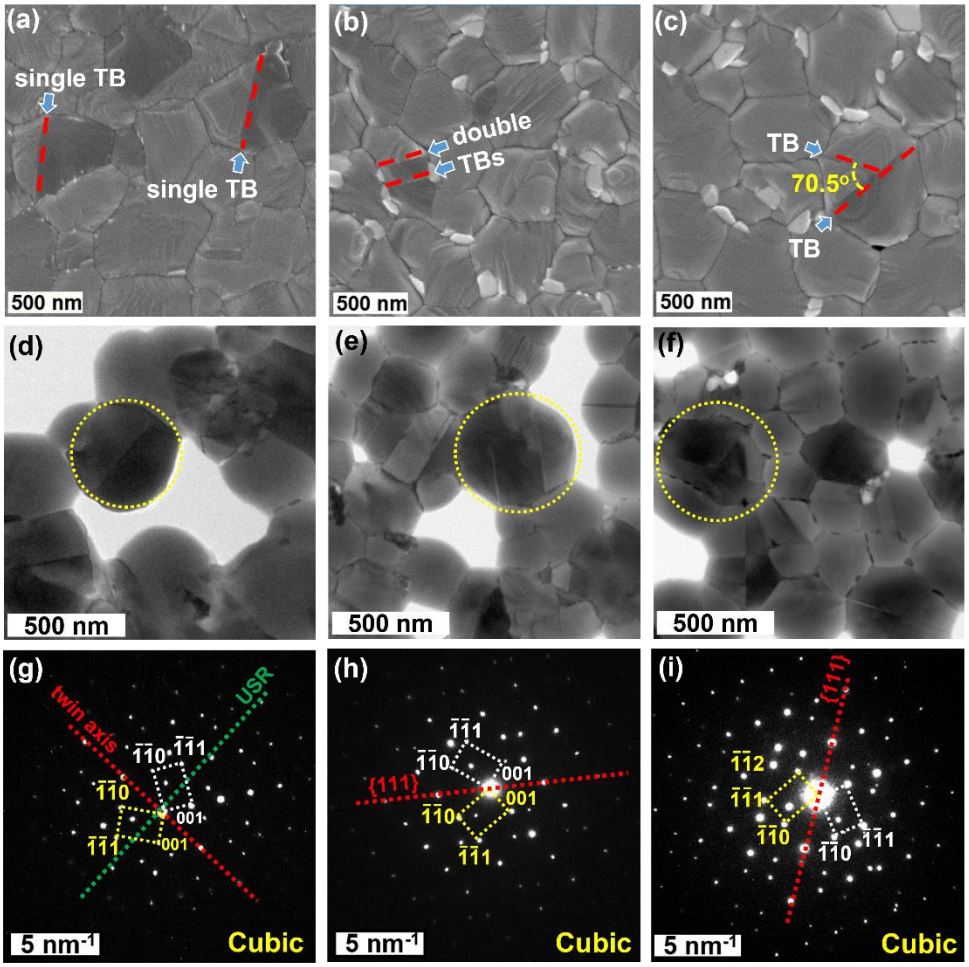

Figure 5.2. Morphology and crystal structure of twinning in multi-cation mixed-halide perovskite film at room temperature. SEM image of (a) single TB, (b) double TBs and (c) two TBs intersecting at an angle of around 70.5°. ⟨110⟩ zone axis BF-TEM image of (d) single TB, (e) double TBs and (f) two TBs intersecting at an angle of around 70.5°. (g) (h) (i) Indexed experimental SAED patterns taken from regions highlighted with a yellow circle in the BF-TEM images (d) (e) (f), respectively.

5.3.2 Simulation crystallography of $\{111\}_c$ twins

In order to understand the crystallography of the twins in cubic structure, we use the CrystalMaker and SingleCrystal software to simulate their electron diffraction patterns and atomic structure. Figure 5.3 shows the simulation results of the $\{111\}_c$ twins for the cubic structure (space group $Pm\bar{3}m$, $a \approx 6.3$ Å). The simulated electron diffraction patterns along the $\langle 110\rangle_c$ zone axis for crystal part A (white colour) and part B (yellow colour) are given in Figures 5.3a and 5.3b respectively, and in Figure 5.3c for overlapping A and B. The transformation

between the twin and the matrix is consistent with a reflection or 180° rotation about the twin axis (perpendicular to the twin plane in Figure 5.3d). Consequently, the diffraction spots are indexed for both $[\bar{1}10]_A$ and $[1\bar{1}0]_B$ oriented crystal parts with coincident reflections along the ⟨111⟩ twin direction common to both A and B and consistent with $\{111\}_c$ TB. Figure 5.3d shows the corresponding atomic structure for cubic crystal structure part A, part B, and the TB. The red dashed line corresponds to the normal to the $\{111\}_c$ twin planes and is also parallel to the twin axis. The line perpendicular to the twin axis passes through the {121} reflections which are also coincident in both crystals in agreement with the experimental USR.[108, 213, 228] Figure 5.3e shows the key atomic positions extracted from Figure 5.3d.

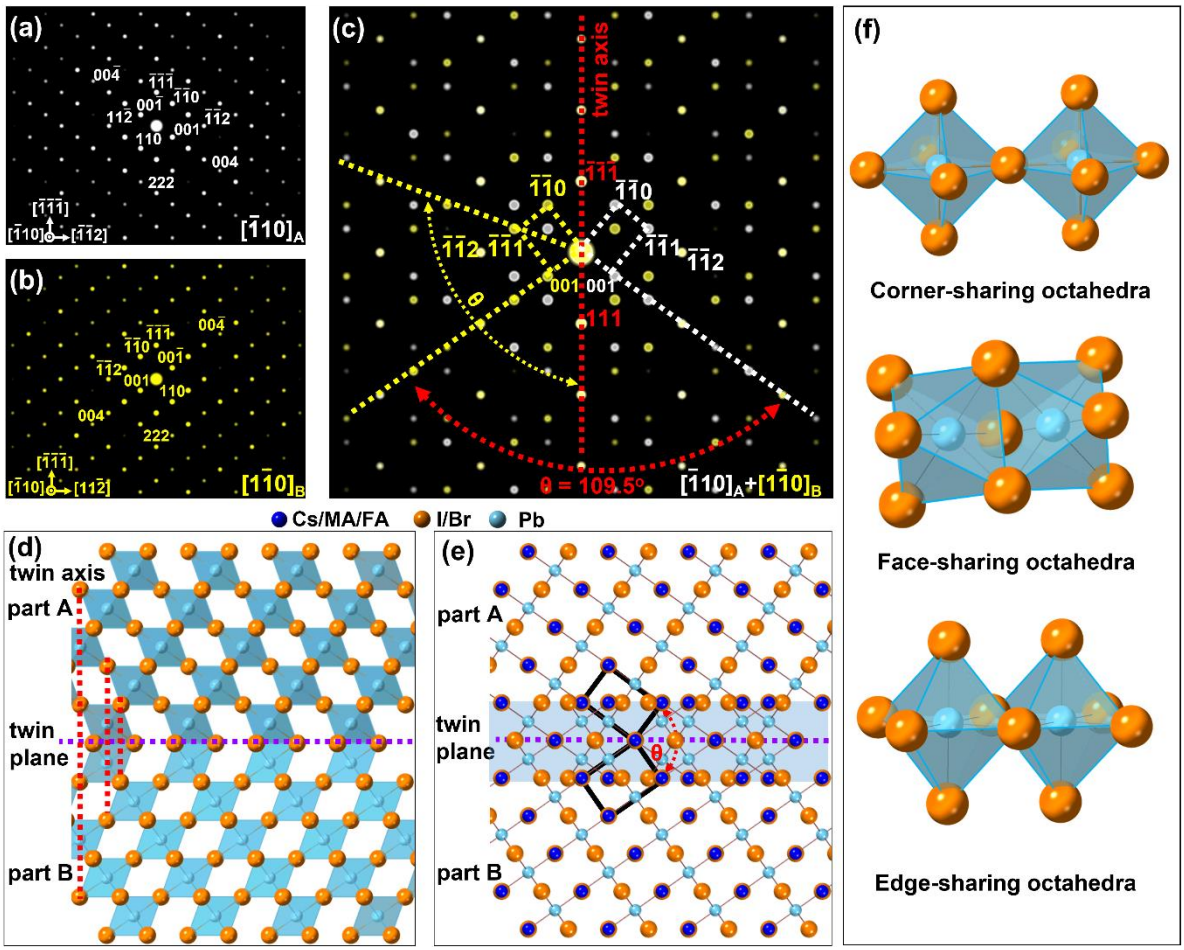

Figure 5.3. Simulation results of twins in cubic structure of multi-cation mixed-halide perovskite film. Simulated electron diffraction pattern of the cubic perovskite material with (a) $[\bar{1}10]$ zone axis for crystal part A, (b) $[1\bar{1}0]$ zone axis for crystal part B, (c) A-B TB viewing from $[\bar{1}10]_A$ + $[1\bar{1}0]_B$. (d) Schematic of twinning structure in the cubic phase. (e) Atomic structure model of TB in the cubic structure. (f) Local atomic geometry of octahedra with face-sharing, corner-sharing, and edge-sharing configurations.

5.3.3 Coincidence-site lattices and atomic structure for $\{111\}_c$ twins

In crystallography, coincidence-site lattices (CSL) are considered as one of the most important tools to evaluate and describe twins and grain boundaries in crystals. With the CSL concept, only the atomic positions are needed. Wu *et al.* mentioned four basic factors contributing to a coincidence-site lattice: (a) the degree of rotation θ, (b) the zone axis [*uvw*] that the lattice rotation appears, (c) the coordinates of a coincidence-site present in coincidence-site lattice in the (*hkl*) plane, and (d) the reciprocal of the density of coincidence sites in the (*hkl*) net (Σ).[107, 229] Ranganathan established the equations for both θ and Σ terms with the coordinates (x, y) of a coincidence site in the plane (*hkl*) as follows:[230]

$$\theta = 2 \tan^{-1} (y/x)(N^{1/2}), \text{ where } N = h^2 + k^2 + l^2$$

and

$$\Sigma = x^2 + y^2 N$$

Applying these factors to the twins in cubic structure, the rotation about the $\langle 110 \rangle$ zone axis was considered for the (110) plane, for which h and k are 1 while $l = 0$, $N = 2$. A coincidence lattice can be formed when $x = 1$ and $y = 1$, $\Sigma = 1^2 + 1^2 \times 2 = 3$. The diffraction pattern in Figure 5.3c clearly shows a rotation angle of $\theta \approx 109.5^o$ between the $[\bar{1}10]_A$ and $[1\bar{1}0]_B$ patterns. Using a pseudo-cubic unit cell, the atomic projections of parts A and B on the (110) plane can be constructed in real space with the same rotation angle of $\theta \approx 109.5^o$ as illustrated in Figure 5.4. A coincidence-site lattice of the superlattice size $\sqrt{3}a \times \sqrt{6}a$ (with supercell cell generated on (110) plane) is produced at the $(111)_A$ TB (Figure 5.4), and using a simple geometrical calculation, the same θ angle is determined:

$$\theta = 2 \tan^{-1} (\sqrt{6}a/\sqrt{3}a), \theta \approx 109.5^o.$$

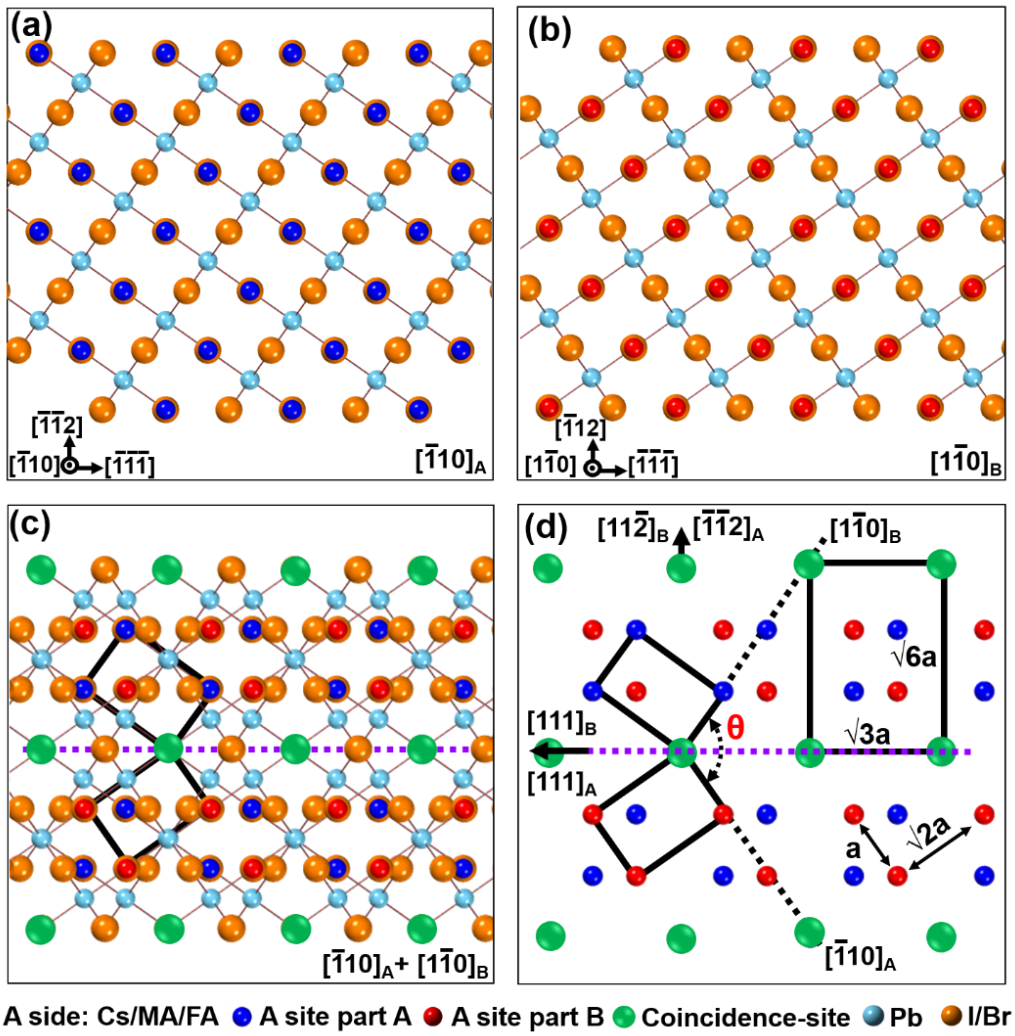

Figure 5.4. Atomic structure model of (a) crystal part A along the $[\bar{1}10]$ zone axis and (b) crystal part B along the $[1\bar{1}0]$ zone axis in cubic perovskite. (c) Atomic structure model of coincident-site lattice net projection on (110) plane viewing from the $[\bar{1}10]_A + [1\bar{1}0]_B$ directions with AX_3 layer at the interface. (d) Atomic structure model of A side atoms with coincident-site lattice from $[\bar{1}10]_A + [1\bar{1}0]_B$.

In the perovskite cubic structure, (111) planes have the highest atomic density with every cation surrounded symmetrically by six anions and every anion surrounded by four other anions and two cations. Along the ⟨111⟩ direction, the A-X_3 (Cs/MA/FA-$(I/Br)_3$) layers (*ABC*) alternate with the Pb layers (*abc*), with a bilayer repeat sequence e.g. *AbCaBcAbC*. By applying a shear operation on (111) planes with a translation by ⅓⟨112⟩ vectors, a twin *CbAcB|cAbC* can be formed. Herein, the $\{111\}_c$ twins identified here are the same as the $\{111\}_c$ twins in the $BaTiO_3$ shown in Chapter 2.[107, 108] The symmetry rule connecting the different oriented

parts can be described either as a reflection in the {111} plane or a 180º rotation around the {111} twin plane or a shear transposition of ⅓⟨112⟩ in the {111} plane. In Figure 5.3d, the atomic models of the twins viewed along the ⟨110⟩ direction are related by a twofold rotation around the ⟨111⟩ twin axis, which is a symmetry element for the supercell but not for the sub-cell (of cubic $Pm\bar{3}m$ where ⟨111⟩ is a threefold rotation axis).

Thus, the TB has two possible interface planes, namely the A-X_3 and the Pb planes. Figure 5.3d shows the atomic configuration where the $\{111\}_c$ TB is an A-X_3 plane and there is a $Pb_2(I/Br)_9$ structure at the interface with two face-sharing octahedra. Various atomic configurations of the neighbouring octahedra such as face-sharing, corner-sharing, and edge-sharing are illustrated in Figure 5.3f. Within a face-sharing octahedral arrangement, the Pb-I/Br octahedral coordination is preserved as clearly illustrated in Figure 5.3d. In contrast, the Pb-centred twin interface will disrupt the Pb-I/Br octahedral arrangement in the perovskite structure as shown in Figure 5.5. The Pb ion at the TB is at the centre of a prism (distorted from the octahedron) with a corner-sharing octahedral arrangement and the octahedra preserved in both twins (Figure 5.5a-d). For the cubic structure, we propose that the A-X_3 centred twin plane is most likely to be the coherent {111} twin interface configuration for similar reasons identified for $BaTiO_3$.[108] This configuration maintains the Pb-I/Br octahedra throughout the twin planes while the Pb plane breaks it. In addition, the exact duplication of the structural unit coordination can be found in both TB as well as the unit cell. When two sub-crystals are related by a twin relationship, they should share either one or two common layers of the structure at the interface.[28] This twin plane configuration maintains the Pb-I/Br octahedral coordination present in the unit cell of the matrix and has four times the number of coincident sites in the B (Pb) plane.

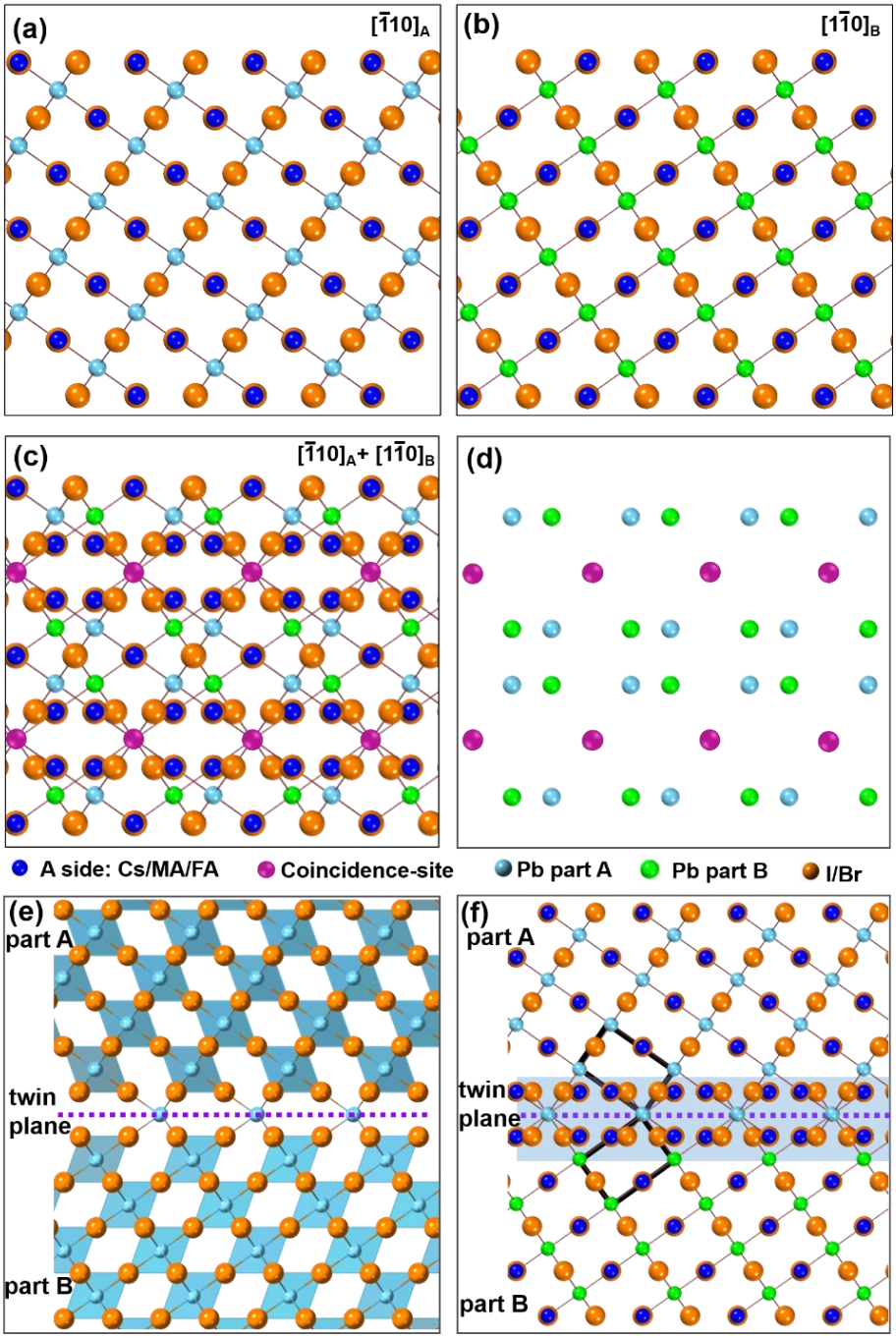

Figure 5.5. Atomic structure model of (a) crystal part A along to $[\bar{1}10]$ zone axis and (b) crystal part B along to $[1\bar{1}0]$ zone axis in cubic perovskite. (c) Atomic structure model of coincident-site lattice net projection on (110) viewing from $[\bar{1}10]_A + [1\bar{1}0]_B$ with Pb layer at the interface in cubic perovskite. (d) Atomic structure model of Pb atoms with coincident-site lattice from $[\bar{1}10]_A + [1\bar{1}0]_B$. (e) Pb-I/Br octahedra are destroyed when a Pb layer is at the interface, a prism containing a Pb atom is formed. (f) Atomic structure of twin plane with Pb layer at the interface in perovskite material.

5.4 Cubic and tetragonal twins in multi-cation mixed halide perovskite

In the multi-cation mixed-halide perovskite film, we have reported both tetragonal and cubic phases in chapter 4.[231] The diffraction pattern from a single grain marked with a yellow circle in Figure 5.6a can be indexed either as the cubic phase (Figure 5.6b) or the tetragonal phase (Figure 5.6c). Note that the ⟨110⟩ zone axis in the cubic phase corresponds to the ⟨100⟩ zone axis in the tetragonal phase (see Figure 4.10, Chapter 4). Consequently, the {001}, $\{\bar{1}\bar{1}1\}$, and $\{\bar{1}\bar{1}0\}$ reflections in the cubic phase are equivalent to the $\{00\bar{2}\}$, $\{02\bar{2}\}$, and {020} reflections in the tetragonal phase, respectively. This is illustrated visually when comparing the indices of the white and yellow rectangles in Figures 5.6b and c. Thus, the {111} TB in the cubic structure corresponds to the {011} TB in the tetragonal phase. The overarching question is: can we differentiate between $\{111\}_c$ twins and $\{011\}_t$ twins?

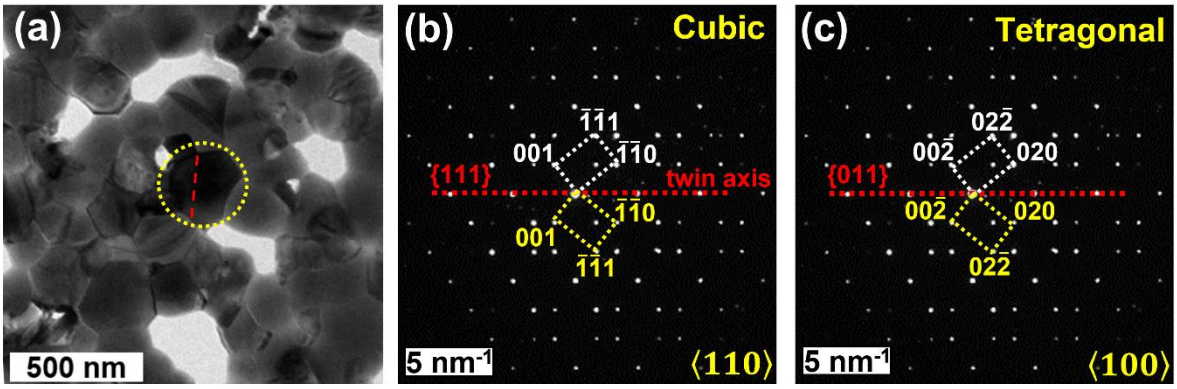

Figure 5.6. Twins in cubic and tetragonal structure of the multi-cation mixed-halide perovskite film at room temperature. (a) BF-TEM image of perovskite film. The SAED pattern taken from a yellow circled grain of BF-TEM image can be indexed either as (b) cubic phase or (c) tetragonal phase.

5.5 Microstructure of the $\{011\}_t$ twins in multi-cation mixed-halide perovskite

5.5.1 Simulation crystallography and atomic structure for $\{011\}_t$ twins

Let us now consider the tetragonal structure with space group *I4cm* or *I4mcm*. Figure 5.7 illustrates the simulation results for twinning in the tetragonal structure of the multi-cation mixed-halide perovskite material. Figures 5.7a, b shows the simulated electron diffraction

patterns along the [100] zone axis for crystal part A (white colour) and its twin part B (yellow colour) with a 180º rotation around the <011> axis respectively. Figure 5.7c is an overlay of the diffraction patterns from both parts assuming a coherent $\{011\}_t$ TB. For a coherent interface, the twin spots have coincident (011) reflections highlighted by the red dashed line which corresponds to the twin axis and the mirror plane for the (011) twinning structure. The series of reflections perpendicular to the mirror plane are the $(02\bar{4})$ reflections and show "splitting" between part A and part B (see Figure 5.7c).

This characteristic separation of twin reflections is often described informally as "split spots' and increases further from the twin axis. The spot splitting originates from a small difference in the simultaneously diffracting g vectors from the two separate sub-crystals. The splitting Δg_{hkl} can be calculated as $\Delta g_{hkl} = g_{hkl} - g_{h'k'l'}$, where g_{hkl} represents the diffraction vector of the upper sub-crystal (part A) and $g_{h'k'l'}$ refers to the diffraction vector of the lower one (part B).[232, 233] In the cubic structure, with a coherent {111} twin plane, the $g_{(-1-12)}$ is precisely perpendicular to the $g_{(111)}$ reflection and exhibits the diffraction vector of crystal part A and $g_{(11-2)}$ is diffraction vector of crystal part B. $\Delta g_{hkl} = g_{(-1-12)A} - g_{(11-2)B} = 0$ and those reflections are coincident for both twins.[108, 234] In the tetragonal structure, the equivalent $g_{(-022)}$ makes an angle of 89º with $g_{(022)}$ (the twin axis). With the 180º rotation around the <011> axis for the twin transformation, this amounts to a 2º "splitting" between the (024) reflections from part A and part B in the simulated diffraction patterns as clearly illustrated in Figure 5.7c. Effectively, the diffraction vector $g_{(0-24)}$ from crystal part A and $g_{(02-4)}$ from crystal part B, respectively are not coincident and hence $\Delta g_{hkl} = g_{(0-24)A} - g_{(02-4)B} \neq 0$. The Δg vector gives the magnitude and direction of the splitting and is parallel to the twin axis for the coherent twin interface.[232]

The atomic structure models for ⟨100⟩ zone axis of the coherent TB for the tetragonal structure are shown in two possible configurations, AX_3 centred and Pb centred. However, as shown in Figure 5.7e, the common face forming a $Pb_2(I/Br)_9$ structure at the interface does not line up because of the octahedral tilt about the *c* axis in the tetragonal structure. The face-sharing octahedral arrangement within an $A\text{-}X_3$ centred twin plane will require significant distortion of the two neighbouring Pb-I/Br octahedra at the TB i.e. two bilayers. In contrast, within a Pb-centred twin interface, the distortion to the octahedral arrangement is limited to the local environment of the Pb layer.

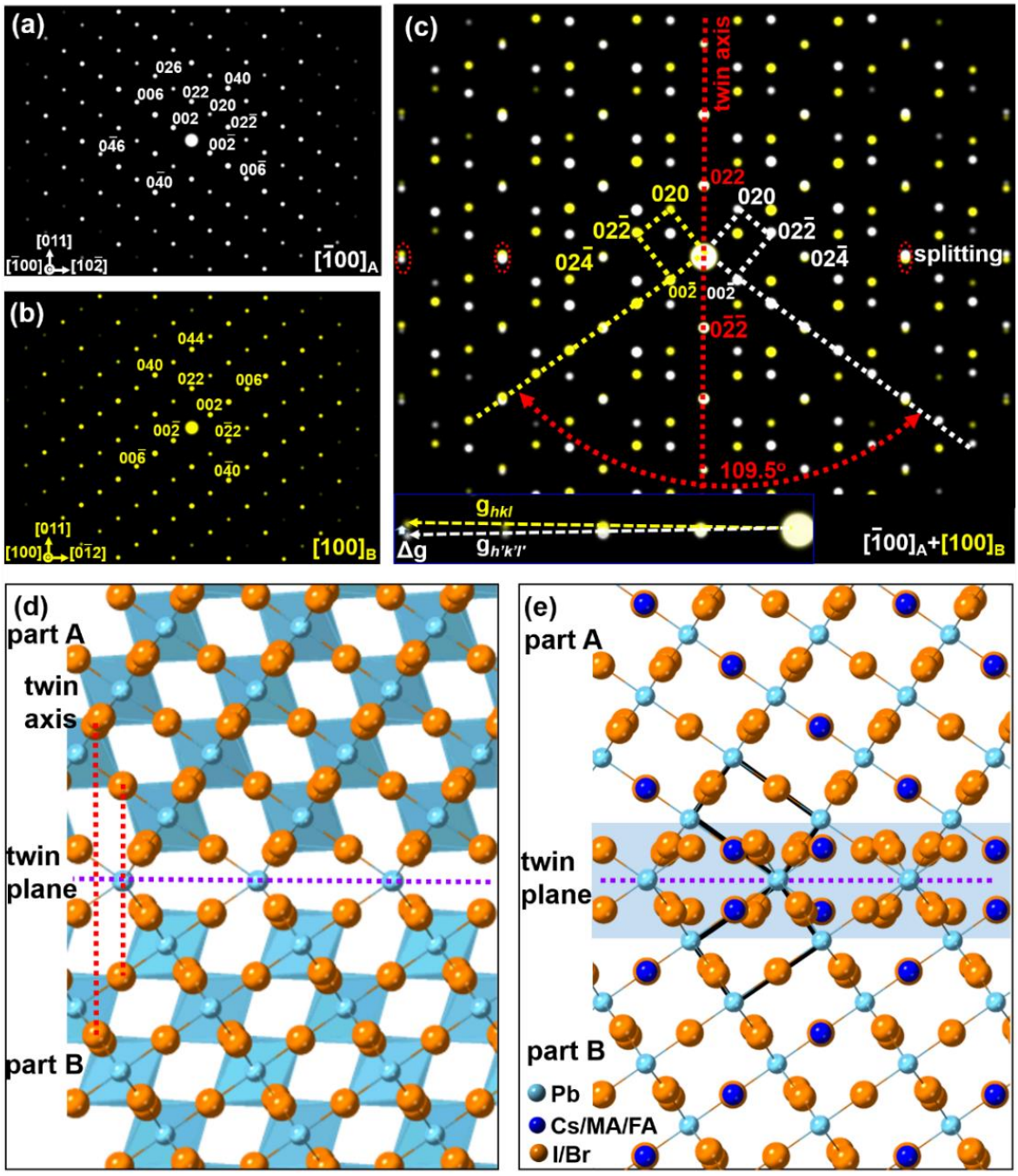

Figure 5.7. Simulation results of twins in tetragonal structure of multi-cation mixed-halide perovskite film. Simulated electron diffraction pattern of the tetragonal perovskite material with (a) $[\bar{1}00]$ zone axis for crystal part A, (b) [100] zone axis for crystal part B, (c) A-B TB viewing from $[\bar{1}00]_A$ + $[100]_B$. (d) Schematic of twinning structure in tetragonal phase. (e) Atomic structure model of TB in tetragonal structure.

5.5.2 Morphology and crystallography of double TBs

The morphology and crystallography of double TBs in the multi-cation mixed-halide perovskite film are shown in Figure 5.8. These double TBs partition three sub-crystal parts A, B and C as shown in Figure 5.8a. For reasons that will become clearer soon, their corresponding SAED patterns from A, B, C are indexed as tetragonal $[\bar{1}00]_A$, $[100]_B$ and $[\bar{1}00]_C$ respectively in Figures 5.8b-d. The SAED from the A-B twin boundary and B-C twin boundary are illustrated in Figures 5.8e and 5.8f respectively with the twin axis highlighted with a red dashed line, normal to the $\{011\}$ plane. The diffraction spots from parts A and B can be clearly resolved in Figure 5.8e and likewise, the twin's structure can be clearly resolved in Figure 5.8f for parts B and C. Interestingly, the splitting spots are observed both with the $g_{\{022\}}$ and the $g_{\{024\}}$ (see green circles) in Figures 5.8e-f. The splitting spots subtended by Δg_{hkl} for both diffraction vectors correspond to 3º. The splitting of the $\{022\}$ spots are a clear indication that the TB is semi-coherent and not exactly on the $\{011\}$ plane in contrast to the $\{111\}_c$ twins discussed earlier. As discussed earlier, with a coherent $\{011\}$ interface, the expected splitting in the $g_{\{024\}}$ reflections is about 2º. The experimental 3º splitting potentially accounts for a 1º tilt between matrix and twin and clearly suggests that the $\{011\}_t$ TB is more complex than its cubic equivalent. The mirror plane and the TB for the tetragonal phase are not necessarily coincident with the TB sometimes straggled as shown in Figure 58a. Quite clearly, the main difference between the $\{111\}_c$ twins and the $\{011\}_t$ twins is the presence of "splitting" spots, which are only observed for $\{011\}_t$ twins.

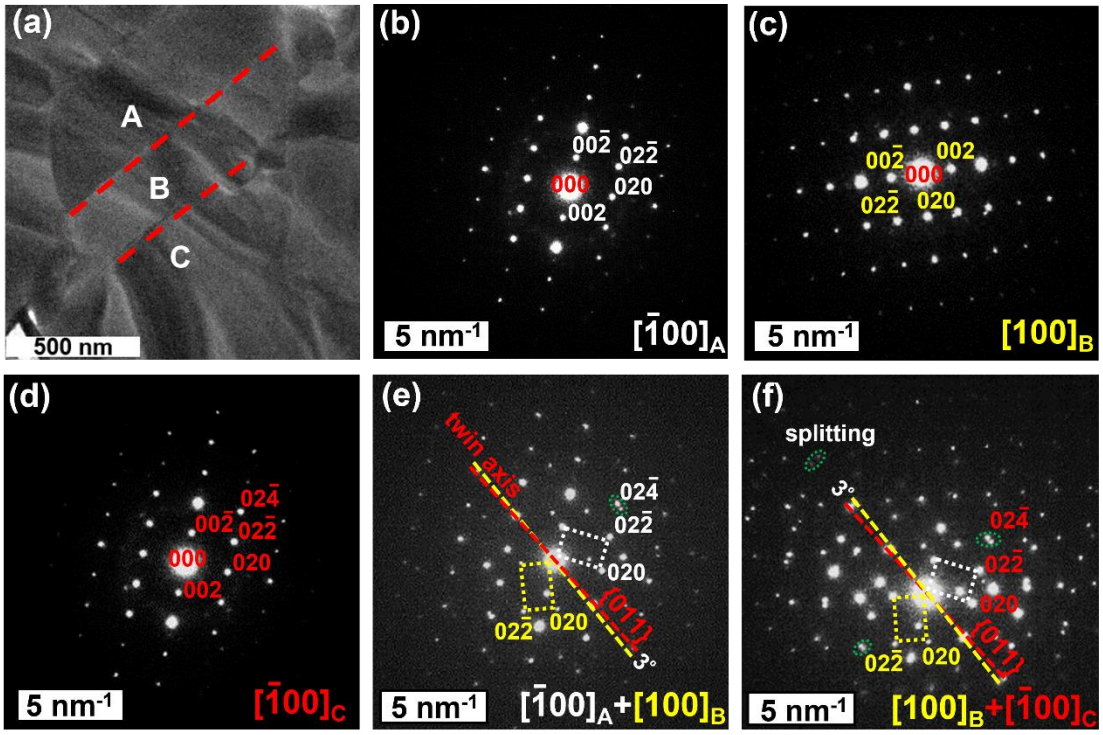

Figure 5.8. The morphology and crystal structure of twinning in multi-cation mixed-halide perovskite film at room temperature. (a) BF-TEM image of double twins. Experimental SAED patterns for three crystal parts for two parallel twin boundaries in the tetragonal perovskite material at the ⟨100⟩ zone axis for (b) crystal part A, (c) crystal part B, (d) crystal part C, (e) A-B twin boundary viewing from $[\bar{1}00]_A$ + $[100]_B$, and (f) B-C twin boundary viewing from $[100]_B$ + $[\bar{1}00]_C$.

Beam damage makes it very difficult to tilt the same crystal to different zone axes and identify the precise nature of the TBs and their relationship. The only way to view the same twins along different orientations is to take diffraction patterns from different crystals. Figure 5.9 gives an overview of images of crystals and their corresponding diffraction patterns showing a clear splitting of the diffraction spots. The SAED patterns in Figure 5.9b can be indexed as tetragonal twins viewed along the [110] zone axes of the tetragonal perovskite material. Yet their corresponding image in Figure 5.9a does not show any evidence of the TBs being viewed edge-on.

The SAED in Figure 5.9b appears at a first glance to be similar to the diffraction pattern reported for {112} tetragonal twins by Rothmann *et al*. with a 1º splitting.[149] However, a detailed analysis of the splitting of the spots shows that the orthogonal planes have a 1º and 3º

splitting. If the twins in Figures 5.9a and b were $\{112\}_t$ twins, there are four edge-on $\{112\}$ planes and two inclined $\{112\}$ planes in this orientation. The TB has an arc-shape as shown in Fig. 5.9a with the red broken line. This arc-shaped TB is consistent with the expected projection of the (011) twinning plane according to the stereogram for this structure (Figure 5.9f). Figure 5.9e shows a simulation of the diffraction pattern for a 180º rotation twin on the (011) plane when viewed along the [110] zone axis combined with a 1º twist. This simulation is consistent with the experimental diffraction in Fig. 5.9b. By using the matrix for the rotation twin on the (011) plane, the twinning relationship between the (110) and (002) reflections can be clearly seen to be in agreement with the experimental observation.

As discussed in the simulation section, the tilted octahedra in the tetragonal case make the AX_3 centred TB with a face-sharing octahedral arrangement very difficult as this atomic configuration will disrupt the octahedral arrangement within two bilayers at the TB. We propose that in the tetragonal structure, the Pb centred TB will restrict the disruption to the perfect octahedral arrangement to the Pb-I/Br layer within the Pb centred TB. In addition, selective cation and anion phase segregation can also explain the misalignment and complex TB geometry between the matrix and the twin.[235, 236] However, the materials' high sensitivity to beam damage makes it difficult to determine the precise geometry and composition of the $\{011\}_t$ twin interface as has been done in other materials system.

An important concern is the role of the TBs in limiting PSC performance. The A-site arrangement (Cs/MA/FA) in multi-cation mixed-halide perovskite films could be a dominant factor for the microstructure induced structural conversion. Selective A-cation segregation at the $A\text{-}X_3$ centred TB can stabilise the TB and change the local composition (and hence bandgap). Indeed, Cs and I atoms co-segregated at TBs are predicted to be more stable than the homogeneous arrangement, especially within an $A\text{-}X_3$ centred cubic TB.[148] This Cs-I rich segregation introduces hole traps and a lower bandgap region and is a potential explanation for the lower V_{OC} observed. The $Pb(I/Br)_6$-prism arrangement proposed for the tetragonal TB is less likely to be a segregation interface for A cations but could play a role in anion segregation at the tetragonal TB given the presence of both Br and I.

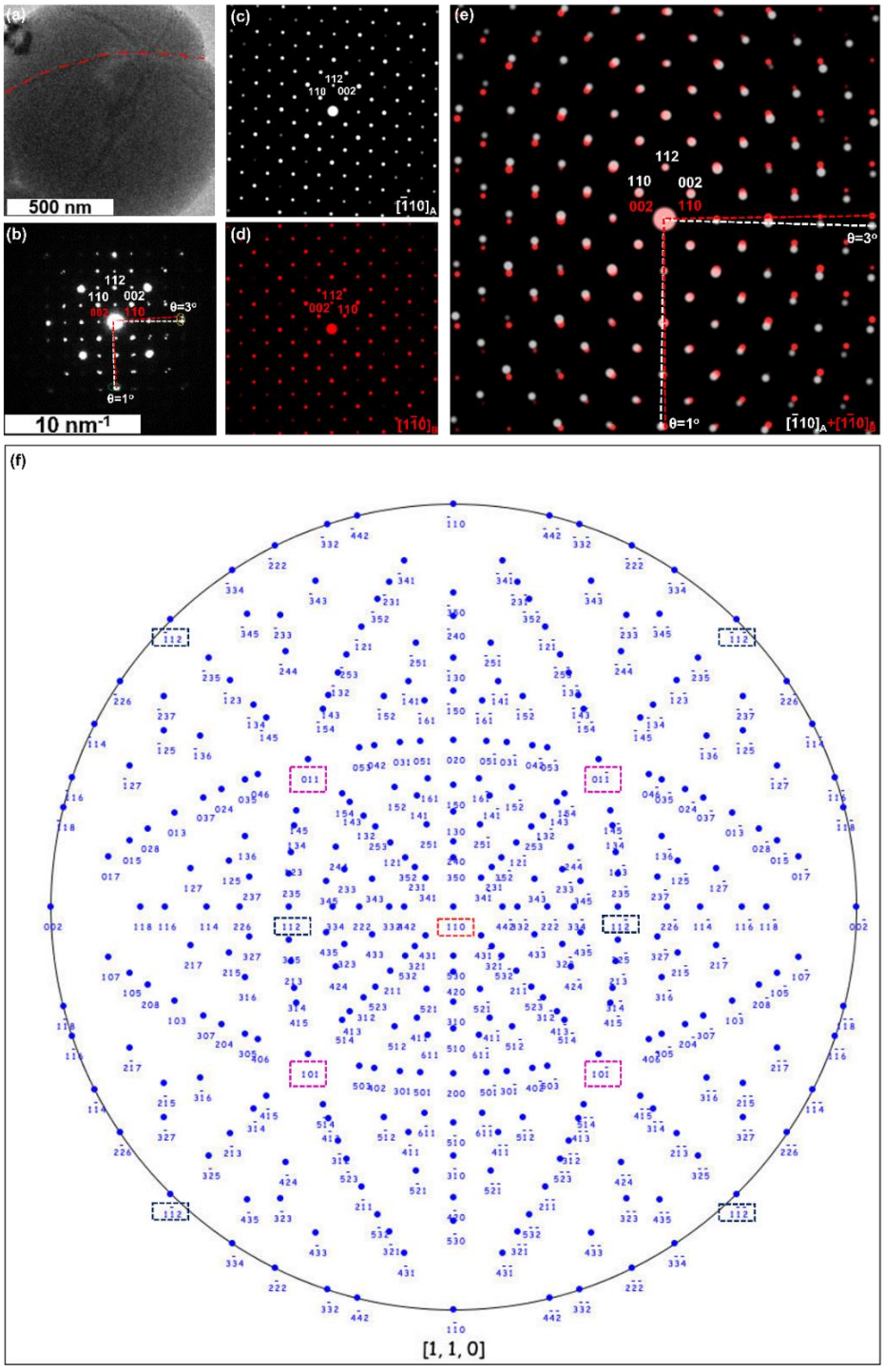

Figure 5.9. The crystal structure of twins in multi-cation mixed-halide perovskite film at room temperature. (a) BF-TEM image. (b) Experimental SAED pattern of (011) twinning viewing [110] zone axis. Simulated electron diffraction pattern of the tetragonal perovskite material with (c) $[\bar{1}10]$ zone axis for crystal part A, (d) $[1\bar{1}0]$ zone axis for crystal part B, (e) A-B twin boundary viewing from $[\bar{1}10]_A + [1\bar{1}0]_B$. (f) Simulated stereogram of tetragonal structure of the perovskite materials using JEMS software, (*hkl*) stereogram along [110] zone axis. The curved red line in Figure (a) indicates the twin boundary.

5.6 Device performance

In this section, we focus on films with the composition $Rb_{0.05}Cs_{0.095}MA_{0.1425}FA_{0.7125}PbI_2Br$, which is very similar to the composition used to fabricate a record efficiency 4-terminal perovskite-silicon tandem cell.[85] We use these films to fabricate solar cells. The J-V curves can be observed from the PCE results in Figure 5.10. The cross-sectional SEM image shows the structure of the solar cell device, which is composed of a back contact layer (Au), HTL (PTAA), the multi-cation mixed-halide perovskite layer, ETL of ms-TiO_2 and cp-TiO_2, and ITO/glass substrate. The as-fabricated device has an efficiency of about 17.53% for forward scan and 17.3% for the reverse scan, which are among state-of-the-art perovskite devices with similar bandgap (1.72 eV). The open-circuit voltage is about 1.23V. These J-V curves reveal that there is little hysteresis in the cell. The result is consistent with microstructure results as the crystallography deals with high-quality materials.

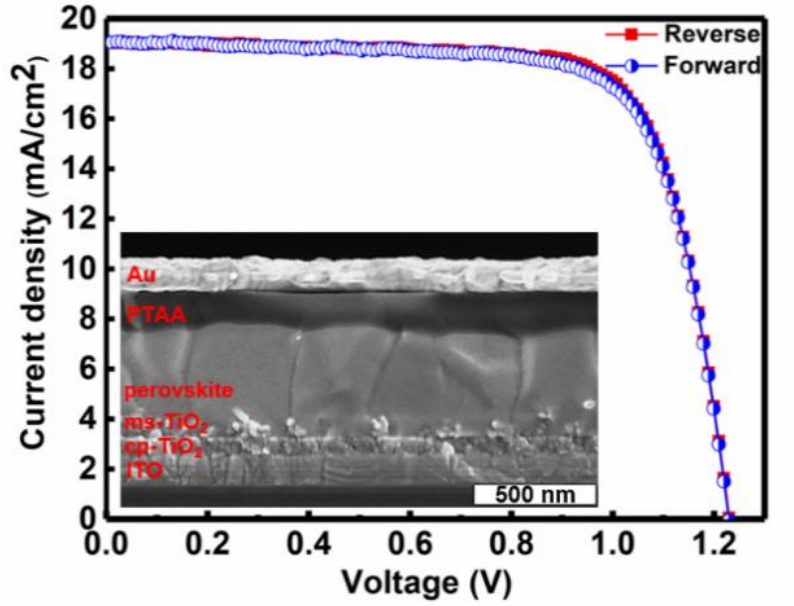

Figure 5.10. J–V curves for the cell using multi-cation mixed-halide perovskite (in reverse (blue) and forward (red) scans) with a scan rate of 50 mV/s.

5.7 Summary

In summary, by employing a low-dose TEM technique combined with detailed simulation, we have shown unambiguously the presence of both $\{111\}_c$ and $\{011\}_t$ twins in multi-cation mixed-halide perovskite films at room temperature. The number of cubic twins in this material

is higher than the number of tetragonal twins observed. A coherent TB was proposed for the cubic phase with no splitting of diffraction spots between the twin and the matrix. In contrast, the interface between the tetragonal matrix and twin is semi-coherent and has a 1º tilt between the two. This was confirmed by the splitting in the twin plane electron diffraction spots between matrix and twin. Additional splitting of spots was ascribed to the octahedral tilt in the tetragonal structure which results in a 2º split for non-coincident spots. A unique way of differentiating the twins in the tetragonal and cubic crystal structure of as-studied perovskite materials is also identified where splitting of spots was only observed for tetragonal twins. Both single and double twin structures were observed for the tetragonal phase. We propose that the cubic twins are more likely to be AX_3 centred while the tetragonal twins are more likely to Pb centred because of the minimum distortion to the Pb-I/Br octahedral arrangement. This has significant implications for A cation and X anion segregation at the twin defects. These results provide a better understanding of the crystal structure defects in multi-cation mixed-halide perovskite materials. Further experimental studies on the effect of twins on the electron-hole recombination and transportation are necessary to elaborate on the best strategy for performance improvement of PSCs in the future.

Chapter 6. Impact of MACl/CsCl on the Formation of NTs, SFs and Cubic Supercell Structure in FA-based Perovskite Solar Cells

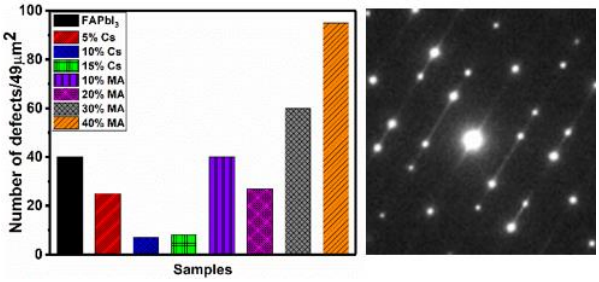

This chapter aims to describe the influence of MACl and CsCl additives on the microstructure, crystal structure, defects (NTs and SFs), optical properties, and PV performance in FA-based PSCs. We find that the addition of MACl and CsCl effectively stabilizes the cubic supercell structure with the $Im\bar{3}$ space group. X-ray diffraction and PL studies show that the addition of MACl and CsCl results in a change in both the lattice parameter and the optical bandgap, respectively. Moreover, the addition of CsCl is shown to minimize the density of defects and improve the PL yield as well as the minority carrier lifetime of the perovskite films. All of these factors contribute to the improved device performance with a maximum efficiency of 21.98% measured for the 10 mol% CsCl perovskite layer.

6.1. Introduction

Solar cells using metal halide perovskites as photoactive layers have exhibited a significant breakthrough in PCEs and are the fastest developing PV technology during the past ten years. The PCEs of single-junction FA-based PSCs have increased to 24.82% (certified at 24.64%), showing their potential to be used in efficient and stable devices for future commercialization.[78, 237-239] There are two main phases of $FAPbI_3$, the yellow hexagonal non-perovskite phase (δ-$FAPbI_3$) and the black cubic perovskite phase (α-$FAPbI_3$).[101] The stabilization of black cubic $FAPbI_3$ perovskite phase can be achieved by controlling different aspects of the fabrication process, namely the annealing temperature, the humidity conditions, the incorporation of additives, and the passivation of surface.[11, 237, 239-242] Additives are

often added to the perovskite precursor solution in order to produce highly efficient and stable PSCs. These additives can improve the quality of the perovskite film in different ways: by acting as crystallization agents or as a source of dopants, or alternatively by modifying the surface morphology and passivating defects.[240, 243] For example, the addition of chlorine anions (Cl^-) to the perovskite precursor mixture has been shown to improve the morphology, crystallinity, grain size, and optoelectronic properties as well as the stability of the cubic phase.[239, 242, 244-247] All these improvements significantly increase the efficiency and stability of PSCs. Alternatively, Kim *et al.* proposed that the MACl additive to cubic $FAPbI_3$ effectively stabilizes an intermediate phase at low temperatures and the optimized device exhibited a PCE of 23.48%.[244] Chavan *et al.* found that the morphology and grain size of the $Cs_xFA_{1-x}PbI_3$ alloy were both dramatically improved by adding CsCl to the $FAPbI_3$ perovskite precursor mixture, leading to increased carrier lifetimes.[245] The average PCE of solar cell devices improved from 16.83% for the reference cell with pure $FAPbI_3$ to 18.87% for an optimal $Cs_xFA_{1-x}PbI_3$ cell with 10 mol% CsCl. Recently, methylenediammonium dichloride ($MDACl_2$) was used to improve the stability of the black α-$FAPbI_3$ perovskite phase and a PCE of 23.7% was successfully maintained above 90% of its original value for 600 h.[237]

The microstructure of the perovskite photoactive layer has a significant impact on the device performance. For instance, a smooth surface and large grains have been shown to improve charge carrier mobility and reduce the recombination sites in the perovskite film.[245] However, the microscopic properties of hybrid metal halide perovskite materials are still not well known predominantly because of the high susceptibility of these materials to electron damage.[12, 168] To date, there are few reports on the microstructure, crystal structure and defect properties of pure $FAPbI_3$ and FA-based perovskites.[136, 148, 231, 248] Two types of planar defects were commonly observed within these perovskite materials: twins and SFs.[136, 148] The formation of twins and SF defects in perovskite films is complex and can significantly affect the properties of materials. NTs are essentially a high density of twins where the thickness of the individual twin is in the nanometre scale. These NTs are potential nanostructures for quantum confinement.[148, 249] Recent work on $FAPbI_3$ has shown the presence of above bandgap oscillatory features in the absorption spectra which are ascribed to quantum confinement effects.[249] The δ-phase TBs are one proposed explanation for intrinsic quantum confinement.

In this chapter, we systematically investigate the impact of MACl and CsCl additives upon the morphology, grain size, crystal structure, defects, optical properties, and PV performance of FA-based PSCs. Electron diffraction analyses show that the pure $FAPbI_3$ is not pure α-phase, but a mixture of different phases including the $Im\bar{3}$ phase, δ-phase as well as a hexagonal phase with rhombohedral symmetry. This is consistent with previous reports of metastability in $FAPbI_3$ during thermal cycling.[250] We demonstrate that the MACl and CsCl additions have a great potential to stabilize the cubic $FAPbI_3$ with a 2 × 2 × 2 supercell expansion and the enhanced formation of the $Im\bar{3}$ space group.

We also investigate the morphology and crystal structure of the NTs and SFs of the perovskite films. A detailed analysis employing SAED patterns shows that both the NTs and SFs are on the $\{111\}_c$ planes. The NT and SF densities can be changed by varying the concentration of the MACl and CsCl additives in the perovskite precursor mixture. The density of NTs is significantly increased when the concentration of MACl is increased. In contrast, the twinned grain is significantly reduced when the amount of CsCl is increased. The density of NTs has an impact on the optical properties and hence the PV performance of PSCs. Interestingly, the MACl and CsCl additions significantly improved the morphology, grain size, and crystallinity of the perovskite films, resulting in enhanced carrier lifetimes. In addition, the optimized PSCs with 10 mol% CsCl exhibit the best device performance with a PCE of 21.98%, which is almost double that of the pure $FAPbI_3$ PSC with a 13.67% PCE. Furthermore, the hysteresis effect is also suppressed with the CsCl addition. These results prove that the incorporation of CsCl in the perovskite precursor mixture is an extremely effective method to obtain high-quality film formation, resulting in a highly efficient and stable PSC device.

6.2 Microstructure and crystal structure of pure $FAPbI_3$ perovskite films

6.2.1 Crystal structure of perovskite films

Figure 6.1 shows the XRD simulations for different possible phases, notably the cubic α-phase structure (space group $Pm\bar{3}m$, a = 6.3506 Å), cubic supercell structure ($Im\bar{3}$, a = 12.5461 Å), the rhombohedral structure ($R\bar{3}$, a = 17.739 Å, c = 10.867 Å) and the δ-phase hexagonal structure ($P6_3/mmc$, a = 8.85737 Å, c = 7.9077 Å). As can be seen, there are several XRD peaks common to the $Pm\bar{3}m$, $Im\bar{3}$ and $R\bar{3}$ phases namely the peaks at 2θ values of 13.9, 19.6, 24.1, 28, 31.5, 34.5, 40, and 42.4°. However, additional peaks can be observed for the $Im\bar{3}$ phase,

namely the (013), (123), (015), (053) and (235) peaks (highlighted by the purple star symbol) and these additional peaks can also be observed for the $R\bar{3}$ phase and are marked with the pink star symbol. The δ-phase has a very different XRD signature with its most prominent peak, the (100) at a 2θ angle of 11.6º.

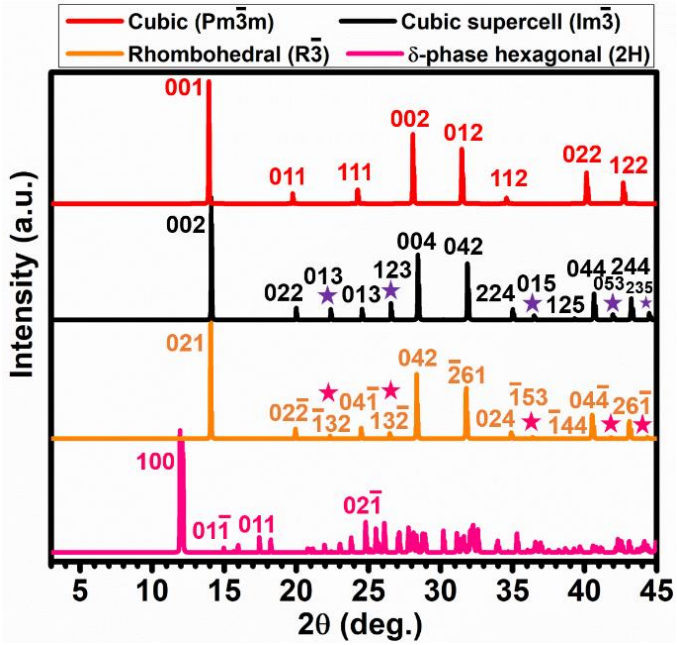

Figure 6.1. Simulations of powder X-ray diffraction of perovskite material for the cubic α-phase structure with space group $Pm\bar{3}m$, the cubic supercell structure with space group $Im\bar{3}$, the rhombohedral structure with space group $R\bar{3}$, and the δ-phase hexagonal 2H structure with space group $P6_3/mmc$. (Additional peaks attributed to the $Im\bar{3}$ and the $R\bar{3}$ phases are labelled with the purple and pink star symbols, respectively.)

6.2.2 Microstructure and crystal structure of $FAPbI_3$ perovskite

TEM is one of the most powerful techniques to investigate the morphology, microstructure, and crystal structure of materials. There are very few reports of twin domains and SFs in pure $FAPbI_3$ and FA-based perovskites.[136, 148] The $FAPbI_3$ perovskite is reported as the black α-phase with space group $Pm\bar{3}m$.[101] For reasons that will be clear later, four possible perovskite space group structures will be considered, namely the $Pm\bar{3}m$ (α-phase), $Im\bar{3}$ (cubic supercell with lattice constant twice that of the α-phase), hexagonal δ-phase and $R\bar{3}$ (rhombohedral structure). Figures 6.2a-b show a typical BF-TEM image of the pure $FAPbI_3$ perovskite film and the experimental SAED pattern of the single grain highlighted in the yellow

circle. The experimental SAED pattern in Figure 6.2b does not agree with the simulation of the SAED pattern along [111] axis shown in Figure 6.2d for the cubic α-phase with $Pm\bar{3}m$ space group (the space group typically associated with $FAPbI_3$).[101] However, this SAED pattern is consistent with the simulation along the [111] axis for the cubic $Im\bar{3}$ phase as shown in Figure 6.2f and alternatively also matches the simulation of the [10$\bar{1}$1] for the rhombohedral structures ($R\bar{3}$) as shown in Figure 6.2h. As clearly seen in the atomic structures viewed along these orientations, the [111] zone axis in the $Im\bar{3}$ structure (see Figure 6.2e) is equivalent to the [10$\bar{1}$1] zone axis in the $R\bar{3}$ structure (see Figure 6.2g).

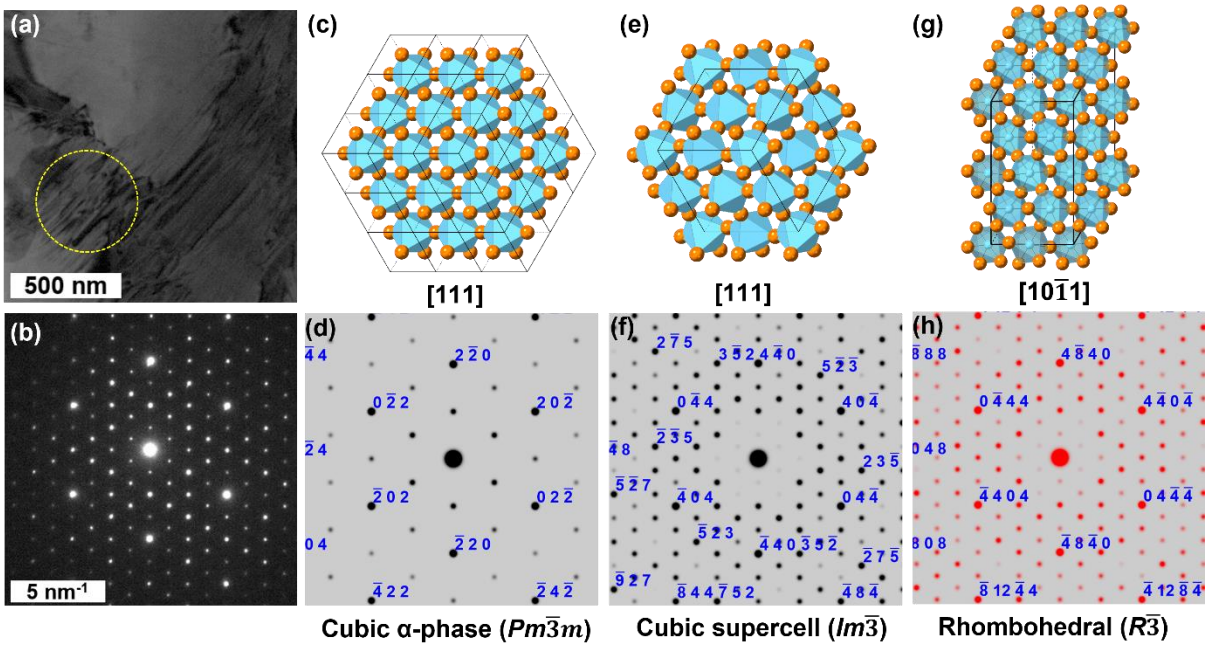

Figure 6.2. (a) BF-TEM image of $FAPbI_3$ perovskite thin film. (b) Corresponding experimental SAED pattern taken from the grain (highlighted in a yellow circle in (a)). (d, f, h) Simulations of the electron diffraction patterns for (d) the cubic α-phase ($Pm\bar{3}m$) along [111] zone axis, (f) the cubic superstructure ($Im\bar{3}$) along [111] zone axis and (h) the rhombohedral structure ($R\bar{3}$) along [10$\bar{1}$1] zone axis. (c, e, g) Views of the atomic structure along the orientations described for the simulations (d), (f) and (h), respectively.

Figure 6.3 shows another set of diffraction analyses for pure $FAPbI_3$ perovskite. The experimental SAED pattern of the grain highlighted in Figure 6.3a is shown in Figure 6.3b and does not match the electron diffraction simulations for the $Im\bar{3}$ structure. The closest match is the electron diffraction of the $Im\bar{3}$ structure along the [021] zone axis in Figure 6.3c and it is evident that there are some superlattice like reflections missing from this pattern as highlighted

in red circles in the experimental SAED. Interestingly, the experimental SAED pattern is in excellent agreement with the simulation of the rhombohedral structure along the [11$\bar{2}$6] zone axis as shown in Figure 6.3d and cannot be matched with simulations of the other phases considered. We note that the $FAPbI_3$ has a high density of NTs, and that twinning can also be a source of additional reflections.[251, 252]

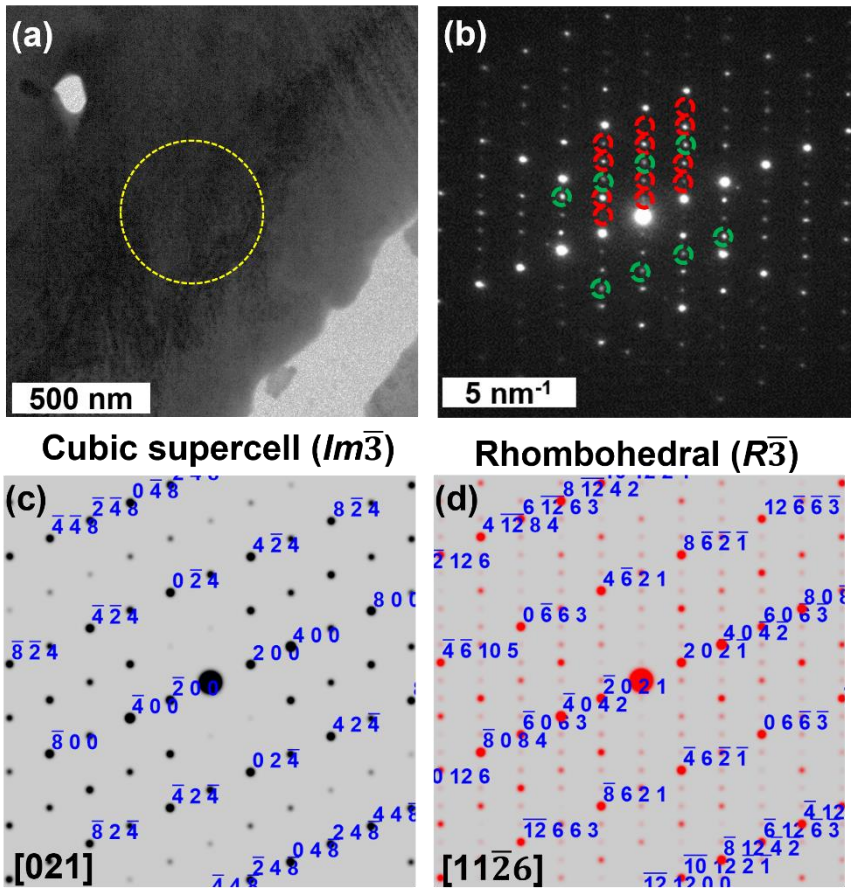

Figure 6.3. (a) BF-TEM image of $FAPbI_3$ perovskite thin film and (b) its corresponding experimental SAED pattern taken from the grain (highlighted in a yellow circle). (c) Simulation of the electron diffraction pattern of the cubic (*Im*$\bar{3}$) perovskite structure along the [021] zone axis. (d) Simulation of the electron diffraction pattern for the rhombohedral (*R*$\bar{3}$) perovskite structure along the [11$\bar{2}$6] zone axis. The strong cubic reflections are highlighted in green circles.

Figure 6.4b illustrates the experimental SAED pattern taken from the region highlighted with a yellow circle in the BF-TEM image in Figure 6.4a. Interestingly, this diffraction could not be assigned to a single crystal structure. The best fit to this diffraction pattern is an overlay

of two electron diffraction pattern simulations, the cubic $Im\bar{3}$ structure (Figure 6.4c) along the [111] zone axis and the δ-phase hexagonal (2H) along the [0001] zone axis (Figure 6.4d). There is perfect agreement between the experimental diffraction pattern (Figure 6.4b) and the overlay of the simulations in Figure 6.4e. We note that the [111] direction in the cubic structure is perpendicular to the (111) plane which can lead to different stacking sequences and hence different crystal structures. Specifically, the δ-phase has the 2H stacking sequence with the [0001] direction parallel to the cubic [111] direction. This is consistent with the presence of NT domains and SFs with {111} TBs and as a result, one can expect to form different polytypes with hexagonal and rhombohedral structures. Each of these different crystal structures would have a different bandgap. However, a high density of NTs (5-54 nm thick) combined with thin layers of hexagonal structures is similar to III-V semiconductor twinning superlattices and SFs and has a different band structure.[122]

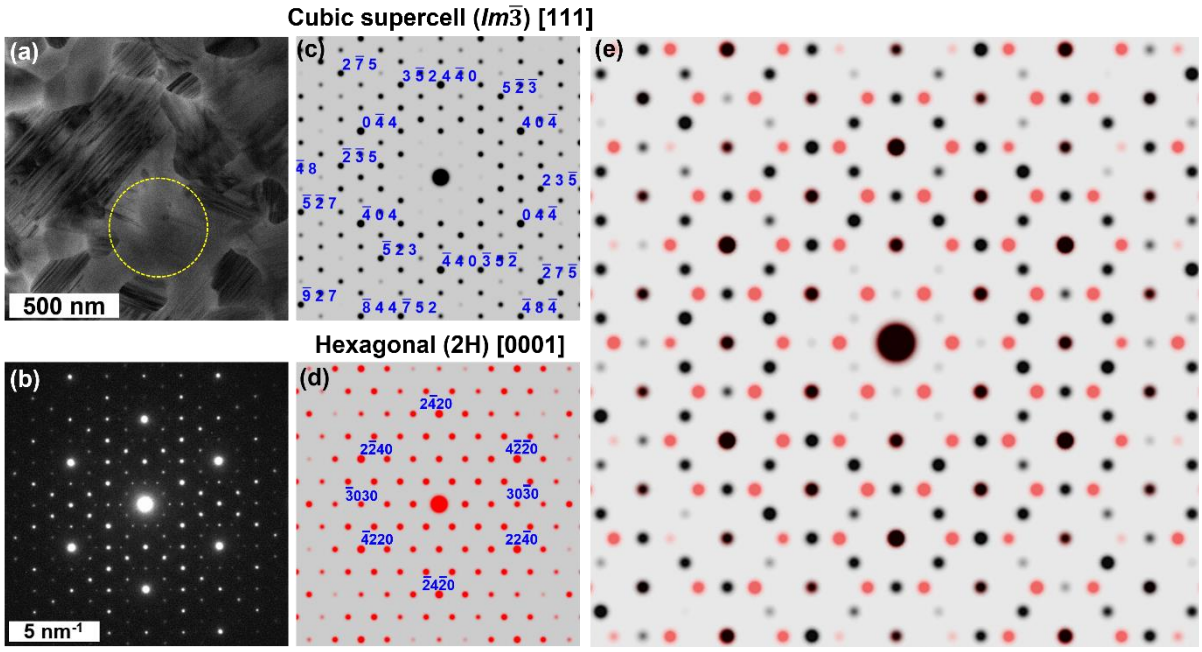

Figure 6.4. (a) BF-TEM image of $FAPbI_3$ perovskite thin film and (b) its corresponding experimental SAED pattern taken from the grain (highlighted in a yellow circle). (c) Simulation of the electron diffraction pattern of perovskite with the cubic supercell ($Im\bar{3}$) structure along [111] zone axis. (d) Simulation of the electron diffraction pattern of perovskite with the hexagonal δ-phase (*2H*) along [0001] zone axis. (e) Overlap of the simulated diffraction patterns of [111] zone axis in $Im\bar{3}$ structure (black) and [0001] zone axis in hexagonal 2H structure (red).

6.3. Impact of MACl on microstructure and crystal structure of FA-based perovskite

6.3.1 Surface morphology and general microstructure of perovskite films

The surface morphology of a semiconductor plays a significant role in determining its properties. In OIMHPs, understanding the surface features and their impact on the optical properties and device performance is becoming increasingly important. Here, the surface morphology and microstructure of the perovskite films with different MACl concentrations were investigated by SEM and TEM. Figure 6.5a illustrates the top-view SEM image of pure $FAPbI_3$ spin-coated on the ITO/glass substrate. The film displays a compact, pinhole-free morphology and irregular grains with an average grain size of around 340 nm. Figures 6.5 b-e show the top-view SEM images of $FAPbI_3$ perovskite films with various MACl concentrations of 10 mol%, 20 mol%, 30 mol%, and 40 mol% (denoted as 10% MACl, 20% MACl, 30% MACl and 40% MACl respectively). The relationship between the average crystal grain size (extracted from SEM images using the ImageJ software) and the MACl molar proportion is illustrated in Figure 6.5k. The average grain size of perovskite films increases with increasing concentration of MACl. The largest grain size was observed for the 40% MACl sample which had an average grain size of 890 nm. The perovskite films show a high number of NTs on many grains as shown in Figures 6.5f-j. The number of NTs on one grain increases with higher MACl concentration. In addition, the lowest number of NTs on one grain was observed in the 20% MACl sample as compared to other concentrations.

The density of twin defects was estimated by counting the number of twinned grains per area of 49 μm^2 from the SEM images and a graph of the density of twin defects with different additive concentrations is shown in Figure 6.5l. The results clearly show that the density of NTs significantly increased when the concentration of MACl was increased. The film with 20% MACl had the best crystal quality with 27 twinned grains/49 μm^2. The 40% MACl sample has the highest density of NTs (95 twinned grains/49 μm^2) and is mostly composed of twinned grains. Rothmann *et al.* have shown that pure $MAPbI_3$ perovskite has twinned grains and this might explain the higher incidence of twinned grains in perovskite films with higher MACl content, notably the 30% and 40% MACl samples.[149] When MACl is added into $FAPbI_3$ precursor solution, the replacement of FA-sites by MA cations may create more defective grains in the film.

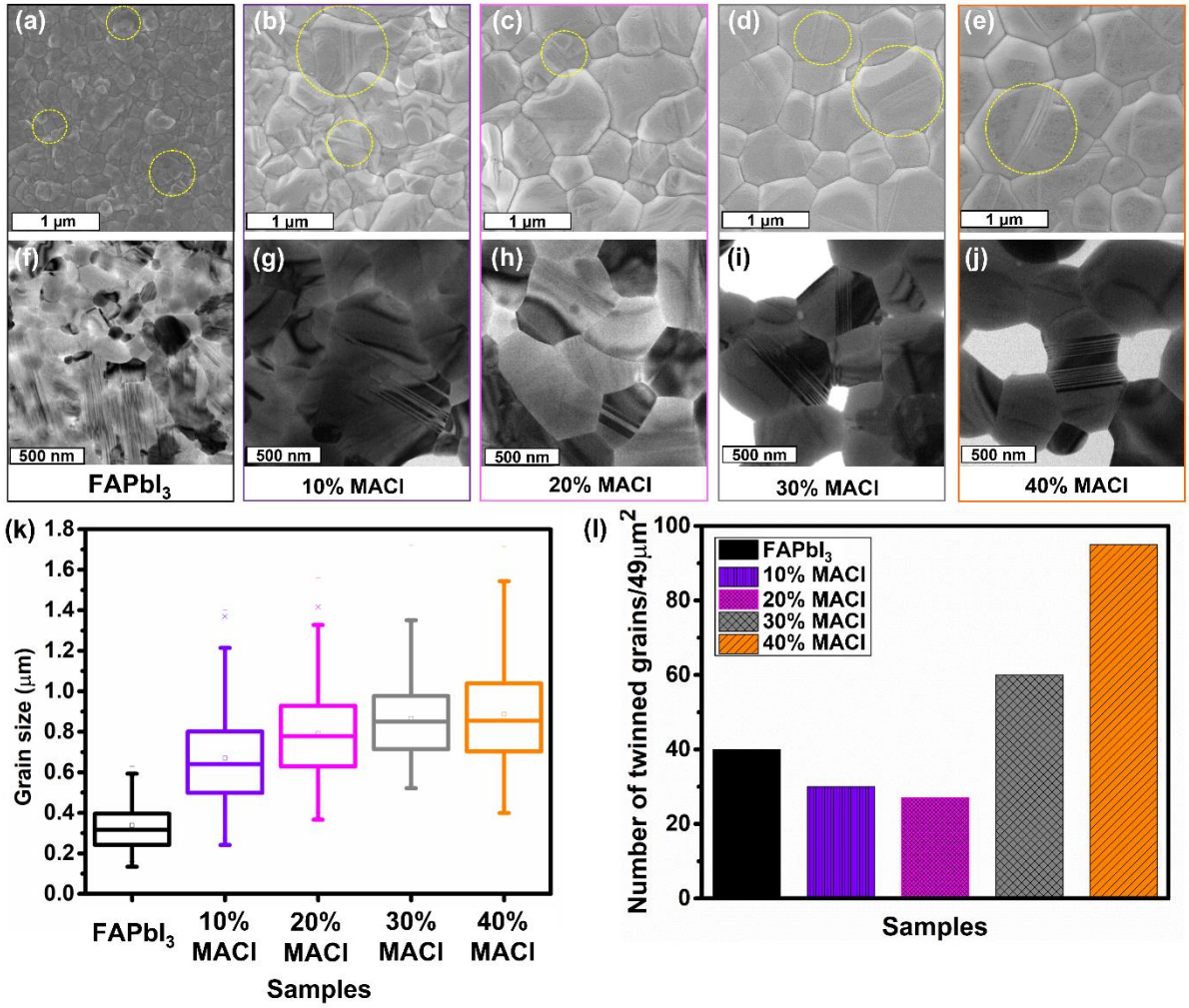

Figure 6.5. Top-view SEM images of perovskite films with different concentrations of MACl (a) pure-$FAPbI_3$, (b) 10% MACl, (c) 20% MACl, (d) 30% MACl, (e) 40% MACl. BF-TEM images of perovskite films with different concentrations of MACl (f) pure-$FAPbI_3$, (g) 10% MACl, (h) 20% MACl, (i) 30% MACl, (j) 40% MACl. (k) Plot showing the variation of the grain size distribution of the perovskite films with various MACl concentrations. (l) Plot of the number of twinned grains per area as a function of the MACl concentration.

6.3.2 Crystal structure and surface chemistry of perovskite films with different concentrations of MACl

The crystallinity of pure $FAPbI_3$ perovskite film and $FAPbI_3$ perovskite with various amounts of MACl additives was analyzed by X-ray diffraction (XRD) measurements. Figure 6.6 illustrate the experimental XRD patterns of the $FAPbI_3$ perovskite with different concentrations of MACl (10, 20, 30, 40 mol%). At a first glance, the XRD pattern of the pure $FAPbI_3$ perovskite in Figure 6.6a appears to match the XRD simulation for the cubic α-phase ($Pm\bar{3}m$

structure) except for a small peak at 11.6º, corresponding to the undesirable hexagonal δ-phase (highlighted by the red star symbol). As shown in the XRD simulations, these prominent peaks are also common to the $Im\bar{3}$ and the $R\bar{3}$ phases. For reasons that will be clearer in the TEM analysis, these peaks were indexed with the $Im\bar{3}$ phase.

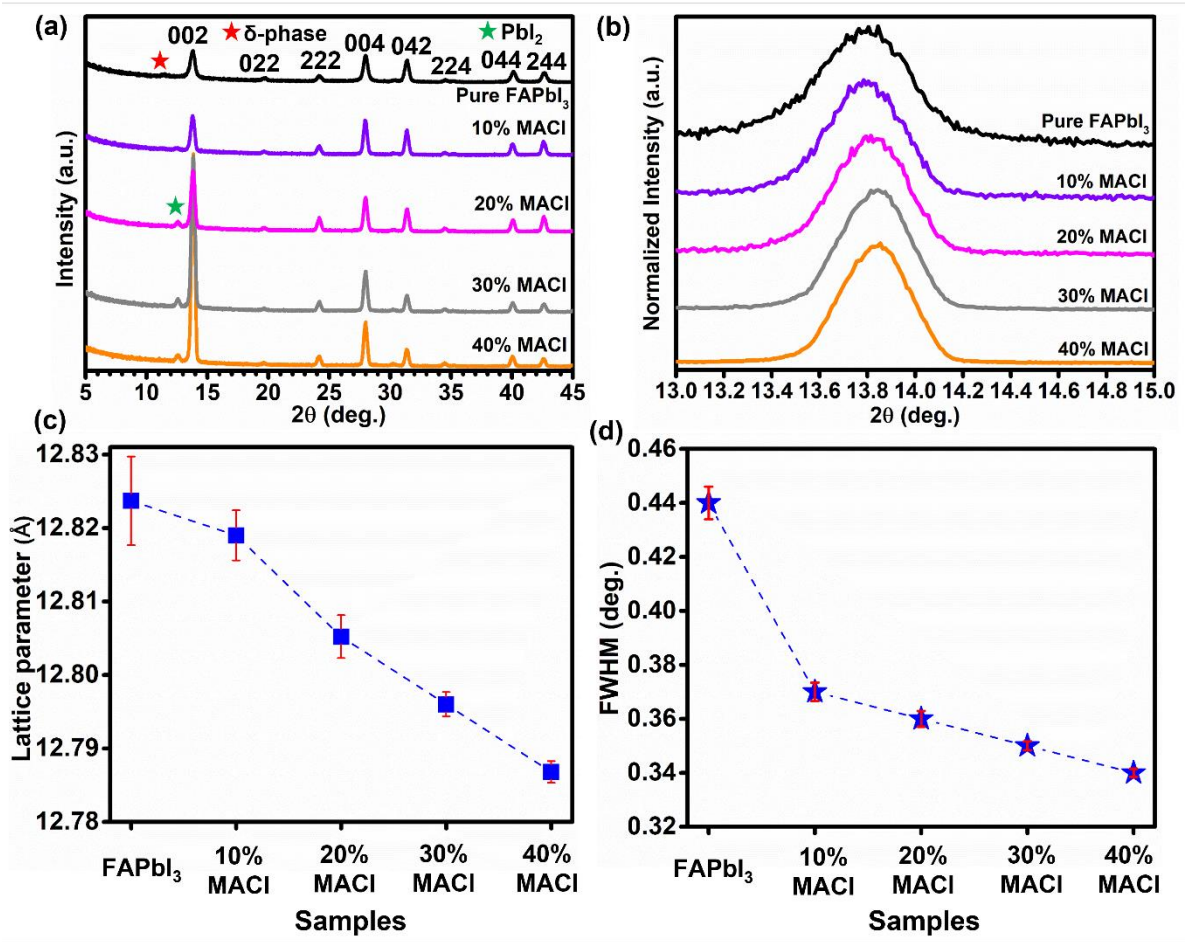

Figure 6.6. (a) Experimental XRD patterns of $FAPbI_3$ perovskite films in pure form and with different concentrations of MACl (10, 20, 30, 40 mol%) additives. (b) XRD plots showing the shift in the (002) perovskite peak to higher diffraction angles, (c) extracted lattice parameter and (d) full width at half maximum (FWHM) of the (002) peak of the perovskite film with different MACl concentrations.

Interestingly, the XRD formation of the hexagonal δ-phase appears to be eliminated with a small addition of MACl, based on the absence of the peak at 11.6º. The intensity of the main cubic phase perovskite peak at 13.9º is dramatically increased after introducing 20, 30, 40 mol% MACl additives to the perovskite precursor solution. However, we observed a small diffraction peak located at $2\theta = 12.5º$ corresponding to PbI_2 phase (highlighted by the green star

symbol). This indicates the formation of PbI_2 phase on the perovskite surface with the incorporation of MACl, which can be attributed to the thermal instability of MA cation during the annealing step at 150^{o}C as reported previously.[253]

The XRD patterns of the MACl-treated $FAPbI_3$ perovskite film show that the (002) peak consistently shifts to higher 2θ angles when the concentration of MACl increases, corresponding to smaller lattice constants (Figure 6.6b). Figure 6.6c shows that the lattice constant decreases with increasing MACl amount and this demonstrates the successful mixing of MA^+ cations and Cl^- anions within the perovskite crystal structure. Figure 6.6d illustrates that the full width at half maximum (FWHM) for the (002) peak is decreased when the amount of MACl increases, indicating an increased X-ray crystallite size. The smallest FWHM value is obtained for 40% MACl perovskite film, indicating larger grain size in this sample.

The surface chemistry of the $FAPbI_3$ film with different MACl concentrations was analysed using XPS measurements. The fine scan of C 1s component (Figure 6.7) revealed the presence of C=N and C-N bonds corresponding to the FA^+ cation in all samples. The presence of MA^+ cation is detected through the higher peak intensity and weighting factor of C-N bond as shown in Figures 6.7a and b. In these figures, the peaks at the binding energy of about 284.8, 284 and 288.5 eV can be attributed to the C-C, C-N and C=N bonds, respectively. There is no peak shifting of the C 1s component in all samples, which is consistent with a homogenous surface chemistry of as-fabricated perovskite films. Figure 6.7c illustrates the relative concentrations of Cl on perovskite films calculated from surface XPS measurement. No Cl is detected in the pure $FAPbI_3$ perovskite film. However, the XPS data shows that Cl^- is incorporated in the $FAPbI_3$ perovskite film with the addition of MACl. Density functional theory (DFT) calculations have shown that a small amount of Cl^- substituted at the anion sites of $FAPbI_3$ will essentially result in a reduced Pb-X bond length and minimise the Pb-X-Pb distortion[254]. This effectively accounts for the stabilization of the cubic phase and explains the lattice contraction observed in the XRD data. The presence of Cl also suppresses the formation of I vacancies because of its higher calculated formation energy.[254]

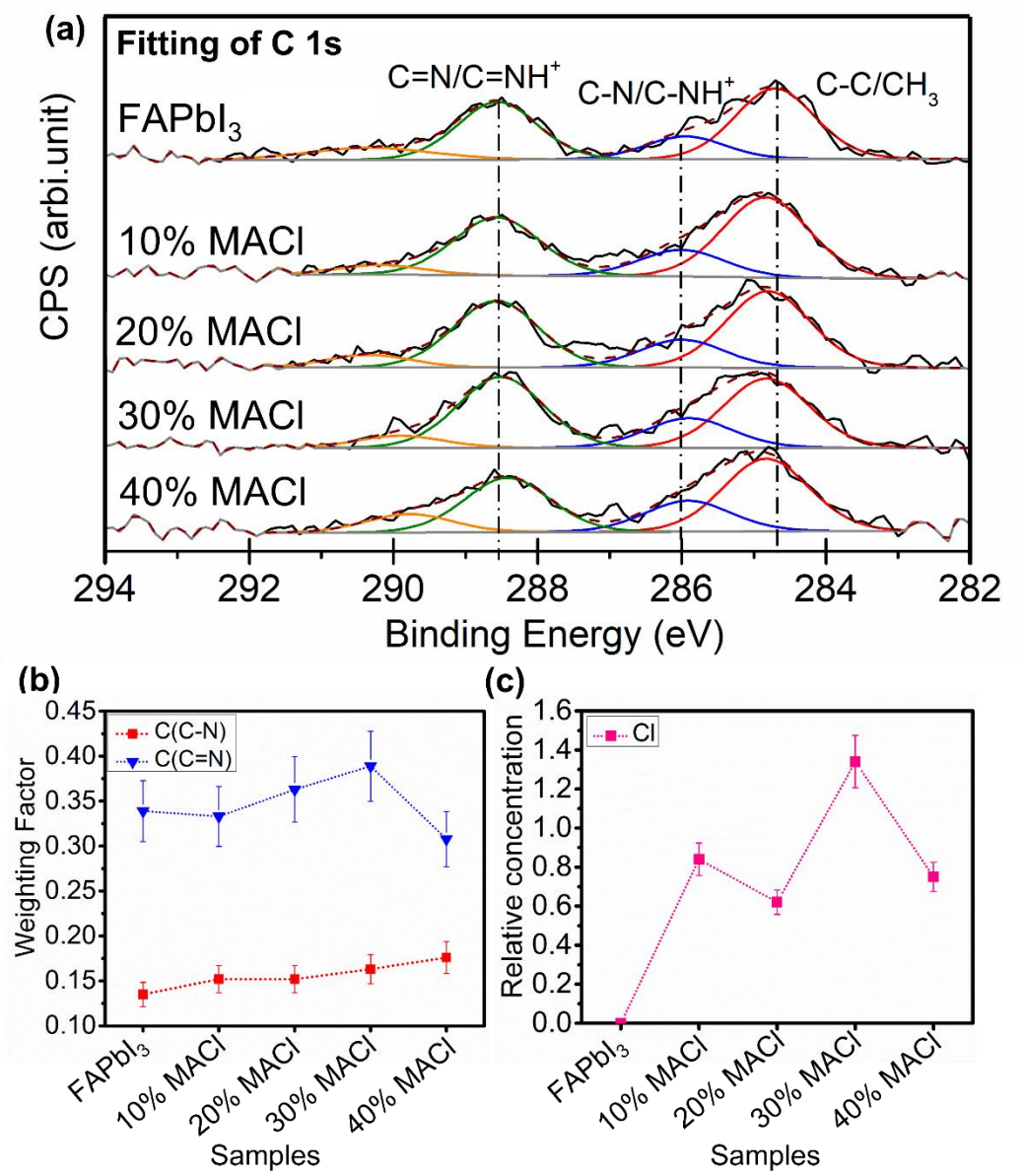

Figure 6.7. (a) Simulations for fitting the high-resolution XPS spectra of C 1s of perovskite films with different concentrations of MACl addition. (b) Weighting factor of the C(C-N) and C(C=N) peaks measured from perovskite films with different amounts of MACl. (c) Relative concentration of Cl on perovskite film with different concentrations of MACl calculated from surface XPS measurement.

6.3.3 Optical properties of perovskite films with different amounts of MACl

The optical characteristics were evaluated using absorbance, PL and TRPL measurements for the perovskite films on glass substrate at room temperature. The recombination process was fitted with the following bi-exponential equation:

$$f(t) = f_0 + A_1exp(-t/\tau_1) + A_2exp(-t/\tau_2)$$

where *f(t)* is the luminescence intensity, f_0 is a constant, A_1 and A_2 are corresponding decay amplitudes, τ_1 and τ_2 are the fast and slow decay time constants, respectively.[237] In addition, the τ_1 and τ_2 decay components are assigned to non-radiative recombination from defects (surface traps near the grain boundaries) and radiative recombination from the bulk perovskite, respectively.[255]

Figures 6.8a-c shows the PL, normalized PL, and absorbance spectra of $FAPbI_3$ perovskite films with and without MACl additive. A slight blueshift is observed in the PL spectra with increasing concentrations of MACl. This is attributed to the incorporation of MA^+ cation and Cl^- anion in the perovskite lattice and is in line with the shift observed in the optical bandgap as shown in Figures 6.8b-c. The PL peak intensity is significantly enhanced in the 10 and 20% MACl perovskite films. In contrast, the PL intensities were reduced with the addition of 30 and 40 mol% MACl to the perovskite films. These results are consistent with SEM and TEM results. The perovskite films with 30 and 40% MACl have a higher density of defects compared to the perovskite films with 10 and 20% MACl, leading to a decrease in the PL intensity and lifetime.

Figure 6.8d compares the TRPL results for different $FAPbI_3$ perovskite films with and without MACl added. The 20% MACl sample shows the longest PL lifetime compared to any other MACl concentrations. This perovskite composition has PL lifetimes τ_1 = 35.8 ns and τ_2 = 6.1 ns (Table 6.1). When the concentration of MACl is further increased to 30% and 40%, the lifetime was reduced. These results suggest that the optical properties of $FAPbI_3$ perovskite show only a small improvement with the MACl addition as shown in Figure 6.8. The 10% MA sample has the highest PL intensity, and 20% MACl sample has longest lifetime out of all the samples.

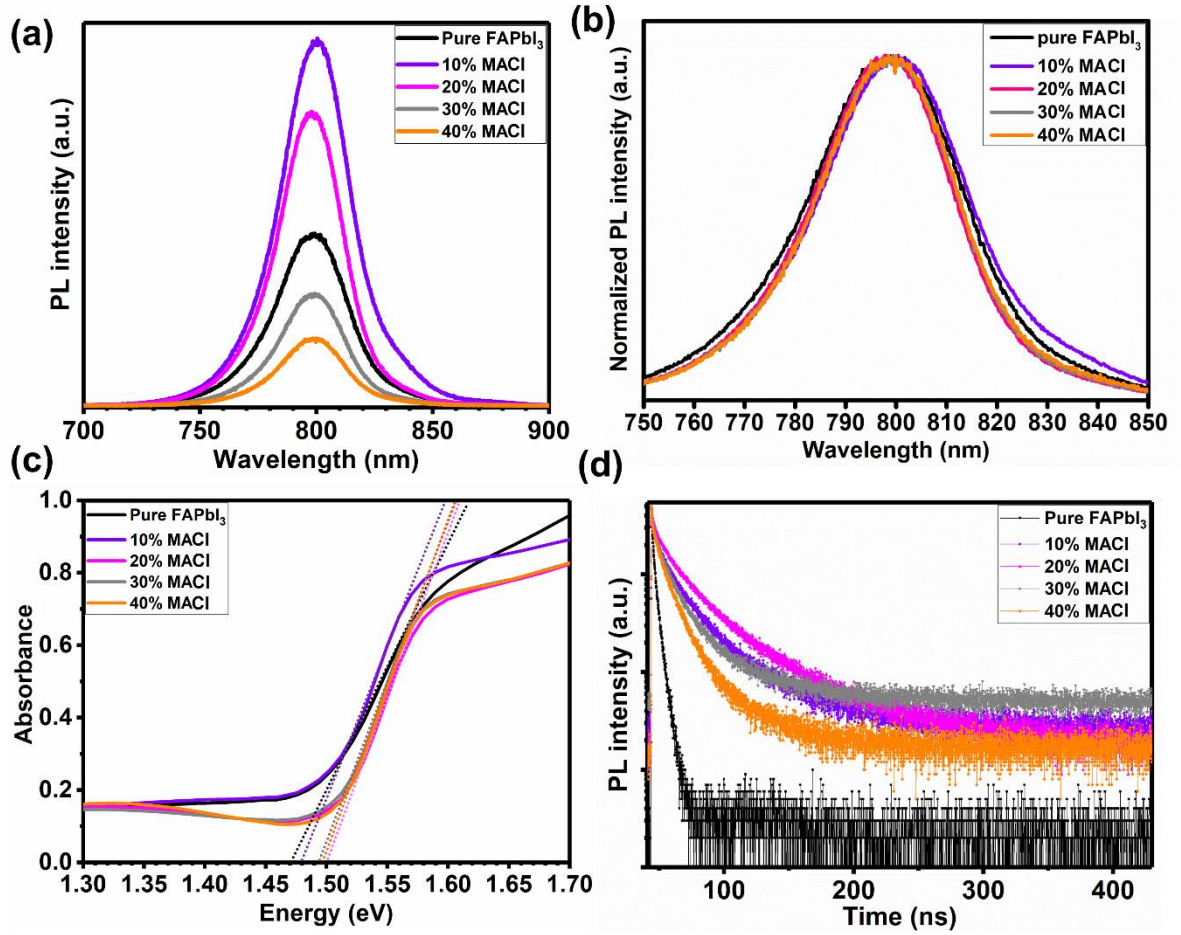

Figure 6.8. (a) The steady-state PL spectra, (b) normalized PL spectra, (c) optical absorbance spectra, and (d) TRPL of the $FAPbI_3$ perovskite in its pure form and with different concentrations of MACl.

Table 6.1. TRPL parameters of perovskite prepared with pure $FAPbI_3$, 10% MACl, 20% MACl, 30% MACl, 40% MACl.

10% MACl		**20% MACl**		**30% MACl**		**40% MACl**	
τ_1 *(ns)*	τ_2 *(ns)*	τ_1 *(ns)*	τ_2 *(ns)*	τ_1 *(ns)*	τ_2 *(ns)*	τ_1 *(ns)*	τ_2 *(ns)*
34.9	5.1	35.8	6.1	16.5	2.6	15.7	3.1

6.3.4 Effect of MACl on the crystal structure of perovskite films

Figure 6.9 gives an overview of the BF-TEM images of the $FAPbI_3$ perovskite film with 20 mol% MACl and their corresponding SAED patterns along the [211], [201], [001], [122], [111],

and [113] zone axes. We also observed the same forbidden reflections (circled in red) along all of the zone axes. These results suggest that the perovskite film with 20% MACl also has a cubic perovskite structure with the $Im\bar{3}$ space group and the lattice parameter 2a (where a is the lattice constant of $Pm\bar{3}m$ cubic perovskite). Moreover, these results are consistent with the simulated electron diffraction patterns shown in Figure 6.10 for the $Im\bar{3}$ space group. Based on these results, we confirm that the MACl additive helps to stabilize the cubic $Im\bar{3}$ phase.

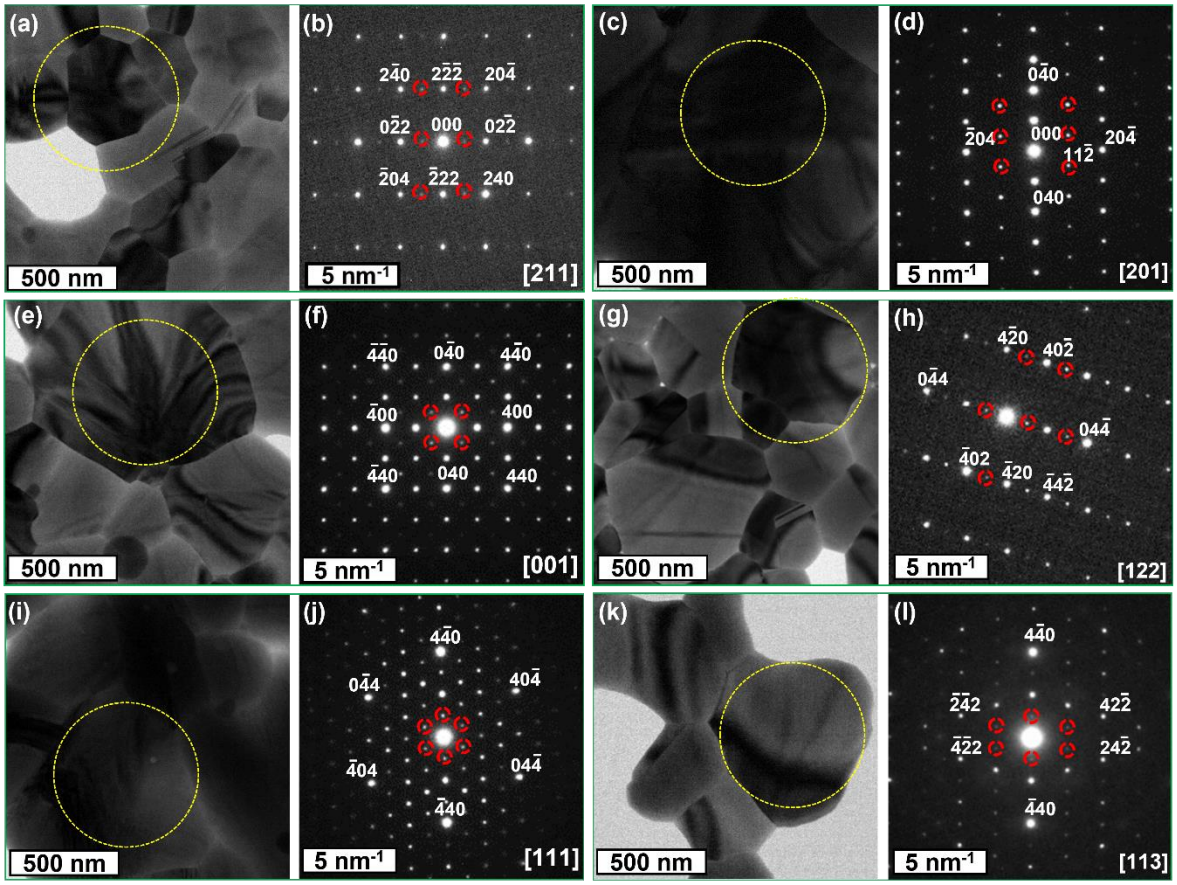

Figure 6.9. BF-TEM images and corresponding SAED patterns taken from grain highlighted in yellow circle of $FAPbI_3$ film with 20 mol% MACl addition along various zone axes including (a, b) [211], (c, d) [201], (e, f) [001], (g, h) [122], (i, j) [111] and (k, l) [113]. The red circles in the SAED patterns correspond to the superlattice reflections.

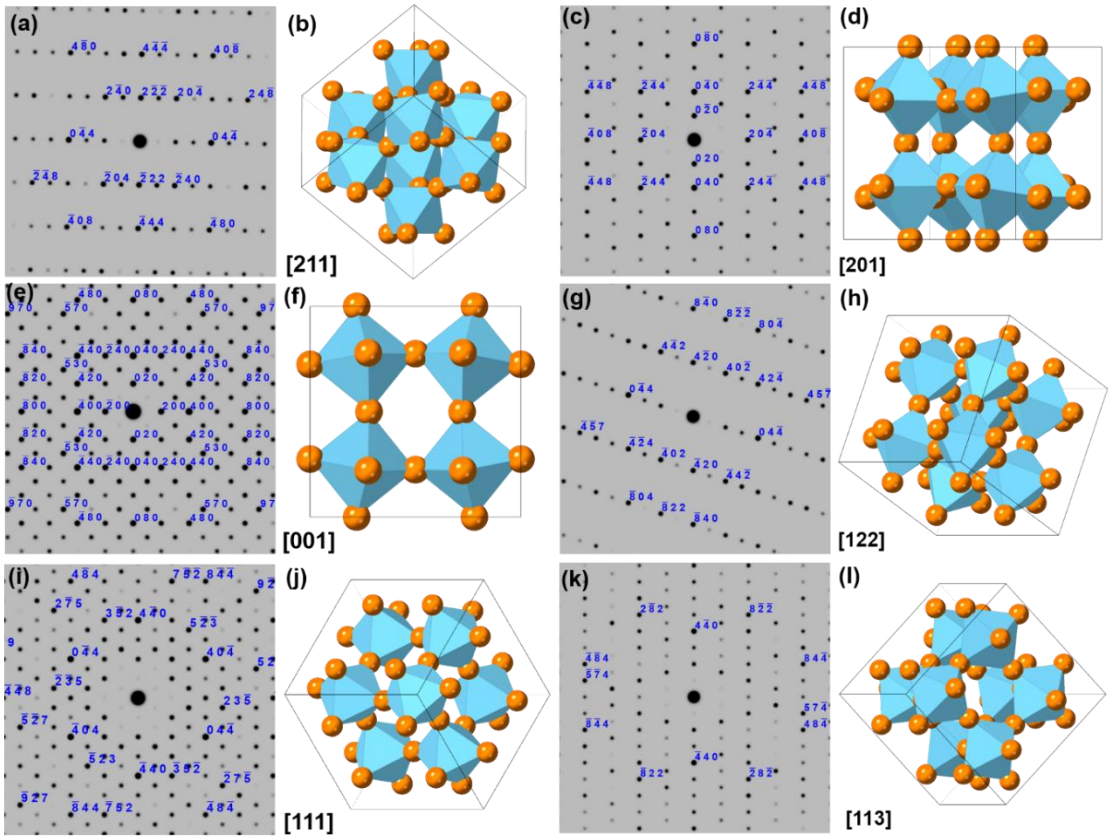

Figure 6.10. Simulation of electron diffraction patterns and atomic structure models of perovskite material with cubic supercell structure along different zone axes (a-b) [211], (c-d) [201], (e-f) [001], (g-h) [122], (i-j) [111], and (k-l) [113] for $Im\bar{3}$ structure.

6.3.5 Morphology, crystallographic of NTs and SFs of perovskite films

In perovskite materials, twinning is a common structural defect, where two sub-crystallites share a facet to form a mirror image. The BF-TEM image of pure $FAPbI_3$ shows that most of the grains have thin parallel stripes as shown in Figure 6.11a. Figure 6.11b shows the SAED pattern from the stripy region highlighted in the yellow circle and the diffraction pattern was indexed to be along the [110] zone axis in cubic structure. The streaking through the $\{111\}_c$ spots in Figure 6.11b is characteristic of SFs on the $\{111\}_c$ plane and is perpendicular to the plane of the SFs in Figure 6.11a.[175] Figures 6.11c-j show the BF-TEM images of $FAPbI_3$ perovskite film with 10, 20, 30 and 40 mol% MACl additives and the corresponding SAED patterns from specific grains highlighted in yellow circles. For $FAPbI_3$ perovskite film with MACl additive, the NTs can be clearly identified as thin parallel stripes which are a few nanometres thick as shown in Figures 6.11a, c, e, g, i. In Figures 6.11b, d, f, h, j the corresponding diffraction patterns can be indexed with a $[110]_c$ orientation and also show a

twinning configuration on the $\{111\}_c$ plane of cubic structure. In the diffraction pattern, streaks can be observed as a result of the shape adjustment of the reciprocal lattice points due to either the shape of the crystal defects or the related lattice strain. The existence of streaks is already in reciprocal space perpendicular to the specimen surface. [256] The streaking in SAED patterns is perpendicular to the SF and TBs observed in the crystal grains in the BF-TEM images (Figure 6.11). There are different densities of NTs inside each grain for samples with different MACl concentrations as can be seen in Figure 6.11. Moreover, the change in contrast between different twin domains is clearly visible as the TBs are viewed edge-on in Figures 6.11 a, c, e, g, i. The density of NTs on one grain is increased with increasing MACl concentration.

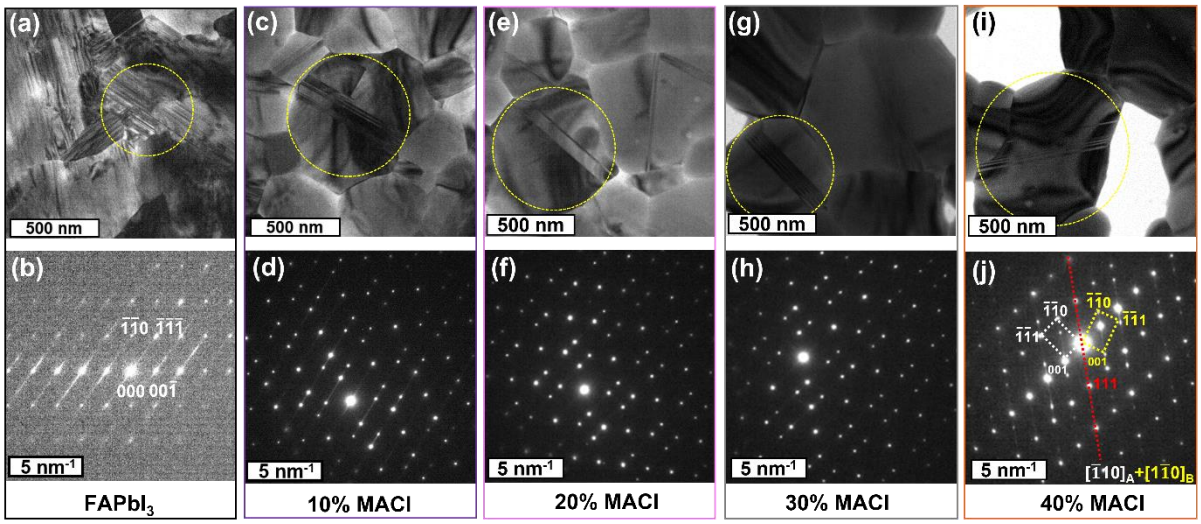

Figure 6.11. BF-TEM images and [110] oriented-SAED patterns taken from grain highlighted in yellow circles of (a, b) pure $FAPbI_3$ and $FAPbI_3$ films with (c, d) 10% MACl, (e, f) 20% MACl, (g, h) 30% MACl, (i, j) 40% MACl.

6.3.6 Photovoltaic cell performance

To systematically study the influence of MACl additive and defect density on PV performance, PSC devices were fabricated using pure $FAPbI_3$ as well as $FAPbI_3$ with various MACl concentrations as the active layer. Figures 6.12a-e show the cross-sectional SEM images of the PSC devices with active layer thicknesses ranging from 550 to 700 nm. The structure of the as-fabricated PSC devices is comprised of glass substrate/ITO/ETL (cp-TiO_2, ms-TiO_2)/pure $FAPbI_3$ perovskite or the $FAPbI_3$ perovskite with different MACl concentrations layer/HTL (Spiro-MeOTAD)/back contact (Au). From cross-section SEM images, we can clearly see that

the perovskite layer has twin defects not only on the surface but also in the bulk as highlighted in yellow circles shown in Figures 6.12a-e.

The efficiency of solar cell devices prepared with pure $FAPbI_3$ was lower than that of the perovskite film with MACl additive as shown in Figure 6.12f and Table 6.2. Notably, by adding 10 mol% MACl, the device efficiency is slightly increased to 15.39%. The highest efficiency was observed with 20 mol% of MACl, with a PCE of 15.46%, a V_{OC} of 1.002 V, a J_{SC} of 24.92 $mAcm^{-2}$, and a FF of 0.619. Nevertheless, with 30 and 40% MACl, the PCE was reduced. This may be due to the residual PbI_2 phase and higher defect density in the perovskite films.

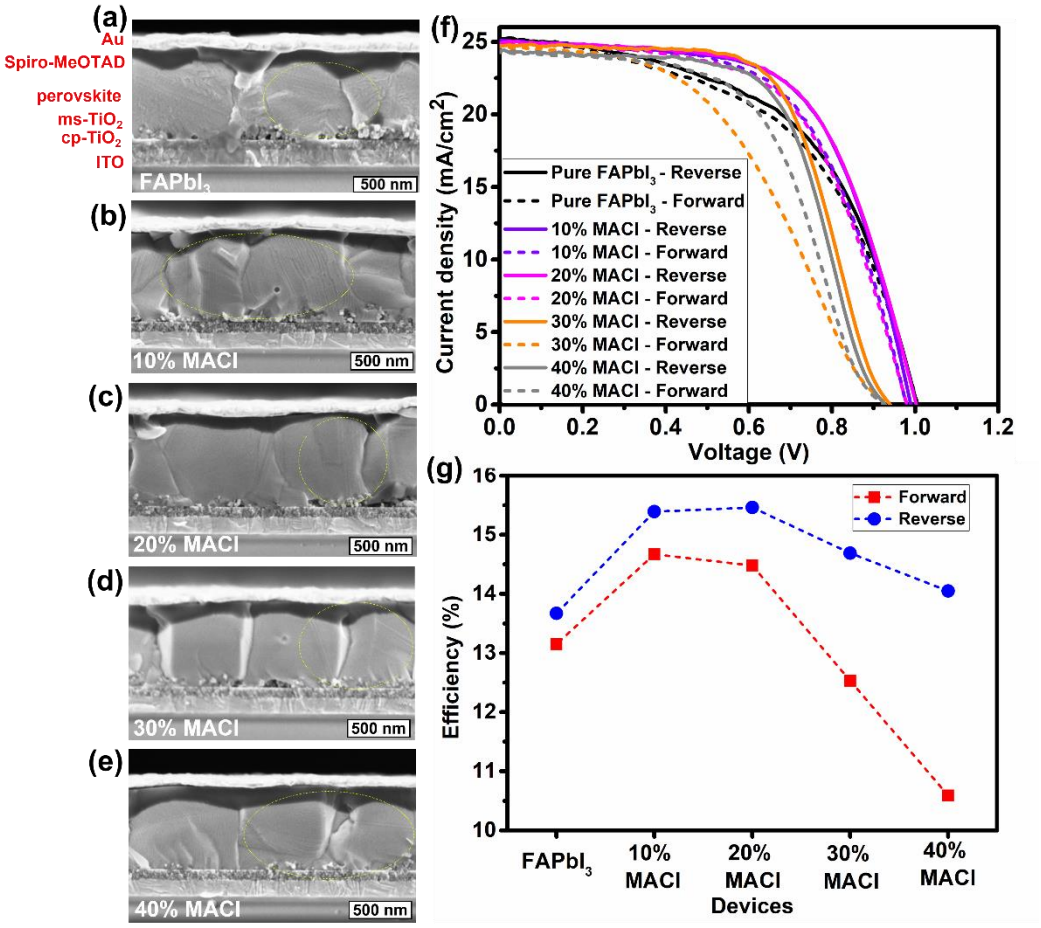

Figure 6.12. Cross-sectional SEM images of the solar cell devices with (a) pure $FAPbI_3$ perovskite film, (b) 10% MACl, (c) 20% MACl, (d) 30% MACl, and (e) 40% MACl, respectively. (f) J-V curves for the cell using pure $FAPbI_3$ and $FAPbI_3$ with different concentrations of MACl with a scan rate of 50 mV/s. (g) Comparison efficiency of pure $FAPbI_3$ and $FAPbI_3$ with different concentrations of MACl with a forward and reverse scan.

The addition of MACl changes the hysteresis of the PSC devices. The hysteresis of the perovskite film with various concentrations of MACl is shown in Figure 6.12g. The hysteresis was significantly increased with increasing concentration of MACl. For example, the 40% MACl PSC device shows the highest J-V hysteresis. These results suggest that the perovskite films with higher density of NTs and SF defects have higher hysteresis in their cell performance.

Table 6.2. Comparison of PV performance parameters (V_{OC}, J_{SC}, FF, and PCE) of various cells with different perovskite compositions in forward and reverse bias with a scan rate of 50 mV/s.

Samples	V_{OC} (V)		J_{SC} (mA/cm^2)		FF		PCE (%)	
	Reverse	Forward	Reverse	Forward	Reverse	Forward	Reverse	Forward
$FAPbI_3$	1.004	1.005	25.21	25.19	0.54	0.519	13.67	13.15
10% MACl	0.989	0.978	25.09	24.9	0.62	0.602	15.39	14.67
20% MACl	1.002	0.979	24.92	24.85	0.619	0.595	15.46	14.48
30% MACl	0.939	0.923	24,78	24.28	0.631	0.595	14.69	12.53
40% MACl	0.927	0.933	24.47	24.68	0.619	0.46	14.05	10.59

6.4 Impact of CsCl on microstructure and crystal structure of FA-based perovskite

6.4.1 Surface morphology and general microstructure of perovskite films

Figures 6.13a-d show the surface SEM images of pure $FAPbI_3$ and the perovskite films with 5 mol%, 10 mol% and 15 mol% CsCl in the precursor solution (denoted as 5% CsCl, 10% CsCl, and 15% CsCl, respectively). While the 5 and 15% CsCl films have an average grain size of about 540 and 900 nm, respectively, the 10% CsCl film has the largest average grain size of about 930 nm. The relationship between the average crystal grain size (extracted from SEM

images using the ImageJ software) and the CsCl molar proportion is illustrated in Figure 6.13i. These results demonstrate that the average grain size of the perovskite film is increased with increasing CsCl concentration. However, cracking was observed in the perovskite film with 15% CsCl as shown in Figure 6.14. Moreover, NT domains and SFs can be clearly seen on many grains from their stripe contrast (circled in yellow).

Figures 6.13e-h show the low magnification BF-TEM images of the perovskite films deposited on the amorphous carbon film of TEM Cu/Au grids for pure $FAPbI_3$ and with 5, 10, 15% CsCl. The morphology and microstructure of perovskite films are consistent with the SEM results. The perovskite films exhibit a parallel striped contrast on many grains and a drastic variation in twin density can be observed by varying the CsCl concentration. Detailed TEM analysis shows that the parallel stripes are twin domains which are separated by a $\{111\}_c$ TB. In all samples, the individual twin domains are between 5 and 54 nm thick and will be referred to as the $\{111\}_c$ NTs. Notably, in heavily twinned perovskite layers, all grains have twins and the variation in twin density is best captured by quantifying the number of NTs per grain. We note that the number of NTs on one grain is reduced with increasing CsCl concentration. In fact, NT formation is significantly suppressed in the 15% CsCl perovskite film and the number of NTs is so low that only a fraction of the grains has few twins (<2 NTs per grain). For these high quality perovskite layers, the trend in twin density is best illustrated by the number of twinned grains per unit area. The TB highlighted in Figures 6.13d, h separates adjacent twin domains which have different image contrast in TEM imaging. Interestingly, angles of 70.5 and 109.5º can be seen between adjacent $\{111\}_c$ TBs within a single grain as shown in Figures 6.13e-f.

The individual NT domains show a periodicity consistent with that observed in the SEM images. Hence, we may conclude that NT domains are visible in both TEM and SEM images. For tetragonal $MAPbI_3$, the domain orientations are identified by the angle between adjacent domain walls.[153, 257, 258] Angles of 70.5 and 109.5º are characteristic of (110) tetragonal TBs and at 0, 90, or 45º in principal planes of the parental phase, respectively. For a cubic crystal structure, the {111} twin domain boundaries are shown to intersect at 70.5º.[259] Figures 6.13e, f indicate that one set of NT domains can sometimes intersect with another set of NT domains at 70.5 and 109.5º angles. These angles are expected between adjacent {111} cubic planes when viewed edge-on. As will be shown, the SFs and TBs are typically on the {111} cubic planes.

The density of twin defects was estimated by counting the number of twinned grains per area of 49 μm^2 from the SEM images and a graph of the density of twin defects with different additive concentrations is shown in Figure 6.13j. The results clearly show that perovskite films with CsCl additive have fewer twinned grains compared to films with MACl additive. In addition, the twinned grain is significantly reduced with the CsCl additive. The film with 10 mol% CsCl had the best crystal quality with 7 twinned grains/49 μm^2.

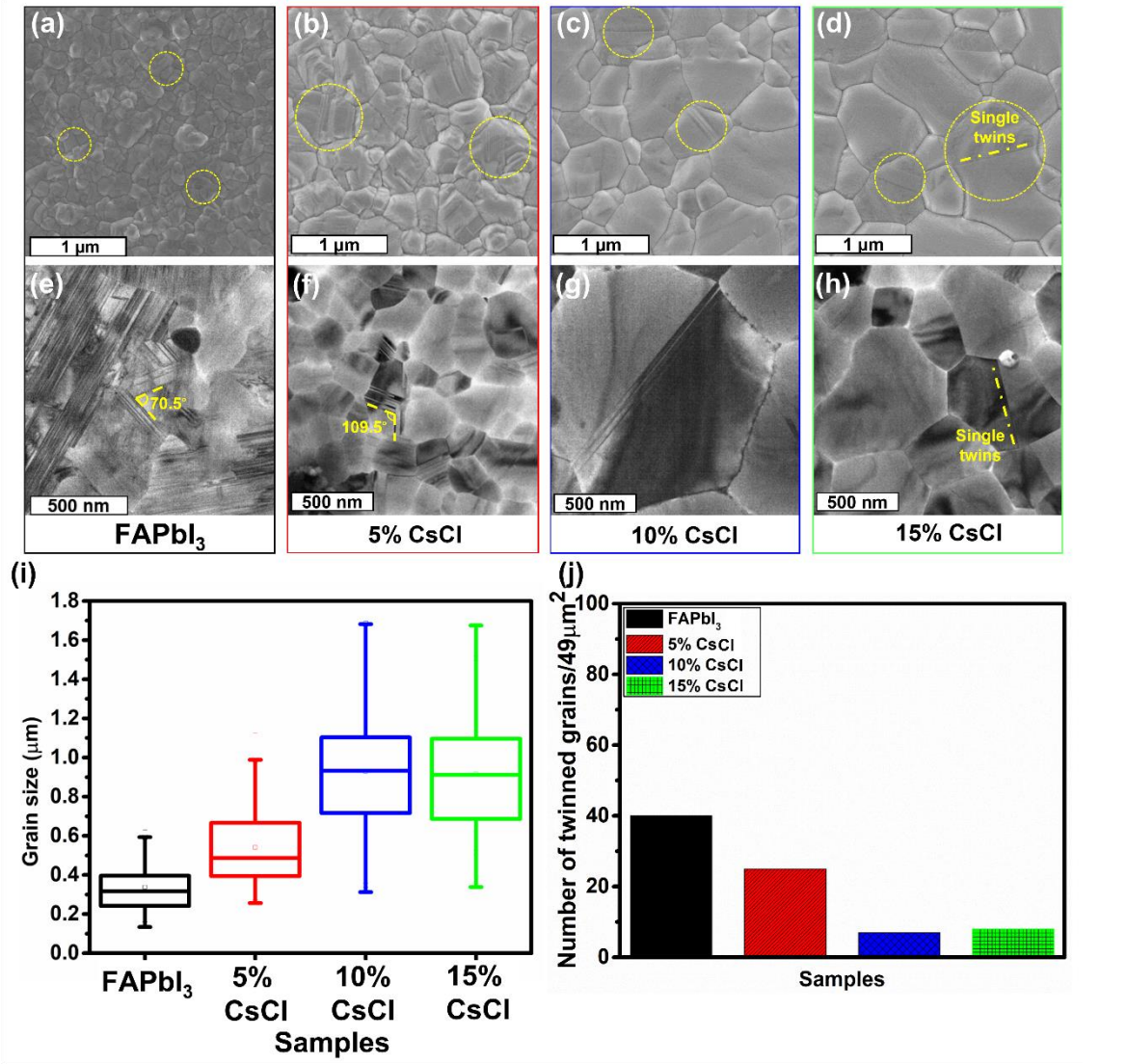

Figure 6.13. Top-view SEM images of perovskite films with different amounts of CsCl (a) pure-$FAPbI_3$, (b) 5% CsCl, (c) 10% CsCl, (d) 15% CsCl. BF-TEM images of perovskite films with different amounts of CsCl (e) $FAPbI_3$, (f) 5% CsCl, (g) 10% CsCl, (h) 15% CsCl. (i) Plot showing the variation of the grain size distribution of the perovskite films with different CsCl concentrations. (j) Plot of the number of twinned grains per area as a function of the CsCl concentration.

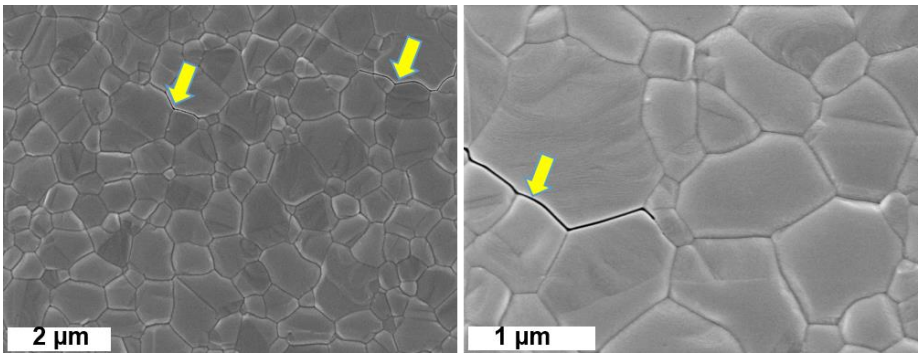

Figure 6.14. Top-view SEM images of $FAPbI_3$ perovskite film with 15 mol% of CsCl addition.

6.4.2 Crystal structure and surface chemistry of perovskite films

The XRD patterns of pure $FAPbI_3$ and $FAPbI_3$ perovskite film with various concentrations of CsCl are shown in Figure 6.15. We note that in Figure 6.15a, the prominent diffraction peaks observed at 2θ values of 13.9, 19.6, 24.1, 28, 31.5, 34.5, 40, and 42.4º are common to the three structures discussed and are indexed as the (002), (022), (222), (004), (042, (224), (044), and (244) planes of the $Im\bar{3}$ structure, respectively. However, the addition of different CsCl concentrations to the perovskite layers results in two progressive changes in the XRD patterns. Firstly, with increasing concentration of CsCl in the perovskite, we observe an increasing intensity in the additional peaks at 2θ values of 22.3, 26.5, 41.8 and 44.4º which cannot be assigned to the $Pm\bar{3}m$ structure.[103] They can be assigned to the (013), (123), (053) and (235) planes for the $Im\bar{3}$ structure respectively. Or alternatively they correspond to the $(\bar{1}32)$, $(13\bar{2})$, $(2\bar{5}4)$ and $(\bar{1}35)$ planes for the $R\bar{3}$ structure. Further evidence of the $Im\bar{3}$ phase will be shown in detail in the TEM results later.

Secondly, the peak position for the (002) plane shifts slightly to a higher 2θ angle with increasing CsCl concentration (Figure 6.15b). Figure 6.15c shows the variation of the (002) lattice constant with different concentrations of CsCl. The lattice constant decreases with increasing CsCl amount and this demonstrates the successful mixing of Cs^+ cations and Cl- anions within the perovskite crystal structure. This is consistent with the expected lattice contraction when the small Cs cations replace FA cations.[245] The sample with 5 mol% CsCl shows a higher peak intensity at 2θ = 31.5º compared to the peak 2θ = 13.9º. In contrast, the peak intensity at 2θ = 13.9º is higher than that at 31.5º for the perovskite film with 10 and 15 mol% CsCl. We note that the XRD peak corresponding to the δ-$FAPbI_3$ phase at 2θ = 11.6º is not observed in the samples with CsCl addition. This suggests that the formation of the

hexagonal δ-$FAPbI_3$ phase is completely suppressed with a small amount of CsCl added into the precursor solution. This may be due to the partial replacement of FA-sites by Cs, leading to the stabilization of the cubic $FAPbI_3$ phase.

Figure 6.15d shows that the FWHM for the (002) peak is decreased when the concentration of CsCl increase, indicating an increased X-ray crystallite size. The smallest FWHM value is obtained for the 10% CsCl perovskite film, indicating larger grain size in this sample.

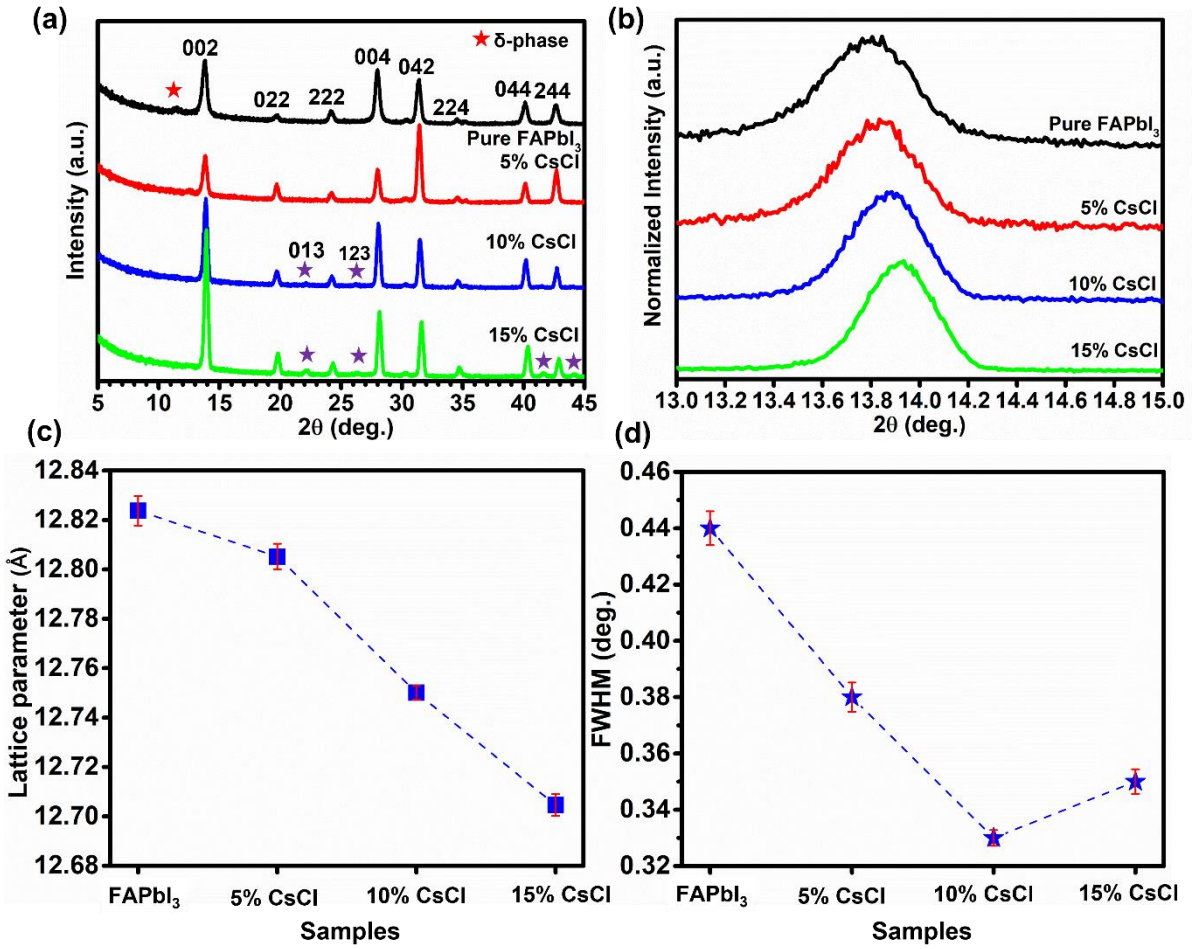

Figure 6.15. (a) Experimental XRD patterns of $FAPbI_3$ perovskite films in pure form and with different concentrations of CsCl (5, 10, 15 mol%) additives. (b) XRD plots showing the shift in the (002) perovskite peak to higher diffraction angles. (c) Extracted lattice parameter and (d) FWHM of the (002) peak of the perovskite film with different CsCl concentrations.

The XPS measurements were used to obtain the surface chemistry of the $FAPbI_3$ film with different CsCl concentrations. Figure 6.16a shows the high-resolution XPS spectra of C

1s of perovskite films with different concentrations of CsCl addition. There is no energy shift in the peaks for the C 1s species in all samples, which is consistent with a homogenous surface chemistry of as-fabricated perovskite films and is consistent with no sample charging during analysis. Figure 6.16c illustrates the relative concentration of Cl and Cs on perovskite films calculated from XPS spectra. No Cl or Cs is detected in the pure $FAPbI_3$ perovskite film, while the relative Cs concentration has no trend with the actual increasing concentration of CsCl. This may suggest that the surface is saturated with Cs^+ cation incorporation even at a low concentration (5 mol%) of CsCl. Furthermore, the XPS data shows that Cl^- is incorporated in the $FAPbI_3$ perovskite film but shows no correlation with the actual concentration of CsCl.

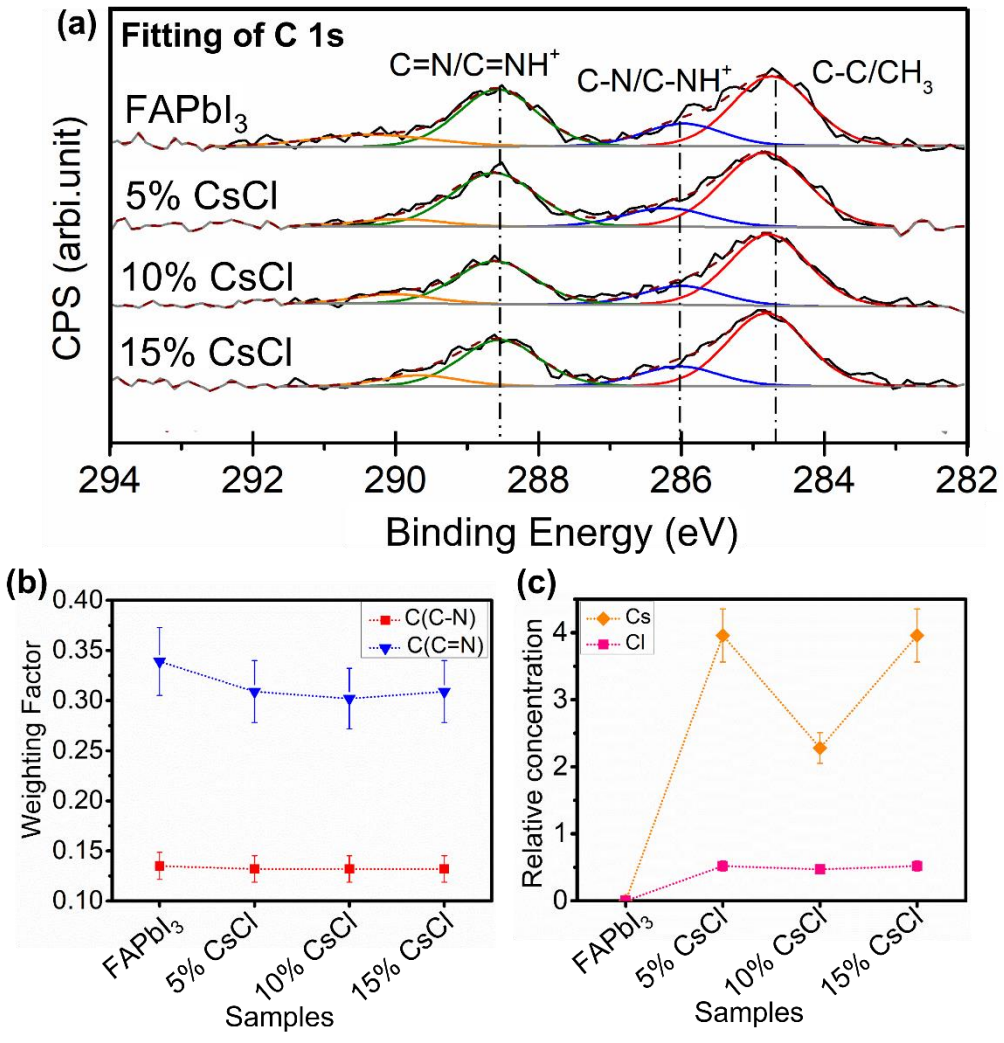

Figure 6.16. (a) Simulations for fitting the high-resolution XPS spectra of C 1s of perovskite films with different concentrations of CsCl addition. (b) Weighting factor of the C(C-N) and C(C=N) peaks measured from perovskite films with different amounts of CsCl. (c) Relative

concentration of Cs and Cl on perovskite film with different concentrations of CsCl calculated from surface XPS measurement.

6.4.3 Optical properties of perovskite films

The steady-state PL spectra of $FAPbI_3$ perovskite films with and without CsCl additive are shown in Figures 6.17a-b. The PL emission peak position exhibits a blueshift with increasing concentration of CsCl additive which is attributed to the contraction of the perovskite lattice, a result of the incorporation of Cl anions and Cs cations in the perovskite lattice. Pure $FAPbI_3$ perovskite film has a PL peak position at 800 nm whereas the perovskite films with 5, 10 and 15% CsCl have the PL peak position at 796, 794, and 790 nm, respectively. The observed blueshift is consistent with previous studies on $Cs_xFA_{1-x}PbI_3$ compositions.[188, 245, 260] In addition, the PL intensity is significantly increased with the CsCl additive.

From the SEM and TEM results, the $FAPbI_3$ perovskite film with 10% CsCl has the highest crystal quality with the largest grain size, fewer NT and SF defects. Consequently, this results in a lower rate of recombination events at defects and explains the high PL intensity observed in the 10% CsCl sample. Figure 6.17c shows the absorbance spectra of perovskite films with different amounts of CsCl. Consistent with the PL spectra, a blueshift in the optical bandgap can be observed with increasing CsCl concentration. The pure $FAPbI_3$ perovskite has an estimated optical bandgap of 1.47 eV whereas the perovskite film with 15% CsCl has the largest optical bandgap (1.53 eV).

TRPL analyses were carried out on perovskite films with various CsCl concentrations deposited on glass substrate and are illustrated in Figure 6.17d and Table 6.3. As shown, the TRPL spectrum shows a bi-exponential decay and two different PL lifetimes τ_1 and τ_2 can be extracted from the plots. The pure-$FAPbI_3$ film has lifetimes of τ_1 (3.5 ns) and τ_2 (0.9 ns) and the longest lifetimes were extracted for the 10% CsCl sample with τ_1 (69.8 ns) and τ_2 (11.2 ns). The improvement in the PL lifetime observed for this sample is consistent with the highest PL intensity observed for the 10% CsCl sample as shown in Figure 6.17a.

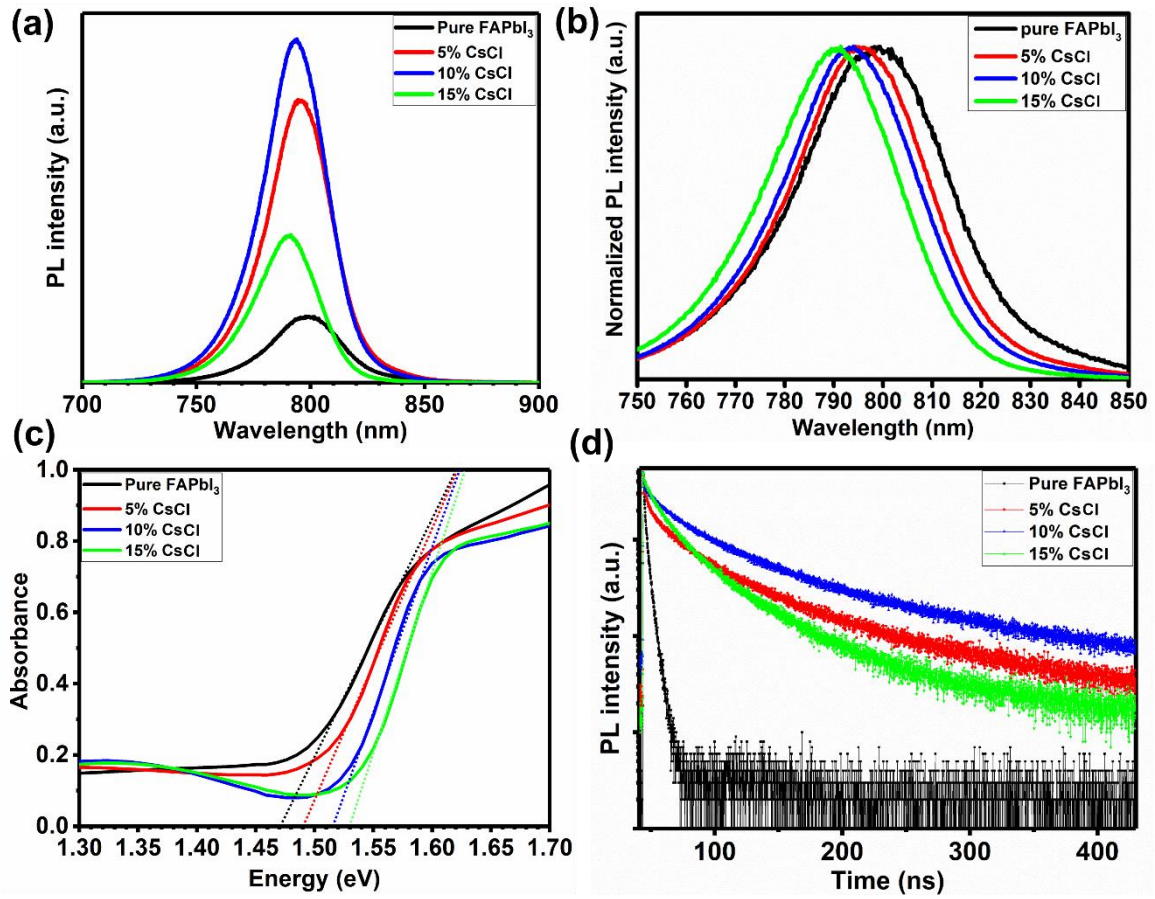

Figure 6.17. (a) The steady-state PL spectra, (b) normalized PL spectra, (c) optical absorbance spectra, and (d) TRPL of the $FAPbI_3$ perovskite in its pure form and with different amounts of CsCl.

Table 6.3. TRPL parameters of perovskite prepared with pure $FAPbI_3$, 5% CsCl, 10% CsCl, 15% CsCl.

No additive		**5% CsCl**		**10% CsCl**		**15% CsCl**	
τ_1 (ns)	τ_2 (ns)	τ_1(ns)	τ_2 (ns)	τ_1 (ns)	τ_2 (ns)	τ_1 (ns)	τ_2 (ns)
3.5	0.9	48.1	3	69.8	11.2	41.7	10

6.4.4 Effect of CsCl on the crystal structure of perovskite films

In order to understand the effect of CsCl on the microstructure of the perovskite films, TEM analyses were carried out on the perovskite layers with different CsCl content. Figure 6.18 gives

an overview of the TEM studies on the perovskite layer with 10% CsCl along three different orientations. Figure 6.18b is the experimental SAED pattern from the region highlighted in the yellow circle in Figure 6.18a and is indexed as the [211] cubic zone axis. The reflections circled in red are forbidden for the cubic $Pm\bar{3}m$ (a = 6.3506 Å) structure but can be indexed with the $Im\bar{3}$ space group as superlattice reflections as labelled in Figure 6.18b. The structural ordering within the lattice effectively doubles the unit-cell parameter ($2a$ = 12.244 Å) with the $Im\bar{3}$ space group and explains the additional superlattice reflections. The experimental SAED pattern (Figure 6.18b) is in agreement with the simulated electron diffraction pattern (Figure 6.18c) for this cubic supercell perovskite with the atomic arrangement shown in Figure 6.18d. Similarly, in the experimental SAED indexed as the [001] zone axis in Figure 6.18f, the extra reflections (highlighted with red circles) are indexed as $\left\{\frac{1}{2}\frac{1}{2}0\right\}$ with a $Pm\bar{3}m$ space group and are hence forbidden reflections. However, these reflections are indexed as $\{110\}$ with the $Im\bar{3}$ space group and hence allowed. The $\{110\}$ reflections are also visible in the experimental diffraction pattern along the [111] zone axis (see Figure 6.18j). All the diffraction patterns show the superlattice reflections along the $\langle 110\rangle$ directions at half of the reciprocal space lattice parameter and are evidence for the $Im\bar{3}$ structure ($2a$ = 12.244 Å).

The SAED patterns along various zone axes shown in Figure 6.18 confirm that the $FAPbI_3$ perovskite with 10 mol% CsCl has a cubic supercell structure with a double lattice parameter ($Im\bar{3}$, $2a$), similar to the previous report on FA-based lead perovskite bulk crystals.[103, 261] The tilting of $[PbI_6]^{4-}$ octahedra results in an expanded ($2 \times 2 \times 2$) supercell with a lattice constant of 12.244 Å. Because of the structural flexibility of a lattice of corner-sharing octahedra, ionic perovskites normally can go through distortions comprised of octahedral tilting and off-centering of the A- and B-site cations. For the $FAPbI_3$ crystal under pressure in a diamond anvil cell, Zhu *et al.* proposed that the supercell cubic structure ($Im\bar{3}$) has drastic $[PbI_6]^{4-}$ octahedral tilt thus bending the Pb-I-Pb bond angle to less than 180º.[103] From both their Tauc plot analysis and DFT calculations, they show a smaller bandgap narrowing with pressure for the $Im\bar{3}$ phase compared to the $Pm\bar{3}m$ phase.[103]

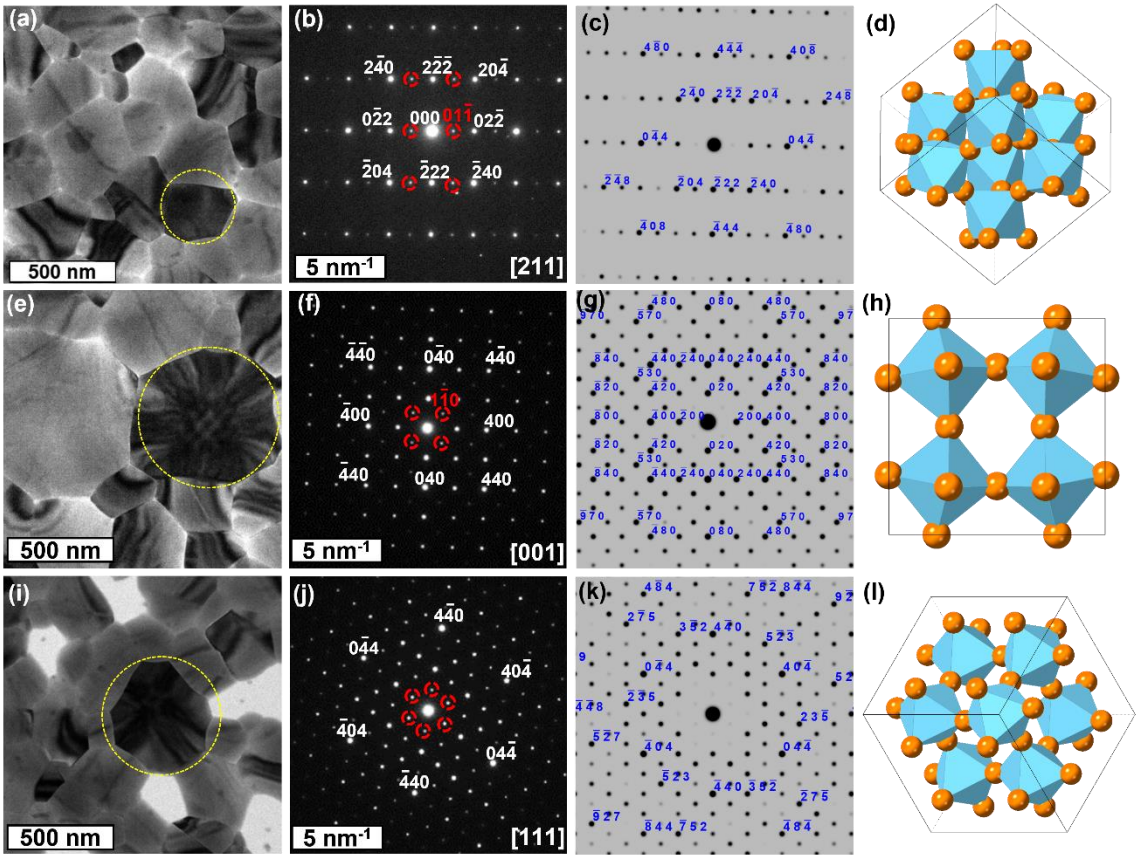

Figure 6.18. BF-TEM images of $FAPbI_3$ with 10% CsCl, corresponding SAED patterns taken from the grain highlighted in yellow circle in the BF-TEM images indexed with the $Im\bar{3}$ crystal structure, simulation of the SAED patterns and corresponding atomic structure models for three different zone axes namely (a-d) [211], (e-h) [001], and (i-l) [111].

6.4.5 Morphology, crystallographic of NTs and SFs of perovskite films

Figure 6.19 shows the BF-TEM images and corresponding SAED patterns of pure $FAPbI_3$ perovskite and $FAPbI_3$ with 5, 10 and 15 mol% CsCl additives. We observed that the number of NTs and SFs inside a single grain decreases with increasing concentration of CsCl as shown in Figures 6.19a, c, e, g. The twins can be recognized by a change in contrast across the TB. Isolated TBs can be seen in Figure 6.19g. The corresponding SAED pattern of this region is shown in Figure 6.19h and the individual twin components are highlighted with a white and a yellow rectangle. The as-mentioned twin spots contributed by both A and B have the unsplit row of reflections, including the common plane shared between two sub-crystals and the coincident reflection reflects the twin direction.[136] The TBs are also a specific kind of SF, in which the octahedra become face-sharing rather than corner-sharing as shown in Figure 6.20.

These TBs are also effectively a unit cell of the 2H structure i.e. unit cell thick layer of δ-phase. Four individual bands can be seen in the region in Figure 6.19e and each individual band is a NT. Furthermore, the grains separated by only one isolated TB are also seen in Figure 6.19g. On the other extreme, when there is a high density of TBs and SFs, the individual twin segments or polytype segments are nanometers thick and form a miniband.[123] These twinning or polytypic superlattices modify the electronic structure and the optical properties of the material with interband and intraband optical transitions. In addition, SFs act as recombination sites in dislocation-free silicon, and edge dislocations reduce the PL intensity in multi-crystalline silicon.[126, 127]

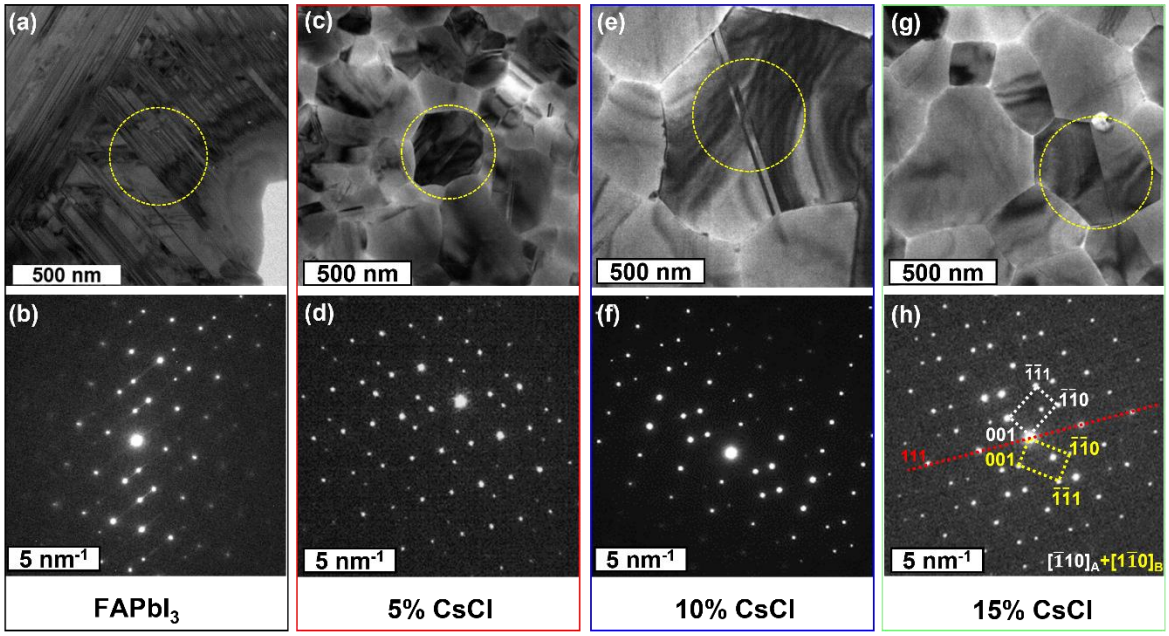

Figure 6.19. BF-TEM images and corresponding $[110]_c$ oriented-SAED pattern taken from grain highlighted in yellow circle for (a, b) pure-$FAPbI_3$ film, $FAPbI_3$ perovskite with (c, d) 5% CsCl, (e, f) 10% CsCl, (g, h) 15% CsCl.

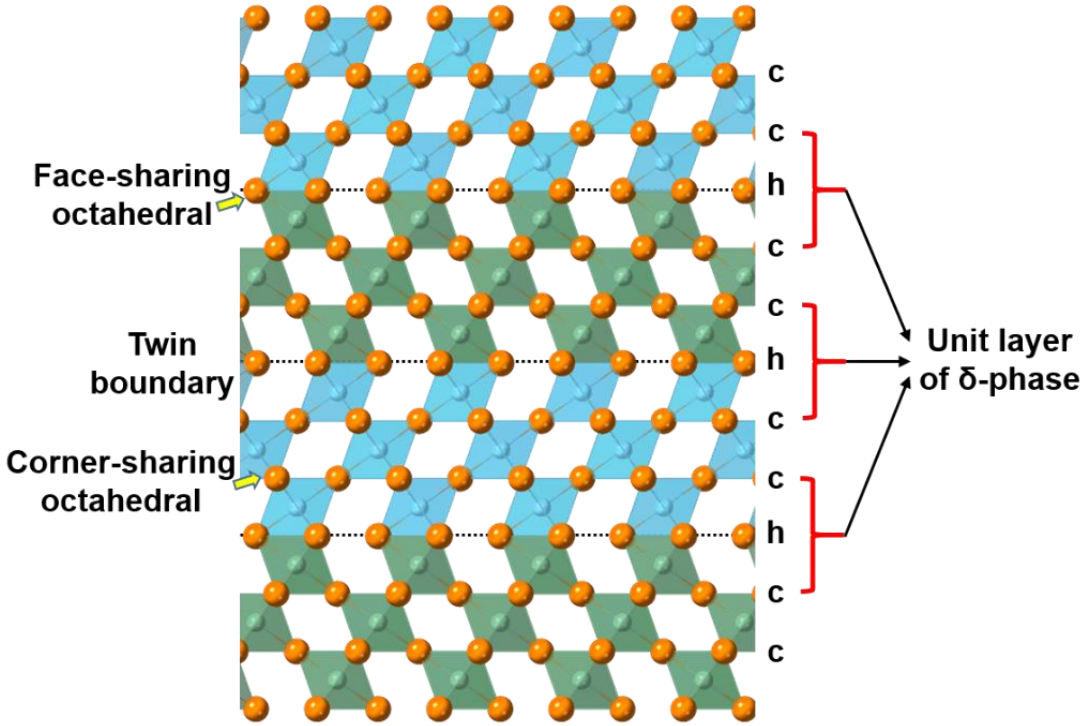

Figure 6.20. Atomic structure of NTs. Note TBs are unit layer of δ-phase (2H).

6.4.6 Photovoltaic cell performance

PSC devices were fabricated using pure $FAPbI_3$ or $FAPbI_3$ with different CsCl concentrations as the active layer. Figures 6.21a-d show the cross-sectional SEM images of the PSC devices with active layer thicknesses ranging from 550 to 700 nm. The structure of the as-fabricated PSC devices is comprised of glass substrate/ITO/cp-TiO_2/ms-TiO_2/pure $FAPbI_3$ perovskite or the $FAPbI_3$ perovskite with different CsCl concentrations layer/Spiro-MeOTAD/Au. From cross-section SEM images, we can clearly see that the perovskite layer has twin defects not only on the surface but also in the bulk as highlighted in yellow circles shown in Figures 6.21a-d.

Figure 6.21e shows the J-V curves for both reverse and forward biasing scans of the PSCs with different perovskite compositions. The estimated values of all collected PV parameters are indicated in Table 6.4. The pure $FAPbI_3$ film based solar cell device exhibits a PCE of 13.63% with a V_{OC} of 1.004 V, a J_{SC} of 25.21 $mAcm^{-2}$, and a FF of 0.54 for the reverse scan. The addition of CsCl to $FAPbI_3$ perovskite improves the overall device performance for all investigated concentrations. By adding 5 mol% CsCl to the perovskite film, the device efficiency dramatically increased to 20.79%. However, the perovskite film with 10 mol% CsCl

is found to have the optimum PV performance, with a maximum PCE of 21.98%. In detail, these devices demonstrate excellent improvement in all individual electrical parameters namely a V_{OC} of 1.112 V, J_{SC} of 24.93 $mAcm^{-2}$ and FF of 0.793. Some possible factors leading to the enhancement of device performance are the increased value of the V_{OC} and FF due to improved optical properties, improved film morphology (such as enlarged grain size) and a reduction in the defect density in the film. However, the PCE is reduced when the amount of CsCl added is further increased to 15 mol%. This is attributed to cracking in the perovskite film, resulting in more surface recombination at the cracked surface. Ye *et al.* has demonstrated that the film cracking is responsible for lowering the PSCs device performance.[262]

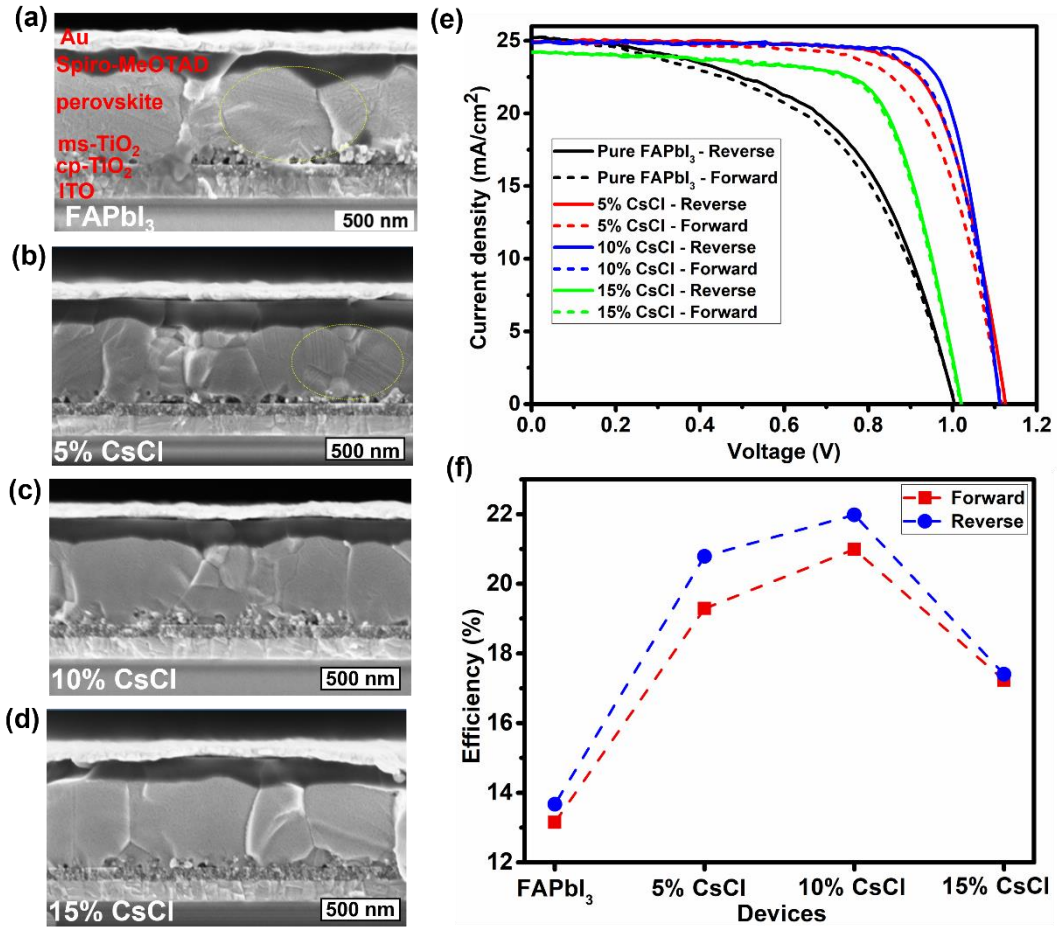

Figure 6.21. Cross-sectional SEM images of the solar cell devices with (a) pure $FAPbI_3$ perovskite film, (b) 5% CsCl, (c) 10% CsCl, (d) 15% CsCl, respectively. (e) J-V curves for the cell using pure $FAPbI_3$ and $FAPbI_3$ with different concentrations of CsCl with a scan rate of 50 mV/s. (f) The PCE and hysteresis of PSCs from perovskite films with different concentrations of CsCl additive. The forward scan PCEs are illustrated by the red squares, the reverse scan PCEs are illustrated by the blue circles.

Table 6.4. Comparison of PV performance parameters (V_{OC}, J_{SC}, FF, and PCE) of various cells with different perovskite compositions in forward and reverse bias with a scan rate of 50 mV/s.

Samples	V_{OC} (V)		J_{SC} (mA/cm^2)		FF		PCE (%)	
	Reverse	Forward	Reverse	Forward	Reverse	Forward	Reverse	Forward
$FAPbI_3$	1.004	1.005	25.21	25.19	0.54	0.519	13.67	13.15
5% CsCl	1.125	1.115	24.94	24.92	0.741	0.694	20.79	19.29
10% CsCl	1.112	1.113	24.93	24.96	0.793	0.755	21.98	20.99
15% CsCl	1.02	1.018	24.21	24.18	0.705	0.699	17.4	17.23

In summary, the cell efficiencies of $FAPbI_3$ perovskite were significantly improved with CsCl addition, but only slightly enhanced with the MACl addition (Figures 6.12 and 6.21, and Tables 6.1 and 6.2). Therefore, it can be concluded that both the incorporation of Cl^- anion and Cs^+ cation have a positive impact on the performance of PSCs. In detail, the V_{OC} and FF were significantly improved when adding CsCl additive into the perovskite solution. The V_{OC} of pure $FAPbI_3$ cell was 1.004 V, but higher values were obtained with 5% CsCl (1.125 V), 10% CsCl (1.131 V), or 15% CsCl (1.02 V). In contrast, the V_{OC} slightly decreased when MACl was added into the perovskite solution. For instance, the V_{OC} of pure $FAPbI_3$ cell was 1.004 V, but lower values were obtained for the 10% MACl (0.989 V), 20% MACl (1.002 V), 30% MACl (0.939 V) or 40% MACl (0.927 V). The V_{OC} is governed by the recombination rate in the perovskite film. Larger grain size, pinhole-free morphology, better crystallinity, fewer defects, and higher PL intensities are the reasons for the improved device performance. For instance, the addition of 10 mol% CsCl resulted in a highly crystalline lattice structure, the lowest defect density, highest intensity of PL peak and longest PL lifetime, which is a major contributor to higher V_{OC} values. The improved device performance is in agreement with the SEM, XRD, absorbance, and PL measurements as discussed above.

6.5 Summary

In this systematic study, we have characterised the effect of MACl and CsCl additives on the structural, morphological and defects of $FAPbI_3$ perovskite film. Electron diffraction analyses of pure $FAPbI_3$ showed that the cubic α-phase is unstable and transforms into a mixture of different phases including the hexagonal δ-phase and an additional unreported phase that is best simulated with a rhombohedral $R\bar{3}$ space group. We demonstrate that the MACl and CsCl additions have a great potential to stabilize the cubic $FAPbI_3$ with a 2 × 2 × 2 supercell expansion and the $Im\bar{3}$ space group. We also systematically studied the morphology and crystal structure of NTs and SF defects of various perovskite compositions. The defect density depends on the concentration of additives added to the perovskite precursor solution. A higher density of defects in the perovskite film resulted in reduced PL intensity and lifetime, leading to poorer cell performance. The MACl additive increased the density of defects in the perovskite film compared to the CsCl additive. The perovskite film with 10 mol% CsCl indicates the lowest defect density.

Interestingly, the incorporation of MACl and CsCl into $FAPbI_3$ changes the lattice parameter and optical properties with the incorporation of Cs^+/MA^+ cations and Cl^- anion. Moreover, higher quality perovskite films were obtained with well-defined grain structure, improved crystallinity, and larger grain size, resulting in a longer carrier lifetime compared to pure $FAPbI_3$ film. The addition of CsCl to the perovskite precursor solution results in a higher PL intensity and a longer lifetime compared to the sample with added MACl. The optimized PSC with 10 mol% CsCl shows the best device performance with low hysteresis and the highest PCE of 21.98%, which is much higher than the PSC with 20 mol% MACl with 15.46% PCE. Our results show that the CsCl additive is a promising candidate for stabilizing the cubic phase and suppressing the undesirable hexagonal δ-phase, paving the way for practical applications of PSCs in the near future.

Chapter 7. Impact of Halide Anions in CsX (X = I, Br, Cl) on the Microstructure and Photovoltaic Performance of $FAPbI_3$ Perovskite Solar Cells

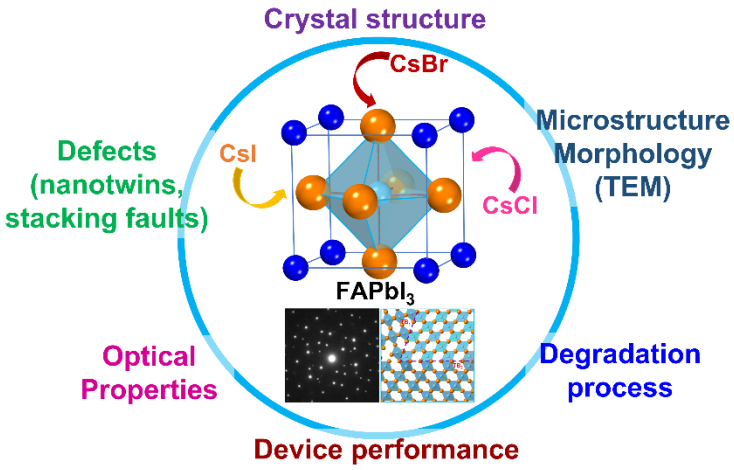

This chapter investigates the key role of Cs cation and X halide anions (X = I, Br, Cl) on the microstructure, crystal structure, structural defects, optoelectronic properties and PV parameters of $FAPbI_3$-based PSCs. The CsCl-$FAPbI_3$ perovskite film shows the highest PL intensity, longest PL lifetime and highest PCE compared to the films compared with the CsI-$FAPbI_3$ and CsBr-$FAPbI_3$ perovskite films. The morphology and crystallography of $\{111\}_c$ NTs and SFs are studied using TEM and SAED. The microstructure, crystallography and atomic structure model of intersecting twin boundaries are presented. Finally, the degradation pathways and the mechanism behind the formation of $FAPbI_3$-based perovskites under ambient conditions are systematically studied. The grain boundaries of the perovskite films are nonuniformly damaged, resulting in many black nanoparticles after 4 weeks. Electron diffraction analyses of the black nanoparticles confirm the hexagonal PbI_2 phase formation in all CsX-$FAPbI_3$ perovskite samples after 4 weeks of ageing.

7.1 Introduction

In the past decade, PSCs have received significant attention thanks to their inexpensive solution processing, outstanding optoelectronic properties (such as high absorption coefficient), adjustable direct bandgaps,[253] low recombination rate [3] and high charge-carrier

mobility.[263] Since 2013, $FAPbI_3$ is one of the leading candidates among OIMHP materials, and has been revealed to be a promising semiconductor for highly efficient and stable PSC devices.[239, 244, 264] Consequently, enormous research efforts have been trying to maximize its performance and long-term stability. Recently, Jeong *et al*. have employed a new chemical modification method that significantly improves the performance of $FAPbI_3$ PSCs using formamidine formate (FAHCOO). They obtained a PSC device with PCE up to 25.6% (certified 25.5%) and operational stability of more than 450 hours.[57]

Efforts to strengthen the long-term operational stability of $FAPbI_3$ PSCs have focused on optimising each of the functional layers and their interfaces, namely the passivation layer, electron transport layer (ETL), hole transport layer (HTL), and the perovskite absorber layer. Recently, various additives have been added to the $FAPbI_3$ perovskite precursor solution to enhance long-term stability.[237, 244, 265] For instance, Min *et al*. used methylenediammonium dichloride ($MDACl_2$) to stabilize the α-$FAPbI_3$ phase and achieved a certified PCE of 23.7% with a long-term stable operation for more than 600 hours.[237] Another study concentrated on optimizing the Spiro-mF of Spiro-OMeTAD as HTL and achieved a PCE of 24.82% (certified 24.64%) with long-term stability for up to 500 hours in humid conditions.[239] Liu *et al*. used interface stabilization strategies to modify the interface between all the relevant layers, and improved the PSC device stability to over 2000 hours in full sunlight.[266] However, the exact mechanism for the improvement in device performance for these PSCs remains unclear.

The composition of the perovskite layer is a determining factor for their stability. In fact, several cations (such as MA^+, Cs^+, Rb^+), anions (Br^-, I^-, thiocyanate (SCN^-), formate ($HCOO^-$)) or a combination of both have been incorporated into the $FAPbI_3$ perovskite precursor solution to enhance the crystallinity and long-term stability.[57, 85, 244, 245, 267-270] Currently, the effect of cations and anions on the microstructure and crystallinity of perovskite films has yet to be elaborated. The alloying of MA or Rb in $FAPbI_3$ results in various problems including phase segregation due to the presence of mixed halide with Rb; the low thermal stability associated with the addition of MA; and the photo-instability due to phase segregation and iodide migration.[85, 271] To solve these issues, one approach is to combine $FAPbI_3$ with Cs^+ cation and Br^- anion; however, the resulting PCE is still low compared to the perovskite films obtained with the FA_xMA_{1-x} double cation.[272] Nevertheless, Cs_xFA_{1-x}

mixed-cation perovskites were found to be thermally more stable than MA_xFA_{1-x} compositions.[265]

Phase segregation under ambient conditions is one of the biggest issues in the OIMHP solar cells. There are no reported solution to prevent the degradation of OIMHP material. In addition, there is limited information about the initial process of degradation and the subsequent catastrophic and irreversible damage on PSCs. The degradation mechanisms of OIMHP materials are extremely complicated and differ for different compositions. For instance, in the case of $MAPbI_3$ perovskite films, the degradation process is initiated by the desorption of I ions, followed by the decomposition of the perovskite material into the hexagonal PbI_2 phase.[273-277] In the case of $FAPbI_3$, the degradation starts first with the transformation of the black photoactive cubic α-$FAPbI_3$ perovskite phase into the yellow photoinactive hexagonal δ-$FAPbI_3$ phase, which then decomposes into PbI_2 under ambient conditions.[278] However, the transformed crystal structure of FA-based perovskites during the degradation process has not been investigated. The degradation usually starts at grain boundaries and interfaces.[182] Especially, grain boundaries of OIMHP film are very sensitive to external factors and usually become the initial spots for the formation of lattice instabilities and defects.

Herein we explore the role of the Cs cation and X anions (X = I, Br, and Cl) on the microstructure, crystal structure, structural defects, optoelectronic properties and PV parameters of $FAPbI_3$-based-PSCs. Among the additives tested, the CsCl-$FAPbI_3$ perovskite film showed the highest PL intensity, longest PL lifetime and highest PCE compared to the CsI-$FAPbI_3$ and CsBr-$FAPbI_3$ films. The PCE of the PSC device dramatically improved from 15.01% to 21.70% for the device using CsCl-$FAPbI_3$ perovskite as an absorber layer, whereas a moderate increase in PCE to 21.09% and 19.89% is observed for CsI-$FAPbI_3$ and CsBr-$FAPbI_3$ films, respectively. The morphology and crystallography of $\{111\}_c$ NTs and SFs are systematically studied using TEM and SAED. The number of twinned grains per area is dramatically reduced for CsCl-$FAPbI_3$ and CsBr-$FAPbI_3$ perovskite films. The microstructure, crystallography and atomic structure model of intersecting $\{111\}_c$ TBs are presented. Finally, we study the pathways and underlying mechanism of the degradation for pure $FAPbI_3$ and CsX-$FAPbI_3$ perovskite films under ambient conditions.

7.2 Surface morphology and general microstructure of perovskite films

To examine the influence of Cs cation and X anions (X = I, Br, Cl) on the morphology, microstructure, crystal structure, optoelectronic properties, and PV parameters of FA-based PSCs, we prepared four different perovskite compositions namely pure $FAPbI_3$, 10 mol% CsI in the $FAPbI_3$ precursor solution with excess PbI_2, 10 mol% CsBr in the $FAPbI_3$ precursor solution with excess $PbBr_2$, and 10 mol% CsCl in the $FAPbI_3$ precursor solution (denoted as pure $FAPbI_3$, CsI-$FAPbI_3$, CsBr-$FAPbI_3$, and CsCl-$FAPbI_3$, respectively).

Figure 7.1 shows the impact of CsX (X = I, Br, Cl) additives on the morphology and microstructure of $FAPbI_3$ perovskite films. Compared to the pure $FAPbI_3$ film with an average grain size of 338 nm (Figure 7.1a), the CsI-$FAPbI_3$ and CsBr-$FAPbI_3$ perovskite films (Figures 7.1b-c) had a larger average grain size of 490 nm and 598 nm, respectively. The average grain size of CsCl-$FAPbI_3$ perovskite film dramatically increased to 900 nm. The boxplot in Figure 7.1e shows the grain size distribution (extracted from top-view SEM images using the ImageJ software) obtained from pure-$FAPbI_3$ and CsX-$FAPbI_3$ perovskite films.

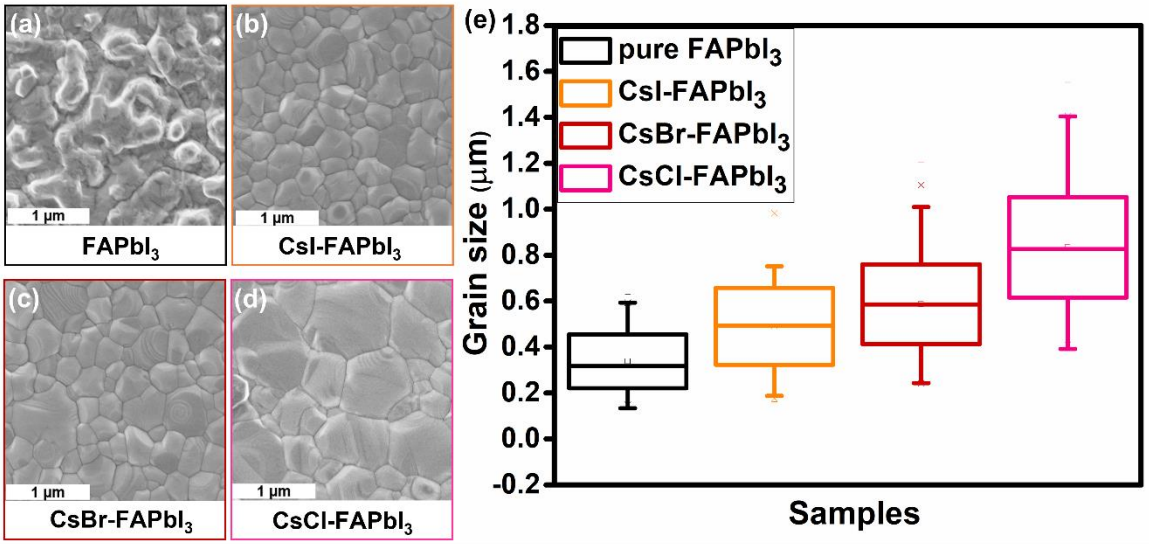

Figure 7.1. Top-view SEM images of perovskite films with different additives (a) pure-$FAPbI_3$, (b) CsI-$FAPbI_3$, (c) CsBr-$FAPbI_3$, and (d) CsCl-$FAPbI_3$. (e) Boxplot showing the grain size distribution for pure-$FAPbI_3$, CsI-$FAPbI_3$, CsBr-$FAPbI_3$, and CsCl-$FAPbI_3$ perovskite films.

To get a comprehensive understanding of the impact of the Cs cation and X anions on the crystallographic structure of $FAPbI_3$ perovskite films, we carried out XRD measurements. Figure 7.2 illustrates the XRD patterns of pure $FAPbI_3$ and CsX-$FAPbI_3$ perovskite films at

room temperature. The pure-$FAPbI_3$ perovskite film shows a small diffraction peak at 11.6º which is assigned to the yellow hexagonal δ-phase (highlighted by the red star symbol). Interestingly, the formation of the δ-phase is eliminated in CsX-$FAPbI_3$ films. We observed a small peak for the PbI_2 phase located at 2θ = 12.5º (highlighted by the pink star symbol) in CsI-$FAPbI_3$ perovskite film.

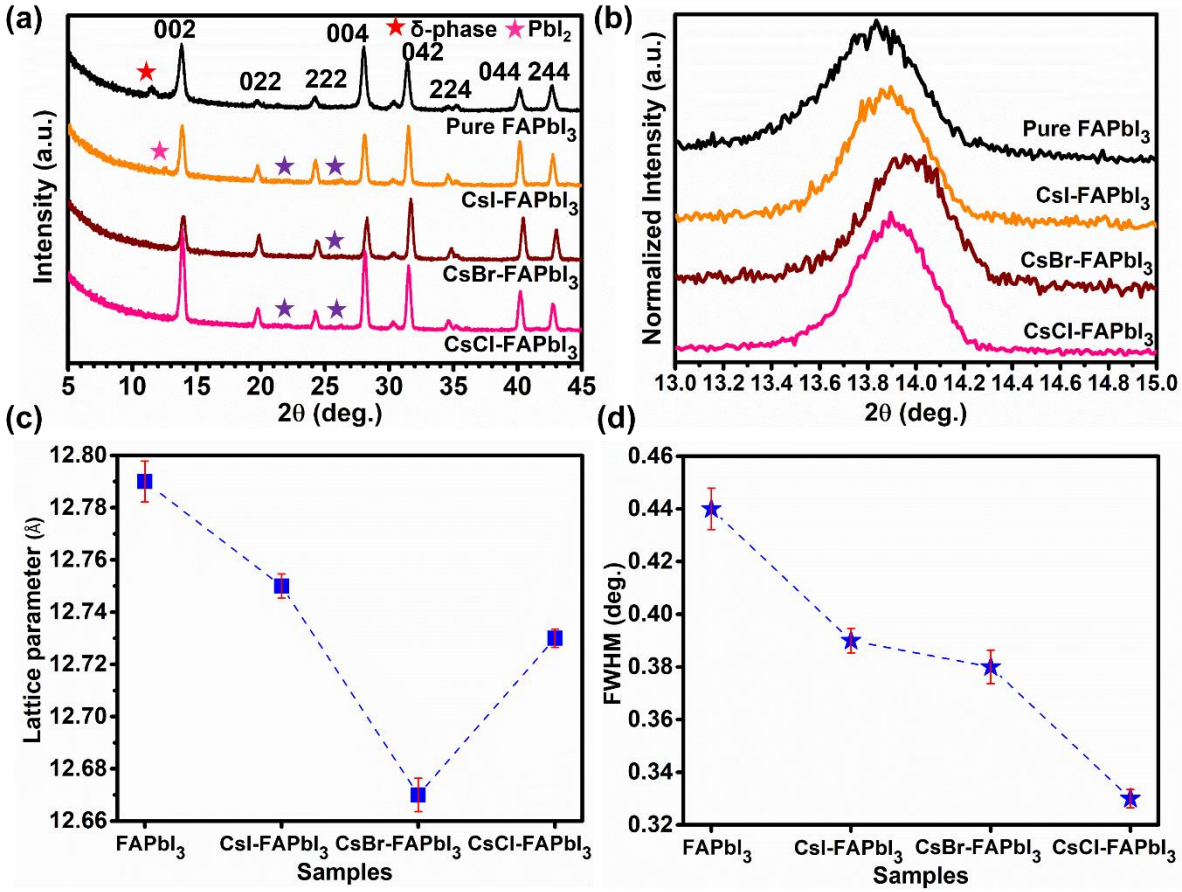

Figure 7.2. (a) X-ray diffraction patterns of perovskite film with different additives. (b) XRD plots showing the shift in the (002) perovskite peak to higher diffraction angles. (c) Extracted lattice parameter full and (d) FWHM of the (002) peak of the perovskite film with different additives.

All the XRD diffraction peaks were indexed with the cubic super structure $Im\bar{3}$ space group. The additional peaks at 2θ values of 22.3º and 26.5º correspond to the (013) and (123) planes for the $Im\bar{3}$ structure, respectively. Further evidence of the $Im\bar{3}$ phase will be demonstrated in detail in the TEM results later. The (002) peak position shifts slightly to a higher 2θ angle for CsI-$FAPbI_3$ and CsCl-$FAPbI_3$ perovskite films. However, the most

prominent shift is observed in the CsBr-$FAPbI_3$ sample (Figure 7.2b). The lattice constant can be extracted from the (002) peak of the XRD patterns and are plotted in Figure 7.2c for pure $FAPbI_3$ and the CsX-$FAPbI_3$ perovskite films. Compared to pure $FAPbI_3$ with a lattice constant of 12.79 Å, the lattice constant is slightly reduced to 12.75 Å and 12.73 Å for CsI-$FAPbI_3$ and CsCl-$FAPbI_3$ perovskite films, respectively. The CsBr-$FAPbI_3$ perovskite film has the smallest lattice constant of 12.67 Å. These results demonstrate the successful incorporation of the Cs^+ cation and I^-, Br^-, Cl^- anions in the perovskite crystal structure.

Figure 7.2d also plots the FWHM for the (002) XRD peak for the different layers and clearly indicates a narrower peak for layers with an additive into the $FAPbI_3$ perovskite precursor solution. This improved crystallinity is in agreement with the increased grain size observed in SEM. Compared to the pure $FAPbI_3$ (FWHM of 0.44º), the FWHM of CsI-$FAPbI_3$ and CsBr-$FAPbI_3$ perovskite films is slightly reduced to 0.39º and 0.38º. The narrowest peak is obtained for the CsCl-$FAPbI_3$ perovskite film with a FWHM of 0.33º.

The surface morphology and microstructure of the perovskite films with various additives were further investigated by TEM. Figure 7.3 shows the low magnification BF-TEM images taken from different regions of pure $FAPbI_3$ and CsX-$FAPbI_3$ perovskite films (spin-coated straight on the TEM Cu/Au grids). The morphology and microstructure of perovskite films are consistent with the SEM and XRD results. In all samples, many grains exhibit parallel striped patterns. These striped patterns are a combination of crystallographic NT domains and SFs. The difference in crystal orientation between the NT domains often leads to differences in contrast in the bright-field TEM images. The pure $FAPbI_3$ perovskite film has a high density of nanoscale twin lamellae and SFs. The CsX-$FAPbI_3$ perovskite films also show many grains with a parallel stripe contrast characteristic of NTs. However, a drastic variation in twin density can be observed by varying the halide anions. The TBs observed are on the $\{111\}_c$ plane with the subscript "c" representing the index in the cubic α-phase structure. The TB orientation can be a critical factor governing the deformation behaviour of NTs in perovskite materials. The TBs are also a specific kind of SF, in which the octahedra become face-sharing rather than corner-sharing as discussed in section 7.3. These TBs are also effectively a unit cell of the 2H structure i.e. unit cell thick layer of δ-phase. The number of NTs and SFs on one grain is significantly reduced when adding CsX additives into the $FAPbI_3$ perovskite precursor solution. It is noted that the TBs intersect at an angle of 70.5°, characteristic of $\{111\}_c$ planes viewed

edge on as shown on the Figures 7.3b-c. The crystal structure of these NTs will be discussed later.

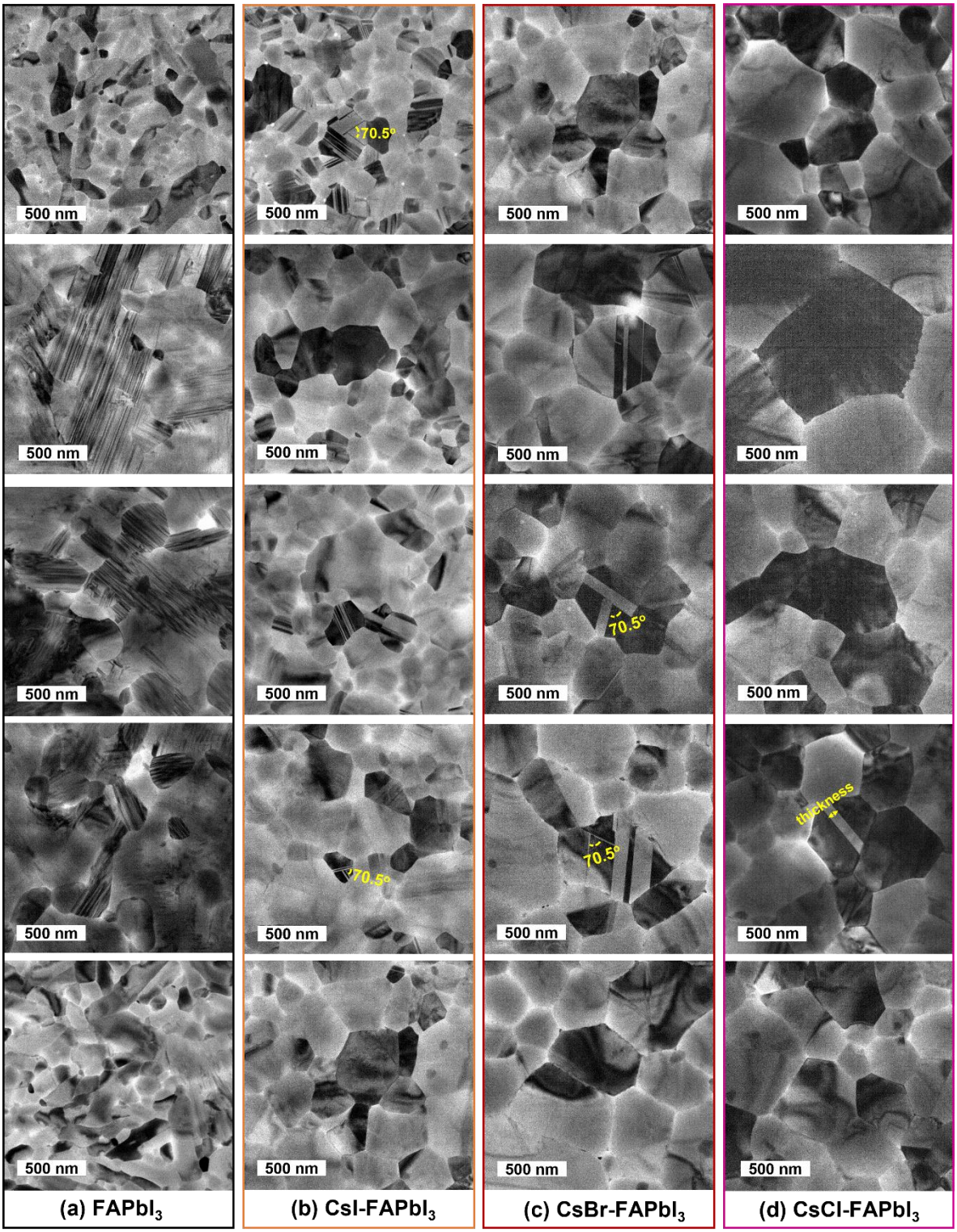

Figure 7.3. BF-TEM images of perovskite films taken from various regions with different additives (a) pure-$FAPbI_3$, (b) CsI-$FAPbI_3$, (c) CsBr-$FAPbI_3$, (d) CsCl-$FAPbI_3$.

The density of NTs was obtained by totalling the number of twinned grains per area of 14 μm^2 using various BF-TEM images in Figure 7.3a. The pure $FAPbI_3$ perovskite film has the highest density of defects (16 twinned grains/14μm^2) as shown in Figure 7.4a. The number of twinned grains slightly decreased to 10 twinned grains/14μm^2 for the CsI-$FAPbI_3$ perovskite film and was significantly reduced for CsBr-$FAPbI_3$ and CsCl-$FAPbI_3$ perovskite films. The CsCl-$FAPbI_3$ perovskite film has the lowest density of defects with only 2 twinned grains per 14 μm^2.

The thickness of NTs was obtained by measuring the distance between two TBs as highlighted in Figure 7.3c. Figure 7.4b illustrates the thickness of NTs for pure $FAPbI_3$ perovskite and CsX-$FAPbI_3$ perovskite films. The NTs in pure $FAPbI_3$ have an average thickness of 15 nm, while the NTs in CsI-$FAPbI_3$, CsCl-$FAPbI_3$ perovskite films are slightly thicker, 19 nm and 21 nm thick, respectively. In the CsBr-$FAPbI_3$ film, the NTs have the largest thickness with an average of 44 nm.

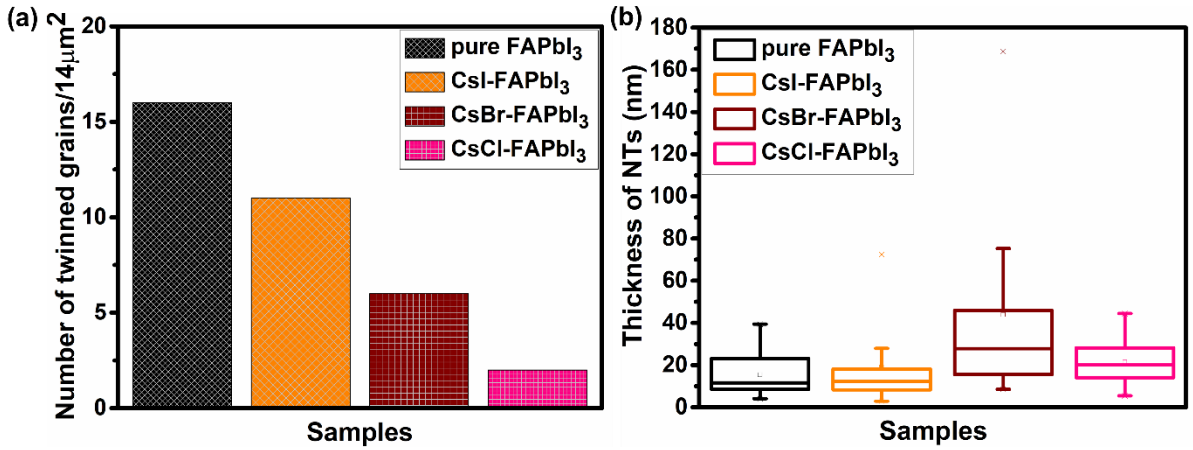

Figure 7.4. (a) Plot of the number of twinned grains per area of various perovskite films including pure $FAPbI_3$, CsI-$FAPbI_3$, CsBr-$FAPbI_3$, CsI-$FAPbI_3$. (b) Boxplot showing the distribution in the twin domain thickness for different perovskite films including pure $FAPbI_3$, CsI-$FAPbI_3$, CsBr-$FAPbI_3$, CsI-$FAPbI_3$.

The impact of the Cs cation and X anions on the microstructure and crystal structure of the $FAPbI_3$ perovskite films was further studied using TEM and SAED analysis. Figure 7.5 shows the BF-TEM images and SAED patterns of the CsX-$FAPbI_3$ perovskite films along three different orientations: [001], [111], and [211]. The superlattice reflections highlighted in red circles are forbidden for the cubic α-phase with the $Pm\bar{3}m$ space group (a = 6.3506 Å). These

diffraction patterns could not be assigned to a cubic α-phase but can be indexed to a cubic superstructure with the $Im\bar{3}$ space group as superlattice reflections. The structural ordering within the lattice and octahedral tilting effectively doubles the unit-cell parameter ($2a$ = 12.79 Å) with the $Im\bar{3}$ space group and explains the additional superlattice reflections. These forbidden reflections were also observed in perovskite films with triple-cation compositions such as $Cs_{0.05}FA_{0.78}MA_{0.17}PbI_3$.[279] Doherty *et al.* reported that these superstructure reflections originate from the octahedral tilting whereby the BX_6 corner-sharing octahedra tilt away from perfect cubic symmetry.[279] Furthermore, the unit-cell parameter with the $Im\bar{3}$ space group is effectively doubled with the structural ordering within the lattice, resulting in the additional superlattice reflections. The experimental SAED pattern (Figure 7.5) is in agreement with the simulated electron diffraction pattern (Figure 6.10, Chapter 6) for this cubic supercell perovskite.

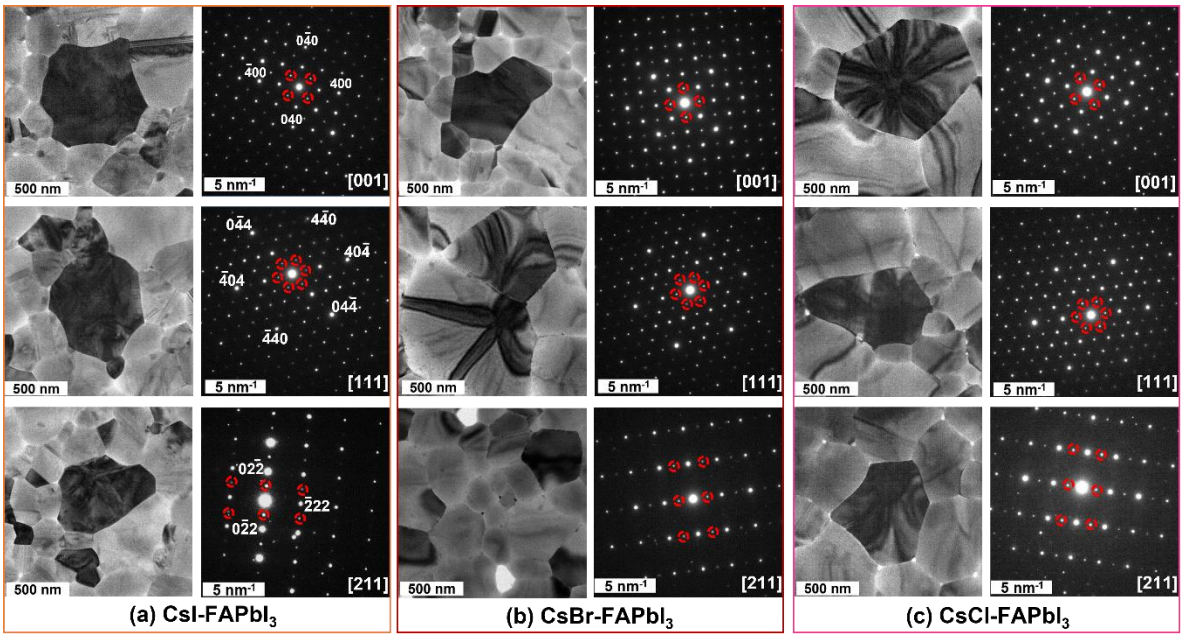

Figure 7.5. BF-TEM images and corresponding SAED patterns taken from the grain highlighted in yellow circle in the BF-TEM images indexed with the $Im\bar{3}$ crystal structure for three different additives (a) CsI-$FAPbI_3$, (b) CsBr-$FAPbI_3$, and (c) CsCl-$FAPbI_3$ along three zone axes [001], [111], and [211].

7.3 Morphology, crystallography of NTs and SFs of perovskite films

In *fcc* metals and inorganic perovskite materials, the crystallography of the twin is the mirroring of the atomic arrangement across the TB plane. This symmetry can be observed most clearly along the $[110]_c$ zone axis which is the intersection of $\{111\}_c$ twinned planes. The $\{111\}_c$ planes viewed edge-on along the $[110]_c$ direction intersect at an angle of 70.5°.[108, 280] Figures 7.6a, e, j show the morphology and microstructure of $FAPbI_3$ perovskite films with CsX additives. In all the samples, $\{111\}_c$ TBs were found. The BF-TEM images indicate a single grain containing multiple $\{111\}_c$ TBs when CsX is incorporated into $FAPbI_3$ perovskite. The yellow dashed lines highlight the TBs. The CsI-$FAPbI_3$ perovskite film has a higher density of NTs and SFs in one grain compared to the CsBr-$FAPbI_3$ and CsCl-$FAPbI_3$ perovskite films. The twin orientation of the crystal domains is confirmed by SAED patterns. Figures 7.6b, f, j show the SAED patterns taken from the stripy region highlighted in the yellow colour in Figure 7.6a, e, i and the diffraction pattern was indexed to be along the $[110]_c$ zone axis. The red dashed line identifies the twin axis which is perpendicular to the $(111)_c$ plane.

The morphology and microstructure of individual twins in CsX-$FAPbI_3$ perovskite films are shown in Figures 7.6c, g, k. The individual TB can be recognized in bright-field TEM images because the two twin domains exhibit a different contrast across the TB. This difference is due to diffraction contrast from the twin domains relative to the incoming beam. In BF-TEM, highly diffracting crystals appear dark and less diffracting crystals appear bright since more electrons pass through the material, as seen in the micrograph. Diffraction patterns obtained from $\{111\}_c$ TB regions in Figures 7.6c, g, f are shown in Figures 7.6d, h, l, respectively. The atomic structure models of nanotwins with single and multiple TBs are shown in Figure 7.7.

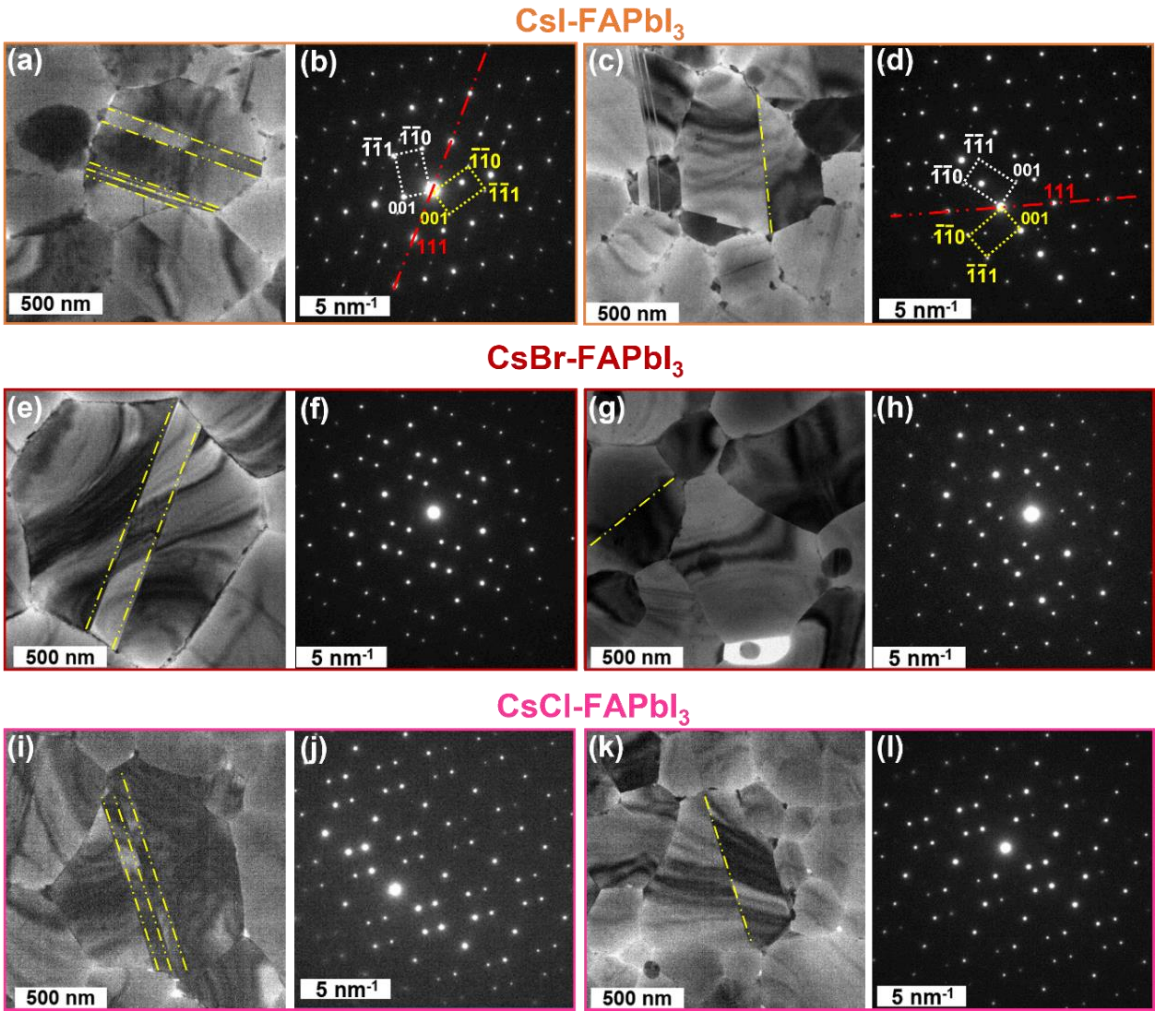

Figure 7.6. BF-TEM images and SAED patterns along $[110]_c$ orientations obtained from (a, b) multiple TBs and (c, d) single TB into one grain for CsI-$FAPbI_3$ perovskite film. BF-TEM images and SAED patterns along $[110]_c$ obtained from (e, f) multiple TBs and (g, h) single TB into one grain for CsBr-$FAPbI_3$ perovskite film. BF-TEM images and SAED patterns along $[110]_c$ obtained from (i, j) multiple TBs and (k, l) single TB into one grain for CsCl-$FAPbI_3$ perovskite film. The yellow dashed lines in BF-TEM images highlight the TB.

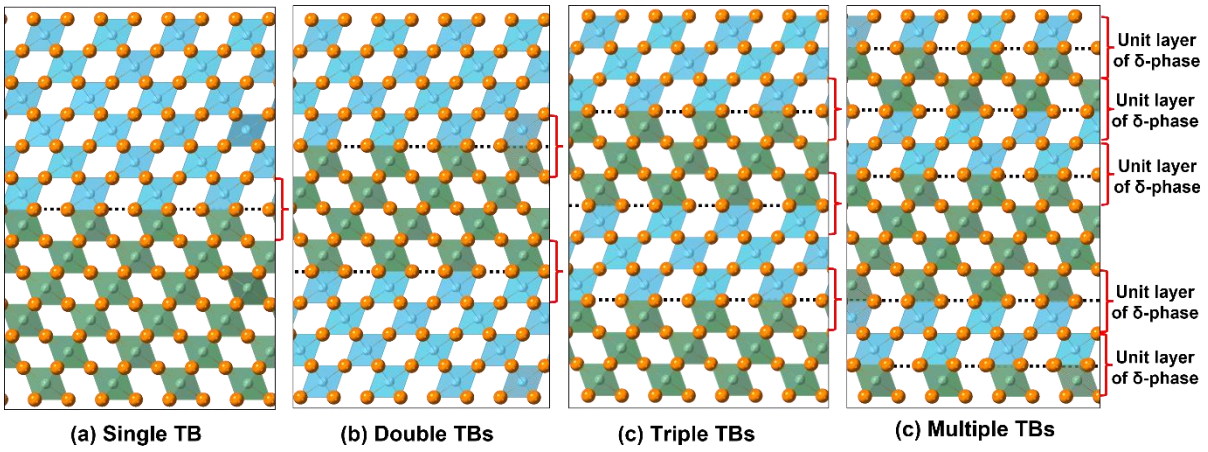

Figure 7.7. Atomic structure model of NTs with (a) single TB, (b) double TBs, (c) triple TBs, and (d) multiple TBs.

The $\{111\}_c$ TBs intersect at 70.5º as commonly observed in perovskite materials.[14-16] Figure 7.8 shows the morphology and crystallography of two $\{111\}_c$ TBs stripes intersecting at an angle of around 70.5° in the CsBr-$FAPbI_3$ perovskite film. The corresponding SAED pattern taken from the twinned grain in Figure 7.8a is shown in Figure 7.8b. We use SingleCrystal and CrystalMaker simulations to reproduce the atomic structure that best matches the diffraction pattern from the intersecting TBs. Figure 7.8c shows the atomic structure that can best simulate the experimental diffraction results. As shown, the structure has three component parts A, B, and C. Figures 7.8d, e, f show the simulated electron diffraction patterns for A, B, and C, respectively. The overlay of the simulations is illustrated in Figure 7.8g and is in excellent agreement with the experimental diffraction pattern in Figure 7.8b. These simulations clearly illustrate that the $\{111\}_c$ TB can be coherent, for example, TB_1 and TB_2 in Figure 7.8c.

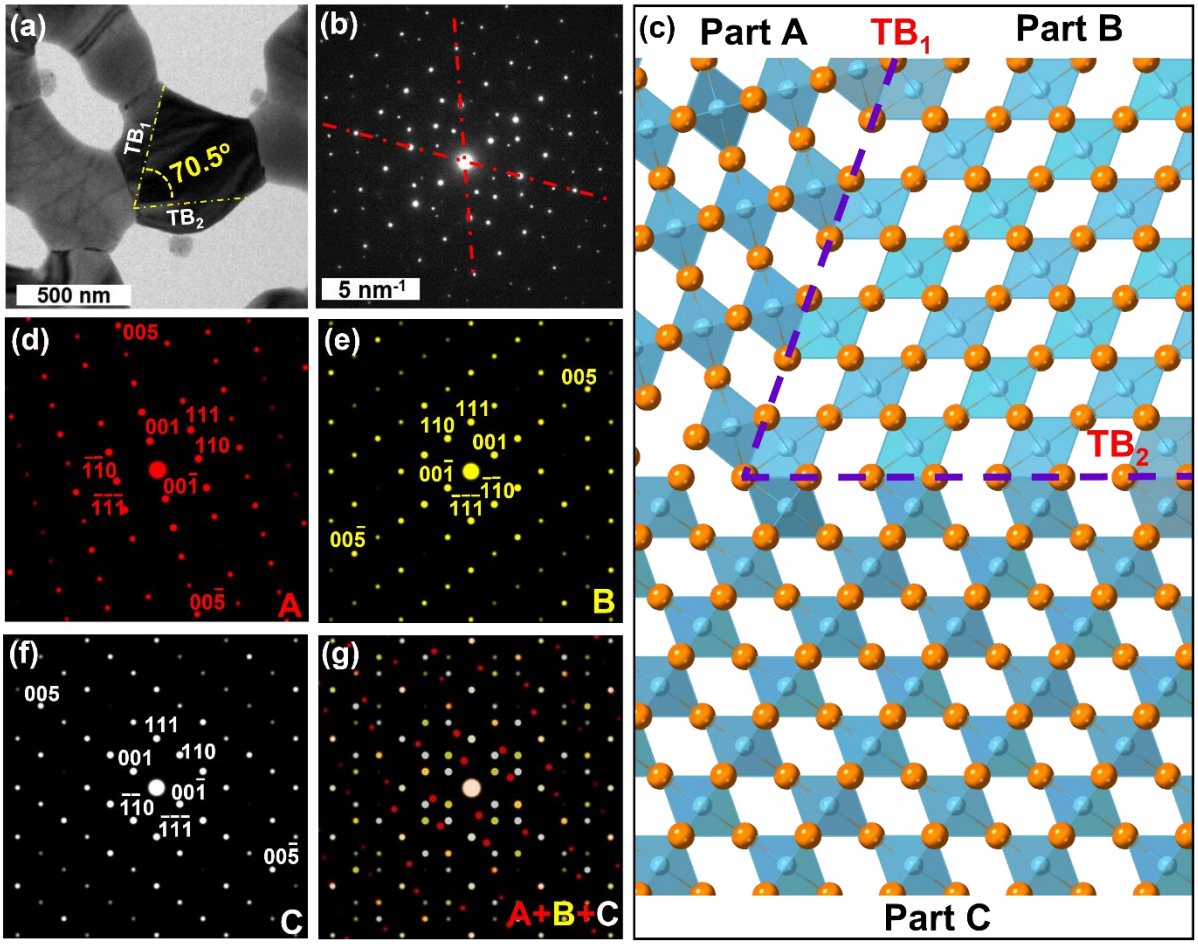

Figure 7.8. (a) BF-TEM image of two TBs intersecting at an angle of around 70.5° and (b) corresponding experimental SAED pattern taken from twinned grain in the CsBr-$FAPbI_3$ perovskite film. (c) Atomic model of two TBs intersecting at an angle of around 70.5°. Simulation of electron diffraction patterns along $[110]_c$ zone axis for the crystal (d) part A, (e) part B, (f) part C. (g) Overlapping the simulated SAED from part A, B, and C.

7.4 Optical properties and device performance

Steady-state PL measurement of $FAPbI_3$ perovskite films with CsX additives on glass substrate shows the highest PL peak intensity for the CsCl-$FAPbI_3$ film, followed by the CsBr-$FAPbI_3$ film, CsI-$FAPbI_3$ film, and pure-$FAPbI_3$, respectively (Figure 7.9a). A small blueshift in the peak PL emission wavelength was observed for the CsI-$FAPbI_3$ and CsCl-$FAPbI_3$ perovskite films compared to pure $FAPbI_3$ films. However, the CsBr-$FAPbI_3$ perovskite film results in a bigger PL blueshift (Figure 7.9b). It also confirms that Cl anion is evaporated during the annealing process and is not incorporated as efficiently as Br, as otherwise, it would have shown

an even bigger PL blueshift. These results demonstrate that the optical bandgap of CsI-$FAPbI_3$ and CsCl-$FAPbI_3$ perovskite films is slightly increased, and it is increased more significantly for the CsBr-$FAPbI_3$ perovskite film (Figure 7.9b). The trend in the variation of the optical bandgap agrees with the observed contraction in the lattice constant as discussed in the XRD results. This clearly suggests that Cs cation and I, Br, Cl anions were successfully incorporated into the perovskite lattice.

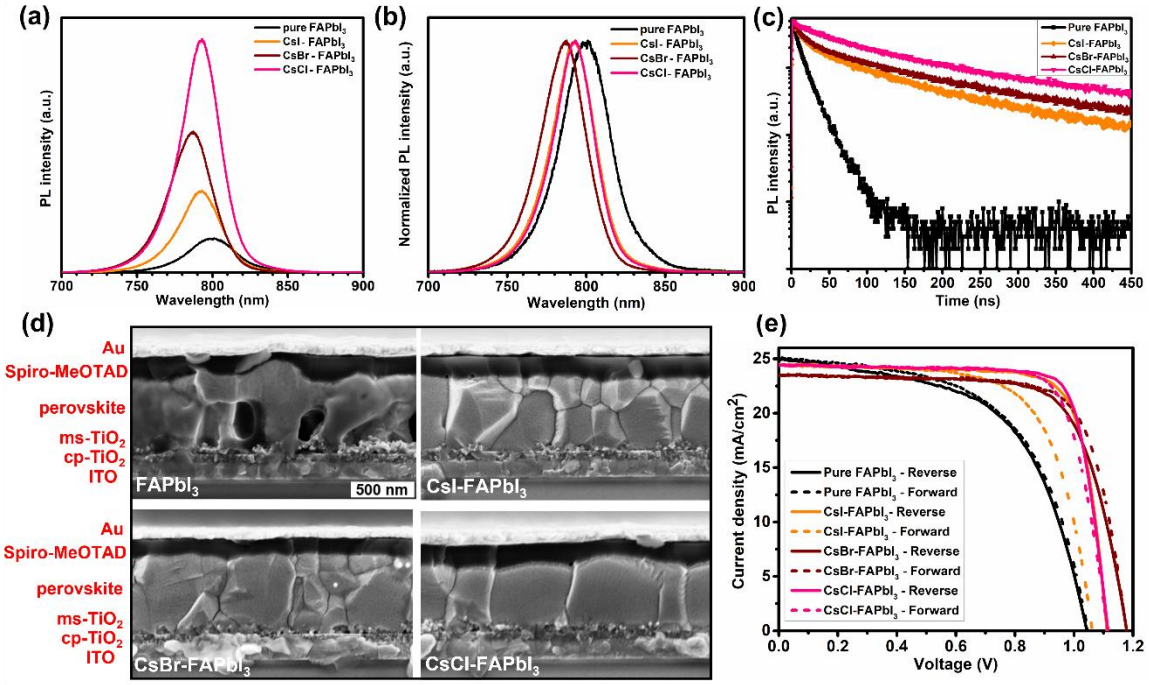

Figure 7.9. (a) The steady-state PL spectra, (b) normalized PL spectra and (c) TRPL of the $FAPbI_3$ perovskites in pure form and CsI-$FAPbI_3$, CsBr-$FAPbI_3$, CsCl-$FAPbI_3$. (d) Cross-sectional SEM images of the PSC devices with pure $FAPbI_3$ perovskite film and $FAPbI_3$ perovskite with various additives of CsI, CsBr, and CsCl, respectively. (e) Forward and reverse J-V curves for the solar cell using pure $FAPbI_3$ film and CsI-$FAPbI_3$, CsBr-$FAPbI_3$, CsCl-$FAPbI_3$ perovskite films with a scan rate of 50 mV/s.

The influence of the Cs cation and X anions on the lifetime of $FAPbI_3$ perovskite films was obtained from TRPL measurements. Figure 7.9c shows that the lifetime of the perovskite films was remarkably improved with CsX additions into $FAPbI_3$. The CsCl-$FAPbI_3$ perovskite film has the longest PL lifetime. The enhancement in the PL lifetime is consistent with the state-steady PL results.

To understand the impact of Cs cation and X anions on the PV performance, solar cell devices were fabricated using pure $FAPbI_3$ and CsX-$FAPbI_3$ films as the active layer. We fabricate the full PSC devices from these layers using a solar cell structure of glass substrate/ITO/cp-TiO_2/ms-TiO_2/pure $FAPbI_3$ perovskite or the CsX-$FAPbI_3$ perovskites layer/Spiro-MeOTAD/Au. Figure 7.9d shows this layout from cross-sectional SEM images of the full PSC devices with the thickness of the absorber layers ranging from 550 to 700 nm. The cross-sectional SEM images confirmed that compared to pure $FAPbI_3$, the grain size was slightly increased with CsI-$FAPbI_3$ and CsBr-$FAPbI_3$ perovskite films and significantly increased with CsCl-$FAPbI_3$ perovskite film.

Given that the CsCl-$FAPbI_3$ perovskite film has a larger crystallite size, higher crystallinity, stronger PL intensity and longer carrier lifetime, it can be expected that the solar cell devices based on these perovskite films will deliver a better performance. Figure 7.9e shows the J-V curves of the PSC devices using pure-$FAPbI_3$ and CsX-$FAPbI_3$ perovskites as absorber layers for both reverse and forward bias scans. The statistical PV parameters of all PSC devices are summarized in Table 7.1. The solar cell device based on pure $FAPbI_3$ film exhibits a reverse scan PCE of 15.01% with a short-circuit photocurrent density (J_{SC}) of 25.08 $mAcm^{-2}$, an open-circuit voltage (V_{OC}) of 1.044 V, and a fill factor (FF) of 0.573 for the reverse scan. The CsX-$FAPbI_3$ perovskites indicate better device performance compared to pure $FAPbI_3$. By using CsBr-$FAPbI_3$ perovskite as an absorber layer, the device efficiency is slightly enhanced to 19.89%. The reverse scan PCE of CsI-$FAPbI_3$ based PSCs is significantly increased to 21.09%. The solar cell devices based on CsCl-$FAPbI_3$ perovskite film shows a maximum reverse scan PCE of 21.70% and the best performing PSC device is improved in all individual PV parameters namely a J_{SC} of 24.38 $mAcm^{-2}$, V_{OC} of 1.114 V, and FF of 0.763. The external quantum efficiency (EQE) of the cell using CsCl-$FAPbI_3$ film is presented in Figure 7.10a, which shows high values in the whole visible spectrum and a sharp edge at the wavelength (~800 nm) corresponding near the band gap (1.5 eV) of the CsCl-$FAPbI_3$ film. Interestingly, the PSC device using CsBr-$FAPbI_3$ perovskite shows the highest V_{OC} of 1.177 V compared to 1.111 V and 1.114 V for CsI-$FAPbI_3$ and CsCl-$FAPbI_3$ perovskite, respectively. The open-circuit voltage is directly related to the bandgap of the active layer in the PSC device. CsBr-$FAPbI_3$ perovskite film has the largest optical bandgap resulting in the highest observed V_{OC}.

The introduction of halide anions in CsX (X = I, Br, Cl) into $FAPbI_3$ perovskite can change the hysteresis of the PSC devices. The J-V plots of the perovskite film with various

anions are shown in Figure 7.9e. There is significant hysteresis in the CsI-$FAPbI_3$ PSC. However, hysteresis was suppressed in the cell using CsBr-$FAPBI_3$ and CsCl-$FAPbI_3$ perovskite layers. These findings suggest that the perovskite films with a higher density of NTs and SFs have more hysteresis in their solar cell performance. Figure 7.10b shows the light stability of the best-performed cell using CsCl-$FAPbI_3$ films, the PCE remains at more than 95% after 120 h of operation.

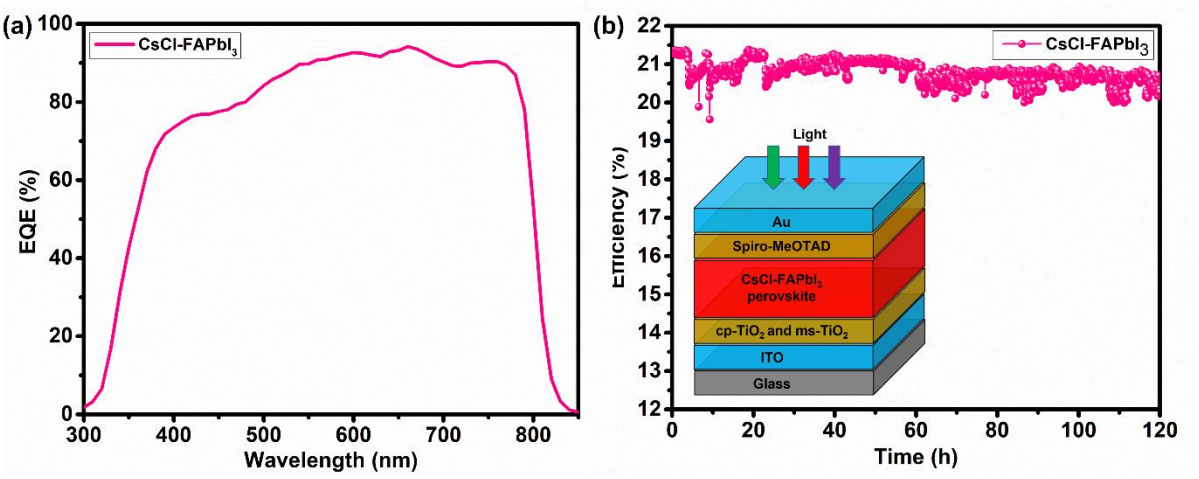

Figure 7.10. External quantum efficiency (EQE) of PSC using CsCl-$FAPbI_3$ perovskite film. The integrated current calculated from the EQE data is 23.8 mA/cm^2. (b) Light stability of CsCl-$FAPbI_3$ perovskite solar cell upon 120 h under continuous illumination (white LED light at the intensity ~ 1 Sun), at fixed voltage close to the maximum power point, in nitrogen environment and the cell temperature is kept at 25 ^oC.

Table 7.1. Comparison of PV performance parameters (V_{OC}, J_{SC}, FF, and PCE) of various cells with different perovskite compositions in forward and reverse bias with a scan rate of 50 mV/s.

Samples	V_{OC} (V)		J_{SC} (mA/cm^2)		FF		PCE (%)	
	Reverse	Forward	Reverse	Forward	Reverse	Forward	Reverse	Forward
$FAPbI_3$	1.044	1.042	25.08	24.91	0.573	0.57	15.01	14.80
CsI	1.111	1.061	24.49	24.39	0.775	0.678	21.09	17.55
CsBr	1.177	1.168	23.54	23.50	0.718	0.747	19.89	20.51
CsCl	1.114	1.113	24.38	24.44	0.799	0.763	21.70	20.77

7.5 Degradation process of CsX-FAPbI$_3$ perovskites

Finally, we investigate the impact of halide anions on the moisture stability of pure FAPbI$_3$ and CsX-FAPbI$_3$ (X = I, Br, Cl) perovskite films. To study the degradation process, the perovskite films were stored at room temperature, in air and a humid environment with relative humidity ranging from 70% to 85% for different lengths of time. Figure 7.11 shows the XRD patterns of fresh pure FAPbI$_3$ and CsX-FAPbI$_3$ perovskite films and samples stored in ambient air over 4 weeks. The formation of the PbI$_2$ phase was observed in all samples after 4 weeks of ageing. However, the XRD measurements are insensitive to local variations and cannot be used to understand the degradation pathway of OIMHP materials.

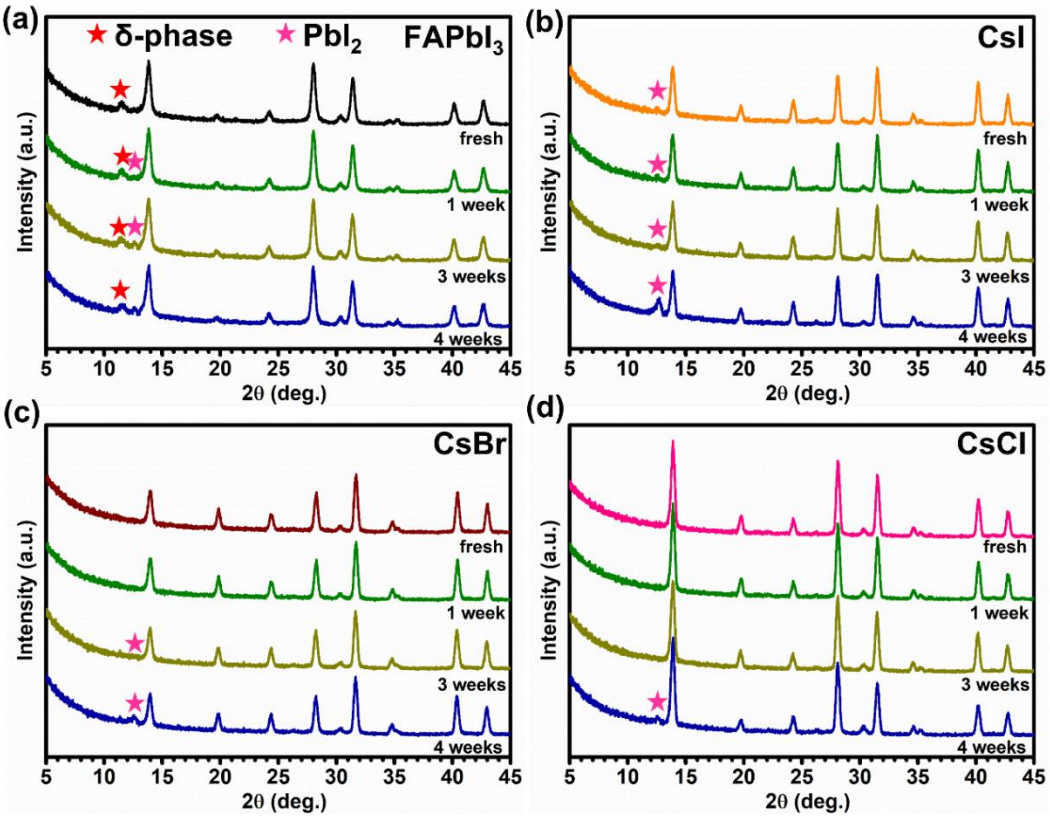

Figure 7.11. The XRD patterns of fresh sample and samples stored in the air at room temperature of pure FAPbI$_3$ and CsX-FAPbI$_3$ perovskite films.

TEM analysis is better suited to understand the morphological, microscopic changes in the perovskite films as a function of humidity exposure. Perovskite films were prepared on TEM Cu/Au grids and the films were stored under ambient conditions for 1 week and 3 weeks, respectively. Figures 7.12a-d show the BF-TEM images of fresh perovskite films including

pure $FAPbI_3$ and various CsX-$FAPbI_3$ perovskite films. The surfaces of fresh samples are mostly smooth, uniform, and clean with distinctive grain boundaries.

The pure $FAPbI_3$ sample with 1 week of ageing shows the presence of many nanovoids highlighted in yellow which are mainly distributed at grain boundaries and less inside the grains (Figure 7.12e). Some black nanoparticles highlighted in red colour were formed around grain boundaries of the pure $FAPbI_3$ perovskite film. The black nanoparticles at grain boundaries in BF-TEM images can be attributed to the presence of the PbI_2 phase. The morphologies of the perovskite grains of pure $FAPbI_3$ film are significantly degraded with 3 more weeks of ageing, as shown in Figure 7.12i. The number of black particles is significantly increased at the grain boundaries. The number of voids dramatically increased not only at grain boundaries but also inside the grains.

For CsX-$FAPbI_3$ perovskite, many black nanoparticles highlighted in red outline were formed around the grain boundaries of the films after 1 week of ageing. We also observed a small number of nanovoids inside the grains for CsI-$FAPbI_3$ sample (Figure 7.12f). The nanovoids were not visible after 1 week of ageing in CsBr-$FAPbI_3$ and CsCl-$FAPbI_3$ perovskite films (Figures 7.12g, h). However, after 3 weeks of degradation, the grain boundaries of CsX-$FAPbI_3$ were destroyed, large interstitial voids are visible and black nanoparticles are formed around the grains. These results are consistent with the report from Yu *et al*. on the degradation of $MAPbI_{3-x}Cl_x$ layers under moisture and oxygen ambient.[281] They demonstrated that grain boundaries are the initial sites for degradation in the perovskite films. Interestingly, we found that the NT domains are very stable under ambient air at room temperature. We observed that the degradation is more severe at the grain boundaries compared to other regions in the perovskite films.

The degradation of OIMHP materials might proceed through various complicated crystallographic and phase transformation routes depending on the composition. Previously, few studies have reported the use of TEM to directly observe the change in the mixed-cation perovskite under subsequent phase transformation and transitions to PbI_2.[13, 181, 182, 282] Manekkathodi *et al*. have observed the formation of PbI_2 phase in $Cs_{0.05}MA_{0.1}FA_{0.85}Pb(I_{0.85}Br_{0.15})_3$ composition using HR-TEM.[182] However, OIMHP materials are very sensitive to intense electron beam especially when imaged using HR-TEM. Consequently, care was exercised to minimise beam related artefacts by recording both the BF-

TEM images and the corresponding SAED patterns in all samples when confirming the formation of PbI_2 phase.

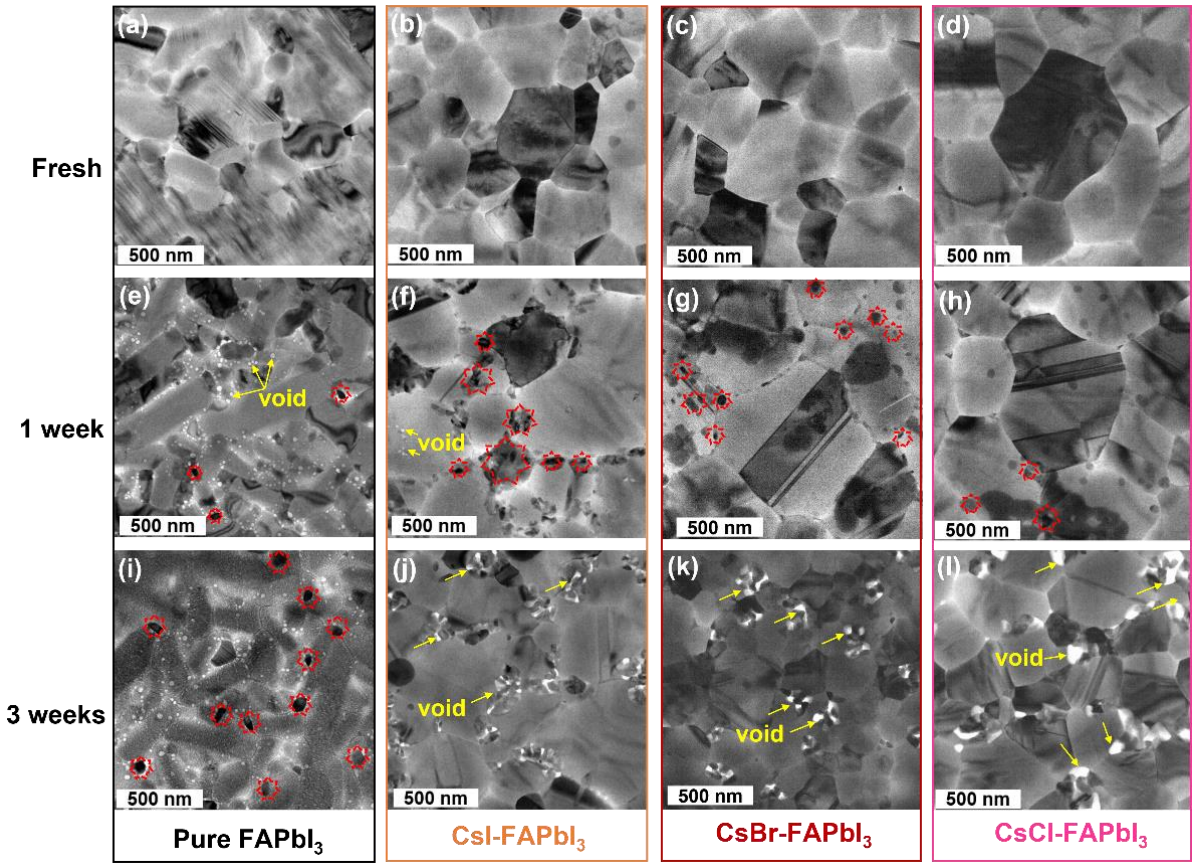

Figure 7.12. BF-TEM images of (a) pure $FAPbI_3$, (b) CsI-$FAPbI_3$, (c) CsBr-$FAPbI_3$, (d) CsCl-$FAPbI_3$ fresh perovskite films. BF-TEM images of (e) pure $FAPbI_3$, (f) CsI-$FAPbI_3$, (g) CsBr-$FAPbI_3$, (h) CsCl-$FAPbI_3$ perovskite films with 1 week of ageing at room temperature. BF-TEM images of (i) pure $FAPbI_3$, (j) CsI-$FAPbI_3$, (k) CsBr-$FAPbI_3$, (l) CsCl-$FAPbI_3$ perovskite films with 3 weeks of ageing.

Figure 7.13 shows the microstructure and crystal structure of CsCl-$FAPbI_3$ perovskites after 3 weeks of ageing. The experimental SAED patterns obtained from grains highlighted in yellow circles confirm that the crystal structure of CsCl-$FAPbI_3$ transforms from the cubic supercell perovskite structure to the rhombohedral (trigonal) structure. In detail, the experimental SAED pattern (Figure 7.13b) taken from the BF-TEM image in Figure 7.13a is consistent with the simulated electron diffraction pattern along the $[2\bar{1}\bar{1}6]$ zone axis (Figure 7.13c) for the perovskite rhombohedral (trigonal) $R\bar{3}$ phase. Similarly, the experimental SAED patterns (Figures 7.13e, h) obtained from the BF-TEM images in Figures 7.13d, g are consistent

with the simulated electron diffraction patterns along the [1 1 $\bar{2}$ 12] and [$\bar{1}$102] zone axes (Figure 7.13c) for the rhombohedral (trigonal) phase, respectively. The formation of the rhombohedral (trigonal) phase was further confirmed for CsI-$FAPbI_3$ and CsBr-$FAPbI_3$ perovskite films after 3 weeks of ageing as shown in Figures 7.14 and 7.15.

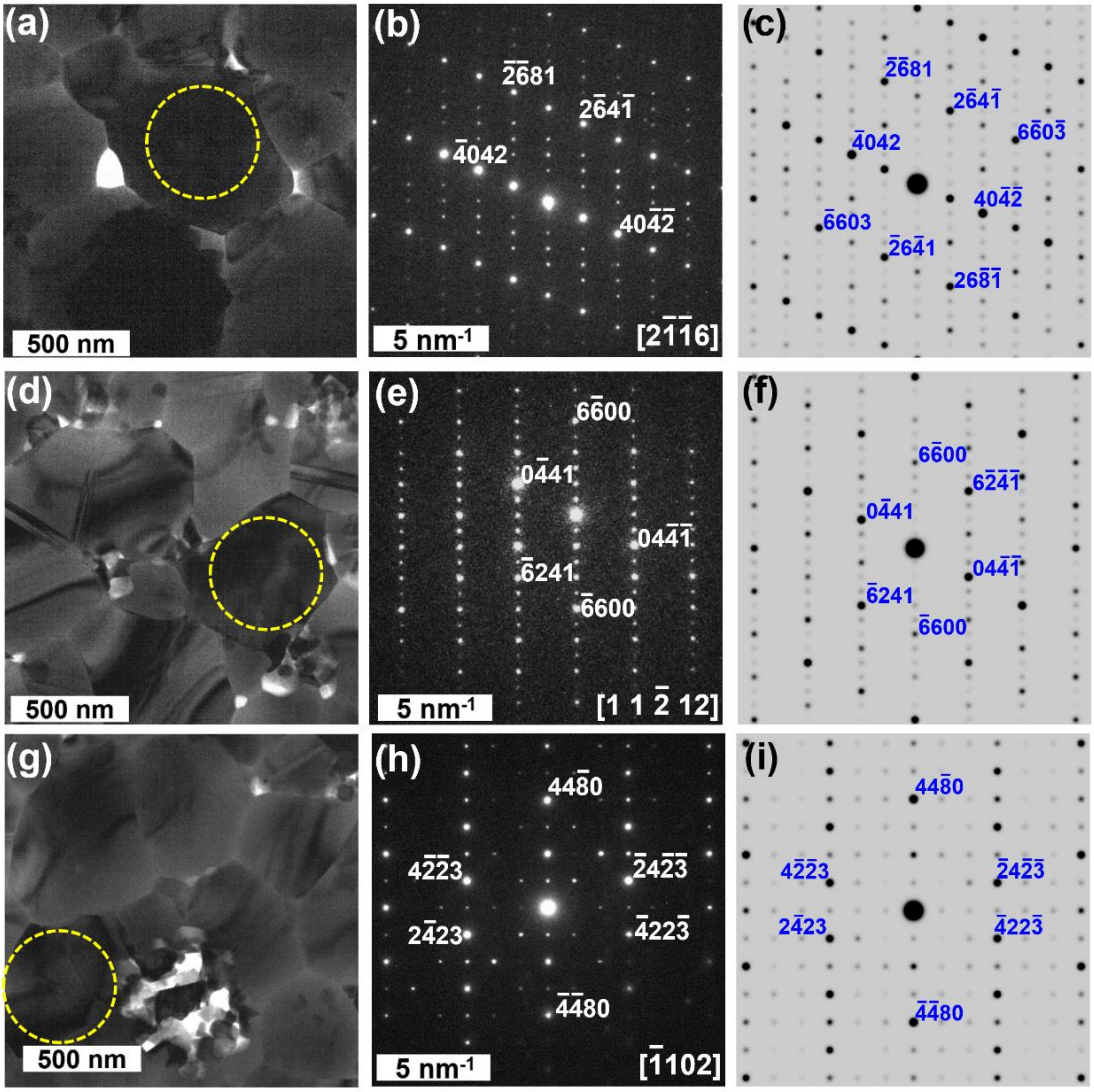

Figure 7.13. BF-TEM images, experimental SAED patterns taken from grain highlighted in yellow circle and simulated electron diffraction patterns along [$2\bar{1}\bar{1}6$], [1 1 $\bar{2}$ 12] and [$\bar{1}$102] zone axes of CsCl-$FAPbI_3$ perovskite films with 3 weeks of ageing.

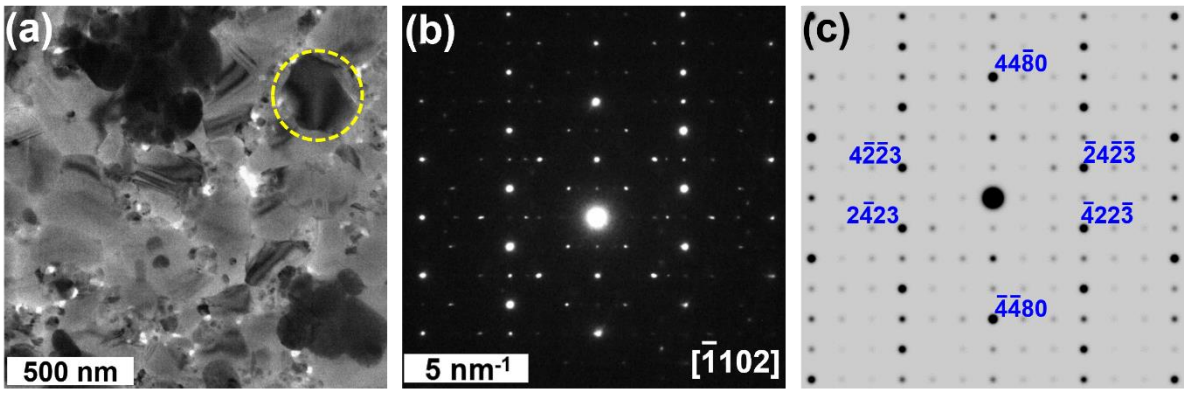

Figure 7.14. BF-TEM images, experimental SAED patterns taken from grain highlighted in yellow circle and simulation electron diffraction patterns of CsI-$FAPbI_3$ perovskite films with 3 weeks of ageing.

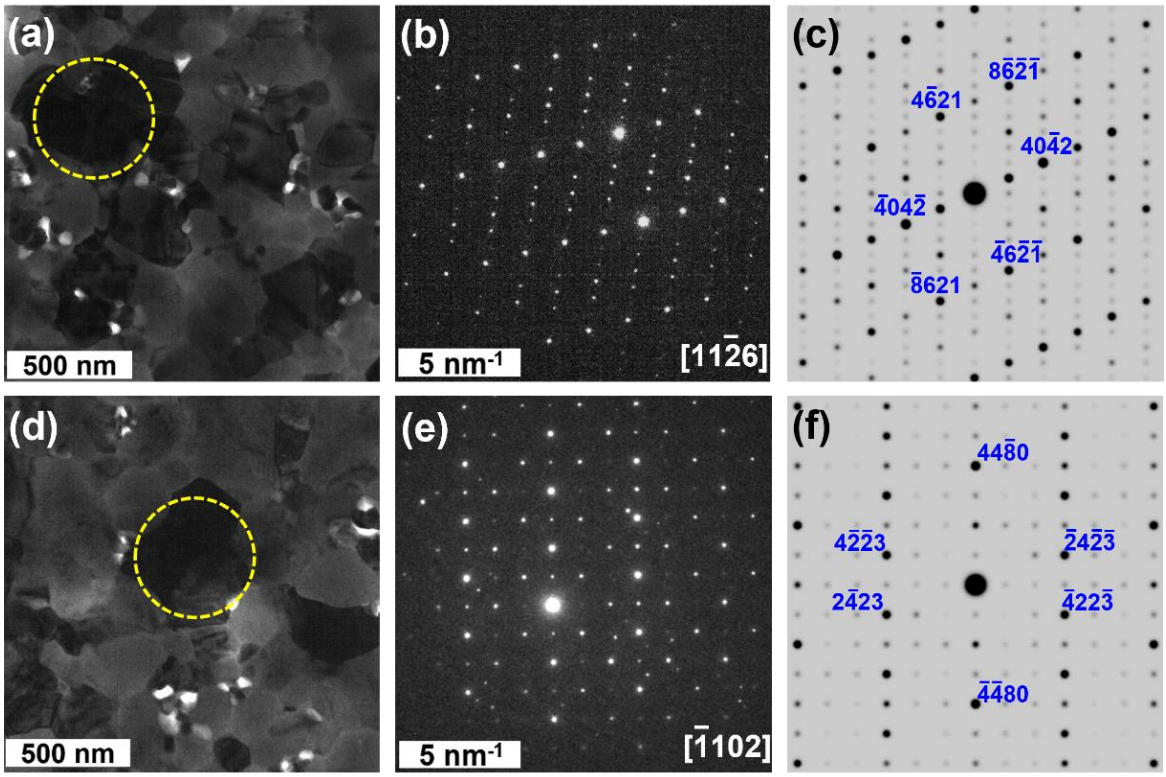

Figure 7.15. BF-TEM images, experimental SAED patterns taken from grain highlighted in yellow circle and simulation electron diffraction patterns of CsBr-$FAPbI_3$ perovskite films with 3 weeks of ageing.

Figure 7.16 illustrates the morphology and crystallography of CsX-$FAPbI_3$ perovskites after 4 weeks of ageing. Figures 7.16a-d show the bright-field TEM images and SAED patterns obtained from the grain highlighted in yellow circles of the CsI-$FAPbI_3$ perovskite film. The

BF-TEM images indicate that at random positions, the grain structure evolves into segregated dark nanoparticles that are associated with degradation. The heterogeneous damage and formation of nonuniformly distributed PbI_2 nanoparticles lead to a single grain. The SAED patterns from the dark nanoparticles are shown in Figures 7.16b, d and index with the hexagonal PbI_2 phase along the $[1\bar{1}01]$ and $[\bar{4}401]$ zone axes, respectively. Figures 7.16e-h illustrate the BF-TEM images and SAED patterns taken from the grain highlighted in yellow circles of the CsBr-$FAPbI_3$ perovskite film. The grain boundaries of perovskite film were nonuniformly damaged, resulting in many nanoparticles. The SAED patterns in Figures 7.16f and h confirmed the formation of the hexagonal PbI_2 phase along $[\bar{8}801]$ and $[8\bar{1}\bar{7}3]$ zone axes, respectively. The BF-TEM images and SAED patterns taken from the grain highlighted in yellow circles of the CsCl-$FAPbI_3$ perovskite film are shown in Figures 7.16i-l. BF-TEM images indicate that the grain boundaries have disappeared in some regions, indicating that many grains coalesced into one bigger grain. The SAED patterns taken from the big grain highlighted in yellow circles are consistent with the hexagonal PbI_2 phase along the $[1\bar{1}01]$ and $[\bar{1}5\bar{4}\bar{3}]$ zone axes. The hexagonal PbI_2 phase was observed in all CsX-$FAPbI_3$ perovskite samples after 4 weeks of ageing.

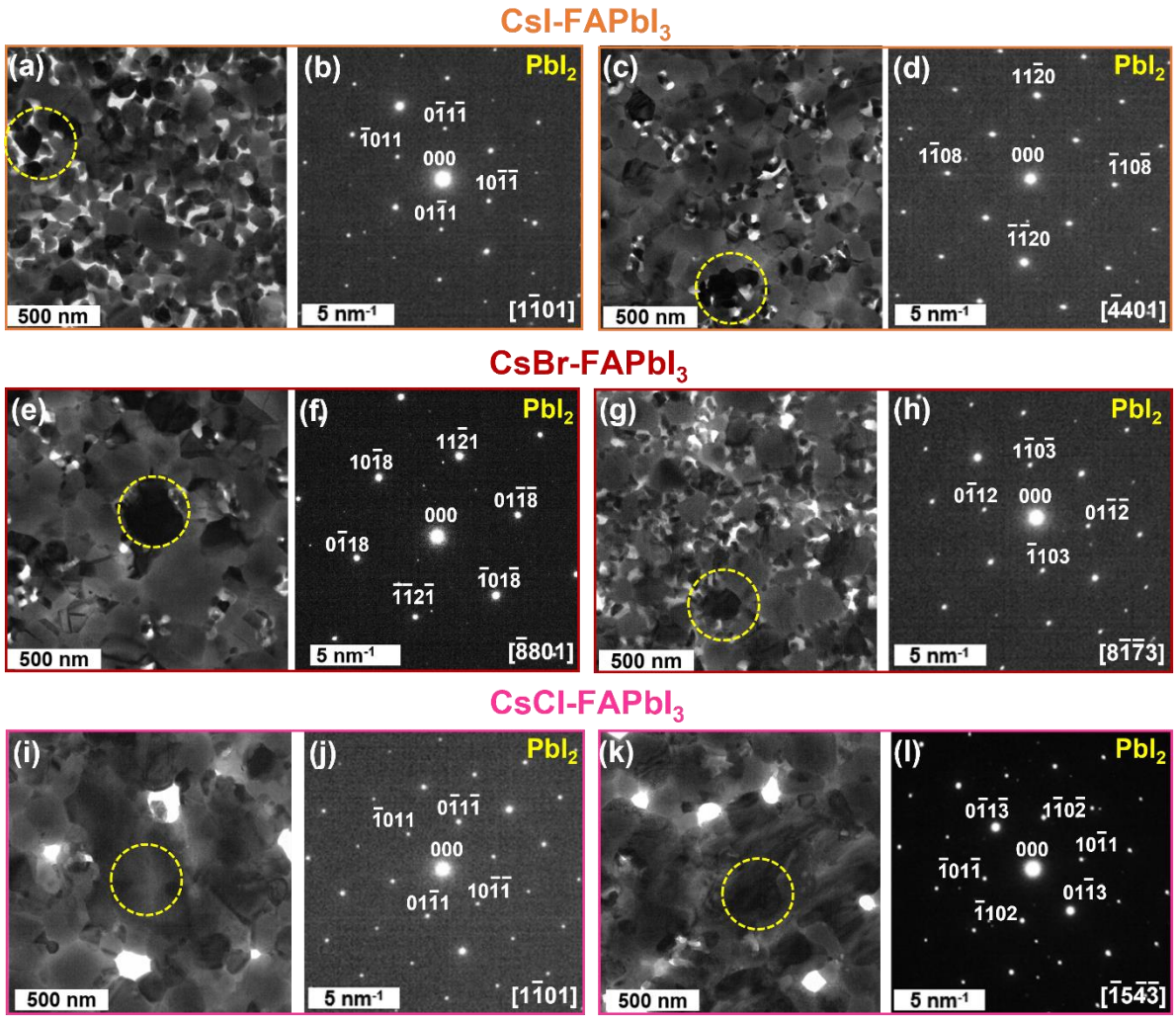

Figure 7.16. BF-TEM images and corresponding SAED pattern taken from grain highlighted in yellow circle for (a-d) CsI-$FAPbI_3$, (e, h) CsBr-$FAPbI_3$, (i, l) CsCl-$FAPbI_3$ perovskite films stored at room temperature for 4 weeks.

7.6 Summary

In this chapter, we systematically study the impact of the Cs cation and halide anions on the microstructure, crystal structure, structural defects, optoelectronic properties and PV parameters of $FAPbI_3$ PSCs with the use of CsX additives (X = I, Br, and Cl). CsX-$FAPbI_3$ perovskite films have a cubic supercell structure with the $Im\bar{3}$ space group. Among the additives tested, the CsCl-$FAPbI_3$ perovskite film shows the highest PL intensity, longest PL lifetime and highest PCE compared to the films with CsI and CsBr. We observed that the PCE and hysteresis were dramatically improved as the density of NTs and SFs decreased. The PCE of the PSC device showed the largest improvement (from 15.01% to 21.70%) after adding CsCl into the

$FAPbI_3$ perovskite. An improvement in PCE is also observed for CsI (21.09%) and CsBr (19.89%) additives. The morphology and crystallography of $\{111\}_c$ NTs and SFs are studied using TEM and SAED. Both single TB and multiple TBs were observed in CsX-$FAPbI_3$ perovskite films. The number of twinned grains per unit area is dramatically reduced when CsCl and CsBr are incorporated into $FAPbI_3$ perovskite. The microstructure, crystallography and atomic structure model of two TBs separating three twins and intersecting at an angle of around 70.5° are also presented.

Finally, we systematically investigate the degradation pathways and their underlying mechanism for CsX-$FAPbI_3$ perovskite under ambient conditions. The pure $FAPbI_3$ sample after 1 week of ageing shows the presence of many nanovoids which are mainly distributed at grain boundaries, with comparatively few nanovoids observed inside the grains. We also observed a small number of nanovoids inside the grains for the CsI-$FAPbI_3$ sample. For CsBr-$FAPbI_3$ and CsCl-$FAPbI_3$ perovskite films, the nanovoids do not appear after 1 week of ageing. However, the surface morphology is slightly changed with many black nanoparticles formed around grain boundaries. The grain boundaries of the perovskite films were nonuniformly damaged, resulting in many black nanoparticles after 3 weeks. The crystal structure of CsX-$FAPbI_3$ changes from cubic supercell perovskite structure to rhombohedral (trigonal) structure after 3 weeks. Electron diffraction analyses of the black nanoparticles confirmed the formation of the hexagonal PbI_2 phase formation in all CsX-$FAPbI_3$ perovskite samples after 4 weeks of ageing. Interestingly, we found that the NTs are very stable under ambient air at room temperature.

Chapter 8. Conclusions and future directions

8.1 Conclusions

8.1.1 Research outcomes

The aim of this thesis is to provide an in-depth understanding of the microstructure, crystal structure, elemental composition, and defects in various perovskite compositions using electron microscopy techniques. Furthermore, the influence of different additives on the microstructure, crystal structure and PV performance is also investigated. Below are the conclusions and discussions extracted from this study.

Chapters 1 to 3 provide the research motivation and background for PSCs. The theory behind the experimental techniques used in this thesis is provided namely for X-ray diffraction, optical and electrical characterization, and various electron microscopy techniques.

The research findings and outcomes were detailed in chapters 4, 5, 6 and 7. A summary of each of these chapters is provided below.

Chapter 4 studies the chemical and structural properties of the $Rb_{0.03}Cs_{0.07}FA_{0.765}MA_{0.135}PbI_{2.55}Br_{0.45}$ perovskite film. The simulation and experimental results clarify the fundamental understanding of the morphology, microstructure, crystal structure, phase segregation, and elemental composition of multi-cation mixed-halide perovskites. In general, it is found that Rb^+ cation was not incorporated into the perovskite crystal structure and only exist separately in the perovskite film as a segregated phase. In contrast, Cs^+ cation was found to be incorporated into the perovskite structure and segregated within a Rb and Cs-rich phase. The Rb^+ and Cs^+ cations were typically segregated at the grain boundaries of the perovskite film as a discrete Rb- and Cs-rich phase. The Rb and Cs rich phase tends to form at the grain boundaries of the perovskite film thus improving the perovskite film stability.

The structure of multi-cation mixed-halide perovskite is also shown to be a mixture of MA and FA phases. The visibility of some forbidden reflections was attributed to three possible explanations, namely (a) superlattice reflections arising from a doubling of the unit cells along the *a* and *b* axes, (b) chemical ordering within the A-site cations and/or the halide site anions and (c) twin formation. Furthermore, we show the evidence for the coexistence of cubic and

tetragonal phases in the diffraction patterns at room temperature. The results presented in this chapter offer additional insights into the cation incorporation in mixed-halide perovskite materials. Finally, the J-V curves of the PSC device using multi-cation mixed-halide perovskite reveal that there is little hysteresis in the cell, and a steady PCE of 20%.

Chapter 5 explores the twinning formation in cubic and tetragonal multi-cation mixed-halide perovskite. We develop a combination of low-dose electron microscopy studies and diffraction simulations of different atomic structures to identify a common twinning structure in both the cubic and tetragonal phases of the $Rb_{0.05}Cs_{0.095}MA_{0.1425}FA_{0.7125}PbI_2Br$ hybrid perovskite. We have shown unambiguously the presence of both $\{111\}_c$ and $\{011\}_t$ twins in multi-cation mixed-halide perovskite films at room temperature. The number of cubic twins in this material is higher than the number of tetragonal twins observed. A coherent TB was proposed for the cubic phase with no splitting of diffraction spots between the twin and the matrix. In contrast, the interface between the tetragonal matrix and twin is semi-coherent and has a 1º tilt between the two. This was confirmed by the splitting in the electron diffraction spots from the matrix and the twin. Additional splitting of spots was ascribed to the octahedral tilt in the tetragonal structure which results in a 2º split for non-coincident spots.

A unique way of differentiating the twins in the tetragonal and cubic crystal structure of as-studied perovskite materials is also identified where splitting of spots was only observed for tetragonal twins. Both single and double twin structures were observed for the tetragonal phase. We propose that the cubic twins are more likely to be AX_3 centred while the tetragonal twins are more likely to Pb centred because of the minimum distortion to the Pb-I/Br octahedral arrangement. This has significant implications for A cation and X anion segregation at the twin defects. These results provide a better understanding of the crystal structure defects in multi-cation mixed-halide perovskite materials. Further experimental studies on the effect of twins on the electron-hole recombination and transportation are necessary to elaborate on the best strategy for performance improvement of PSCs in the future.

Chapter 6 studies the effect of MACl and CsCl additives on the structure, morphology, and defect structures in $FAPbI_3$ perovskite film. Electron diffraction analyses of pure $FAPbI_3$ showed that the cubic α-phase is unstable and transforms into a mixture of different phases including the hexagonal δ-phase and an additional unreported phase that is best simulated with a rhombohedral $R\bar{3}$ space group. We demonstrate that the MACl and CsCl additions have a great potential to stabilize the cubic $FAPbI_3$ with a $2 \times 2 \times 2$ supercell expansion and the $Im\bar{3}$

space group. The $\{111\}_c$ twins were observed in all samples. We also systematically studied the morphology and crystal structure of NTs and SFs in various perovskite compositions. The defect density depends on the concentration of additives added to the perovskite precursor solution. A higher density of defects in the perovskite film resulted in reduced PL intensity and lifetime, leading to poorer cell performance. The MACl additive increased the density of defects in the perovskite film compared to the CsCl additive. The perovskite film with 10 mol% CsCl has the lowest defect density.

Interestingly, the incorporation of MACl and CsCl into $FAPbI_3$ changes the lattice parameter and optical properties with the incorporation of Cs/MA cations and Cl anion. Moreover, higher quality perovskite films were obtained with larger grain size, well-defined grain structure, and improved crystallinity, resulting in a longer carrier lifetime compared to pure $FAPbI_3$ film. The addition of CsCl to the $FAPbI_3$ perovskite precursor solution results in a higher PL intensity and a longer lifetime compared to the sample with added MACl. The optimized PSC with 10 mol% CsCl shows the best device performance with low hysteresis and the highest PCE of 21.98%, which is much higher than the PSC for 20 mol% MACl with 15.46% PCE. Our results show that the CsCl additive is a promising candidate for stabilizing the cubic phase and suppressing the undesirable hexagonal δ-phase, paving the way for practical applications of PSCs in the near future.

Chapter 7 investigates the key role of Cs cation and halide anions on the microstructure, crystal structure, structural defects, optoelectronic properties and PV parameters of $FAPbI_3$ PSCs with the use of CsX additives (X = I, Br, and Cl). CsX-$FAPbI_3$ perovskite compositions have a cubic structure with the expansion of the unit cell to a $2 \times 2 \times 2$ supercell and the space group $Im\bar{3}$. By introducing CsCl addition into $FAPbI_3$, the perovskite film showed the highest PL intensity, longest PL lifetime and highest PCE compared to the films with CsI and CsBr additions. The PCE of PSC device dramatically improved from 15.1% to 21.70% after adding CsCl into $FAPbI_3$ perovskite, whereas a moderate increase in PCE to 21.09% and 19.89% is observed for CsI and CsBr, respectively.

The morphology and crystallography of $\{111\}_c$ NTs and SFs are studied using TEM and SAED. The NTs structure including single, double, and multiple TBs were observed in CsX-$FAPbI_3$ perovskite compositions. The number of twinned grains per unit area is dramatically reduced when CsCl and CsBr additions are incorporated into $FAPbI_3$ perovskite.

The morphology, microstructure, crystallography and atomic structure of two TBs intersecting at an angle of around 70.5º are presented.

Finally, we systematically studied the degradation pathways and their underlying mechanism for CsX-$FAPbI_3$ perovskite compositions under ambient conditions. The pure $FAPbI_3$ sample with 1 week of ageing shows the presence of many nanovoids which are mainly distributed at grain boundaries and fewer nanovoids are observed on the surfaces of grains. We also observed small numbers of nanovoids inside the grains for CsI-$FAPbI_3$ sample. For CsBr-$FAPbI_3$ and CsCl-$FAPbI_3$ perovskite films, the nanovoids do not appear after 1 week of ageing. However, the surface morphology is slightly changed with many black nanoparticles formed around grain boundaries. The grain boundaries of the perovskite film were nonuniformly damaged, resulting in many nanoparticles after 4 weeks. Electron diffraction analyses of the black nanoparticles confirmed the formation of the hexagonal PbI_2 phase formation in all CsX-$FAPbI_3$ perovskite samples after 4 weeks of ageing. More interesting, we found that the NT domains are very stable at room temperature under ambient conditions.

8.1.2. The key achievements of the study in the context of current research

Along with the objective achievement, this PhD thesis also brings out some other valuable scientific discoveries, which are very useful for the future research and development of PSCs.

Since the first PSC have been introduced in 2009, enormous international research efforts have focused on improving PV device performance. However, the microstructure, crystal structure, atomic structure and defects of OIMHP materials remain unknown. In many perovskite compositions, even the space group remains in dispute. In this thesis, we used low-dose electron microscopy to study the microstructure of various perovskite compositions. A comprehensive evaluation about the microstructure, crystal structure and defects of various OIMHP materials has been discussed in this thesis. This contributes to the materials design for achieving more stable and highly perovskite PV device performance. We demonstrated that the microstructure and defects of OIMHP materials can also play a significant role, providing further scope for the optimisation of this exciting PV technology. This would allow the low-cost and highly efficient solar cell technology based on perovskite materials to commercialisation.

We have also developed protocols for minimising beam damage using electron microscopy to ensure reliable structural measurements. In order to minimise the damage of OIMHP materials under electron beam, we employ the low-dose TEM technique with a dose rate of about 2 e $Å^{-2}$ s^{-1} and rapid acquisition condition. The condenser aperture size is 40 μm, an exposure time is 0.5 seconds, a spot size of 3 to 5 was used (depending on the thickness of the specimen) and the beam was spread to reduce the dose rate. To enhance the contrast of BF-TEM images, the 20 μm objective aperture was used. All TEM images and SAED patterns were recorded from the non-exposed regions of the sample. When collecting the SAED pattern, we used the selected area aperture to select the region of interest. With these protocols, this study has clarified some of the key information in the structure evolution and the degradation mechanism of OIMHP materials. All of the structural findings using electron microscopy techniques in this thesis are highly useful to fundamentally understand the intrinsic structure and the degradation mechanism of these materials, and contribute to the development of OIMHP-based solar cells. We also demonstrated that defects are one of the reasons for the increase of hysteresis in the PSCs devices.

Some of research protocols and characterisation approaches in this study may be also useful for other research fields, for example, investigating the microstructure and crystal structure of beam sensitive materials such as metallic glasses, and organic materials…

8.2 Future directions

The outcomes of this thesis demonstrate the importance of microstructure, crystal structure and defects in the OIMHP layer to understand and improve the optical properties as well as PSC device performance. The main obstacles in employing various microscopy instruments to study OIMHP materials have been investigated. Based on the outcomes and remaining challenges, we may be able to suggest several future directions for improving the basic understanding of the microstructure of OIMHP materials and the device performance of PSCs.

In some OIMHP materials, the space group is still under debate. Precession electron diffraction (PED) improves the symmetry determination and helps to reduce the dynamical effect. The convergent beam electron diffraction (CBED) has been considered as one of the best techniques to determine the crystal symmetry. However, the perovskite materials are highly sensitive to electron beam and not compatible to some electron microscopy techniques,

including CBED. To minimise the electron beam damage, low dose four-dimensional STEM (4D-STEM) can be the promising technique to study the CBED in OIMHP materials.

Another phenomenon emerging in the investigation of FA-based PSC is the appearance of NT domains and SFs, which is highly promising to further discover, especially observing the atomic structure of NTs, TB, and SFs. HR-TEM is very powerful and useful to be employed in the characterization of crystal structures on extremely small scale. However, OIMHP materials are highly sensitive and easily damage under intense electron beam irradiation, thus making high-resolution electron microscopy extremely challenging. For example, $MAPbI_3$ decomposes into PbI_2 at a total dose irradiation higher than 150 $eÅ^{-2}s^{-1}$.[13] However, the common electron dose in a normal HR-TEM is around 800–2000 $eÅ^{-2}s^{-1}$, which is much higher than the affordable dose for $MAPbI_3$ perovskite.[283, 284] To minimise the electron beam damage, low dose STEM and 4D-STEM techniques should be explored more thoroughly in obtaining atomic resolution images of twin domains, twin boundaries, and stacking faults in OIMHP materials. [285, 286]

Moreover, the effect of NTs on the band structure and optical properties of perovskite compositions remains to be confirmed. The bandgap of organic-inorganic semiconductor materials is defined by the number of iodine anions shared between two neighbouring Pb ions and is enlarged by higher connectivity.[145] In OIMHP materials, nanotwins and stacking faults have been observed. Wright *et al*. have proposed that the δ-phase twin boundaries are one of the reasons for intrinsic quantum confinement.[249] However, until now there is no direct evidence to confirm the influence of NT and SF on the band structure in OIMHP materials. Further experimental and theoretical methods should be employed together to further confirm this problem.

For multi-cation mixed-halide perovskite composition, there is no clear understanding on how all components form in the system, e.g. homogeneously alloyed or partial compositional and/or structural phase separation in the materials. Furthermore, the forbidden reflections become visible on various zone axes in the SAED patterns. The visibility of some forbidden reflections was attributed to four possible explanations, namely (a) superlattice reflections with a doubling of the unit cells along the *a* and *b* axes, (b) chemical ordering within the A-site cations and/or the halide site anions, (c) octahedral tilting and (d) twin formation. Further investigations are required to confirm the mechanism behind the forbidden reflections.

Most of the research efforts have concentrated on enhancing the efficiency and long-term stability of PSC devices. Recently, the introduction of different additives into the perovskite precursor solution holds the record for the highest PCE and long-term stability.[57, 244] However, the way that the additives are incorporated into the perovskite crystal structure, including twin domains, superlattice reflections or modulated structures, is still unclear, which is essential to understand the differences in the PSC device performance. For instance, several additives (MACl, CsCl, CsI, CsBr, FAHCOO, PACl) are added into the $FAPbI_3$ perovskite precursor solution to stabilize the cubic phase.[15, 57, 244, 245, 267, 287] The research have demonstrated that MACl, CsCl, CsI, CsBr are incorporated into perovskite crystal structures.[244, 245, 267] However, the atomic structure of these perovskite compositions is still not properly investigated. Zhang *et al*. reported that *n*-propylammonium (PA) cation have a large ionic radius that cannot be incorporated into the perovskite lattice structure.[287] They currently do not have direct evidence that PA cation is formed at grain boundaries of the perovskite film. Cryo-TEM operated at 200 kV with a full plunge-freezing method may be highly suitable for obtaining the atomic structure of OIMHP materials.[181]

The degradation process in OIMHP materials is one of the main challenges for bringing this technology to the market. However, this process has not been properly understood for many different perovskite compositions. Especially, the atomic structure and microstructure of OIMHP solar cell devices under operational conditions such as light illumination, heat, oxygen, moisture, and applied bias have not been fully elucidated. For this purpose, in-situ measurements can be used to understand the microstructure and atomic structure of solar cell devices under light illumination, bias, and temperature. Cross-sectional TEM lamellae can be prepared on a nanochip with a piece of sample sliced from full PSC devices by FIB. The contacts between the nanochip and mounted PSC device sample can be used to apply the temperature and bias to these devices in-situ in a suitable TEM holder. FIB is a powerful tool for TEM lamellae preparation with high precision, and often allows for detailed study of the different layers and interfaces found in the full PSC device structures. FIB sample preparation involves milling away the bulk structure on either side of a thin lamella, which is polished on both sides using low voltage gallium ions beam. This process is known to embed gallium ions in perovskite crystal structures and can be highly damaging to the crystal of the OIMHP materials.[12] So, an additional FIB technique needs to minimise the electron beam damage on the PSC sample. For in-situ TEM measurement, we also must employ low-dose techniques to reduce the electron beam damage.

References

[1] NREL, https://www.nrel.gov/pv/assets/pdfs/pv-efficiency-chart.20181221.pdf., (**2021**).

[2] C. Wehrenfennig, M. Liu, H.J. Snaith, M.B. Johnston, L.M. Herz, Charge Carrier Recombination Channels in the Low-Temperature Phase of Organic-Inorganic Lead Halide Perovskite Thin Films, *APL Materials*, 2 (**2014**) 081513.

[3] S.D. Stranks, G.E. Eperon, G. Grancini, C. Menelaou, M.J.P. Alcocer, T. Leijtens, L.M. Herz, A. Petrozza, H.J. Snaith, Electron-Hole Diffusion Lengths Exceeding 1 Micrometer in an Organometal Trihalide Perovskite Absorber, *Science*, 342 (**2013**) 341-344.

[4] G. Xing, N. Mathews, S. Sun, S.S. Lim, Y.M. Lam, M. Grätzel, S. Mhaisalkar, T.C. Sum, Long-Range Balanced Electron- and Hole-Transport Lengths in Organic-Inorganic $Ch_3nh_3pbi_3$, *Science*, 342 (**2013**) 344-347.

[5] J.H. Noh, S.H. Im, J.H. Heo, T.N. Mandal, S.I. Seok, Chemical Management for Colorful, Efficient, and Stable Inorganic–Organic Hybrid Nanostructured Solar Cells, *Nano Lett.*, 13 (**2013**) 1764-1769.

[6] G.E. Eperon, S.D. Stranks, C. Menelaou, M.B. Johnston, L.M. Herz, H.J. Snaith, Formamidinium Lead Trihalide: A Broadly Tunable Perovskite for Efficient Planar Heterojunction Solar Cells, *Energy Environ. Sci.*, 7 (**2014**) 982-988.

[7] J.Y. Kim, J.-W. Lee, H.S. Jung, H. Shin, N.-G. Park, High-Efficiency Perovskite Solar Cells, *Chem. Rev.*, 120 (**2020**) 7867-7918.

[8] L. Qiu, L.K. Ono, Y. Qi, Advances and Challenges to the Commercialization of Organic–Inorganic Halide Perovskite Solar Cell Technology, *Materials Today Energy*, 7 (**2018**) 169-189.

[9] Q. Lin, R.C.R. Nagiri, P.L. Burn, P. Meredith, Considerations for Upscaling of Organohalide Perovskite Solar Cells, *Adv. Opt. Mater.*, 5 (**2017**) 1600819.

[10] A.A. Asif, R. Singh, G.F. Alapatt, Technical and Economic Assessment of Perovskite Solar Cells for Large Scale Manufacturing, *J. Renew. Sustain. Energy*, 7 (**2015**) 043120.

[11] S. Masi, A.F. Gualdrón-Reyes, I. Mora-Seró, Stabilization of Black Perovskite Phase in $FAPbI_3$ and $CsPbI_3$, *ACS Energy Lett.*, 5 (**2020**) 1974-1985.

[12] M.U. Rothmann, W. Li, Y. Zhu, A. Liu, Z. Ku, U. Bach, J. Etheridge, Y.-B. Cheng, Structural and Chemical Changes to $Ch_3nh_3pbi_3$ Induced by Electron and Gallium Ion Beams, *Adv.Mater.*, 30 (**2018**) 1800629.

[13] S. Chen, X. Zhang, J. Zhao, Y. Zhang, G. Kong, Q. Li, N. Li, Y. Yu, N. Xu, J. Zhang, K. Liu, Q. Zhao, J. Cao, J. Feng, X. Li, J. Qi, D. Yu, J. Li, P. Gao, Atomic Scale Insights into Structure Instability and Decomposition Pathway of Methylammonium Lead Iodide Perovskite, *Nat. Commun.*, 9 (**2018**) 4807.

[14] R. Pandey, G. Vats, J. Yun, C.R. Bowen, A.W.Y. Ho-Baillie, J. Seidel, K.T. Butler, S.I. Seok, Mutual Insight on Ferroelectrics and Hybrid Halide Perovskites: A Platform for Future Multifunctional Energy Conversion, *Adv. Mater.*, 31 (**2019**) 1807376.

[15] H.T. Pham, Y. Yin, G. Andersson, K.J. Weber, T. Duong, J. Wong-Leung, Unraveling the Influence of CsCl/MACl on the Formation of Nanotwins, Stacking Faults and Cubic Supercell Structure in Fa-Based Perovskite Solar Cells, *Nano Energy*, 87 (**2021**) 106226.

[16] E. Strelcov, Q. Dong, T. Li, J. Chae, Y. Shao, Y. Deng, A. Gruverman, J. Huang, A. Centrone, $CH_3NH_3PbI_3$ Perovskites: Ferroelasticity Revealed, *Sci. Adv.*, 3 (**2017**) e1602165.

[17] P. Roy, N. Kumar Sinha, S. Tiwari, A. Khare, A Review on Perovskite Solar Cells: Evolution of Architecture, Fabrication Techniques, Commercialization Issues and Status, *Solar Energy*, 198 (**2020**) 665-688.

[18] P.K. Nayak, S. Mahesh, H.J. Snaith, D. Cahen, Photovoltaic Solar Cell Technologies: Analysing the State of the Art, *Nature Reviews Materials*, 4 (**2019**) 269-285.

[19] M.A. Green, Solar Cells : Operating Principles, Technology, and System Applications, Prentice-Hall, Englewood Cliffs, N.J, (**1982**).

[20] D.M. Chapin, C.S. Fuller, G.L. Pearson, A New Silicon P-N Junction Photocell for Converting Solar Radiation into Electrical Power, *J. Appl. Phys.*, 25 (**1954**) 676-677.

[21] K. Masuko, M. Shigematsu, T. Hashiguchi, D. Fujishima, M. Kai, N. Yoshimura, T. Yamaguchi, Y. Ichihashi, T. Mishima, N. Matsubara, T. Yamanishi, T. Takahama, M. Taguchi, E. Maruyama, S. Okamoto, Achievement of More Than 25% Conversion Efficiency with Crystalline Silicon Heterojunction Solar Cell, *IEEE Journal of Photovoltaics*, 4 (**2014**) 1433-1435.

[22] K. Yoshikawa, H. Kawasaki, W. Yoshida, T. Irie, K. Konishi, K. Nakano, T. Uto, D. Adachi, M. Kanematsu, H. Uzu, K. Yamamoto, Silicon Heterojunction Solar Cell with

Interdigitated Back Contacts for a Photoconversion Efficiency over 26%, *Nature Energy*, 2 (**2017**) 17032.

[23] M.M. Lee, J. Teuscher, T. Miyasaka, T.N. Murakami, H.J. Snaith, Efficient Hybrid Solar Cells Based on Meso-Superstructured Organometal Halide Perovskites, *Science*, 338 (**2012**) 643-647.

[24] W. Shockley, H.J. Queisser, Detailed Balance Limit of Efficiency of P-N Junction Solar Cells, *J. Appl. Phys.*, 32 (**1961**) 510-519.

[25] M. Fathi, A. Mefoued, A. Messaoud, Y. Boukennous, Cost-Effective Photovoltaics with Silicon Material, *Physics Procedia*, 2 (**2009**) 751-757.

[26] T.D. Lee, A.U. Ebong, A Review of Thin Film Solar Cell Technologies and Challenges, *Renew. Sustain. Energy Rev*, 70 (**2017**) 1286-1297.

[27] L.L. Kazmerski, F.R. White, G.K. Morgan, Thin-Film $CuInSe_2$/CdS Heterojunction Solar Cells, *Appl. Phys. Lett.*, 29 (**1976**) 268-270.

[28] M. Nakamura, K. Yamaguchi, Y. Kimoto, Y. Yasaki, T. Kato, H. Sugimoto, Cd-Free $Cu(In,Ga)(Se,S)_2$ Thin-Film Solar Cell with Record Efficiency of 23.35%, *IEEE Journal of Photovoltaics*, 9 (**2019**) 1863-1867.

[29] T.D. Lee, A.U. Ebong, A Review of Thin Film Solar Cell Technologies and Challenges, *Renew. Sustain. Energy Rev.*, 70 (**2017**) 1286-1297.

[30] D. Bonnet, H. Rabenhorst, New Results on the Development of a Thin Film p-CdTe-n-CdS Heterojunction Solar Cell, *IEEE, Silver Springs, MD*, (**1972**) 219.

[31] K.L. Chopra, P.D. Paulson, V. Dutta, Thin-Film Solar Cells: An Overview, *Prog. Photovolt: Res. Appl.*, 12 (**2004**) 69-92.

[32] E. Buitrago, A.M. Novello, T. Meyer, Third-Generation Solar Cells: Toxicity and Risk of Exposure, *Helvetica Chimica Acta*, 103 (**2020**) e2000074.

[33] G. Boschloo, Improving the Performance of Dye-Sensitized Solar Cells, *Frontiers in Chemistry*, 7 (**2019**).

[34] S. Shalini, R. Balasundara prabhu, S. Prasanna, T.K. Mallick, S. Senthilarasu, Review on Natural Dye Sensitized Solar Cells: Operation, Materials and Methods, *Renew. Sustain. Energy Rev*, 51 (**2015**) 1306-1325.

[35] S. Mathew, A. Yella, P. Gao, R. Humphry-Baker, B.F.E. Curchod, N. Ashari-Astani, I. Tavernelli, U. Rothlisberger, M.K. Nazeeruddin, M. Grätzel, Dye-Sensitized Solar Cells with 13% Efficiency Achieved through the Molecular Engineering of Porphyrin Sensitizers, *Nature Chemistry*, 6 (**2014**) 242-247.

[36] J. Gong, J. Liang, K. Sumathy, Review on Dye-Sensitized Solar Cells (DSSCs): Fundamental Concepts and Novel Materials, *Renew. Sustain. Energy Rev.*, 16 (**2012**) 5848-5860.

[37] P.D. Antunez, D.M. Bishop, Y. Luo, R. Haight, Efficient Kesterite Solar Cells with High Open-Circuit Voltage for Applications in Powering Distributed Devices, *Nature Energy*, 2 (**2017**) 884-890.

[38] K. Sun, C. Yan, F. Liu, J. Huang, F. Zhou, J.A. Stride, M. Green, X. Hao, Over 9% Efficient Kesterite Cu_2ZnSnS_4 Solar Cell Fabricated by Using $Zn_{1-X}Cd_xS$ Buffer Layer, *Adv. Energy Mater.*, 6 (**2016**) 1600046.

[39] F.A. Jhuma, M.Z. Shaily, M.J. Rashid, Towards High-Efficiency Czts Solar Cell through Buffer Layer Optimization, *Mater. Renew. Sustain. Energy*, 8 (**2019**) 6.

[40] C. Yan, J. Huang, K. Sun, S. Johnston, Y. Zhang, H. Sun, A. Pu, M. He, F. Liu, K. Eder, L. Yang, J.M. Cairney, N.J. Ekins-Daukes, Z. Hameiri, J.A. Stride, S. Chen, M.A. Green, X. Hao, Cu_2ZnSnS_4 Solar Cells with over 10% Power Conversion Efficiency Enabled by Heterojunction Heat Treatment, *Nature Energy*, 3 (**2018**) 764-772.

[41] W. Wang, M.T. Winkler, O. Gunawan, T. Gokmen, T.K. Todorov, Y. Zhu, D.B. Mitzi, Device Characteristics of CZTSSe Thin-Film Solar Cells with 12.6% Efficiency, *Adv. Energy Mater.*, 4 (**2014**) 1301465.

[42] A. Polman, M. Knight, E.C. Garnett, B. Ehrler, W.C. Sinke, Photovoltaic Materials: Present Efficiencies and Future Challenges, *Science*, 352 (**2016**) aad4424.

[43] O. Inganäs, Organic Photovoltaics over Three Decades, *Adv. Mater.*, 30 (**2018**) 1800388.

[44] Y. Cui, H. Yao, L. Hong, T. Zhang, Y. Tang, B. Lin, K. Xian, B. Gao, C. An, P. Bi, W. Ma, J. Hou, Organic Photovoltaic Cell with 17% Efficiency and Superior Processability, *National Science Review*, 7 (**2019**) 1239-1246.

[45] O.E. Semonin, J.M. Luther, M.C. Beard, Quantum Dots for Next-Generation Photovoltaics, *Materials Today*, 15 (**2012**) 508-515.

[46] R.J. Ellingson, M.C. Beard, J.C. Johnson, P. Yu, O.I. Micic, A.J. Nozik, A. Shabaev, A.L. Efros, Highly Efficient Multiple Exciton Generation in Colloidal Pbse and PbS Quantum Dots, *Nano Lett.*, 5 (**2005**) 865-871.

[47] P.R. Brown, D. Kim, R.R. Lunt, N. Zhao, M.G. Bawendi, J.C. Grossman, V. Bulović, Energy Level Modification in Lead Sulfide Quantum Dot Thin Films through Ligand Exchange, *ACS Nano*, 8 (**2014**) 5863-5872.

[48] J. Jasieniak, M. Califano, S.E. Watkins, Size-Dependent Valence and Conduction Band-Edge Energies of Semiconductor Nanocrystals, *ACS Nano*, 5 (**2011**) 5888-5902.

[49] D.B. Mitzi, K. Chondroudis, C.R. Kagan, Design, Structure, and Optical Properties of Organic−Inorganic Perovskites Containing an Oligothiophene Chromophore, *Inorg. Chem.*, 38 (**1999**) 6246-6256.

[50] A. Kojima, K. Teshima, Y. Shirai, T. Miyasaka, Organometal Halide Perovskites as Visible-Light Sensitizers for Photovoltaic Cells, *J. Am. Chem. Soc.*, 131 (**2009**) 6050-6051.

[51] H.-S. Kim, C.-R. Lee, J.-H. Im, K.-B. Lee, T. Moehl, A. Marchioro, S.-J. Moon, R. Humphry-Baker, J.-H. Yum, J.E. Moser, M. Grätzel, N.-G. Park, Lead Iodide Perovskite Sensitized All-Solid-State Submicron Thin Film Mesoscopic Solar Cell with Efficiency Exceeding 9%, *Sci. Rep.*, 2 (**2012**) 591.

[52] N.-G. Park, Halide Perovskite Photovoltaics: History, Progress, and Perspectives, *MRS Bulletin*, 43 (**2018**) 527-533.

[53] J. Burschka, N. Pellet, S.-J. Moon, R. Humphry-Baker, P. Gao, M.K. Nazeeruddin, M. Grätzel, Sequential Deposition as a Route to High-Performance Perovskite-Sensitized Solar Cells, *Nature*, 499 (**2013**) 316-319.

[54] M. Liu, M.B. Johnston, H.J. Snaith, Efficient Planar Heterojunction Perovskite Solar Cells by Vapour Deposition, *Nature*, 501 (**2013**) 395-398.

[55] W.S. Yang, J.H. Noh, N.J. Jeon, Y.C. Kim, S. Ryu, J. Seo, S.I. Seok, High-Performance Photovoltaic Perovskite Layers Fabricated through Intramolecular Exchange, *Science*, 348 (**2015**) 1234-1237.

[56] W.S. Yang, B.-W. Park, E.H. Jung, N.J. Jeon, Y.C. Kim, D.U. Lee, S.S. Shin, J. Seo, E.K. Kim, J.H. Noh, S.I. Seok, Iodide Management in Formamidinium-Lead-Halide–Based Perovskite Layers for Efficient Solar Cells, *Science*, 356 (**2017**) 1376-1379.

[57] J. Jeong, M. Kim, J. Seo, H. Lu, P. Ahlawat, A. Mishra, Y. Yang, M.A. Hope, F.T. Eickemeyer, M. Kim, Y.J. Yoon, I.W. Choi, B.P. Darwich, S.J. Choi, Y. Jo, J.H. Lee, B. Walker, S.M. Zakeeruddin, L. Emsley, U. Rothlisberger, A. Hagfeldt, D.S. Kim, M. Grätzel, J.Y. Kim, Pseudo-Halide Anion Engineering for α-$FAPbI_3$ Perovskite Solar Cells, *Nature*, 592 (**2021**) 381-385.

[58] Perovskites Take Steps to Industrialization, *Nature Energy*, 5 (**2020**) 1-1.

[59] P. Löper, S.-J. Moon, S. Martín de Nicolas, B. Niesen, M. Ledinsky, S. Nicolay, J. Bailat, J.-H. Yum, S. De Wolf, C. Ballif, Organic–Inorganic Halide Perovskite/Crystalline Silicon Four-Terminal Tandem Solar Cells, *Phys. Chem. Chem. Phys.*, 17 (**2015**) 1619-1629.

[60] J.P. Mailoa, C.D. Bailie, E.C. Johlin, E.T. Hoke, A.J. Akey, W.H. Nguyen, M.D. McGehee, T. Buonassisi, A 2-Terminal Perovskite/Silicon Multijunction Solar Cell Enabled by a Silicon Tunnel Junction, *Appl. Phys. Lett.*, 106 (**2015**) 121105.

[61] E.L. Unger, E.T. Hoke, C.D. Bailie, W.H. Nguyen, A.R. Bowring, T. Heumüller, M.G. Christoforo, M.D. McGehee, Hysteresis and Transient Behavior in Current–Voltage Measurements of Hybrid-Perovskite Absorber Solar Cells, *Energy Environ. Sci.*, 7 (**2014**) 3690-3698.

[62] D.-H. Kang, N.-G. Park, On the Current–Voltage Hysteresis in Perovskite Solar Cells: Dependence on Perovskite Composition and Methods to Remove Hysteresis, *Adv. Mater.*, 31 (**2019**) 1805214.

[63] H.J. Snaith, A. Abate, J.M. Ball, G.E. Eperon, T. Leijtens, N.K. Noel, S.D. Stranks, J.T.-W. Wang, K. Wojciechowski, W. Zhang, Anomalous Hysteresis in Perovskite Solar Cells, *J. Phys. Chem. Lett.*, 5 (**2014**) 1511-1515.

[64] W. Tress, N. Marinova, T. Moehl, S.M. Zakeeruddin, M.K. Nazeeruddin, M. Grätzel, Understanding the Rate-Dependent J–V Hysteresis, Slow Time Component, and Aging in $CH_3NH_3PbI_3$ Perovskite Solar Cells: The Role of a Compensated Electric Field, *Energy Environ. Sci.*, 8 (**2015**) 995-1004.

[65] H.-S. Kim, I.-H. Jang, N. Ahn, M. Choi, A. Guerrero, J. Bisquert, N.-G. Park, Control of I–V Hysteresis in $CH_3NH_3PbI_3$ Perovskite Solar Cell, *J. Phys. Chem. Lett*, 6 (**2015**) 4633-4639.

[66] T. Zhang, C. Hu, S. Yang, Ion Migration: A "Double-Edged Sword" for Halide-Perovskite-Based Electronic Devices, *Small Methods*, 4 (**2020**) 1900552.

[67] P. Zhao, B.J. Kim, H.S. Jung, Passivation in Perovskite Solar Cells: A Review, *Materials Today Energy*, 7 (**2018**) 267-286.

[68] S. V. Reenen, M. Kemerink, H.J. Snaith, Modeling Anomalous Hysteresis in Perovskite Solar Cells, *J. Phys. Chem. Lett.*, 6 (**2015**) 3808-3814.

[69] P. Calado, A.M. Telford, D. Bryant, X. Li, J. Nelson, B.C. O'Regan, P.R.F. Barnes, Evidence for Ion Migration in Hybrid Perovskite Solar Cells with Minimal Hysteresis, *Nat. Commun.*, 7 (**2016**) 13831.

[70] D. Walter, A. Fell, Y. Wu, T. Duong, C. Barugkin, N. Wu, T. White, K. Weber, Transient Photovoltage in Perovskite Solar Cells: Interaction of Trap-Mediated Recombination and Migration of Multiple Ionic Species, *J. Phys. Chem. C*, 122 (**2018**) 11270-11281.

[71] P. Liu, W. Wang, S. Liu, H. Yang, Z. Shao, Fundamental Understanding of Photocurrent Hysteresis in Perovskite Solar Cells, *Adv. Energy Mater.*, 9 (**2019**) 1803017.

[72] J. Cui, H. Yuan, J. Li, X. Xu, Y. Shen, H. Lin, M. Wang, Recent Progress in Efficient Hybrid Lead Halide Perovskite Solar Cells, *Sci. Technol. Adv. Mater*, 16 (**2015**) 036004.

[73] S. Liu, Y. Guan, Y. Sheng, Y. Hu, Y. Rong, A. Mei, H. Han, A Review on Additives for Halide Perovskite Solar Cells, *Adv. Energy Mater.*, 10 (**2020**) 1902492.

[74] N.J. Jeon, J.H. Noh, Y.C. Kim, W.S. Yang, S. Ryu, S.I. Seok, Solvent Engineering for High-Performance Inorganic–Organic Hybrid Perovskite Solar Cells, *Nat. Mater.*, 13 (**2014**) 897-903.

[75] K.L. Gardner, J.G. Tait, T. Merckx, W. Qiu, U.W. Paetzold, L. Kootstra, M. Jaysankar, R. Gehlhaar, D. Cheyns, P. Heremans, J. Poortmans, Nonhazardous Solvent Systems for Processing Perovskite Photovoltaics, *Adv. Energy Mater.*, 6 (**2016**) 1600386.

[76] G.E. Eperon, V.M. Burlakov, P. Docampo, A. Goriely, H.J. Snaith, Morphological Control for High Performance, Solution-Processed Planar Heterojunction Perovskite Solar Cells, *Adv. Funct. Mater.*, 24 (**2014**) 151-157.

[77] M. Xiao, F. Huang, W. Huang, Y. Dkhissi, Y. Zhu, J. Etheridge, A. Gray-Weale, U. Bach, Y.-B. Cheng, L. Spiccia, A Fast Deposition-Crystallization Procedure for Highly Efficient Lead Iodide Perovskite Thin-Film Solar Cells, *Angew. Chem. Int. Ed.*, 53 (**2014**) 9898-9903.

[78] T. Duong, H. Pham, T.C. Kho, P. Phang, K.C. Fong, D. Yan, Y. Yin, J. Peng, M.A. Mahmud, S. Gharibzadeh, B.A. Nejand, I.M. Hossain, M.R. Khan, N. Mozaffari, Y. Wu, H.

Shen, J. Zheng, H. Mai, W. Liang, C. Samundsett, M. Stocks, K. McIntosh, G.G. Andersson, U. Lemmer, B.S. Richards, U.W. Paetzold, A. Ho-Ballie, Y. Liu, D. Macdonald, A. Blakers, J. Wong-Leung, T. White, K. Weber, K. Catchpole, High Efficiency Perovskite-Silicon Tandem Solar Cells: Effect of Surface Coating Versus Bulk Incorporation of 2D Perovskite, *Adv. Energy Mater.*, 10 (**2020**) 1903553.

[79] F. Huang, M. Li, P. Siffalovic, G. Cao, J. Tian, From Scalable Solution Fabrication of Perovskite Films Towards Commercialization of Solar Cells, *Energy Environ. Sci.*, 12 (**2019**) 518-549.

[80] N.-G. Park, K. Zhu, Scalable Fabrication and Coating Methods for Perovskite Solar Cells and Solar Modules, *Nat. Rev. Mater*, 5 (**2020**) 333-350.

[81] N.-G. Park, Methodologies for High Efficiency Perovskite Solar Cells, *Nano Converg*, 3 (**2016**) 15-15.

[82] Q. Dong, Y. Yuan, Y. Shao, Y. Fang, Q. Wang, J. Huang, Abnormal Crystal Growth in $CH_3NH_3PbI_{3-X}Cl_x$ Using a Multi-Cycle Solution Coating Process, *Energy Environ. Sci.*, 8 (**2015**) 2464-2470.

[83] C. Roldán-Carmona, O. Malinkiewicz, A. Soriano, G. Mínguez Espallargas, A. Garcia, P. Reinecke, T. Kroyer, M.I. Dar, M.K. Nazeeruddin, H.J. Bolink, Flexible High Efficiency Perovskite Solar Cells, *Energy Environ. Sci.*, 7 (**2014**) 994-997.

[84] P. Gao, M. Grätzel, M.K. Nazeeruddin, Organohalide Lead Perovskites for Photovoltaic Applications, *Energy Environ. Sci.*, 7 (**2014**) 2448-2463.

[85] T. Duong, Y. Wu, H. Shen, J. Peng, X. Fu, D. Jacobs, E.-C. Wang, T.C. Kho, K.C. Fong, M. Stocks, E. Franklin, A. Blakers, N. Zin, K. McIntosh, W. Li, Y.-B. Cheng, T.P. White, K. Weber, K. Catchpole, Rubidium Multication Perovskite with Optimized Bandgap for Perovskite-Silicon Tandem with over 26% Efficiency, *Adv. Energy Mater.*, 7 (**2017**) 1700228.

[86] M. Saliba, T. Matsui, J.-Y. Seo, K. Domanski, J.-P. Correa-Baena, M.K. Nazeeruddin, S.M. Zakeeruddin, W. Tress, A. Abate, A. Hagfeldt, M. Grätzel, Cesium-Containing Triple Cation Perovskite Solar Cells: Improved Stability, Reproducibility and High Efficiency, *Energy Environ. Sci.*, 9 (**2016**) 1989-1997.

[87] M.R. Filip, G.E. Eperon, H.J. Snaith, F. Giustino, Steric Engineering of Metal-Halide Perovskites with Tunable Optical Band Gaps, *Nat. Commun.*, 5 (**2014**) 5757.

[88] V.M. Goldschmidt, Die Gesetze Der Krystallochemie, *Naturwissenschaften*, 14 (**1926**) 477-485.

[89] W. Li, E. Ionescu, R. Riedel, A. Gurlo, Can We Predict the Formability of Perovskite Oxynitrides from Tolerance and Octahedral Factors?, *J. Mater. Chem. A*, 1 (**2013**) 12239-12245.

[90] I.M. Reaney, E.L. Colla, N. Setter, Dielectric and Structural Characteristics of Ba- and Sr-Based Complex Perovskites as a Function of Tolerance Factor, *Jpn. J. Appl. Phys.*, 33 (**1994**) 3984-3990.

[91] Z. Li, M. Yang, J.-S. Park, S.-H. Wei, J.J. Berry, K. Zhu, Stabilizing Perovskite Structures by Tuning Tolerance Factor: Formation of Formamidinium and Cesium Lead Iodide Solid-State Alloys, *Chem. Mater.*, 28 (**2016**) 284-292.

[92] A. Glazer, The Classification of Tilted Octahedra in Perovskites, *Acta Crystallographica Section B*, 28 (**1972**) 3384-3392.

[93] A. Glazer, Simple Ways of Determining Perovskite Structures, *Acta Crystallographica Section A*, 31 (**1975**) 756-762.

[94] C.J. Howard, H.T. Stokes, Group-Theoretical Analysis of Octahedral Tilting in Perovskites, *Acta Crystallographica Section B*, 54 (**1998**) 782-789.

[95] C.C. Stoumpos, C.D. Malliakas, M.G. Kanatzidis, Semiconducting Tin and Lead Iodide Perovskites with Organic Cations: Phase Transitions, High Mobilities, and near-Infrared Photoluminescent Properties, *Inorg. Chem.*, 52 (**2013**) 9019-9038.

[96] Z. Chen, B. Turedi, A.Y. Alsalloum, C. Yang, X. Zheng, I. Gereige, A. AlSaggaf, O.F. Mohammed, O.M. Bakr, Single-Crystal $MAPbI_3$ Perovskite Solar Cells Exceeding 21% Power Conversion Efficiency, *ACS Energy Lett.*, 4 (**2019**) 1258-1259.

[97] P.S. Whitfield, N. Herron, W.E. Guise, K. Page, Y.Q. Cheng, I. Milas, M.K. Crawford, Structures, Phase Transitions and Tricritical Behavior of the Hybrid Perovskite Methyl Ammonium Lead Iodide, *Sci. Rep.*, 6 (**2016**) 35685.

[98] R. Comin, M.K. Crawford, A.H. Said, N. Herron, W.E. Guise, X. Wang, P.S. Whitfield, A. Jain, X. Gong, A.J.H. McGaughey, E.H. Sargent, Lattice Dynamics and the Nature of Structural Transitions in Organolead Halide Perovskites, *Phys. Rev. B*, 94 (**2016**) 094301.

[99] W. Rehman, R.L. Milot, G.E. Eperon, C. Wehrenfennig, J.L. Boland, H.J. Snaith, M.B. Johnston, L.M. Herz, Charge-Carrier Dynamics and Mobilities in Formamidinium Lead Mixed-Halide Perovskites, *Adv. Mater.*, 27 (**2015**) 7938-7944.

[100] C.L. Davies, J. Borchert, C.Q. Xia, R.L. Milot, H. Kraus, M.B. Johnston, L.M. Herz, Impact of the Organic Cation on the Optoelectronic Properties of Formamidinium Lead Triiodide, *J. Phys. Chem. Lett.*, 9 (**2018**) 4502-4511.

[101] M.T. Weller, O.J. Weber, J.M. Frost, A. Walsh, Cubic Perovskite Structure of Black Formamidinium Lead Iodide, α-$[HC(NH_2)_2]PbI_3$, at 298 K, *J. Phys. Chem. Lett.*, 6 (**2015**) 3209-3212.

[102] J.-W. Lee, D.-J. Seol, A.-N. Cho, N.-G. Park, High-Efficiency Perovskite Solar Cells Based on the Black Polymorph of $HC(NH_2)_2PbI_3$, *Adv. Mater.*, 26 (**2014**) 4991-4998.

[103] H. Zhu, T. Cai, M. Que, J.-P. Song, B.M. Rubenstein, Z. Wang, O. Chen, Pressure-Induced Phase Transformation and Band-Gap Engineering of Formamidinium Lead Iodide Perovskite Nanocrystals, *J. Phys. Chem. Lett.*, 9 (**2018**) 4199-4205.

[104] P. Uttam, V. Kumar, K.-H. Kim, A. Deep, Nanotwinning: Generation, Properties, and Application, *Materials & Design*, 192 (**2020**) 108752.

[105] H. Zhou, M. Guo, L. Wang, J. Zhao, Effect of Thickness for Nanotwins on the Mechanical Properties of a Hastelloy, *Applied Nanoscience*, 10 (**2020**) 1475-1480.

[106] F. Duan, Y. Lin, J. Pan, L. Zhao, Q. Guo, D. Zhang, Y. Li, Ultrastrong Nanotwinned Pure Nickel with Extremely Fine Twin Thickness, *Science Advances*, 7 (**2021**) eabg5113.

[107] Y.-C. Wu, C.-C. Lee, H.-Y. Lu, D.E. McCauley, M.S.H. Chu, The {111} Growth Twins in Tetragonal Barium Titanate, *J. Am. Ceram. Soc.*, 89 (**2006**) 1679-1686.

[108] O. Eibl, P. Pongratz, P. Skalicky, Crystallography of (111) Twins in $BaTiO_3$, *Philos. Mag. B*, 57 (**1988**) 521-534.

[109] K. Lu, L. Lu, S. Suresh, Strengthening Materials by Engineering Coherent Internal Boundaries at the Nanoscale, *Science*, 324 (**2009**) 349-352.

[110] K. Lu, Stabilizing Nanostructures in Metals Using Grain and Twin Boundary Architectures, *Nature Reviews Materials*, 1 (**2016**) 16019.

[111] J.W. Edington, Electron Diffraction in the Electron Microscope, Macmillan, London, (**1975**).

[112] M. Song, G. Zhou, N. Lu, J. Lee, E. Nakouzi, H. Wang, D. Li, Oriented Attachment Induces Fivefold Twins by Forming and Decomposing High-Energy Grain Boundaries, *Science*, 367 (**2020**) 40-45.

[113] J. Arbiol, S. Estradé, J.D. Prades, A. Cirera, F. Furtmayr, C. Stark, A. Laufer, M. Stutzmann, M. Eickhoff, M.H. Gass, A.L. Bleloch, F. Peiró, J.R. Morante, Triple-Twin Domains in Mg Doped Gan Wurtzite Nanowires: Structural and Electronic Properties of This Zinc-Blende-Like Stacking, *Nanotechnology*, 20 (**2009**) 145704.

[114] O. Bouaziz, S. Allain, C. Scott, Effect of Grain and Twin Boundaries on the Hardening Mechanisms of Twinning-Induced Plasticity Steels, *Scripta Materialia*, 58 (**2008**) 484-487.

[115] Q. Ma, H. El Kadiri, A.L. Oppedal, J.C. Baird, B. Li, M.F. Horstemeyer, S.C. Vogel, Twinning Effects in a Rod-Textured AM30 Magnesium Alloy, *Int. J. Plast.*, 29 (**2012**) 60-76.

[116] R.E. Algra, M.A. Verheijen, M.T. Borgström, L.-F. Feiner, G. Immink, W.J.P. van Enckevort, E. Vlieg, E.P.A.M. Bakkers, Twinning Superlattices in Indium Phosphide Nanowires, *Nature*, 456 (**2008**) 369-372.

[117] P. Caroff, K.A. Dick, J. Johansson, M.E. Messing, K. Deppert, L. Samuelson, Controlled Polytypic and Twin-Plane Superlattices in III–V Nanowires, *Nat. Nanotechnol.*, 4 (**2009**) 50-55.

[118] S. Kauffmann-Weiss, M.E. Gruner, A. Backen, L. Schultz, P. Entel, S. Fähler, Magnetic Nanostructures by Adaptive Twinning in Strained Epitaxial Films, *Phys. Rev. Lett.*, 107 (**2011**) 206105.

[119] D.Y. Cong, Y.D. Zhang, C. Esling, Y.D. Wang, J.S. Lecomte, X. Zhao, L. Zuo, Microstructural and Crystallographic Characteristics of Interpenetrating and Non-Interpenetrating Multiply Twinned Nanostructure in a Ni–Mn–Ga Ferromagnetic Shape Memory Alloy, *Acta Materialia*, 59 (**2011**) 7070-7081.

[120] A. Aird, E.K.H. Salje, Sheet Superconductivity in Twin Walls: Experimental Evidence of WO_{3-X}, *J. Phys. Condens. Matter.*, 10 (**1998**) L377-L380.

[121] J. Bao, D.C. Bell, F. Capasso, J.B. Wagner, T. Mårtensson, J. Trägårdh, L. Samuelson, Optical Properties of Rotationally Twinned Inp Nanowire Heterostructures, *Nano Lett.*, 8 (**2008**) 836-841.

[122] Z. Ikonić, G.P. Srivastava, J.C. Inkson, Electronic Properties of Twin Boundaries and Twinning Superlattices in Diamond-Type and Zinc-Blende-Type Semiconductors, *Phys. Rev. B*, 48 (**1993**) 17181-17193.

[123] Z. Ikonic, G.P. Srivastava, J.C. Inkson, Optical Properties of Twinning Superlattices in Diamond-Type and Zincblende-Type Semiconductors, *Phys. Rev. B*, 52 (**1995**) 14078-14085.

[124] Z. Ikonic, G.P. Srivastava, J.C. Inkson, Electronic Properties of PbS(111) Twin Boundaries and Twinning Superlattices, *Superlattices and Microstructures*, 17 (**1995**) 393-396.

[125] Y.Q. Wang, R. Smirani, G.G. Ross, Nanotwinning in Silicon Nanocrystals Produced by Ion Implantation, *Nano Lett.*, 4 (**2004**) 2041-2045.

[126] L.C. Kimerling, H.J. Leamy, J.R. Patel, The Electrical Properties of Stacking Faults and Precipitates in Heat-Treated Dislocation-Free Czochralski Silicon, *Appl. Phys. Lett.*, 30 (**1977**) 217-219.

[127] H. Sugimoto, M. Inoue, M. Tajima, A. Ogura, Y. Ohshita, Analysis of Intra-Grain Defects in Multicrystalline Silicon Wafers by Photoluminescence Mapping and Spectroscopy, *J. Appl. Phys.*, 45 (**2006**) L641-L643.

[128] R.L. Woo, R. Xiao, Y. Kobayashi, L. Gao, N. Goel, M.K. Hudait, T.E. Mallouk, R.F. Hicks, Effect of Twinning on the Photoluminescence and Photoelectrochemical Properties of Indium Phosphide Nanowires Grown on Silicon (111), *Nano Lett.*, 8 (**2008**) 4664-4669.

[129] K.-C. Chen, W.-W. Wu, C.-N. Liao, L.-J. Chen, K.N. Tu, Stability of Nanoscale Twins in Copper under Electric Current Stressing, *J. Appl. Phys.*, 108 (**2010**) 066103.

[130] M.A. García, M.L. Ruiz-González, G.F. de la Fuente, P. Crespo, J.M. González, J. Llopis, J.M. González-Calbet, M. Vallet-Regí, A. Hernando, Ferromagnetism in Twinned Pt Nanoparticles Obtained by Laser Ablation, *Chem. Mater.*, 19 (**2007**) 889-893.

[131] V. Kopecký, O. Heczko, Change of Magnetic Domain Structure by Mechanically Induced Twin Boundary Motion in Ni-Mn-Ga Single Crystal, *J. Phys.: Conf. Ser.*, 903 (**2017**) 012013.

[132] S.-H. Yoo, K.T. Butler, A. Soon, A. Abbas, J.M. Walls, A. Walsh, Identification of Critical Stacking Faults in Thin-Film Cdte Solar Cells, *Appl. Phys. Lett.*, 105 (**2014**) 062104.

[133] L. Sun, X. He, J. Lu, Nanotwinned and Hierarchical Nanotwinned Metals: A Review of Experimental, Computational and Theoretical Efforts, *Computational Materials*, 4 (**2018**) 6.

[134] T. Suzuki, Y. Nishi, M. Fujimoto, Ruddlesden–Popper Planar Faults and Nanotwins in Heteroepitaxial Nonstoichiometric Barium Titanate Thin Films, *J. Am. Ceram. Soc.*, 83 (**2000**) 3185-3195.

[135] F. Bertolotti, L. Protesescu, M.V. Kovalenko, S. Yakunin, A. Cervellino, S.J.L. Billinge, M.W. Terban, J.S. Pedersen, N. Masciocchi, A. Guagliardi, Coherent Nanotwins and Dynamic Disorder in Cesium Lead Halide Perovskite Nanocrystals, *ACS Nano*, 11 (**2017**) 3819-3831.

[136] H.T. Pham, T. Duong, K.J. Weber, J. Wong-Leung, Insights into Twinning Formation in Cubic and Tetragonal Multi-Cation Mixed-Halide Perovskite, *ACS Materials Letters*, 2 (**2020**) 415-424.

[137] Y.M. Wang, F. Sansoz, T. LaGrange, R.T. Ott, J. Marian, T.W. Barbee, A.V. Hamza, Defective Twin Boundaries in Nanotwinned Metals, *Nat. Mater.*, 12 (**2013**) 697-702.

[138] K.-C. Chen, W.-W. Wu, C.-N. Liao, L.-J. Chen, K.N. Tu, Observation of Atomic Diffusion at Twin-Modified Grain Boundaries in Copper, *Science*, 321 (**2008**) 1066-1069.

[139] X.-M. Luo, X.-F. Zhu, G.-P. Zhang, Nanotwin-Assisted Grain Growth in Nanocrystalline Gold Films under Cyclic Loading, *Nat. Commun.*, 5 (**2014**) 3021.

[140] Y.T. Zhu, X.Z. Liao, X.L. Wu, Deformation Twinning in Nanocrystalline Materials, *Progress in Materials Science*, 57 (**2012**) 1-62.

[141] K.-C. Kim, J. Lee, B.K. Kim, W.Y. Choi, H.J. Chang, S.O. Won, B. Kwon, S.K. Kim, D.-B. Hyun, H.J. Kim, H.C. Koo, J.-H. Choi, D.-I. Kim, J.-S. Kim, S.-H. Baek, Free-Electron Creation at the 60° Twin Boundary in Bi_2Te_3, *Nat. Commun.*, 7 (**2016**) 12449.

[142] H.D. Megaw, Crystal Structures : A Working Approach, WB Saunders Company, Philadelphia; London; Toronto, **(1973)**.

[143] J.-S. Park, Z. Li, J.N. Wilson, W.-J. Yin, A. Walsh, Hexagonal Stacking Faults Act as Hole-Blocking Layers in Lead Halide Perovskites, *ACS Energy Lett.*, 5 (**2020**) 2231-2233.

[144] P. Gratia, I. Zimmermann, P. Schouwink, J.-H. Yum, J.-N. Audinot, K. Sivula, T. Wirtz, M.K. Nazeeruddin, The Many Faces of Mixed Ion Perovskites: Unraveling and Understanding the Crystallization Process, *ACS Energy Lett.*, 2 (**2017**) 2686-2693.

[145] M.E. Kamminga, G.A. de Wijs, R.W.A. Havenith, G.R. Blake, T.T.M. Palstra, The Role of Connectivity on Electronic Properties of Lead Iodide Perovskite-Derived Compounds, *Inorg. Chem.*, 56 (**2017**) 8408-8414.

[146] R.W. Cahn, Twinned Crystals, *Adv. Phys.*, 3 (**1954**) 363-445.

[147] Twinning, Crystallography and Crystal Defects, pp. 335-361.

[148] K.P. McKenna, Electronic Properties of {111} Twin Boundaries in a Mixed-Ion Lead Halide Perovskite Solar Absorber, *ACS Energy Lett.*, 3 (**2018**) 2663-2668.

[149] M.U. Rothmann, W. Li, Y. Zhu, U. Bach, L. Spiccia, J. Etheridge, Y.-B. Cheng, Direct Observation of Intrinsic Twin Domains in Tetragonal $CH_3NH_3PbI_3$, *Nat. Commun.*, 8 (**2017**) 14547.

[150] Y. Liu, L. Collins, R. Proksch, S. Kim, B.R. Watson, B. Doughty, T.R. Calhoun, M. Ahmadi, A.V. Ievlev, S. Jesse, S.T. Retterer, A. Belianinov, K. Xiao, J. Huang, B.G. Sumpter, S.V. Kalinin, B. Hu, O.S. Ovchinnikova, Chemical Nature of Ferroelastic Twin Domains in $CH_3Nh_3PbI_3$ Perovskite, *Nat. Mater.*, 17 (**2018**) 1013-1019.

[151] H. Röhm, T. Leonhard, M.J. Hoffmann, A. Colsmann, Ferroelectric Domains in Methylammonium Lead Iodide Perovskite Thin-Films, *Energy Environ. Sci.*, 10 (**2017**) 950-955.

[152] W.-J. Yin, T. Shi, Y. Yan, Unique Properties of Halide Perovskites as Possible Origins of the Superior Solar Cell Performance, *Adv. Mater.*, 26 (**2014**) 4653-4658.

[153] I.M. Hermes, S.A. Bretschneider, V.W. Bergmann, D. Li, A. Klasen, J. Mars, W. Tremel, F. Laquai, H.-J. Butt, M. Mezger, R. Berger, B.J. Rodriguez, S.A.L. Weber, Ferroelastic Fingerprints in Methylammonium Lead Iodide Perovskite, *J. Phys. Chem. C*, 120 (**2016**) 5724-5731.

[154] T.W. Kim, S. Uchida, T. Matsushita, L. Cojocaru, R. Jono, K. Kimura, D. Matsubara, M. Shirai, K. Ito, H. Matsumoto, T. Kondo, H. Segawa, Self-Organized Superlattice and Phase Coexistence inside Thin Film Organometal Halide Perovskite, *Adv. Mater.*, 30 (**2018**) 1705230.

[155] Y. Liu, L. Collins, A. Belianinov, S.M. Neumayer, A.V. Ievlev, M. Ahmadi, K. Xiao, S.T. Retterer, S. Jesse, S.V. Kalinin, B. Hu, O.S. Ovchinnikova, Dynamic Behavior of CH3Nh3PbI3 Perovskite Twin Domains, *Appl. Phys. Lett.*, 113 (**2018**) 072102.

[156] X. Xiao, W. Li, Y. Fang, Y. Liu, Y. Shao, S. Yang, J. Zhao, X. Dai, R. Zia, J. Huang, Benign Ferroelastic Twin Boundaries in Halide Perovskites for Charge Carrier Transport and Recombination, *Nat. Commun.*, 11 (**2020**) 2215.

[157] Y. Liu, P. Trimby, L. Collins, M. Ahmadi, A. Winkelmann, R. Proksch, O.S. Ovchinnikova, Correlating Crystallographic Orientation and Ferroic Properties of Twin Domains in Metal Halide Perovskites, *ACS Nano*, 15 (**2021**) 7139-7148.

[158] X. Qian, M. Kawai, H. Goto, J. Li, Effect of Twin Boundaries and Structural Polytypes on Electron Transport in GaAs, *Computational Materials Science*, 108 (**2015**) 258-263.

[159] M. Liu, D. Jing, Z. Zhou, L. Guo, Twin-Induced One-Dimensional Homojunctions Yield High Quantum Efficiency for Solar Hydrogen Generation, *Nat. Commun.*, 4 (**2013**) 2278.

[160] C. Eames, J.M. Frost, P.R.F. Barnes, B.C. O'Regan, A. Walsh, M.S. Islam, Ionic Transport in Hybrid Lead Iodide Perovskite Solar Cells, *Nat. Commun.*, 6 (**2015**) 7497.

[161] D. Kim, J.S. Yun, P. Sharma, D.S. Lee, J. Kim, A.M. Soufiani, S. Huang, M.A. Green, A.W.Y. Ho-Baillie, J. Seidel, Light- and Bias-Induced Structural Variations in Metal Halide Perovskites, *Nat. Commun.*, 10 (**2019**) 444.

[162] H.P. Meyers, H.P. Myers, Introductory Solid State Physics, Second Edition, Taylor & Francis, (**1997**).

[163] D.R. Baer, S. Thevuthasan, Chapter 16 - Characterization of Thin Films and Coatings, in: P.M. Martin (Ed.) Handbook of Deposition Technologies for Films and Coatings (Third Edition), William Andrew Publishing, Boston, (**2010**), pp. 749-864.

[164] Introduction, X-Ray Photoelectron Spectroscopy, (**2011**), pp. 1-12.

[165] K. Volgmann, F. Voigts, W. Maus-Friedrichs, The Interaction of H_2O Molecules with Iron Films Studied with MIES, UPS and XPS, *Surface Science*, 606 (**2012**) 858-864.

[166] S. Oswald, Growth Studies of Ti-Based Films Deposited on Si and SiO_2 Using Angle-Resolved XPS, *Surf. Interface Anal*, 42 (**2010**) 1289-1294.

[167] C. Wagner, Sensitivity Factors for XPS Analysis of Surface Atoms, *Journal of Electron Spectroscopy and Related Phenomena*, 32 (**1983**) 99-102.

[168] M.U. Rothmann, W. Li, J. Etheridge, Y.-B. Cheng, Microstructural Characterisations of Perovskite Solar Cells – from Grains to Interfaces: Techniques, Features, and Challenges, *Adv. Energy Mater.*, 7 (**2017**) 1700912.

[169] G. Joseph, N. Dale, M. Joseph, R. Nicholas, S. John Henry, J. David, Scanning Electron Microscopy and X-Ray Microanalysis, Springer, New York, (**2018**).

[170] R. Ludwig, Scanning Electron Microscopy: Physics of Image Formation and Microanalysis, Springer-Verlag Berlin Heidelberg, (**1998**).

[171] J. Hidalgo, A.-F. Castro-Méndez, J.-P. Correa-Baena, Imaging and Mapping Characterization Tools for Perovskite Solar Cells, *Adv. Energy Mater.*, 9 (**2019**) 1900444.

[172] T. Sui, B. Song, J. Dluhos, L. Lu, A.M. Korsunsky, Nanoscale Chemical Mapping of Li-Ion Battery Cathode Material by FIB-SEM and Tof-SIMS Multi-Modal Microscopy, *Nano Energy*, 17 (**2015**) 254-260.

[173] J.A. Whitby, F. Ostlund, P. Horvath, M. Gabureac, J.L. Riesterer, I. Utke, M. Hohl, V. Friedli, M. Bechelany, J. Michler, High Spatial Resolution Time-of-Flight Secondary Ion Mass Spectrometry for the Masses: A Novel Orthogonal Tof-FIB-SIMS Instrument with in Situ Afm, *Advances in Materials Science and Engineering*, 2012 (**2012**) 13.

[174] J.P. Hofmann, M. Rohnke, B.M. Weckhuysen, Recent Advances in Secondary Ion Mass Spectrometry of Solid Acid Catalysts: Large Zeolite Crystals under Bombardment, *Physical Chemistry Chemical Physics*, 16 (**2014**) 5465-5474.

[175] D.B. Williams, C.B. Carter, *Transmission Electron Microscopy: A Textbook for Materials Science*, Springer, New York, (**2009**).

[176] R.F. Egerton, P. Li, M. Malac, Radiation Damage in the Tem and Sem, *Micron*, 35 (**2004**) 399-409.

[177] P. Li, Electron Irradiation Damage to Organic Light-Emitting Materials, University of Alberta, (**2004**).

[178] H. Gu, G. Li, C. Liu, F. Yuan, F. Han, L. Zhang, S. Wu, Considerable Knock-on Displacement of Metal Atoms under a Low Energy Electron Beam, *Sci. Rep.*, 7 (**2017**) 184.

[179] M. K. Rao, D.N. Sangeetha, M. Selvakumar, Y.N. Sudhakar, M.G. Mahesha, Review on Persistent Challenges of Perovskite Solar Cells' Stability, *Solar Energy*, 218 (**2021**) 469-491.

[180] W. Xiang, S. Liu, W. Tress, A Review on the Stability of Inorganic Metal Halide Perovskites: Challenges and Opportunities for Stable Solar Cells, *Energy Environ. Sci.*, 14 (**2021**) 2090-2113.

[181] Y. Li, W. Zhou, Y. Li, W. Huang, Z. Zhang, G. Chen, H. Wang, G.-H. Wu, N. Rolston, R. Vila, W. Chiu, Y. Cui, Unravelling Degradation Mechanisms and Atomic Structure of Organic-Inorganic Halide Perovskites by Cryo-Em, *Joule*, 3 (**2019**) 2854-2866.

[182] A. Manekkathodi, A. Marzouk, J. Ponraj, A. Belaidi, S. Ashhab, Observation of Structural Phase Transitions and PbI_2 Formation During the Degradation of Triple-Cation Double-Halide Perovskites, *ACS Appl. Energy Mater.*, 3 (**2020**) 6302-6309.

[183] M. Zhang, J.S. Yun, Q. Ma, J. Zheng, C.F.J. Lau, X. Deng, J. Kim, D. Kim, J. Seidel, M.A. Green, S. Huang, A.W.Y. Ho-Baillie, High-Efficiency Rubidium-Incorporated Perovskite Solar Cells by Gas Quenching, *ACS Energy Lett.*, 2 (**2017**) 438-444.

[184] Y.H. Park, I. Jeong, S. Bae, H.J. Son, P. Lee, J. Lee, C.-H. Lee, M.J. Ko, Inorganic Rubidium Cation as an Enhancer for Photovoltaic Performance and Moisture Stability of $HC(NH_2)_2PbI_3$ Perovskite Solar Cells, *Adv. Funct. Mater.*, 27 (**2017**) 1605988.

[185] T. Duong, H.K. Mulmudi, H. Shen, Y. Wu, C. Barugkin, Y.O. Mayon, H.T. Nguyen, D. Macdonald, J. Peng, M. Lockrey, W. Li, Y.-B. Cheng, T.P. White, K. Weber, K. Catchpole, Structural Engineering Using Rubidium Iodide as a Dopant under Excess Lead Iodide Conditions for High Efficiency and Stable Perovskites, *Nano Energy*, 30 (**2016**) 330-340.

[186] M. Saliba, T. Matsui, K. Domanski, J.-Y. Seo, A. Ummadisingu, S.M. Zakeeruddin, J.-P. Correa-Baena, W.R. Tress, A. Abate, A. Hagfeldt, M. Grätzel, Incorporation of Rubidium Cations into Perovskite Solar Cells Improves Photovoltaic Performance, *Science*, 354 (**2016**) 206-209.

[187] J.-W. Lee, D.-H. Kim, H.-S. Kim, S.-W. Seo, S.M. Cho, N.-G. Park, Formamidinium and Cesium Hybridization for Photo- and Moisture-Stable Perovskite Solar Cell, *Adv. Energy Mater.*, 5 (**2015**) 1501310.

[188] C. Yi, J. Luo, S. Meloni, A. Boziki, N. Ashari-Astani, C. Grätzel, S.M. Zakeeruddin, U. Röthlisberger, M. Grätzel, Entropic Stabilization of Mixed a-Cation Abx_3 Metal Halide Perovskites for High Performance Perovskite Solar Cells, *Energy Environ. Sci.*, 9 (**2016**) 656-662.

[189] D.P. McMeekin, G. Sadoughi, W. Rehman, G.E. Eperon, M. Saliba, M.T. Hörantner, A. Haghighirad, N. Sakai, L. Korte, B. Rech, M.B. Johnston, L.M. Herz, H.J. Snaith, A Mixed-Cation Lead Mixed-Halide Perovskite Absorber for Tandem Solar Cells, *Science*, 351 (**2016**) 151-155.

[190] S.-H. Turren-Cruz, A. Hagfeldt, M. Saliba, Methylammonium-Free, High-Performance, and Stable Perovskite Solar Cells on a Planar Architecture, *Science*, 362 (**2018**) 449-453.

[191] B. Philippe, M. Saliba, J.-P. Correa-Baena, U.B. Cappel, S.-H. Turren-Cruz, M. Grätzel, A. Hagfeldt, H. Rensmo, Chemical Distribution of Multiple Cation (Rb^+, Cs^+, MA^+, and FA^+) Perovskite Materials by Photoelectron Spectroscopy, *Chem. Mater*, 29 (**2017**) 3589-3596.

[192] S. Shukla, S. Shukla, L.J. Haur, S.S.H. Dintakurti, G. Han, A. Priyadarshi, T. Baikie, S.G. Mhaisalkar, N. Mathews, Effect of Formamidinium/Cesium Substitution and PbI_2 on the Long-Term Stability of Triple-Cation Perovskites, *ChemSusChem*, 10 (**2017**) 3804-3809.

[193] Y. Hu, M.F. Aygüler, M.L. Petrus, T. Bein, P. Docampo, Impact of Rubidium and Cesium Cations on the Moisture Stability of Multiple-Cation Mixed-Halide Perovskites, *ACS Energy Lett.*, 2 (**2017**) 2212-2218.

[194] P. Yadav, M.I. Dar, N. Arora, E.A. Alharbi, F. Giordano, S.M. Zakeeruddin, M. Grätzel, The Role of Rubidium in Multiple-Cation-Based High-Efficiency Perovskite Solar Cells, *Adv.Mater.*, 29 (**2017**) 1701077.

[195] Q. Jeangros, M. Duchamp, J. Werner, M. Kruth, R.E. Dunin-Borkowski, B. Niesen, C. Ballif, A. Hessler-Wyser, In Situ Tem Analysis of Organic–Inorganic Metal-Halide Perovskite Solar Cells under Electrical Bias, *Nano Lett.*, 16 (**2016**) 7013-7018.

[196] T.W. Kim, N. Shibayama, L. Cojocaru, S. Uchida, T. Kondo, H. Segawa, Real-Time in Situ Observation of Microstructural Change in Organometal Halide Perovskite Induced by Thermal Degradation, *Adv. Funct. Mater.*, 28 (**2018**) 1804039.

[197] N. Onoda-Yamamuro, T. Matsuo, H. Suga, Calorimetric and Ir Spectroscopic Studies of Phase Transitions in Methylammonium Trihalogenoplumbates (Ii)†, *J. Phys. Chem. Solids*, 51 (**1990**) 1383-1395.

[198] Y. Zhou, A.L. Vasiliev, W. Wu, M. Yang, S. Pang, K. Zhu, N.P. Padture, Crystal Morphologies of Organolead Trihalide in Mesoscopic/Planar Perovskite Solar Cells, *J. Phys. Chem. Lett.*, 6 (**2015**) 2292-2297.

[199] M. Yang, Y. Zhou, Y. Zeng, C.-S. Jiang, N.P. Padture, K. Zhu, Square-Centimeter Solution-Processed Planar $CH_3NH_3PbI_3$ Perovskite Solar Cells with Efficiency Exceeding 15%, *Adv. Mater.*, 27 (**2015**) 6363-6370.

[200] D.-Y. Son, J.-W. Lee, Y.J. Choi, I.-H. Jang, S. Lee, P.J. Yoo, H. Shin, N. Ahn, M. Choi, D. Kim, N.-G. Park, Self-Formed Grain Boundary Healing Layer for Highly Efficient $CH_3NH_3PbI_3$ Perovskite Solar Cells, *Nat. Energy*, 1 (**2016**) 16081.

[201] N. Pellet, P. Gao, G. Gregori, T.-Y. Yang, M.K. Nazeeruddin, J. Maier, M. Grätzel, Mixed-Organic-Cation Perovskite Photovoltaics for Enhanced Solar-Light Harvesting, *Angew. Chem. Int. Ed.*, 53 (**2014**) 3151-3157.

[202] A. Binek, F.C. Hanusch, P. Docampo, T. Bein, Stabilization of the Trigonal High-Temperature Phase of Formamidinium Lead Iodide, *J. Phys. Chem. Lett.*, 6 (**2015**) 1249-1253.

[203] Y. Zhang, Z. Zhou, F. Ji, Z. Li, G. Cui, P. Gao, E. Oveisi, M.K. Nazeeruddin, S. Pang, Trash into Treasure: δ-$FAPbI_3$ Polymorph Stabilized $MAPbI_3$ Perovskite with Power Conversion Efficiency Beyond 21%, *Adv.Mater.*, 30 (**2018**) 1707143.

[204] X. Zheng, C. Wu, S.K. Jha, Z. Li, K. Zhu, S. Priya, Improved Phase Stability of Formamidinium Lead Triiodide Perovskite by Strain Relaxation, *ACS Energy Lett.*, 1 (**2016**) 1014-1020.

[205] T. Duong, Y. Wu, H. Shen, J. Peng, S. Zhao, N. Wu, M. Lockrey, T. White, K. Weber, K. Catchpole, Light and Elevated Temperature Induced Degradation (LETID) in Perovskite Solar Cells and Development of Stable Semi-Transparent Cells, *Sol. Energy Mater. Sol. Cells*, 188 (**2018**) 27-36.

[206] D. Alberts, L. von Werra, F. Oestlund, U. Rohner, M. Hohl, J. Michler, J.A. Whitby, Design and Performance of Two Orthogonal Extraction Time of Flight Secondary Ion Mass Spectrometers for Focused Ion Beam Instruments, *Instrumentation Science & Technology*, 42 (**2014**) 432-445.

[207] D.-H. Lim, P. Ramasamy, D.-H. Kwak, J.-S. Lee, Solution-Phase Synthesis of Rubidium Lead Iodide Orthorhombic Perovskite Nanowires, *Nanotechnology*, 28 (**2017**) 255601.

[208] M.-H. Jung, S.H. Rhim, D. Moon, TiO_2/$RbPbI_3$ Halide Perovskite Solar Cells, *Solar Energy Materials and Solar Cells*, 172 (**2017**) 44-54.

[209] T. Baikie, Y. Fang, J.M. Kadro, M. Schreyer, F. Wei, S.G. Mhaisalkar, M. Graetzel, T.J. White, Synthesis and Crystal Chemistry of the Hybrid Perovskite $(CH_3NH_3)PbI_3$ for Solid-State Sensitised Solar Cell Applications, *J. Mater. Chem. A*, 1 (**2013**) 5628-5641.

[210] D.J. Kubicki, D. Prochowicz, A. Hofstetter, S.M. Zakeeruddin, M. Grätzel, L. Emsley, Phase Segregation in Cs-, Rb- and K-Doped Mixed-Cation $(MA)_X(FA)_{1-X}PbI_3$ Hybrid Perovskites from Solid-State NMR, *J. Am. Chem. Soc.*, 139 (**2017**) 14173-14180.

[211] B. Fultz, J.M. Howe, *Transmission Electron Microscopy and Diffractometry of Materials*, Springer, (**2013**).

[212] Y. Wang, F. Guyot, R.C. Liebermann, Electron Microscopy of (Mg,Fe)SiO_3 Perovskite: Evidence for Structural Phase Transitions and Implications for the Lower Mantle, *Journal of Geophysical Research: Solid Earth*, 97 (**1992**) 12327-12347.

[213] W.-L. Wang, H.-Y. Lu, Phase-Transformation-Induced Twinning in Orthorhombic $LaGaO_3$: {121} and [010] Twins, *Am. Ceram. Soc.*, 89 (**2006**) 281-291.

[214] S.-Y. Cheng, N.-J. Ho, H.-Y. Lu, Transformation-Induced Twinning: The 90° and 180° Ferroelectric Domains in Tetragonal Barium Titanate, *J. Am. Ceram. Soc.*, 89 (**2006**) 2177-2187.

[215] G. Richardson, S.E.J. O'Kane, R.G. Niemann, T.A. Peltola, J.M. Foster, P.J. Cameron, A.B. Walker, Can Slow-Moving Ions Explain Hysteresis in the Current–Voltage Curves of Perovskite Solar Cells?, *Energy Environ. Sci.*, 9 (**2016**) 1476-1485.

[216] B. Chen, M. Yang, S. Priya, K. Zhu, Origin of J–V Hysteresis in Perovskite Solar Cells, *J. Phys. Chem. Lett.*, 7 (**2016**) 905-917.

[217] F. Liu, F. Wang, K.R. Hansen, X.Y. Zhu, Bimodal Bandgaps in Mixed Cesium Methylammonium Lead Bromide Perovskite Single Crystals, *J. Phys. Chem. C*, 123 (**2019**) 14865-14870.

[218] Y. Zhou, Z. Zhou, M. Chen, Y. Zong, J. Huang, S. Pang, N.P. Padture, Doping and Alloying for Improved Perovskite Solar Cells, *J. Mater. Chem. A*, 4 (**2016**) 17623-17635.

[219] M. Kulbak, S. Gupta, N. Kedem, I. Levine, T. Bendikov, G. Hodes, D. Cahen, Cesium Enhances Long-Term Stability of Lead Bromide Perovskite-Based Solar Cells, *J. Phys. Chem. Lett.*, 7 (**2016**) 167-172.

[220] T. Duong, J. Peng, D. Walter, J. Xiang, H. Shen, D. Chugh, M. Lockrey, D. Zhong, J. Li, K. Weber, T.P. White, K.R. Catchpole, Perovskite Solar Cells Employing Copper Phthalocyanine Hole-Transport Material with an Efficiency over 20% and Excellent Thermal Stability, *ACS Energy Lett.*, 3 (**2018**) 2441-2448.

[221] X. Tang, M. van den Berg, E. Gu, A. Horneber, G.J. Matt, A. Osvet, A.J. Meixner, D. Zhang, C.J. Brabec, Local Observation of Phase Segregation in Mixed-Halide Perovskite, *Nano Lett.*, 18 (**2018**) 2172-2178.

[222] Y. Hu, E.M. Hutter, P. Rieder, I. Grill, J. Hanisch, M.F. Aygüler, A.G. Hufnagel, M. Handloser, T. Bein, A. Hartschuh, K. Tvingstedt, V. Dyakonov, A. Baumann, T.J. Savenije, M.L. Petrus, P. Docampo, Understanding the Role of Cesium and Rubidium Additives in

Perovskite Solar Cells: Trap States, Charge Transport, and Recombination, *Adv. Energy Mater.*, 8 (**2018**) 1703057.

[223] H.X. Dang, K. Wang, M. Ghasemi, M.-C. Tang, M. De Bastiani, E. Aydin, E. Dauzon, D. Barrit, J. Peng, D.-M. Smilgies, S. De Wolf, A. Amassian, Multi-Cation Synergy Suppresses Phase Segregation in Mixed-Halide Perovskites, *Joule*, 3 (**2019**) 1746-1764.

[224] W. Li, M.U. Rothmann, A. Liu, Z. Wang, Y. Zhang, A.R. Pascoe, J. Lu, L. Jiang, Y. Chen, F. Huang, Y. Peng, Q. Bao, J. Etheridge, U. Bach, Y.-B. Cheng, Phase Segregation Enhanced Ion Movement in Efficient Inorganic $CsPbIBr_2$ Solar Cells, *Adv. Energy Mater.*, 7 (**2017**) 1700946.

[225] J.S. Yun, A. Ho-Baillie, S. Huang, S.H. Woo, Y. Heo, J. Seidel, F. Huang, Y.-B. Cheng, M.A. Green, Benefit of Grain Boundaries in Organic–Inorganic Halide Planar Perovskite Solar Cells, *J. Phys. Chem. Lett.*, 6 (**2015**) 875-880.

[226] D.W. De Quilettes, S.M. Vorpahl, S.D. Stranks, H. Nagaoka, G.E. Eperon, M.E. Ziffer, H.J. Snaith, D.S. Ginger, Impact of Microstructure on Local Carrier Lifetime in Perovskite Solar Cells, *Science*, 348 (**2015**) 683-686.

[227] J.-S. Park, J. Calbo, Y.-K. Jung, L.D. Whalley, A. Walsh, Accumulation of Deep Traps at Grain Boundaries in Halide Perovskites, *ACS Energy Lett.*, 4 (**2019**) 1321-1327.

[228] C. Boulesteix, J. van Landuyt, S. Amelinckx, Identification of Rotation and Reflection Twin by Diffraction and Contrast Experiments in the Electron Microscope, *Phys. Status Solidi (a)*, 33 (**1976**) 595-606.

[229] R. Abbaschian, R.E. Reed-Hill, Physical Metallurgy Principles - Si Version, Cengage Learning, (**2009**).

[230] S. Ranganathan, On the Geometry of Coincidence-Site Lattices, *Acta Crystallographica*, 21 (**1966**) 197-199.

[231] H.T. Pham, T. Duong, W.D.A. Rickard, F. Kremer, K.J. Weber, J. Wong-Leung, Understanding the Chemical and Structural Properties of Multiple-Cation Mixed Halide Perovskite, *J. Phys. Chem. C*, (**2019**).

[232] S. Amelinckx, J. Van Landuyt, The Study of Plannar Interfaces by Means of Electron Microscopy, Diffraction and Imaging Techniques in Material Science (Second Edition), Elsevier (**1978**), 107-151.

[233] C. Boulesteix, J. van Landuyt, S. Amelinckx, Identification of Rotation and Reflection Twin by Diffraction and Contrast Experiments in the Electron Microscope, *Phys. Status Solidi (a)*, 33 (**1976**) 595-606.

[234] W.-L. Wang, H.-Y. Lu, Phase-Transformation-Induced Twinning in Orthorhombic $LaGaO_3$: {121} and [010] Twins, *J. Am. Ceram. Soc.*, 89 (**2006**) 281-291.

[235] J. Zhang, G. Xi, X. Wan, 101-1 Twin Boundary Showing Very Large Deviation from the Theoretical One in Deformed Magnesium Alloy, *Materials Characterization*, 132 (**2017**) 280-283.

[236] Q. Sun, X. Fang, Y. Wang, L. Tan, X. Zhang, Changes in Misorientations of {101-1} Twin Boundaries in Deformed Magnesium Alloy, *J. Mater. Sci*, 53 (**2018**) 7834-7844.

[237] H. Min, M. Kim, S.-U. Lee, H. Kim, G. Kim, K. Choi, J.H. Lee, S.I. Seok, Efficient, Stable Solar Cells by Using Inherent Bandgap of α-Phase Formamidinium Lead Iodide, *Science*, 366 (**2019**) 749-753.

[238] G. Kim, H. Min, K.S. Lee, D.Y. Lee, S.M. Yoon, S.I. Seok, Impact of Strain Relaxation on Performance of α-Formamidinium Lead Iodide Perovskite Solar Cells, *Science*, 370 (**2020**) 108-112.

[239] M. Jeong, I.W. Choi, E.M. Go, Y. Cho, M. Kim, B. Lee, S. Jeong, Y. Jo, H.W. Choi, J. Lee, J.-H. Bae, S.K. Kwak, D.S. Kim, C. Yang, Stable Perovskite Solar Cells with Efficiency Exceeding 24.8% and 0.3 V Voltage Loss, *Science*, 369 (**2020**) 1615-1620.

[240] J.-W. Lee, Z. Dai, T.-H. Han, C. Choi, S.-Y. Chang, S.-J. Lee, N. De Marco, H. Zhao, P. Sun, Y. Huang, Y. Yang, 2d Perovskite Stabilized Phase-Pure Formamidinium Perovskite Solar Cells, *Nat. Commun.*, 9 (**2018**) 3021.

[241] Y. Liu, S. Akin, A. Hinderhofer, F.T. Eickemeyer, H. Zhu, J.-Y. Seo, J. Zhang, F. Schreiber, H. Zhang, S.M. Zakeeruddin, A. Hagfeldt, M.I. Dar, M. Grätzel, Stabilization of Highly Efficient and Stable Phase-Pure $FAPbI_3$ Perovskite Solar Cells by Molecularly Tailored 2D-Overlayers, *Angew. Chem. International Edition*, 59 (**2020**) 15688-15694.

[242] T. Zhang, Q. Xu, F. Xu, Y. Fu, Y. Wang, Y. Yan, L. Zhang, Y. Zhao, Spontaneous Low-Temperature Crystallization of α-$FAPbI_3$ for Highly Efficient Perovskite Solar Cells, *Science Bulletin*, 64 (**2019**) 1608-1616.

[243] Y. Fu, T. Wu, J. Wang, J. Zhai, M.J. Shearer, Y. Zhao, R.J. Hamers, E. Kan, K. Deng, X.Y. Zhu, S. Jin, Stabilization of the Metastable Lead Iodide Perovskite Phase Via Surface Functionalization, *Nano Lett.*, 17 (**2017**) 4405-4414.

[244] M. Kim, G.-H. Kim, T.K. Lee, I.W. Choi, H.W. Choi, Y. Jo, Y.J. Yoon, J.W. Kim, J. Lee, D. Huh, H. Lee, S.K. Kwak, J.Y. Kim, D.S. Kim, Methylammonium Chloride Induces Intermediate Phase Stabilization for Efficient Perovskite Solar Cells, *Joule*, 3 (**2019**) 2179-2192.

[245] R.D. Chavan, D. Prochowicz, P. Yadav, M.M. Tavakoli, A. Nimbalkar, S.P. Bhoite, C.K. Hong, Effect of Cscl Additive on the Morphological and Optoelectronic Properties of Formamidinium Lead Iodide Perovskite, *Solar RRL*, 3 (**2019**) 1900294.

[246] M. Kim, T.K. Lee, I.W. Choi, H.W. Choi, Y. Jo, J. Lee, G.-H. Kim, S.K. Kwak, D.S. Kim, Effects of Cation Size and Concentration of Cationic Chlorides on the Properties of Formamidinium Lead Iodide Based Perovskite Solar Cells, *Sustainable Energy & Fuels*, 4 (**2020**) 3753-3763.

[247] K. Odysseas Kosmatos, L. Theofylaktos, E. Giannakaki, D. Deligiannis, M. Konstantakou, T. Stergiopoulos, Methylammonium Chloride: A Key Additive for Highly Efficient, Stable, and up-Scalable Perovskite Solar Cells, *Energy Environ. Mater.* , 2 (**2019**) 79-92.

[248] J.A. Aguiar, S. Wozny, T.G. Holesinger, T. Aoki, M.K. Patel, M. Yang, J.J. Berry, M. Al-Jassim, W. Zhou, K. Zhu, In Situ Investigation of the Formation and Metastability of Formamidinium Lead Tri-Iodide Perovskite Solar Cells, *Energy Environ. Sci*, 9 (**2016**) 2372-2382.

[249] A.D. Wright, G. Volonakis, J. Borchert, C.L. Davies, F. Giustino, M.B. Johnston, L.M. Herz, Intrinsic Quantum Confinement in Formamidinium Lead Triiodide Perovskite, *Nat. Mater.*, (**2020**).

[250] O.J. Weber, D. Ghosh, S. Gaines, P.F. Henry, A.B. Walker, M.S. Islam, M.T. Weller, Phase Behavior and Polymorphism of Formamidinium Lead Iodide, *Chem. Mater.*, 30 (**2018**) 3768-3778.

[251] Y. Wang, F. Guyot, A. Yeganeh-Haeri, R.C. Liebermann, Twinning in $MgSiO_3$ Perovskite, *Science*, 248 (**1990**) 468-471.

[252] W.-L. Wang, H.-Y. Lu, 〈111〉 Rotation Twins in an Orthorhombic $LaGaO_3$ Perovskite, *Am. Ceram. Soc.*, 90 (**2007**) 264-271.

[253] G.E. Eperon, S.D. Stranks, C. Menelaou, M.B. Johnston, L.M. Herz, H.J. Snaith, Formamidinium Lead Trihalide: A Broadly Tunable Perovskite for Efficient Planar Heterojunction Solar Cells, *Energy Environ. Sci.*, 7 (**2014**) 982-988.

[254] M.I. Saidaminov, J. Kim, A. Jain, R. Quintero-Bermudez, H. Tan, G. Long, F. Tan, A. Johnston, Y. Zhao, O. Voznyy, E.H. Sargent, Suppression of Atomic Vacancies Via Incorporation of Isovalent Small Ions to Increase the Stability of Halide Perovskite Solar Cells in Ambient Air, *Nat. Energy*, 3 (**2018**) 648-654.

[255] D.-Y. Son, J.-W. Lee, Y.J. Choi, I.-H. Jang, S. Lee, P.J. Yoo, H. Shin, N. Ahn, M. Choi, D. Kim, N.-G. Park, Self-Formed Grain Boundary Healing Layer for Highly Efficient $CH_3NH_3PbI_3$ Perovskite Solar Cells, *Nature Energy*, 1 (**2016**) 16081.

[256] J.W. Edington, Electron Diffraction in the Electron Microscope, Palgrave, London**1975**.

[257] E. Strelcov, Q. Dong, T. Li, J. Chae, Y. Shao, Y. Deng, A. Gruverman, J. Huang, A. Centrone, $CH_3NH_3PbI_3$ Perovskites: Ferroelasticity Revealed, *Science Advances*, 3 (**2017**) e1602165.

[258] H. Röhm, T. Leonhard, M.J. Hoffmann, A. Colsmann, Ferroelectric Domains in Methylammonium Lead Iodide Perovskite Thin-Films, *Energy Environ. Sci.*, 10 (**2017**) 950-955.

[259] H. Tang, T.-F.M. Chang, Y.-W. Chai, C.-Y. Chen, T. Nagoshi, D. Yamane, H. Ito, K. Machida, K. Masu, M. Sone, Nanoscale Hierarchical Structure of Twins in Nanograins Embedded with Twins and the Strengthening Effect, *Metals*, 9 (**2019**) 987.

[260] Y. Yu, C. Wang, C.R. Grice, N. Shrestha, J. Chen, D. Zhao, W. Liao, A.J. Cimaroli, P.J. Roland, R.J. Ellingson, Y. Yan, Improving the Performance of Formamidinium and Cesium Lead Triiodide Perovskite Solar Cells Using Lead Thiocyanate Additives, *ChemSusChem*, 9 (**2016**) 3288-3297.

[261] L. Wang, K. Wang, B. Zou, Pressure-Induced Structural and Optical Properties of Organometal Halide Perovskite-Based Formamidinium Lead Bromide, *J. Phys. Chem. Lett.*, 7 (**2016**) 2556-2562.

[262] J. Ye, G. Liu, L. Jiang, H. Zheng, L. Zhu, X. Zhang, H. Wang, X. Pan, S. Dai, Crack-Free Perovskite Layers for High Performance and Reproducible Devices Via Improved Control of Ambient Conditions During Fabrication, *Applied Surface Science*, 407 (**2017**) 427-433.

[263] L.M. Herz, Charge-Carrier Mobilities in Metal Halide Perovskites: Fundamental Mechanisms and Limits, *ACS Energy Lett.*, 2 (**2017**) 1539-1548.

[264] W. Hui, L. Chao, H. Lu, F. Xia, Q. Wei, Z. Su, T. Niu, L. Tao, B. Du, D. Li, Y. Wang, H. Dong, S. Zuo, B. Li, W. Shi, X. Ran, P. Li, H. Zhang, Z. Wu, C. Ran, L. Song, G. Xing, X. Gao, J. Zhang, Y. Xia, Y. Chen, W. Huang, Stabilizing Black-Phase Formamidinium Perovskite Formation at Room Temperature and High Humidity, *Science*, 371 (**2021**) 1359-1364.

[265] Y. Deng, S. Xu, S. Chen, X. Xiao, J. Zhao, J. Huang, Defect Compensation in Formamidinium–Caesium Perovskites for Highly Efficient Solar Mini-Modules with Improved Photostability, *Nat. Energy*, 6 (**2021**) 633-641.

[266] Z. Liu, L. Qiu, L.K. Ono, S. He, Z. Hu, M. Jiang, G. Tong, Z. Wu, Y. Jiang, D.-Y. Son, Y. Dang, S. Kazaoui, Y. Qi, A Holistic Approach to Interface Stabilization for Efficient Perovskite Solar Modules with over 2,000-Hour Operational Stability, *Nat. Energy*, 5 (**2020**) 596-604.

[267] M. Lyu, N.-G. Park, Effect of Additives AX (A = FA, MA, Cs, Rb, NH_4, X = Cl, Br, I) in $FAPbI_3$ on Photovoltaic Parameters of Perovskite Solar Cells, *Solar RRL*, 4 (**2020**) 2000331.

[268] D. Kim, H.J. Jung, I.J. Park, B.W. Larson, S.P. Dunfield, C. Xiao, J. Kim, J. Tong, P. Boonmongkolras, S.G. Ji, F. Zhang, S.R. Pae, M. Kim, S.B. Kang, V. Dravid, J.J. Berry, J.Y. Kim, K. Zhu, D.H. Kim, B. Shin, Efficient, Stable Silicon Tandem Cells Enabled by Anion-Engineered Wide-Bandgap Perovskites, *Science*, 368 (**2020**) 155-160.

[269] H. Lu, Y. Liu, P. Ahlawat, A. Mishra, W.R. Tress, F.T. Eickemeyer, Y. Yang, F. Fu, Z. Wang, C.E. Avalos, B.I. Carlsen, A. Agarwalla, X. Zhang, X. Li, Y. Zhan, S.M. Zakeeruddin, L. Emsley, U. Rothlisberger, L. Zheng, A. Hagfeldt, M. Grätzel, Vapor-Assisted Deposition of Highly Efficient, Stable Black-Phase $FAPbI_3$ Perovskite Solar Cells, *Science*, 370 (**2020**) eabb8985.

[270] N.J. Jeon, J.H. Noh, W.S. Yang, Y.C. Kim, S. Ryu, J. Seo, S.I. Seok, Compositional Engineering of Perovskite Materials for High-Performance Solar Cells, *Nature*, 517 (**2015**) 476-480.

[271] E.T. Hoke, D.J. Slotcavage, E.R. Dohner, A.R. Bowring, H.I. Karunadasa, M.D. McGehee, Reversible Photo-Induced Trap Formation in Mixed-Halide Hybrid Perovskites for Photovoltaics, *Chemical Science*, 6 (**2015**) 613-617.

[272] L. Luo, Y. Zhang, N. Chai, X. Deng, J. Zhong, F. Huang, Y. Peng, Z. Ku, Y.-B. Cheng, Large-Area Perovskite Solar Cells with $Cs_xfa_{1-X}pbi_{3-Y}br_y$ Thin Films Deposited by a Vapor–Solid Reaction Method, *J. Mater. Chem. A*, 6 (**2018**) 21143-21148.

[273] S. Kundu, T.L. Kelly, In Situ Studies of the Degradation Mechanisms of Perovskite Solar Cells, *EcoMat*, 2 (**2020**) e12025.

[274] C. Zheng, O. Rubel, Unraveling the Water Degradation Mechanism of $CH_3NH_3PbI_3$, *J. Phys. Chem. C*, 123 (**2019**) 19385-19394.

[275] A. Alberti, C. Bongiorno, E. Smecca, I. Deretzis, A. La Magna, C. Spinella, Pb Clustering and Pbi_2 Nanofragmentation During Methylammonium Lead Iodide Perovskite Degradation, *Nat. Commun.*, 10 (**2019**) 2196.

[276] W.L. Leong, Z.-E. Ooi, D. Sabba, C. Yi, S.M. Zakeeruddin, M. Graetzel, J.M. Gordon, E.A. Katz, N. Mathews, Identifying Fundamental Limitations in Halide Perovskite Solar Cells, *Adv. Mater.*, 28 (**2016**) 2439-2445.

[277] S. Wang, Y. Jiang, Emilio J. Juarez-Perez, Luis K. Ono, Y. Qi, Accelerated Degradation of Methylammonium Lead Iodide Perovskites Induced by Exposure to Iodine Vapour, *Nat. Energy*, 2 (**2016**) 16195.

[278] C.C. Boyd, R. Cheacharoen, T. Leijtens, M.D. McGehee, Understanding Degradation Mechanisms and Improving Stability of Perovskite Photovoltaics, *Chemical Reviews*, 119 (**2019**) 3418-3451.

[279] T.A.S. Doherty, S. Nagane, D.J. Kubicki, Y.-K. Jung, D.N. Johnstone, A.N. Iqbal, D. Guo, K. Frohna, M. Danaie, E.M. Tennyson, S. Macpherson, A. Abfalterer, M. Anaya, Y.-H. Chiang, P. Crout, F.S. Ruggeri, S. Collins, C.P. Grey, A. Walsh, P.A. Midgley, S.D. Stranks, Stabilized Tilted-Octahedra Halide Perovskites Inhibit Local Formation of Performance-Limiting Phases, *Science*, 374 (**2021**) 1598-1605.

[280] Y.T. Zhu, X.Z. Liao, R.Z. Valiev, Formation Mechanism of Fivefold Deformation Twins in Nanocrystalline Face-Centered-Cubic Metals, *Appl. Phys. Lett.*, 86 (**2005**) 103112.

[281] H.M. Yu, H.M. Oh, D.Y. Park, M.S. Jeong, Nanochemical Investigation of Degradation in Organic–Inorganic Hybrid Perovskite Films Using Infrared Nanoscopy, *J. Phys. Chem. C*, 124 (**2020**) 3915-3922.

[282] L. Liu, J. Lu, H. Wang, Z. Cui, G. Giorgi, Y. Bai, Q. Chen, A-Site Phase Segregation in Mixed Cation Perovskite, *Materials Reports: Energy*, (**2021**) 100064.

[283] S. Chen, P. Gao, Challenges, Myths, and Opportunities of Electron Microscopy on Halide Perovskites, *J. Appl. Phys.*, 128 (**2020**) 010901.

[284] Y.H. Deng, L.G. Nest, Analysis of Misidentifications in TEM Characterisation of Organic-Inorganic Hybrid Perovskite Material, *J. Microsc.*, 282 (**2021**) 195-204.

[285] L. Liu, D. Zhang, Y. Zhu, Y. Han, Bulk and Local Structures of Metal–Organic Frameworks Unravelled by High-Resolution Electron Microscopy, *Commun. Chem.*, 3 (**2020**) 99.

[286] K.C. Bustillo, S.E. Zeltmann, M. Chen, J. Donohue, J. Ciston, C. Ophus, A.M. Minor, 4D-STEM of Beam-Sensitive Materials, *Accounts of chemical research*, 54 (**2021**) 2543-2551.

[287] Y. Zhang, Y. Li, L. Zhang, H. Hu, Z. Tang, B. Xu, N.-G. Park, Propylammonium Chloride Additive for Efficient and Stable $FAPbI_3$ Perovskite Solar Cells, *Adv. Energy Mater.*, 2102538.